Advanced design of periodical structures by laser interference metallurgy in the micro/nano scale on macroscopic areas

Dissertation

zur Erlangung des Grades des
Doktors der Ingenieurwissenschaften
der Naturwissenschaftlich-Technischen Fakultät III
Chemie, Pharmazie, Bio- und Werkstoffwissenschaften
der Universität des Saarlandes

von

Andrés Fabián Lasagni

Saarbrücken, Germany
2006

Dedicado a mis padres Renata y Norberto,
a la "nonna" Emma, a mis hermanos Fernando,
Reny y Viviana, y a mi amor Barbara

Contents

Acknowledgements

Symbols and abbreviations

List of Symbols

\<AN\>	cumulative absorption
α	absorption coefficient
α_j	angle of the *j*-beam respected to the perpendicular to the interference-plane
A	area
β_j	angle of the *j*-beam respected to the interference-plane
c	speed of light
c_p	specific heat
Δ	dielectric resistive loss term
ΔT_{0m}	is a temperature range, over which the melting transition occurs
ΔT_{0b}	is a temperature range, over which the melting transition occurs
d	period
ε	complex dielectric function
ε_0	dielectric constant in vacuum
ε_1	real part of the complex dielectric function
ε_2	imaginary part of the complex dielectric function
e	electron charge
E	electric field
E_0	electric field amplitude
ϕ	incidence angle of light
f_{LV}	fraction solid-vapour
f_{SL}	fraction solid-liquid
F_{R1}	threshold laser fluence needed to initiate the structuring
F_{R1-2}	threshold laser fluence for the transition R1-R2
F_{R2-3}	threshold laser fluence for the transition R2-R3

xii

h	height of rectangular well
H	magnetic field
H_0	magnetic field amplitude
h_0	layer thickness
i	imaginary
I	intensity
I_0	intensity amplitude, laser fluence
$I(x,y)$	intensity distribution of the interference pattern
$\tilde{I}(x,y)$	intensity distribution of the desired interference pattern
k	wave number
k_r	proportionality constant for total reflectance depending on temperature
k_T	thermal conductivity
k_x	wave-vector coordinate
k_y	wave-vector coordinate
λ	wavelength
λ^*	wavelength
L_b	latent heat of vaporisation
L_c	coherence length
L_m	latent heat of fusion
μ_e	mobility of the electron
n'	complex refractive index of medium
n_1	real part of the complex refractive
n_2	imaginary part of the complex refractive (extinction coefficient)
N_e	number of free chargers
NA	numerical aperture
P^*	desired period
q_a	added power per unit of volume
q_b	power per unit volume required to vaporize

q_m	power per unit volume required to melt
θ_i	incident angle of radiation for the individual beam i
ρ	density
r	cylindrical coordinate of radii
r_b	beam radius
R	total reflectance
R_0	origin ordinate for total reflectance depending on temperature
Rn	resolution
R_p	total reflectance for plane polarisation p (parallel)
R_s	total reflectance for plane polarisation s (perpendicular)
R_{Tm}	reflectance at melting point
σ	electrical conductivity
τ_e	collision time
τ_p	pulse duration
t	time
t_p	pulse time
T	temperature
T_b	boiling temperature
T_g	glass-transition temperature
T_m	melting temperature
$T(x, z, t)$	temperature at the position (x, z) at time t
V	volume
ω	angular frequency
ω_p	is the electron plasma frequency
w	width of rectangular well
z	axial coordinate

List of Abbreviations

AFM	acoustic force microscope
Al-MR	aluminium melting range
DUV	deep ultraviolet
EDS	energy dispersive spectroscopy
EDX	energy dispersive X-rays
FIB	focus ion beam
FFT	fast Fourier transform
FWHM	full width at half maximum
LIMET	laser interference metallurgy
µCP	microcontact printing
µTM	microtransfer moulding
MEMS	micro-electromechanical systems
MIMIC	micromoulding in capillaries
Nd:YAG	Yttrium-Aluminium-Granat crystal doted with 1% Neodymium(3+)-ions
PET	polyethylene terephthalate
PBG	photonic band gap
PVD	physical vapour deposition
R1	regime 1
R2	regime 2
R3	regime 3
REM	replica moulding
SAMIM	solvent-assisted micromoulding
SAMs	self-assembled monolayers
SD	structure depth
SEM	scanning electron microscope
STEM	scanning transmission electron microscope
TEM	transmission electron microscopy

UV   ultraviolet

WLI   white light interferometry

UV   ultraviolet

Abstract

Methods for micro- and nanofabrication of structures are essential for many applications in different scientific areas like physics, chemistry, and materials science. In particular, interference lithography is a widely used method to produce periodic patterns over large areas. However, this method normally requires multiple steps to obtain the final structured surface. The Laser interference Metallurgy method is similar to the interference lithography technique in that an interference pattern is used. However, when using the interference metallurgy method the only step of processing is the irradiation of the surface of the sample with an interference pattern of a high-power pulsed laser without any subsequent steps like development of a photo resist and etching. This results in a direct, periodical, and local heating of the metal based on photo-thermal nature mechanisms with a well-defined long-range order.

In this work, different aspects of the "Laser Interference Metallurgy" method were studied. By means of the interference theory it was demonstrated that many different periodical patterns can be explored. Moreover, the design of advanced patterns has been verified by calculating the solution of the inverse problem. This means that, for a desired periodical pattern, it is possible to establish a configuration of electromagnetic waves that reproduces the pattern.

Several metallic systems were irradiated with the laser interference patterns. In the case of thin metallic film systems, the changes in the topographic types that can be obtained can be explained in terms of the laser fluence which is required to melt or vaporize one or more of the layers of the film. Moreover, it was demonstrated that the local and periodical heat of the interference pattern can successfully serve to create a phase array in a microstructural scale. Bulk metals are structured by the flow of molten material along the surface tension gradient resulting from the temperature gradient. In several cases, the results were compared to thermal simulations. Laser fluences necessary to produce different topography regimes are consistent with the thermal simulations. The consistency of the thermal simulations with the experiments was further verified by means of in-situ electrical measurements. As examples of potential applications of metallic surfaces structured by laser interference metallurgy, the modulation of optical and tribological properties is discussed.

Kurzfassung

Methoden zur Mikro- und Nanostrukturierung sind unabdingbar für viele Anwendungen in unterschiedlichen Wissenschaftszweigen wie z.B. der Physik, Chemie oder in den Materialwissenschaften. Insbesondere die Interferenz-Lithographie ist eine weit verbreitete Methode, um periodische großflächige Mikrostrukturen zu erzeugen. Allerdings beinhaltet die Anwendung dieser Methode mehrere Prozeßschritte um die gewünschte Strukturierung zu realisieren. Bei der Laser Interferenz Metallurgie wird ähnlich wie bei der Interferenz Lithographie die Probe mit einem Interferenzmuster belichtet. Dieser Belichtungsschritt ist im Gegensatz zur Lithographie der einzige Bearbeitungsschritt. Weitere Schritte wie Entwicklung oder Ätzen entfallen. Bei der Laser-Interferenzmetallurgie erfolgt die Belichtung mit einem gepulsten Hochleistungslaser. Dabei werden einzelne kohärente Lichtstrahlen an der Oberfläche zur Interferenz gebracht, woraus eine direkte, ferngeordnet periodische und lokale Aufheizung des Metalls aufgrund photothermischer Wechselwirkungen erfolgt.

In dieser Arbeit werden verschiedene Aspekte der Laser-Interferenzmetallurgie untersucht. Durch die Anwendung der entsprechenden Interferenz-Theorie wird gezeigt, daß verschiedenste periodische Muster bzw. Strukturen verwirklicht werden können. Eine bestimmte Form eines Interferenzmusters kann mittels Lösung des inversen Problems eingestellt werden. Daher kann für beliebige Interferenzmuster die entsprechende Konfiguration von elektromagnetischen Strahlen berechnet werden, die bei Interferenz dieses Muster reproduzieren.

Mehrere metallische Systeme wurden mit Laser Interferenzmustern bestrahlt. Im Fall von metallischen Dünnfilmen können die Änderungen in der Topographie mit der Laserfluenz erklärt werden, die nötig ist, um ein oder mehrere Schichten zu schmelzen oder zu verdampfen. Desweiteren wurde demonstriert, daß der lokale und periodische Wärmeeintrag durch das Interferenzmuster erfolgreich zur Bildung neuer intermetallischer Phasen führen kann. Die Strukturierung von Bulk-Metallen erfolgt durch Materialfluss entlang des Oberflächenspannungsgradienten, der aus dem Temperaturgradienten resultiert. In verschiedenen Fällen wurden die Ergebnisse mit thermischen Simulationen verglichen. Die Laserfluenz, die nötig ist, um ein bestimmtes Topographie-Regime zu verwirklichen, ist konsistent mit den thermischen Simulationen. Die Konsistenz der thermischen Simulationen mit den Experimenten wurde weiterhin durch elektrische in-situ Messungen verifiziert. Als Beispiele für potentielle Anwendungen der mittels Laserinterfernzmetallurgie strukturierten Oberflächen wird die Modulation von optischen und tribologischen Eigenschaften diskutiert.

Summary

Methods for micro- and nanofabrication of structures are essential for many applications in different scientific areas like physics, chemistry, and materials science. In particular, interference lithography is a widely used method to produce periodic patterns over large areas. However, this method normally requires multiple steps to obtain the final structured surface. The Laser interference Metallurgy method is similar to the interference lithography technique in that an interference pattern is used. However, when using the interference metallurgy method the only step of processing is the irradiation of the surface of the sample with an interference pattern of a high-power pulsed laser without any subsequent steps like development of a photo resist and etching. This results in a direct, periodical, and local heating of the metal based on photo-thermal nature mechanisms with a well-defined long-range order. In this work, different aspects of the "Laser Interference Metallurgy" method were studied.

By means of the interference theory it was demonstrated that many different periodical patterns can be explored. Moreover, the design of advanced patterns has been verified by calculating the solution of the inverse problem. This means that, for a desired periodical pattern, it is possible to establish a configuration of electromagnetic waves that reproduces the pattern.

Due to the photo-thermal interaction of laser light with metals, the produced and calculated interference patterns can be replicated on metallic surfaces obtaining several kinds of surface arrays with a well-defined long-range order. Two situations related to the energy per unit area of the laser-beams can be distinguished. For low laser fluences, the relative height of the structure increases at the interference maxima positions, while for high values the opposite is true.

Since the interaction of laser light with metals is relatively well-known, quantitative thermal simulations of the laser interference experiments were developed. In the case of thin metallic film systems, the changes in the topographical types can be explained in terms of the laser fluence which is required to melt or vaporise one or more of the layers of the film. The in-situ electrical measurements, which describe the thermal history of the samples during the laser-pulse interaction, demonstrated the consistency of the thermal simulations. For metallic thin films, the duration of the whole structuring process is between 400 and 600 ns according to both experimental measurements and the numerical calculations.

Furthermore, the structuring mechanisms in the different studied cases are described. For metallic thin film systems, different configurations related to the number of metallic layers and their relative position in the film were studied. EDS analyses of the structured samples have brought valuable information for the interpretation of the layered structure. They permitted the study of the constitutive elements of the film indicating that the intensity of the respective elements of the layer follows their relative thicknesses.

In several cases it was demonstrated that the local and periodical intensity distribution of the interference pattern can successfully serve to create a phase array in a microstructural scale. In this way, it is possible to transform unordered metallic alloys or films into patterns of intermetallic compounds and a lateral intermetallic-metallic composite.

The special characteristic of the structuring of bulk materials must be taken into account. In general, few laser pulses and large periods produce more homogeneous structures. For small periods, due to the large thermal conductivity of metals, the heat is easier evacuated from the interference maxima toward the interference minima and thus the difference in temperature between both regions is low. This effect makes difficult to melt the metal only at the interference maxima.

Two potential applications of patterned metallic surfaces were studied.

1) Photo-thermal solar absorbers: spectral properties of the structured samples indicate that the larger the aspect ratio, the better the solar absorbance. Moreover, due to the increase of the surface roughness, the diffuse reflectance also increases. Due to the small period of the structures, thermal emittance does not increase considerably at room temperature. These observations were also confirmed by numerical calculations.

2) Tribological properties of line-like periodical structures: it was verified that surface texturing by laser interference metallurgy is an effective key to friction reduction. The reduction of the friction coefficient is due to the lower contact area of the patterned surface. Moreover, thanks to the very short time which is required for the surface processing in comparison with other techniques like direct laser writing, the laser interference metallurgy presents ideal characteristic for industrial applications.

Zusammenfassung

Methoden zur Mikro- und Nanostrukturierung sind unabdingbar für viele Anwendungen in unterschiedlichen Wissenschaftszweigen wie z.B. der Physik, Chemie oder in den Materialwissenschaften. Insbesondere die Interferenz-Lithographie ist eine weit verbreitete Methode, um periodische großflächige Mikrostrukturen zu erzeugen. Allerdings beinhaltet die Anwendung dieser Methode mehrere Prozeßschritte um die gewünschte Strukturierung zu realisieren. Bei der Laser Interferenz Metallurgie wird ähnlich wie bei der Interferenz Lithographie die Probe mit einem Interferenzmuster belichtet. Dieser Belichtungsschritt ist im Gegensatz zur Lithographie der einzige Bearbeitungsschritt. Weitere Schritte wie Entwicklung oder Ätzen entfallen. Bei der Laser-Interferenzmetallurgie erfolgt die Belichtung mit einem gepulsten Hochleistungslaser. Dabei werden einzelne kohärente Lichtstrahlen an der Oberfläche zur Interferenz gebracht, woraus eine direkte, ferngeordnet periodische und lokale Aufheizung des Metalls aufgrund photothermischer Wechselwirkungen erfolgt. In dieser Arbeit werden verschiedene Aspekte der Laser-Interferenzmetallurgie untersucht.

Durch die Anwendung der entsprechenden Interferenz-Theorie wird gezeigt, daß verschiedenste periodische Muster bzw. Strukturen verwirklicht werden können. Eine bestimmte Form eines Interferenzmusters kann mittels Lösung des inversen Problems eingestellt werden. Daher kann für beliebige Interferenzmuster die entsprechende Konfiguration von elektromagnetischen Strahlen berechnet werden, die bei Interferenz dieses Muster reproduzieren.

Unter Verwendung der photothermischen Wechselwirkung des Laserlichts mit Metallen, können die hergestellten und berechneten Interferenzmuster auf metallischen Oberflächen nachgebildet werden. Dabei können mehrere Formen von Oberflächengittern mit definierter Fernordnung erzielt werden. Es können zwei Fälle hinsichtlich der Energie der Laserstrahlen je Einheitsfläche unterschieden werden. Bei niedrigen Laserfluenzen nimmt die relative Höhe der Struktur an den Positionen der Interferenzmaxima zu, während bei hohen Fluenzwerten der umgekehrte Fall eintritt.

Aufgrund der Tatsache, dass die Wechselwirkung zwischen Laserlicht und Metallen verhältnismäßig gut verstanden ist, konnten quantitative thermische Simulationen der Laserinterferenz-Experimente entwickelt werden. Im Falle von metallischen Dünnschichtsystemen können die Änderungen in den topographischen Typen durch die Laserfluenz ausgedrückt werden, die zum Schmelzen oder zum Verdampfen einer oder mehrerer Schichtlagen benötigt wird. Die in-situ durchgeführten elektrischen Messungen, welche die thermische Geschichte der Proben während der Laserpulswechselwirkung erfassen, bestätigen die Konsistenz der thermischen Simulationen. Bei metallischen dünnen Schichten dauert der gesamte Strukturierungsprozess zwischen 400 und 600 ns in

Übereinstimmung sowohl mit den experimentellen Messungen als auch mit den numerischen Berechnungen.

Zudem werden die Mechanismen der Strukturierung der verschiedenen betrachteten Fälle beschrieben. So werden bei metallischen Dünnschichten Konfigurationen untersucht, die sich durch die Anzahl der metallischen Lagen und deren relative Position innerhalb der Dünnschicht unterscheiden. Die EDS-Analyse der strukturierten Proben lieferten auf indirektem Weg wertvolle Informationen über die Gestalt und Dickenverhältnisse der einzelnen Schichtlagen. Diese konnten zur Interpretation des Aufbaus der Multischicht verwendet werden. Dabei zeigte sich, dass die Signalintensität der die Lagen aufbauenden Elemente deren jeweiligen relativen Dicken folgt.

In vielen Fällen konnte nachgewiesen werden, dass die lokale periodische Energieverteilung des Interferenzmusters erfolgreich dazu eingesetzt werden kann, ein Phasengitter auf mikrostruktureller Skala herzustellen. Auf diese Art und Weise ist es möglich, ungeordnete metallische Legierungen oder Schichten in geordnete Muster intermetallischer Verbindungen zu überführen, die zusammen ein lateral strukturiertes intermetallisch-metallisches Komposit ergeben.

Ebenso muss das herausragende Charakteristikum strukturierter Volumenmaterialien berücksichtigt werden. Im Allgemeinen erzeugen wenige Laserpulse und große Perioden Strukturen größerer Homogenität. Bei kleinen Perioden wird aufgrund der großen thermischen Leitfähigkeit der Metalle die Wärme von den Interferenzmaxima leichter abgeführt, weshalb der zwischen den beiden Regionen bestehende Temperaturunterschied gering ist. Durch diesen Effekt bedingt ist es schwer, das Schmelzen des Metalls ausschließlich an den Interferenzmaxima stattfinden zu lassen.

Es wurden zwei potenzielle Anwendungen für strukturierte metallische Oberflächen untersucht.

1) Photo-thermische Solarabsorber: Die spektralen Eigenschaften der strukturierten Proben lassen darauf schließen, dass mit zunehmendem Aspektverhältnis die Absorption von Sonnenlicht ansteigt. Zudem wird durch die Zunahme der Oberflächenrauigkeit der diffuse Anteil der Reflexion gesteigert. Aufgrund der geringen Strukturperiode nimmt die thermische Strahlungsdichte bei Raumtemperatur nicht wesentlich zu. Auch diese Beobachtungen wurden anhand von numerischen Simulationen bestätigt.

2) Tribologische Eigenschaften linienartiger periodischer Strukturen: Es konnte nachgewiesen werden, dass die Oberflächentexturierung mittels Laser-Interferenz-Metallurgie ein effektiver Weg zur Reduzierung der Reibung darstellt. Die Abnahme des Reibungskoeffizienten ergibt sich aus der geringeren effektiven Kontaktfläche der strukturierten Oberfläche. Darüber hinaus weist die Laser-Interferenz-Metallurgie Eigenschaften auf, die ideal für die Bedürfnisse einer industriellen Anwendung zugeschnitten sind. Insbesondere ist dies durch die geringe Prozesszeit im Vergleich zu anderen Techniken wie Direct-Laser-Writing gegeben.

Chapter 1

Introduction

Methods for micro- and nanofabrication of structures are essential to scientific and technological progresses in many areas of biology, physics, chemistry, and materials science. In particular, interference lithography is a widely used method to produce periodic patterns over large areas. In most applications, interference fringes of two mutually coherent beams are recorded to obtain one-dimensional patterns. For applications that require two-dimensional periodic patterns, interference lithography offers alternative routes. For example, the substrate can be rotated by 90° between two exposures to record a square array of holes. Alternatively multiple beams can be used to form a two-dimensional pattern in a single exposure. However, this method normally requires multiple steps (i.e. exposure of a photoresist, etching, and development of the photoresist) to obtain the final structured surface.

The laser interference structuring of metallic systems makes use of the interference lithography method but with the additional advantage of irradiating the sample surface with an interference pattern of a high-power pulsed laser. This results in a direct, periodical, and local heating of the metal based on photo-thermal interaction. Thus, different metallurgical effects such as melting, recrystallisation, recovery, defect, and phase formation in the lateral scale of the microstructure can be initiated. Additionally, a long-range order given by the interference periodicity is obtain. Due to these reasons, the method is called "Laser Interference Metallurgy".

This PhD thesis intends to explain the basis of the structuring mechanisms of metallic systems. The studied metallic systems include single and multi-layer thin films as well as bulk materials. The determinations of the experimental factors that control the structuring process are the focus of interest of this study. These factors include physical and thermodynamic properties of the utilised metals, the geometrical configuration of the samples, and the characteristics of the interference patterns. As example of application of the structured metallic surfaces, the modulation of optical and tribological properties is discussed showing the possibility to fabricate selective solar absorbers and low-friction surfaces, respectively.

This work is composed of eight chapters accompanied by four appendices:

The first two chapters represent the introductory part of this work. In order to offer the reader a general approach of the structuring process, different patterning techniques (including methods based on printing, moulding and embossing, and methods which are activated by light, electrons or ions) are reviewed in chapter 2. The patterning techniques are compared with each other in order to show their individual advantages and limitations.

Chapter 3 describes the basics of the interaction between light and metals. In particular the Drude theory and the Hagen-Rubens relation are presented. Special attention is dedicated to the parameters which affect the absorption of light. This effect is relevant for the thermal simulation model. Finally, the effects of the laser pulse-duration (nanosecond, picosecond and femtosecond lasers) on the mechanisms which govern the absorption of laser light are discussed.

Chapter 4 is focused on three different theoretical aspects which are essential in this PhD thesis. The first part of the chapter is dedicated to the interference phenomena. A general equation is presented for the calculation of the interference patterns produced by multiple laser-beams with different geometrical arrangements as well as different partial energies. After that, an approximation to resolve the so-called *inverse problem* for relatively regular structures is described. Finally, a thermal simulation model, which was developed in this thesis, is presented.

Chapter 5 describes the details of the experimental techniques used to design the structure of the materials as well to analyse the dynamics of the laser-pulse interaction with metals, the topography of the periodical structures, and different metallurgical effects which are induced due to the local and periodical laser heating.

Chapter 6 presents and discusses the experimental results related to the structuring mechanism on thin metallic films (with different number of layers and configurations) and bulk materials. In most of the cases, the results are compared to thermal simulations. These are very important to understand the thermal effects which occur during the structuring. The consistency of the thermal simulations is also investigated by comparing them to electrical time-resolved measurements with nanosecond resolution.

Chapter 7 is devoted to the study of the optical and tribological properties of the periodical surfaces. In the case of optical properties investigations, the dependence of the total absorptance on the geometrical parameters of the structures is demonstrated. Measurements of the kinetic friction coefficient on structured samples as well as polished surfaces are also compared. This chapter is presented as an example of the various applications which this technology might have.

Chapter 8 summarises the main results of this work, draws the conclusions and provides an outlook for future projects which would continue the exciting research lines opened during this work.

The appendices given at the end of this study are of great help to visualise different facets of the laser interference technique. In appendix 1, different examples of calculated interference patterns for 3 and 4 laser-beams are shown, which bring a global idea of the possible structures that can be produced. Appendix 2 extends the conception of the inverse problem to more difficult periodical structures. The thermodynamic and physical properties of the metals (some of them temperature dependent) used in the thermal simulations are given in appendix 3. In appendix 4, the structuring of mixed oxide films is described, as example of other types of materials which can be structured by means of this technique.

Chapter 2

Patterning techniques

In the last years, different methods for the fabrication of micro and nano-functional devices have emerged. They also form enabling technologies for applications ranging from microfluidic devices to micro-optical components, from molecular diagnostics to plastic electronics or nano-electromechanical systems. In many cases, these advances are aided by the highly engineered and successful lithographic techniques that are used for microelectronics [1].

Patterning techniques can be principally divided into two groups: (1) methods which require mechanical processes to produce the patterning, and (2) methods which are activated by light, electrons or ions.

The first group includes techniques based on printing, moulding and embossing. These techniques represent new conceptual approaches to the fabrication and manufacturing of new types of structures and devices on planar, curved or flexible substrates. It also appears to be a promising route to structures and systems for emerging applications in biotechnology [2].

The second group includes optical lithography, E-Beam lithography, laser writing, holographic patterning and direct laser interference structuring among others.

Many of the basic principles of these methods are, of course, not conceptually new; embossed gold coins were first produced around 600 BC, and the printing press was invented in the 15th century. Nevertheless, recent research proves that these ideas, and their variations, can be dramatically improved and extended into the nanometre range by introducing advanced materials, chemistries, and processing techniques. The resulting methods possess truly remarkable patterning capabilities.

The process of patterning is also commonly referred to as lithography. It involves a flow of information that typically begins with the design of a pattern in the form of a dataset and ends at a patterned array of features on the surface of a substrate [3]. There can be many steps in between, and each one of these steps may cause a loss of information or result in pattern distortion. In general, a lithographic technique is built upon following key elements:

a) a pre-designed set of patterns in the form of a mask or a master,

b) means to mediate the transfer or replication patterns,

c) a responsive medium, which is usually a functional material capable of serving as the resist for subsequent steps,

d) and tools that ensure appropriated metrology.

Depending on the application, the requirements of a successful lithographic process can vary substantially. The critical feature size of the test patterns is probably the most obvious issue. One has to consider it, when selecting a proper lithographic technique (see Table 2.1).

Method	*Resolution**	*Ref*
injection moulding	10 nm	[4, 5]
embossing (imprinting)	25 nm	[6, 7]
cast moulding	50 nm	[8, 9]
laser ablation	70 nm	[10, 11]
micromachining with a sharp stylus	100 nm	[12]
laser-induced deposition	1 µm	[13]
electrochemical micromachining	1 µm	[14]
silver halide photography	5 µm	[15]
pad printing	20 µm	[16]
screen printing	20 µm	[17]
ink-jet printing	50 µm	[18, 19]
electrophotography (xerography)	50 µm	[20]
stereolithography	100 µm	[21]
soft lithography		
microcontact printing (µCP)	35 nm	[22]
replica moulding (REM)	30 nm	[23]
microtransfer moulding (µTM)	1 µm	[24]
micromoulding in capillaries (MIMIC)	1 µm	[25]
solvent-assisted micromoulding (SAMIM)	60 nm	[26]

Table 2.1. *Non-photolithographic methods for micro- and nanofabrication. (*) The lateral dimension of the smallest feature that has been generated.*

This chapter intends to provide a general review of the various techniques of patterning. Several of the topics presented here demonstrate the power of these lithographic techniques through their application to functional prototype systems that would be difficult or impossible to realize with conventional approaches. At the end of this chapter (sections 2.7 and 2.8), a more detailed review of "Holographic patterning" and "Direct laser interference structuring" is given, introducing the method employed

in this study. The most relevant past results in polymers, semiconductors and metals are illustrated.

2.1- Optical lithography

The name optical lithography comes from the early application where the exposing energy was visible light. While those wavelengths can still be used, the push to reduce the size of feature sizes has lead to the use of shorter wavelengths to increase resolution. Ultraviolet (UV) and deep ultraviolet (DUV) sources are also now employed. These sources include excimer lasers which operate at wavelengths of 248 nm, 193 nm, and less. Visible wavelengths end in the red at about 400 nm. At these shorter wavelengths, particularly 193 nm, optical materials and even air absorb the energy very well [27].

In optical lithography, printing is the process of projecting the image of the patterns onto the substrate surface using a light source and a photo-mask. Patterned masks, usually composed of glass or chromium, are used during printing to cover areas of the photoresist layer that shouldn't get exposed to light. Development of the photoresist in a developer solution after its exposure to light produces a resist pattern on the substrate, which defines which areas of the substrate are exposed for material deposition or removal (Fig. 2.1).
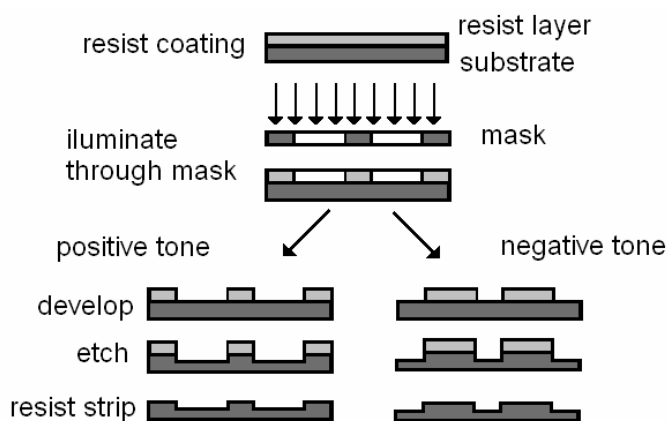
Figure 2.1. Optical lithography method. The projection optical system is used to expose the resist film to light in the shape of desired patterns. This exposure creates a chemical change in the resist film which depending on the tone of the resist makes the exposed resist region more or less soluble in a developing solvent. The resist film is developed to produce desired protective relief pattern. The resist pattern is used in subsequent processes such as etching, and the resist film is finally removed.

There are two types of photoresist material, namely, negative and positive photoresist. Negative resists are those that become less soluble in the developer solution when exposed to light, forming negative images of the mask patterns on the

wafer. On the other hand, positive resists are those that become more soluble in the developer when exposed to light, forming positive images of the mask patterns on the substrate.

Commercial negative photoresists normally consist of two parts: 1) a chemically inert polyisoprene rubber; and 2) a photoactive agent. When exposed to light, the photoactive agent reacts with the rubber, promoting cross-linking between the rubber molecules that make them less soluble in the developer. Such cross-linking is inhibited by oxygen, so this light exposure process is usually done in a nitrogen atmosphere.

Positive resists also have two major components: 1) a resin; and 2) a photoactive compound dissolved in a solvent. The photoactive compound in its initial state is an inhibitor of dissolution. Once this photoactive dissolution inhibitor is destroyed by light, however, the resin becomes soluble in the developer. A disadvantage of negative resists is the fact that their exposed portions swell as their unexposed areas are dissolved by the developer. This swelling, which is simply volume increase due to the penetration of the developer solution into the resist material, results in distortions in the pattern features.

Since optical lithography works so well (producing 180 nm features in modern Intel fabs), the question becomes: "Why not simply use masks with ever smaller features?" Obviously smaller mask features translates to smaller surface features. While this is true, there is another limitation to any optical system: the wavelength of light used. The resolution of any optical system (be it a microscopy or lithographic system) is limited both by configuration and the wavelength of light [28, 29]:

$$Rn = k \frac{\lambda}{NA}$$
(2.1)

where the resolution, *Rn,* is defined by configuration features (k is usually on the order of 1) and NA, the numerical aperture, on the order of 1.6, and λ the wavelength of light.

This effect is called the diffraction limit. Diffraction is an inevitable consequence of the wave nature of light, and is responsible for the spreading of light as it passes through, for example, a slit cut into a screen. This means that feature sizes can typically only be made on the order of the wavelength of light used. At best, features at half the wavelength of light can be created, but no smaller.

2.2- E-Beam lithography

For lateral structuring below the resolution limit of photolithography (> 200 nm), electron-beam lithography is by far the widest spread lithography tool. Compared to other nanostructuring methods, it combines high resolution with excellent flexibility and reasonable patterning speed.
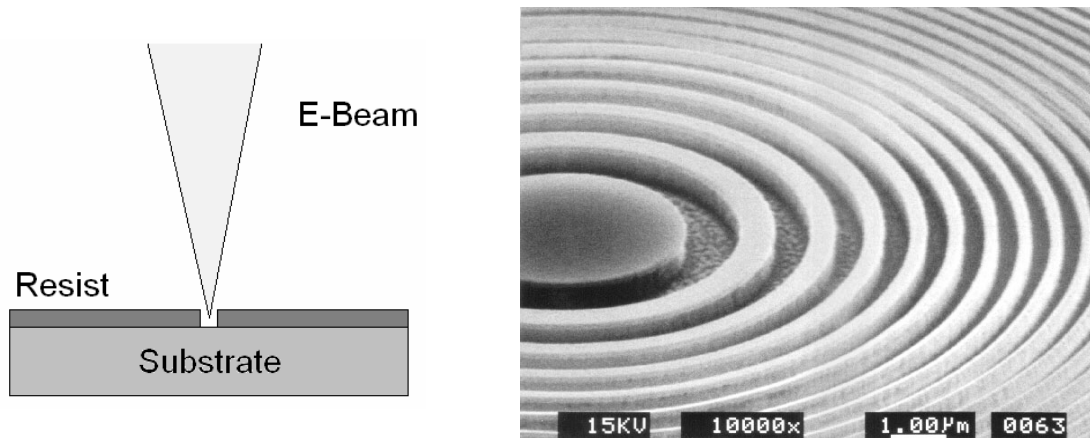
Figure 2.2. *(a) Schema of a focused electron-beam inducing changes in a resist material. (b) A Bragg-Fresnel lens for x-rays exposed in continuous path control mode and etched into Si* [30].

The setup of E-beam Lithography is similar to a Scanning Electron Microscope and often a scanning electron microscope is used. The dissipation of beam energy can proceed in a number of different ways and may include various types of physical and chemical processes, depending on the type of radiation, its dose, and the materials that are involved. Generally, the patterning process can be additive, involving the deposition of species in or close to the illuminated spot, or subtractive, due to the removal of material from the surface of a substrate [31].

The scan rate is adjusted to deliver a critical dose of electrons to a selected area of the resist. Any structure desired can be created as a CAD file and written directly using suitable control software. Thus this method is ideally suited for developing prototypes and no masks are required.

The resist is either developed in a chemical bath similar to photolithography, or the electron-beam interacts with the material sufficiently to remove the resist material (Fig. 2.2). The result from exposing a resist is that the molecular linear chain is broken and the average molecular weight of the polymer exposed area is reduced. Reducing the molecular weight of the polymer is accompanied by an increase of the solubility, and therefore in the etching rate. Thus, the principal result from exposure is a pattern drawn in terms of etching rate.

2.3- Imprint lithography

Imprint lithography involves two steps: imprinting and pattern-transfer (Fig. 2.3). In the imprinting step, a mould with nanostructures on its surface is used to deform a thin resist film or an active material deposited on a substrate. In the pattern-transfer step, an anisotropic etching process such as reactive ion-etching is used to remove the residual resist in the compressed area, transferring the thickness-contrast pattern created by the imprint into the entire resist [30, 32].
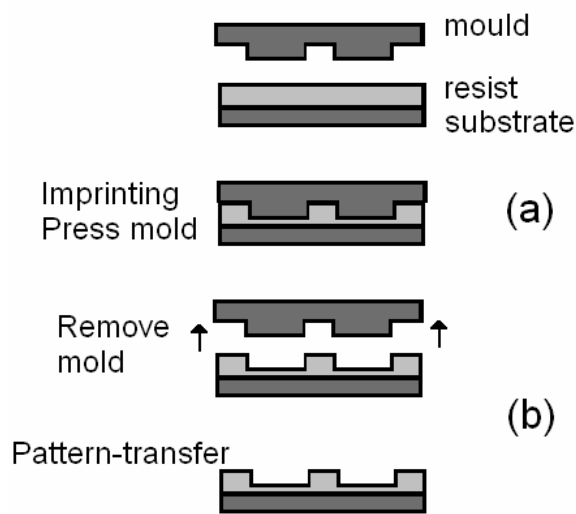
Figure 2.3. Schematic illustration of the imprint lithography process:
(a) Imprinting, using a mould to create a thickness contrast in a resist.
(b) Pattern-transfer, using anisotropic etching (reactive ion etching) to remove residue resist in the compressed areas.
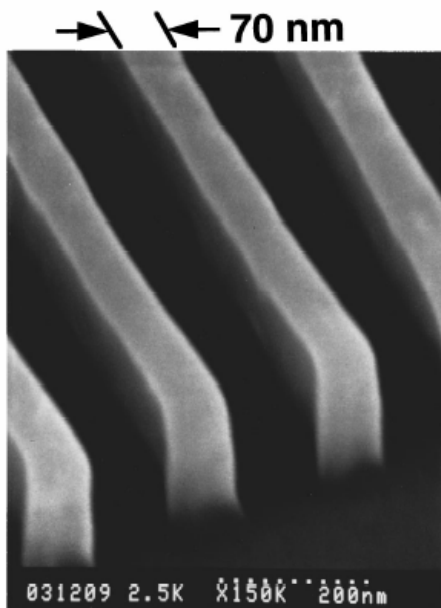
Figure 2.4. SEM micrograph of a perspective view of strips formed into a PMMA film by imprint. The strips are 70 nm wide and 200 nm tall, have a high aspect ratio, a surface roughness less than 3 nm, and nearly perfect 90° corners [33].

The polymer must be either thermoplastic, UV- or thermically curable, or otherwise deformable to adapt the shape of the patterns on the master. In the case of thermoplastic materials, the substrate must be heated above its glass-transition temperature (T_g) during imprinting, and then cooled below T_g before it is separated from the master. When the polymer is a UV- or thermally curable material, it is imprinted in its liquid state, and then hardened into patterned structures through a UV- or thermal-curing process. In most cases, residual films of the polymer remain in the compressed areas, which can be removed using a dry etching process.

Imprint lithography is primarily a physical-deformation process and is fundamentally different from other lithographic methods such as "stamping" with self-assembling "ink" [22]. Its simple yet unique principle allows this method to avoid many problems inherent in other lithographic methods and to achieve high resolution and high throughput at a low cost. The resolution of imprint lithography is determined by the mechanical strength of the mold and polymer.

Imprint lithography can be carried out using three different types of imprinting machines: single-imprint, step-and-repeat, and roller. The single-imprint machine imprints an entire wafer at one time (Fig. 2.3). The step-and-repeat machine imprints a small area (called a die) of a wafer at a time and then moves to a new area of the wafer. The process is repeated until the entire wafer is imprinted. One advantage of the step-and-repeat method is that it is easier to achieve higher alignment accuracy in a smaller area than in a larger area. A second advantage, and probably the most significant advantage for many applications, is that it allows the use of a very small mould to create a large imprint area or a large imprint mould. It takes several days of current electron-beam lithography to expose 10 nm features over the entire area of a 1 cm x 1 cm mold. Using step-and-repeat imprint lithography, the 1 cm x 1 cm mould can be used to pattern a much larger mould (e.g., an 8 in. diameter mould) in just few minutes. Fig. 2.4 shows 70 nm lines fabricated on a PMMA resist.

Roller-nanoimprinting machines have the advantage of better uniformity, less imprint force, simple construction, and the ability to use a mask continuously on a large substrate [34]. There are two ways to use Roller-nanoimprinting (Fig. 2.5). One uses a cylindrical mould, which can be made by bending a thin metal mould around a smooth roller. The other uses a smooth roller over a flat mould. To keep the shape of previously imprinted patterns while imprinting other areas, the substrate is held at a temperature below T_g of the resist, but above T_g of the mould.

2.4- Replica moulding

Replica moulding duplicates the information – for example, the shape, the morphology, and the structure – present in a master (see Fig. 2.6). It is a procedure that accommodates a wider range of materials than does photolithography. It also allows duplication of three-dimensional topologies in a single step, whereas photolithography is not able to replicate such structures. It has been used for the mass production of surface relief structures such as diffraction gratings, holograms, compact disks (CDs), and micro-tools. Replica moulding with an appropriate material (usually in the form of a precursor) enables highly complex structures in the master to be faithfully duplicated into multiple copies with nanometre resolution in a reliable, simple, and inexpensive way [35, 36].
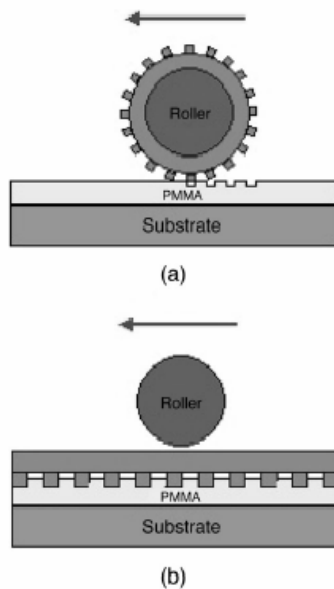
Figure 2.5. Two ways for roller nanoimprint: (a) imprints using a cylinder mould: bending a compact master disk into cylinder shape, mounting it around the roller, and rolling the roller on the substrate; (b) imprints using a flat mould: putting the mould directly on the substrate, and rotating the roller on top of the mould [34]*.*

The fidelity of replica moulding is determined by Van der Waals interactions, wetting, and kinetic factors such as filling of the mould. These physical interactions should allow more accurate replication of features that are smaller than 100 nm than does photolithography, which is limited by optical diffraction.

The procedure for replica moulding of [23] differs from conventional procedures in the use of an elastomeric mould rather than a rigid mould. The elasticity and low surface energy of the elastomeric mould allows it to be released easily. An elastomeric mould also offers the opportunity to manipulate the size and shape of features present on the mould by mechanical deformation. The capability and versatility of this new procedure has been demonstrated for nano-manufacturing. Conventional high-resolution nano-lithographic techniques are used to make

12

masters, and these structures are then duplicated into multiple copies by replica moulding with organic polymers. This technique has also been adapted for the fabrication of topologically complex, optically functional surfaces that would be difficult to fabricate with other techniques.

(a) **(b)**
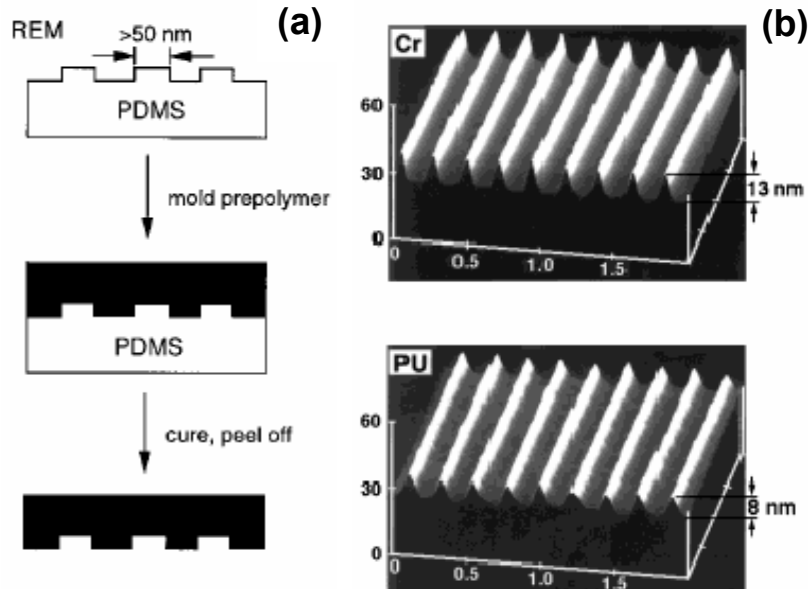
Figure 2.6. (a) Schematic illustration of procedures for replica moulding; REM: Replica moulding, PDMS: polydimethyl-siloxane.
(b) AFM images of chromium structures on a master and a PU (polyurethane) replica prepared from a PDMS mould cast from this master [23]. *The width is given in micrometers; the depth and height are given in nanometres.* [35]

Replica moulding against elastomeric moulds is possible with a resolution on the nanometre scale. For example, in Fig. 2.6b AFM images of chromium structures on a master and a PU replica prepared from a poly(dimethylsiloxane) mould cast against this master are shown. The most important feature of this replicated polyurethane is the accuracy with which the vertical dimension is reproduced. The heights of the chromium lines on the original master were about 13 nm; the heights of the polyurethane lines were about 8 nm. The prepolymer of polyurethane used here shrinks less than 3% upon curing. These images demonstrate that this replica moulding procedure duplicated structures within a few nanometres over substantial areas (ca. 1 mm^2).

2.5- Microcontact printing

Microcontact printing (µC-printing) is a flexible, non-photolithographic method that routinely forms patterned self-assembled monolayers (SAMs) containing regions terminated by different chemical functionalities with submicron lateral dimensions.

This technique uses a silicone stamp to deposit molecules on surfaces. The stamp is first 'inked' with a solution of molecules, often proteins or thiols that then

either coat the stamp or, in the case of small molecules, are absorbed into the silicone in the form of a solid solution. The stamp is dried and pressed onto the surface to be patterned (see Fig. 2.7). The soft silicone stamp makes conformal contact with the surface and molecules are transferred directly from the stamp to the surface in the space of a few seconds. After that, a different SAM can be formed on the untreated regions by washing the patterned substrate with a dilute solution containing the second molecule.
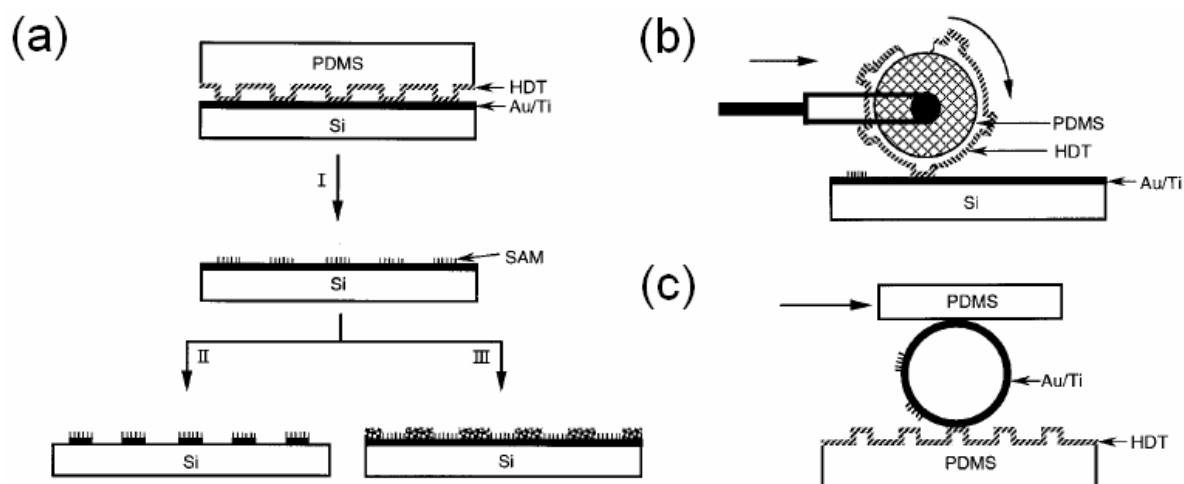
Figure 2.7. Schematic illustration of procedures for micro-contact printing of hexadecanethiol (HDT) on a gold surface: (a) printing on a planar surface with a planar stamp (I: printing of the SAM, II: etching, III: deposition) (b) large-area printing on a planar surface with a rolling stamp, (c) printing on a non planar surface with a planar stamp. After the ™ink (ca. 2 mm HDT in ethanol) was applied to the PDMS stamp with a cotton swab, the stamp was dried in a stream of N2 (ca. 1 min) and then brought into contact with the gold surface (ca. 10 ± 20 s) [35].
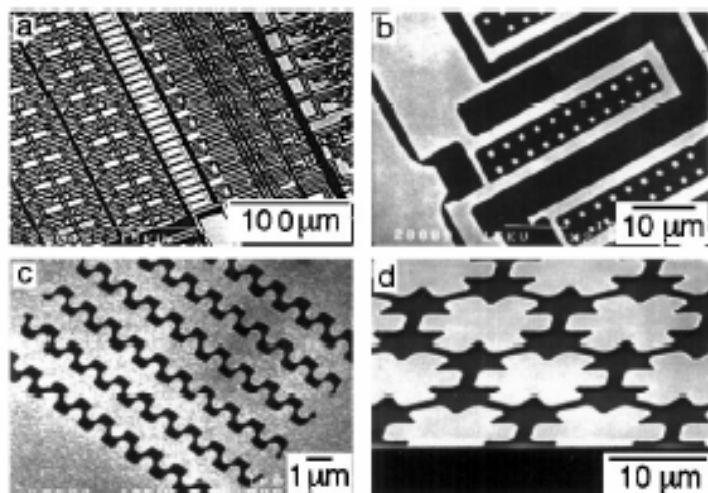
Figure 2.8. SEM images of test patterns of silver (a–c, 50 nm thick; d, 200 nm thick) that were fabricated using microcontact printing with hexadecanethiol, followed by wet chemical etching. The patterns in (a) and (b) were printed with rolling stamps (see Fig.2.7b); the patterns in (c–d) were printed with planar stamps (see Fig. 2.7a). The bright regions are metals; the dark regions are Si/SiO2 exposed where the etchant has removed the unprotected metals [36].

Some examples of test patterns in silver that were fabricated using microcontact printing with hexadecanethiol, followed by wet chemical etching are presented in Fig. 2.8.

The stamps for microcontact printing are normally made using micromachined silicon wafers. The wafers form part of a mould in which liquid silicone is polymerised. On demoulding, a flexible transparent stamp is obtained, with structures that can be as small as 100 nm.

2.6- Laser writing

Writing based on two-photon absorption has emerged as an attractive and versatile tool for generating 3D structures in various polymeric resists [37]. Two-photon excitation provides a means of activating chemical or physical processes with high spatial resolution in three dimensions and has made possible the development of three-dimensional fluorescence imaging, optical data storage and lithographic microfabrication. These applications take advantage of the fact that the two-photon absorption probability depends quadratically on intensity, so under tight-focusing conditions, the absorption is confined at the focus to a volume of order λ^3 (where λ is the laser wavelength). Any subsequent process, such as fluorescence or a photo-induced chemical reaction, is also localised in this small volume.
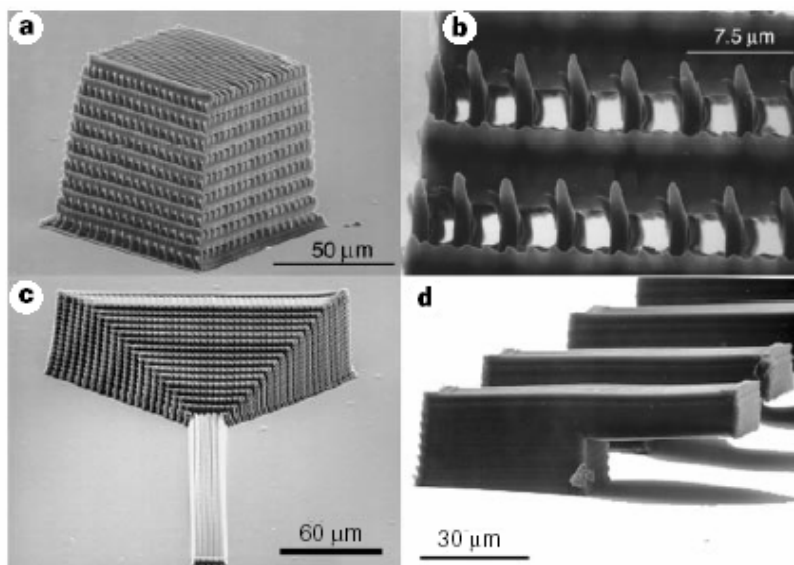
Figure 2.9. *Three-dimensional microstructures produced by two-photon initiated polymerisation. (a) Photonic band-gap structure. (b), Magnified top-view of structure in (a). (c) Tapered waveguide structure. (d) Array of cantilevers. The films were exposed to Ti: sapphire laser pulses (150 fs, 76 MHz, at a wave-length near the two-photon absorption peak of the initiator* [37]*.*

In this technique, photo-polymerisation occurs only in the vicinity of the focal point of a laser-beam thus generating a voxel, which is a 3D volume element of solidified resist. The patterning procedure is performed by pinpoint-scanning a focused laser according to a pre-programmed pattern design in the form of a voxel matrix. The dimensions of such voxel are mainly determined by the spot size and pulse energy of the laser-beam, and can go beyond the limitation of the Rayleight limit.

To illustrate an example of the utility of laser writing, let's consider the fabrication of potentially interesting 3D structures in a photopolymer system. Three-dimensional periodic structures are needed for photonic band gap (PBG) materials, which have unique optical properties. These structures are difficult to fabricate on micrometer or sub-micrometer length scales as needed for applications in the infrared and visible spectral regions. Fig. 2.9a and 2.9b shows views of a "stack-of-logs" structure which, given a sufficiently high refractive index, should exhibit PBG properties in the infrared spectral region. High-refractive-index structures, based for example on refractory ceramics, could be fabricated by using the polymer structure as a preform. Other structures of arbitrary pattern and periodicity down to ~1 µm length scales could be readily obtained with this photopolymer system. Two-photon 3D laser writing could also find application in the production of tapered optical waveguides, such as those shown in Fig. 2.9c. For the example shown, the waveguide cross-section varies along the length from a 100 x 100 µm² square aperture to a 2 x 10 µm² rectangular aperture. Tapered optical waveguides have the potential to reduce optical loss in the coupling of waveguide components with disparate cross-sections. Micro-electromechanical systems (MEMS) are often produced using two-dimensional lithography, and 3D structures are built up by an iteration of processing steps. As an example of MEMS structures easily fabricated with a single development step, we produced the array of polymeric cantilevers shown in Fig. 2.9d.

2.7- Holographic patterning

Holographic patterning involves the interference of two or more laser-beams and allows rapid fabrication (~seconds) and high design flexibility not limited by multi-phase equilibrium [38]. The major advantage of this technique is that it is a relatively simple and fast process which consists of *two steps*: exposure and development.

In the case of two mutually coherent laser-beams interfering, the resultant pattern of field intensity can be readily recorded in a thin film of photoresist. After

development, an array of parallel lines will be created in the photoresist film, in which the spacing (*d*) between the lines is:

$$d = \frac{\lambda}{2n} \sin(\theta/2)$$

(2.2)

where λ is the wavelength of the laser light, *n* is the refractive index of the resist, and θ is the angle of intersection between the two beams [39].
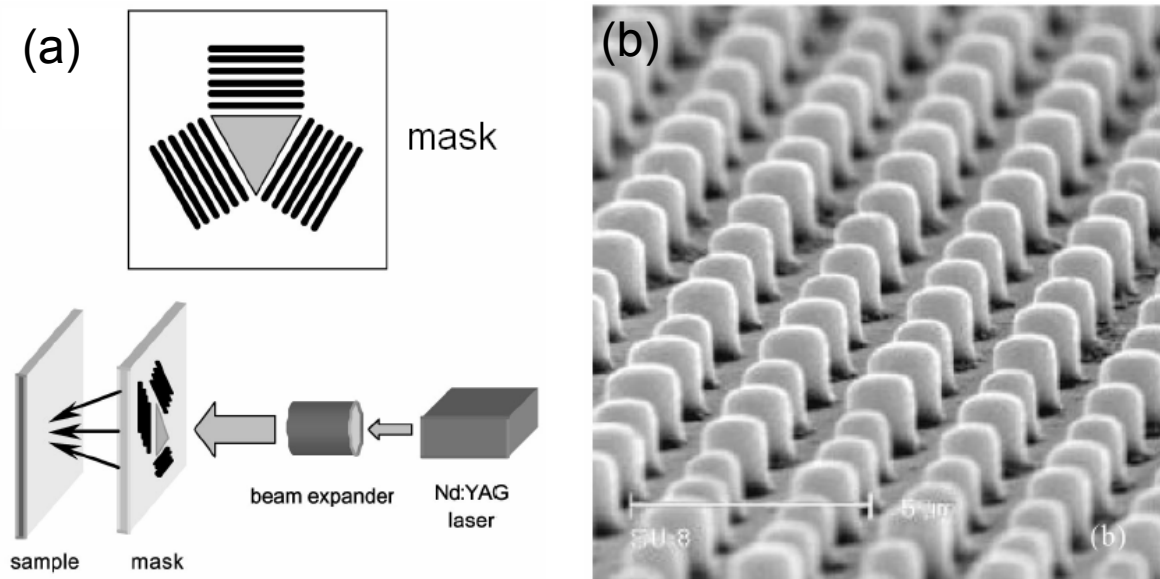
Figure 2.10. *Schematic representation of the (a) three-grating diffraction mask and optical setup for creating the hexagonal interference pattern on the photoresist substrate. (b) SEM image showing the side view of the negative photoresist columns created by interference lithography* [40].

This method is commonly used to fabricate photonic crystals by forming a polymer template exposing the photoresist to the interference pattern [40, 41].

Normally, a diffraction-mask is employed to produce the interference patterns [40-45]. For example Fig. 2.10 shows the interference pattern produced with a collimated Nd:YAG laser-beam impinging on a mask that has three gratings oriented 120° relative to one another. Each grating has 2 mm wide, 4 mm long features separated by 2 mm. The photoresist sample is exposed by placing it at the focal point of the diffraction pattern, yielding a hexagonal array of photoresist columns.

By exposing the same photoresist film to the interference pattern twice (orthogonal to each other), a 2D array of posts will be generated. This technique is widely used in the photonic industry to manufacture holographic diffraction gratings and anti-reflection coatings [11].

More complex pattern can be formed by intersecting more than two laser-beams or by using multiple sequential exposures. For example, when four coherent laser-beams are focused onto the same spot, a 3D periodic lattice will be generated after the exposed regions have been removed by selective dissolution [46, 47]. For example, if the configuration shown in Fig. 2.11a of four wave vectors is employed, the 3D interference pattern shown in Fig. 2.11b is obtained.
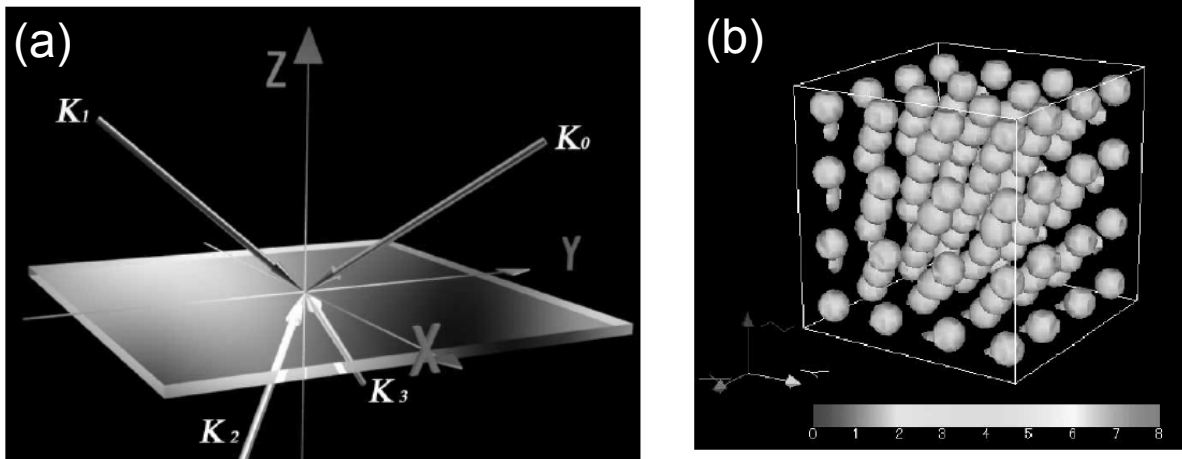
Figure 2.11. *(a) Appearance of four wave vectors that create b.c.c. inference fringe pattern. The four beams are symmetrically arranged. (b) Three-dimensional display of the light intensity distribution for the arrangement shown in (a). Only parts that have intensity greater than the 50%of the maximum value are displayed. The length of each edge is 1.4 µm* [46].

A particularly interesting application of this technique is the fabrication of 3D photonic crystals [47]. Multiple interference between waves scattered from each unit cell of the structure may open a "photonic band gap"; a range of frequencies, analogous to the electronic band gap of a semiconductor, within which no propagating electromagnetic modes exist. Numerous device principles that exploit this property have been identified. Considerable progress has been made in constructing two- and three-dimensional structures using conventional lithography. In the case of three-dimensional holographic lithography, the production of three-dimensional structures with sub-micrometer periodicity was carried out by [47]. With this technique they have made micro-periodic polymeric structures and complementary structures have been produced by using these polymers as templates.

The 3D-periodic microstructure is generated by interference of four non-coplanar laser-beams in a film of photoresist typically 30 µm thick. The intensity distribution in the interference pattern has three-dimensional translational symmetry; its primitive reciprocal lattice vectors are equal to the differences between the wave

vectors of the beams. Highly exposed photoresist is rendered insoluble. Unexposed areas are dissolved away to reveal a three dimensionally periodic structure formed of cross-linked polymer with air-filled voids. The four laser-beam wave vectors determine the translational symmetry and lattice constant of the interference pattern. There remain eight parameters, describing the intensities and polarisation vectors of the four beams that are required to define the intensity distribution within a unit cell (that is, the basis of the interference pattern). These parameters allow considerable freedom in determining the distribution of dielectric material within the unit cell, which in turn determines the photonic band structure. In Fig. 2.12 different SEM micrographs of photonic crystals generated by holographic lithography are shown. The period of the structures is about 0.4 µm.

Figure 2.12. *SEM images of photonic crystals generated by holographic lithography. (a) Polymeric photonic crystal generated by exposure of a 10 µm film of photoresist. The top surface is a (111) plane; the film has been fractured along the {11$\overline{1}$} cleavage planes. Scale bar, 10 µm. (b) Close-up of a (111) surface. Scale bar, 1 µm. (c) Close-up of a (11$\overline{1}$) surface. Scale bar, 1 µm. (d) Inverse replica in titania made by using the polymeric structure as a template. The surface is slightly tilted from the (111) plane. Scale bar, 1 µm. (e) {$\overline{1}$02} surface of a b.c.c. polymeric photonic crystal. Scale bar, 1 µm* [47].
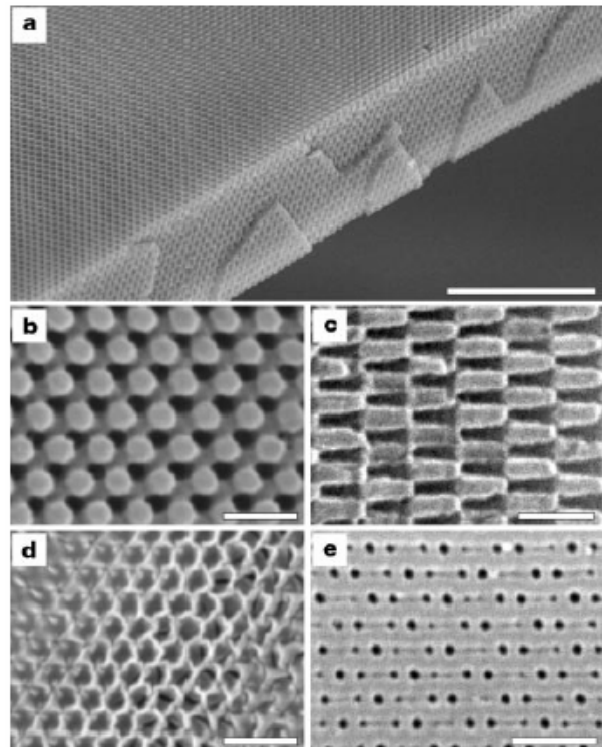
2.8- Direct laser interference structuring

The "direct laser interference structuring " method makes use of interference of two or more laser-beams, like in holographic patterning, but in this case no development of the irradiated sample is needed [48-57]. The most important requirement to produce the periodical structures with this method is that the material to be processed must absorb the energy of the laser at the selected wavelength and the laser must be of high-power. The method allows the production of periodic

structures of features with a well defined long-range order in the scale of typical microstructures (i.e. from the sub micrometer level up to micrometers). The microstructuring process is based on mechanisms of photo-thermal, photo-physical or photo-chemical nature, depending on the type of material [58].

Several types of materials have been processed with this technique using femto- and nanosecond laser pulses. Next, different examples of structured periodical surfaces in semiconductors, polymers, and metals are presented.

2.8.1- Semiconductors

The applicability of illumination with intense laser interference patterns for direct permanent structuring on semiconductor systems were carried out with femto- and nanosecond lasers by [57] and [59], respectively.

(a)

(b)
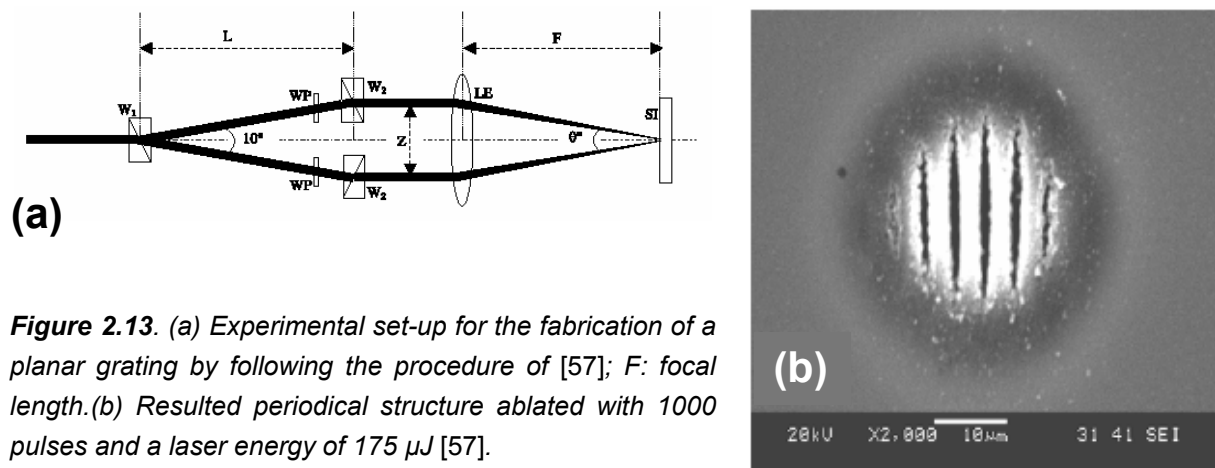
Figure 2.13. (a) Experimental set-up for the fabrication of a planar grating by following the procedure of [57]; F: focal length.(b) Resulted periodical structure ablated with 1000 pulses and a laser energy of 175 µJ [57].

A femtosecond pulse produces extremely high peak power in the range of several hundred TW/cm². This makes femtosecond pulses capable of breaking down almost all materials including transparent materials. The experimental configuration to produce interference patterns with femtosecond pulsed lasers is very difficult because of the short coherence length (micrometers) which is related with the extremely short duration of the pulses [60]. Therefore, an alternative technique to split and to focus two laser-beams at the same position must be used in comparison with nanosecond pulsed lasers [57, 61-63]. One of these possible configurations is shown in Fig. 2.13a [57]. The primary beam is firstly circularly polarised with a quarter waveplate and subsequently made to pass through a 10° Wollaston prism. The outputs of the Wollaston prism are therefore two orthogonally polarised beams with

an angle of 10° between them. In order to obtain parallel beams, the two partial beams are made to pass through 5° Wollaston prisms and then a lens is used to focus the two beams on the sample. Since both the beams are collimated and are parallel to each other, the two beams will interfere only at the focal point of the lens [57]. This technique is optimal for low-power femtosecond pulsed lasers.

As Fig. 2.13b shows the surface is clearly ablated at the interference maxima. The period obtained was 4 µm. In [59, 64], the formation of periodical structures in semiconductors by overlapping nanosecond laser-beams is reported. Two mechanisms related to the internal (where important properties are modulated bellow the surface) and external structuring (where the surface is topographically altered) were described. Internal structuring is based on the manipulation of energy band levels in multilayer epitaxial films of $Al_{1-x}Ga_xAs$. In such systems the band levels are manipulated in the vertical direction (growth) of the films by alteration of the composition and doping of the films. The goal of the laser structuring is to add additional modulation in the lateral directions. External surface structuring was explained because of the melting and oxidation processes which take place at the heated areas (interference maxima) of the pattern. This results in raised regions of a few nanometres [59].

2.8.2- Polymers

The structuring in polymers is conducted by a selective laser ablation process [51, 53-54, 65-66]. The ablation takes place only when the laser-beam is absorbed by the polymer, under the condition that the polymer is exited. Absorption of photons corresponding to ultraviolet and visible regions of the electromagnetic spectrum results in transitions between electronic energy levels in macromolecules. The exited polymer can either decompose directly (photo-chemical ablation) or undergo at first a process of non-radiation relaxation to heat the polymer up to pyrogenation temperature (photo-thermal ablation) [67]. Therefore, the ablation mechanism is influenced by the polymer properties, such as the light absorption coefficient, thermal conductivity, photo-chemical and photo-thermal stability. On the other side, the micro-patterning characteristics (pattern depth, aspect ratio, quality of the periodical structures) is controlled by the laser parameters such as wavelength, repetition rate, pulse width, fluence, and pulse number. It means that for a definite polymer and laser system, the fluence and pulse number can be used to control the pattern depth.

The influence of the laser fluence and the pulse number on the structure depth (height of the micro-patterns) for the polymers polyethylene terephthalate (PET) and

Thermanox ® is shown in Fig. 2.14. Micro-patterning can be normally observed when the fluence exceeds a laser fluence threshold (in these cases about 0.05 J/cm²). This threshold value is related to the minimal energy which is required to initiate the ablation mechanism. The depth of the micro-patterns on both polymers increases linearly until above 0.2 J/cm² (Fig. 2.14a). Above this value, the depth on PET remains nearly stable while increasing on Thermanox ® but in a relative low rate. The influence of the pulse number is given by Fig. 2.14b where a linear increase with the pulse number is observed in both materials up to 10 pulses. These results indicate the most important factors which must be taken into account to control the structure parameters. At a wavelength of 266 nm, no evidence of photo-chemical decomposition was observed [65]. AFM photographs with a higher resolution show regular cracks on the structured surface which are caused by shrinkage of the melted layer during solidification. Additionally, laser ablation also caused variation in the adhesion force of the micro-patterns [66].

(a)   **(b)**
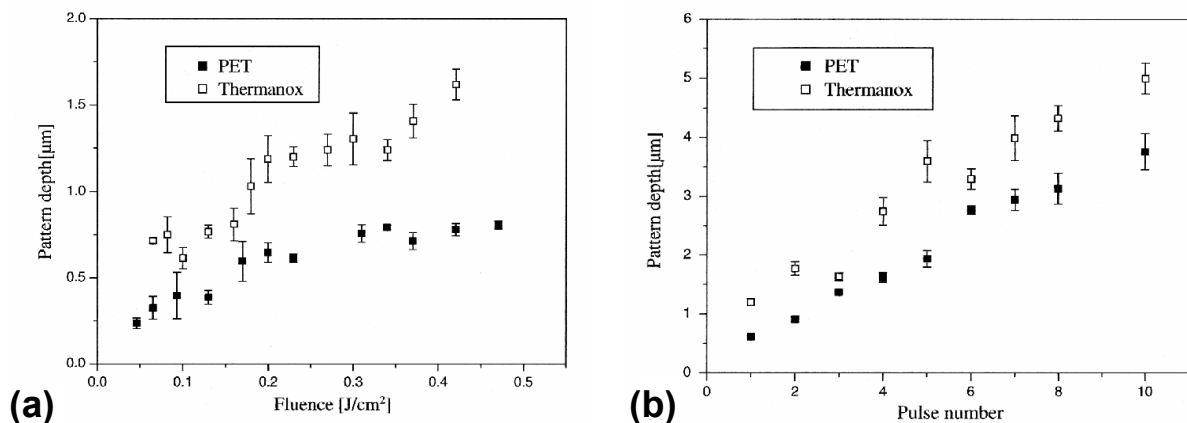
Figure 2.14. *Dependence of the depth of micro-patterns on the laser fluence (a) and number of the laser pulses (b)* [65].

2.8.3- Metals

Laser interference irradiation has been proven to produce periodic structures with surface micro-/nano-structures in the size scale of grains in polycrystals [48]. Due to the short duration of thermal exposure by pulse laser, the phases and morphology e.g. of deposited films can be modified under precise control. Generally speaking, this technique is used to initiate metallurgical processes such as melting, recrystallisation, recovery, defect, and phase formation in the lateral scale of the microstructure itself and with an additional long-range order given by the interference periodicity. Thus, in the case of metals, the technique receives the name of "Laser Interference Metallurgy" [48].

Beside the melting and deformation effects, the possibility of formation of intermetallic phases through the supply of periodical thermal energy in the small scale of a few microns corresponding to the interference periodicity was tested. This allows intermetallic patterning and formation of surface composites and therefore a new kind of tailoring mechanical properties [53].

On a silicon-substrate (silicon wafer c-Si(100)) a Ni–Al film was deposited with a film thickness of 900 nm at 400°C by magnetron sputtering. The atomic ratio of the layer was kept 3:1 for Ni:Al, which is the stoichiometric ratio for Ni_3Al. X-ray diffraction was applied to prove whether or not an intermetallic reaction occurred between Ni and Al. For the characterisation of the consequences in the mechanical properties, a nano-indenter mounted in an AFM was applied to directly check the local hardness of the structured surface within intervals of 200 nm. The hardness in the laser treated area, where laser intensity exceeded a certain threshold level, is substantially higher than that of the area in-between, where the laser intensity was below this threshold level. The average hardness in the laser treated area is close to 10 GPa, while for the 'in-between' area it is around 4 GPa, which is close to the untreated state (Fig. 2.15). The formation of the intermetallic phase Ni_3Al was observed at the interference maxima positions.
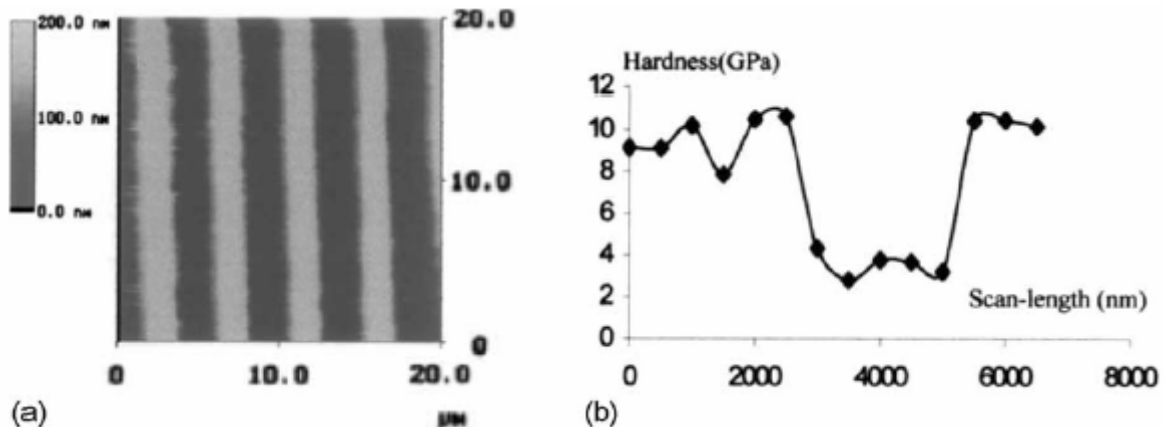
Figure 2.15. AFM image (a) of the Ni–Al structured sample, and (b) the corresponding hardness distribution along the scan length in one period. The line was only drawn for the assistance of eyes [53].

Chapter 3

Review of laser-matter interaction

Laser light, in order to produce any lasting effect on a material, must first be absorbed. The manner in which the energy of the laser is absorbed is basically described by two parameters, the absorption coefficient and the optical reflectance. These two properties not only define the absorbed energy by the material, but also the volume in which it is cumulated.

This chapter introduces the basics of laser-matter interaction. Firstly, the Drude theory and the Hagen-Rubens relation are presented. Secondly, different factors which affect the reflectance in metals are explained. Finally, the effect of the laser pulse-time and the fluence on the physical mechanism which takes place during the absorption of the laser energy are described.

3.1- Fundamental optics properties

The simplest form of light is a monochromatic, linearly polarised plane wave. This is a sufficient approximation of a real laser beam. The electric field of a wave propagating in a homogeneous and non-absorbing medium can be represented as [68]:

$$E = E_0 \, e^{i(2\pi z / \lambda - \omega t)},$$
(3.1)

where z is the coordinate along the direction of propagation, ω is the angular frequency, and λ is the wavelength. The last two variables are related through the phase velocity c / n', c being the speed of light, and n' the refractive index of medium.

An expression analogous to (3.1) also holds for the magnetic field B. The magnetic and electric field amplitudes are related by:

$$E_0 = c \, B_0 ,$$
(3.2)

The energy flux per unit area of the wave is termed irradiance and given by

$$I = \frac{1}{\mu_0} |E \times B| = \frac{1}{c\mu_0} \frac{E_0^2}{2} , \tag{3.3}$$

where μ_0 is the permeability in vacuum.

The concept of a beam implies that the irradiance is maximal near the optical axis and falls off laterally. The most common lateral distribution (cylindrically symmetric Gaussian distribution) is given by:

$$I(r) = I_0 e^{\left(-r^2/r_b^2\right)} , \tag{3.4}$$

where I_0 is the intensity on axis (r = 0) and r_b is referred as to the beam radius.

In absorbing media, the real refractive index n' must be replaced by a complex index $n = n_1 + i\, n_2$. The term n_2 is also called extinction coefficient or damping constant. Introducing this complex index in equation (3.1), the electric field, upon propagation over a distance z, decreases by the factor $exp(\omega\, n_2\, z/c)$, indicating that some of the light energy is absorbed. The absorption coefficient for the irradiance (3.3) is:

$$\alpha = -\frac{1}{I}\frac{dI}{dz} = \frac{2\omega n_2}{c} = \frac{4\pi n_2}{\lambda} . \tag{3.5}$$

In inhomogeneous media the refractive index varies in space, and in certain crystals it even depends on the direction of propagation. Spatial variations of the refractive index deform the wave front, bend the beam path, and cause secondary waves to split off from the primary one. The well-known formula for reflection of a wave perpendicularly incident from vacuum or air onto the plane boundary of a solid with refractive index n is:

$$R = \left|\frac{n-1}{n+1}\right|^2 = \frac{(1-n_1)^2 + n_2^2}{(1+n_1)^2 + n_2^2} . \tag{3.6}$$

The connection between the refractive index and the properties of the medium of propagation is formally provided by Maxwell's equations. Using these, the complex refractive index n can be related with the property ε defined as the complex dielectric function. The real and imaginary parts of n and ε are related by

$$\varepsilon_1 = n_1^2 - n_2^2 \quad ; \quad \varepsilon_2 = 2 n_1 n_2 \tag{3.7}$$

$$n_1^2 = \frac{|\varepsilon| + \varepsilon_1}{2} \quad ; \quad n_2^2 = \frac{|\varepsilon| - \varepsilon_1}{2} \tag{3.8}$$

3.2 - Optical response in metals

3.2.1- Drude theory

Electromagnetic radiation can be represented as an electric vector field and a magnetic vector field (see 3.1.1). When it passes over a small elastically bound charge particle, the particle will be set in motion by the electric force from the electric field E. Provided that the frequency of the radiation does not correspond to a natural resonance frequency of the particle, then fluorescence or absorption will not occur but a forced vibration would be initiated. The force induced by the electric field is very small to vibrate atomic nucleus. We are therefore discussing photons interacting with electrons which are either free or bound.

The optical response of a metal is dominated by the conduction electrons. Since the electron gas is degenerate, only electrons in states close to the Fermi level, referred to as free electrons, contribute to the optical properties. The dielectric complex index can be written as [68]:

$$\varepsilon = 1 + \omega_p^{\;2} \frac{-\tau_e^{\;2} + i\,\tau_e/\omega}{1 + \omega^2\,\tau_e^{\;2}} \quad ; \quad \omega_p = \sqrt{\frac{N_e\,e^2}{m_e\,\varepsilon_0}}\;, \tag{3.9}$$

where ω_p is the electron plasma frequency, τ_e is the collision time, N_e is the number of free chargers, and e is the electron charge.

From (3.9) we can calculate the real and imaginary part of the dielectric complex function as well as its module:

$$\varepsilon_1 = 1 + \omega_p^{\;2}\frac{-\tau_e^{\;2}}{1+\omega^2\,\tau_e^{\;2}} \quad ; \quad \varepsilon_2 = \omega_p^{\;2}\frac{\tau_e}{\omega + \omega^3\,\tau_e^{\;2}}$$

$$\text{(3.10)}$$

$$|\varepsilon| = \sqrt{\varepsilon_1^{\;2} + \varepsilon_2^{\;2}}$$

Solving equation (3.6), the reflectivity can be written as:

$$R = \left(\frac{n_1^{\;2} + n_2^{\;2} - 1}{\left(n_1 + 1\right)^2 + n_2^{\;2}}\right)^2 + \left(\frac{2n_2}{\left(n_1 + 1\right)^2 + n_2^{\;2}}\right)^2 \tag{3.11}$$

where n_1 and n_2 are a function of ε, and this last one can be written as a function of the collision time τ_e and the number of free chargers N_e.

The dependence of these terms with the temperature can be found when introducing the Drude formula [69, 70]:

$$\sigma = N_e\, e^2\, \frac{\tau_e}{m_e} = \omega_p^{\,2}\, \varepsilon_0\, \tau_e\ ,\qquad (3.12)$$

where σ is the electrical conductivity

The microscopic definition of conductivity σ is given by:

$$\sigma = N_e\, e\mu_e\ ,\qquad (3.13)$$

where μ_e is the mobility of the electron.

Comparing (3.13) with (3.12), the mobility μ_e can be defined as:

$$\mu_e = \frac{\tau_e\, e}{m_e}\ .\qquad (3.14)$$

For a homogeneous and isotropic material (e.g. polycrystalline metals or single crystal of cubic semiconductors), the concentration of carriers N_e and their mobility μ_e do not depend on the coordinates - they have the same value everywhere in the material and the specific conductivity σ is a scalar.

In general terms, we may have more than one kind of carriers (this is the common situation in semiconductors) and N_e and μ_e could still be more or less complicated functions of the temperature T, of the local field strength resulting from an applied external voltage, of the detailed structure of the material (e.g. the defects in the lattice), and so on.

These complications are the essence of advanced electronic materials, especially the semiconductors, but in order to simplify the problem, we now will restrict ourselves to the special class of Ohmic materials. We have seen before that this requires N_e and μ_e to be independent of the local field strength. We still may have a temperature dependence of σ; even commercial Ohmic resistors, after all, do show a more or less pronounced temperature dependence which increases roughly linearly with T.

In short, we are treating metals, characterised by a constant density of one kind of carriers (= electrons) in the order of 1, 2 or 3 electrons per atom in the metal. Then we can consider the mobility μ_e as a function of the electrical conductivity and the number of free chargers. Because the dependence of electrical conductivity with the temperature, we can write de mobility μ_e as a function of this last one and the

number of free chargers (considered to be the number of valence electrons per unit volume).

$$\mu_e = \frac{\tau_e\, e}{m_e} = \frac{\sigma(T)}{N_e\, e}. \tag{3.15}$$

From (3.15), the collision time τ_e can be calculated as:

$$\tau_e = \frac{m_e\, \sigma(T)}{N_e\, e^2}. \tag{3.16}$$
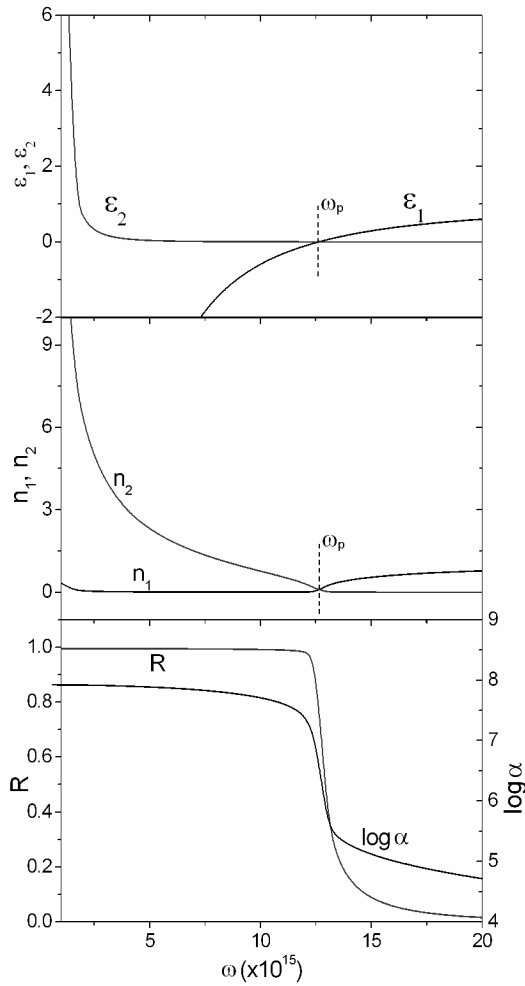
Figure 3.1. *Frequency dependence of the dielectric function, the refractive index, the Fresnel reflectance and the absorption coefficient. $T = 298\ K$, $\tau_e = 3.29 \times 10^{-14}\ s$, and $N_e = 5 \times 10^{28}\ 1/m^3$.*

Replacing (3.16) in (3.9) and using (3.8), the absorption coefficient and the reflectivity can be directly calculated from (3.5) and (3.6), respectively.

If $T = 298\ K$, $\tau_e = 3.29 \times 10^{-14}\ s$, and $N_e = 5 \times 10^{28}\ 1/m^3$, the frequency dependence of the dielectric function, the refractive index, the Fresnel reflectance and the absorption coefficient illustrated in Fig. 3.1 are obtained. The figure indicates that at the plasma frequency ω_p, both ε (ε_1, ε_2) and n (n_1, n_2) vanish and the optical properties change from large R and α (for $\omega < \omega_p$) to small R and α (for $\omega > \omega_p$).

Fig. 3.2 shows the calculation of the absorption coefficient and the reflectivity as a function of the temperature for gold.

(a)

(b)
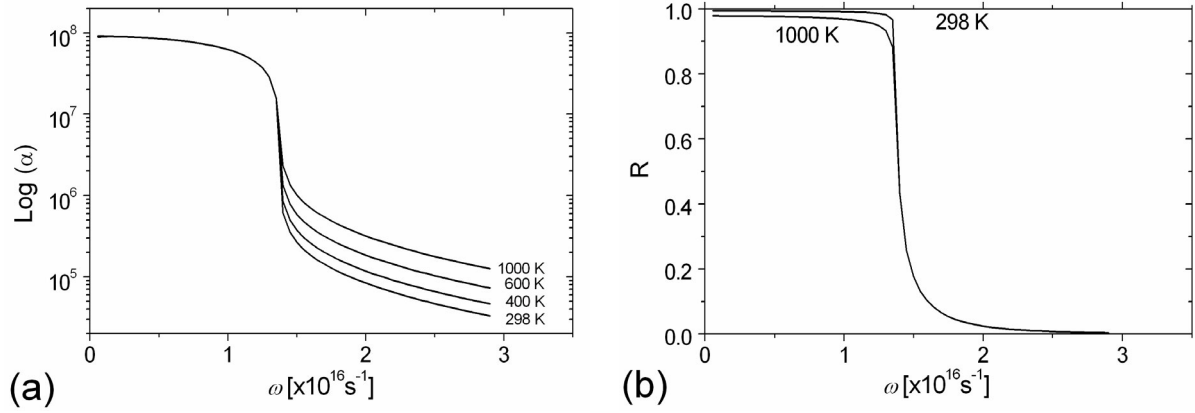
Figure 3.2. *(a) Absorption coefficient and (b) optical reflectance calculated for Au by the Drude theory at different temperatures.*

3.2.2- Hagen-Rubens relation

The complex index of refraction depends on a number of thermo-physical properties of the metal and, as such, is wavelength dependent. For long wavelengths (λ > 10 μm) the Hagen–Rubens [71] relation postulates that

$$n \approx n_2 \approx \sqrt{30\lambda\sigma} \ , \ \ \lambda\sigma \ \text{in} \ [\Omega^{-1}] \tag{3.17}$$

Substituting in equation (3.17) into (3.6) and equation (3.17) into (3.5) leads to

$$R \approx \frac{\left(\sqrt{30\lambda\sigma}-1\right)^2+30\lambda\sigma}{\left(\sqrt{30\lambda\sigma}+1\right)^2+30\lambda\sigma} \tag{3.18}$$

$$\alpha = \frac{4\pi\sqrt{30\lambda\sigma}}{\lambda} \tag{3.19}$$

As with the Drude theory [68], the electrical conductivity can be written as a function of temperature. That will allow us to calculate the reflectivity R and the absorption coefficient α as a function of the temperature T.

3.3 - Factors which affect the reflectance in metals

In real metals the simple free-electron behaviour is modified by a number of secondary effects, in particular by inter-band transitions [68]. The interband

transitions produce oscillations in R and α, generally at wavelength between 200 and 600nm (visible – ultraviolet regions) [72]. For example in metals like gold, silver and copper, the d-electrons make a bound-type positive contribution to the dielectric function, therefore shifting the plasma frequency ω_p to a lower frequency. These transitions can not be predicted by the models presented above.

The optical properties predicted by the Drude theory and the Hagen-Rubens relation are bulk properties. In practice, metals present lower reflectance than the bulk due to several effects (adsorbates, surface purity, preparation, treatments, etc.). In the following text, several factors which affect the optical reflectance in metals are presented.

3.3.1- Effect of temperature
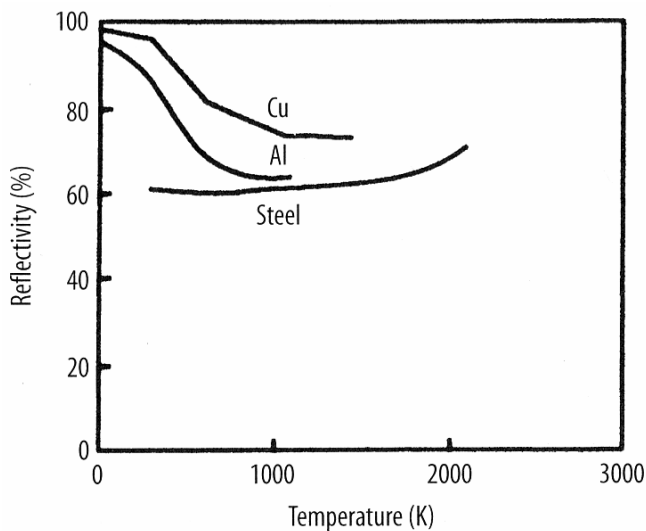
Figure 3.3. Reflectivity as a function of temperature for 1.0 µm radiation [72].

As temperature of the structure rises, there is an increase in the phonon population causing more phonon-electron collisions. Thus the electrons are more likely to interact with the structure rather than oscillate and re-radiate. There is thus a fall in the reflectivity and an increase in the absorptance with a rise in temperature, as seen in Fig. 3.3 [72].

Experimental observations have shown that if the initial reflectivity of a metal is large at the given wavelength, its decrease with the temperature rise can significantly accelerate the heating rate. If, however, the initial reflectivity is sufficiently small, even large variations of the reflectivity affect negligibly the heating rate [57-73].

3.3.2 - Effect of angle of incidence

The variation of the reflectivity with both angle of incidence and plane polarisation was studied by Drude [69]. If the plane of polarisation is in the plane of incidence, the ray is said to be a "p" ray (parallel). If the ray has its plane of polarisation at right angles to the plane of incidence, it is said to be an "s" ray (senkrecht = perpendicular). The reflectivity for these two rays reflected from perfectly flat surfaces are given by:

$$R_p = \frac{[n_1 - (1/\cos\phi)]^2 + n_2^{\,2}}{[n_1 + (1/\cos\phi)]^2 + n_2^{\,2}}$$ (3.20)

$$R_s = \frac{[n_1 - \cos\phi]^2 + n_2^{\,2}}{[n_1 + \cos\phi]^2 + n_2^{\,2}},$$ (3.21)

ϕ being the incidence angle.

The variation of the reflectivity with the angle of incidence is shown in Fig. 3.4. At certain angles the surface electrons may be constrained from vibrating, since if they did vibrate, they would leave the surface. This would necessarily lead to a disturbance of the matrix, i.e. absorption of the phonon. Thus, if the electric vector is in the plane of incidence, the vibration of the electron is inclined to interfere with the surface and absorption is high. However, if the plane is at right angles to the plane of incidence, then the vibration can proceed without reference to the surface, and reflection is increased.
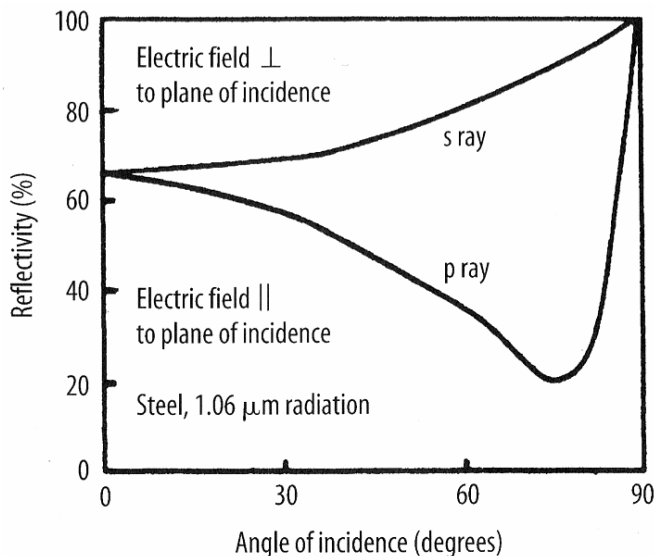
Figure 3.4. *Reflectivity of steel to polarised 1.0 µm radiation* [76].

3.3.3 - Effect of surface roughness

Roughness has a large effect on absorption due to multiple reflections in the undulations. Provided the roughness (in both height and width) is less than the laser wavelength, the radiation will not suffer these events and hence will perceive the surface as flat. The reflected phase front from a rough surface will no longer be the same as the incident beam and will spread in all directions as a diffuse reflection [72].

Ang *et al.* [77] have developed a simple model to estimate the cumulative absorption coefficient of an ultraviolet laser (λ between 1 and 400 nm) impinging on a pure metal, including effects of surface roughness whose scale is much larger than the wavelength λ.

To apply the model, the following conditions must be satisfied:

$$\Delta = (\omega \varepsilon_0 / \sigma)(\omega_p / \omega)^4 < 1 \quad ; \quad \omega \varepsilon_0 / \sigma < 1 \quad ; \quad \omega_p / \omega > 1 \qquad (3.22)$$

where Δ is the resistive loss term.

By matching the electric field and magnetic fields across the vacuum-metal interface [78], the absorption coefficient for the *s*- and *p*-polarisation can be calculated:

$$A(\theta_i) = \frac{2\Delta \cos\theta_i}{(\omega_p / \omega)^2 \sqrt{(\omega_p / \omega)^2 - \cos^2\theta_i}} \qquad \text{(\textit{s}-polarisation)} \qquad (3.23)$$

$$A(\theta_i) = \frac{2\Delta \cos\theta_i}{(\omega_p / \omega)^2 \sqrt{(\omega_p / \omega)^2 - \cos^2\theta_i}} \times \frac{(\omega_p / \omega)^2 - \cos 2\theta_i}{(\omega_p / \omega)^2 \cos^2\theta_i - \cos 2\theta_i} , \qquad (3.24)$$

$$\text{(\textit{p}-polarisation)}$$

where θ_i is the incident angle of the radiation according to Fig. 3.5.

To calculate the effects of the surface roughness that causes the laser light to undergo multiple reflections, a model with a distribution of rectangular wells with height *h* and width *w* is considered (see Fig. 3.5). As shown in Fig. 3.5, a photon strikes the well at incident position *a* with incident angle θ_i, bounces back and forth between the walls, and finally leaves the well after *N* bounces.

The cumulative absorption of a photon incident on a rough surface as a function of *h/w*, which can be defined as the degree of roughness [77], is given by Eq. 3.25.

$$\langle AN \rangle = \frac{4\alpha\,\Omega^2}{\pi - 2\cos^{-1}\mu} \left\{ \ln\left|\frac{\Omega+1}{\sqrt{\Omega^2-\mu^2}+\sqrt{1-\mu^2}}\right| + \ln\left|\frac{\sqrt{\Omega^2-1+\mu^2}+\mu}{\sqrt{\Omega^2-1}}\right| + 2G_{mn}\frac{h}{w}\left[\frac{\ln\left|2(1-\Omega^{-2})/(1-\mu)\right|}{2\sqrt{\Omega^2-1}} - \sin^{-1}\left(\frac{\mu}{\Omega}\right)\right] \right\}$$
(3.25)

where

$$\Omega = \omega_p / \omega, \quad \mu = w/\left(\lambda^2 + w^2\right)^{1/2}, \quad \alpha = \omega\varepsilon_0 / \sigma.$$
(3.26)

G_{mn} can be taken as 1.3 with an accuracy of 30% in most cases [77].

The simple formulas derived from this model provide an immediate assessment of the relative importance of the surface roughness on laser absorption, when the surface roughness scale is much larger than the laser wavelength.
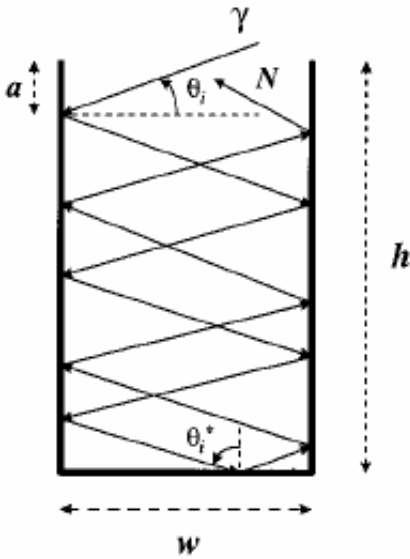
Figure 3.5. *Surface roughness representation with rectangular well that has height h, and with w. The incident angle is θ_i [77].*

3.4 - Mechanisms of structuring by laser light

3.4.1 - Photo-thermal and photo-chemical processes

Laser interaction with matter can be described on the basis of photo-thermal and photo-chemical models. The interaction of laser light with materials starts with single photon or multiphoton material excitation. If the excitation energy is instantaneously transformed into heat, the increase in temperature changes the

optical properties of the material and thereby the absorbed laser power (see chapter 3.3.1).

The simplest example of photo-thermal mechanism is laser melting. This is the case when the laser energy density is not high enough to induce the direct laser ablation, and this mainly concerns metals, semiconductors, and some ceramics. In the photo-thermal process, the thermalisation of the excitation is faster than other initial processing steps, i.e., desorption of species from the surface, or structural rearrangements of atoms or molecules, or initial steps in a chemical reaction. The detailed excitation mechanisms become therefore irrelevant, and the laser can be considered simply as a heating source. The temperature rise can also result in material ablation (vaporisation) with or without surface melting. This will be explained with more detail in chapter 3.4.2.

If the photo energy is high enough, laser light excitation can result in direct bond breaking. As a consequence, single atoms, molecules, clusters or fragments are desorbed from the surface. The photo-chemically dissociated bonds can build up stresses which result in ablation. Both the direct and indirect path can take place, in principle, without any change in surface temperature. For this reason this process is called photo-chemical ablation.

For processes in which both thermal and non-thermal mechanisms contribute to the overall ablation rate, one calls these a photo-physical ablation. An example would be a system in which the lifetime of electronically excited species or of broken bonds is so long that the species desorbs from the surface before the total excitation energy is dissipated into heat. This desorption of excited species is enhanced by the temperature rise. Similarly, thermally and non-thermally generated defects, stresses, and volume changes may again influence the overall process. The above defined photo-thermal and photo-chemical ablations can be considered as limiting cases of the photo-physical ablation mechanism.

3.4.2 - Effect of laser-pulse duration

The interaction between photons and the free electrons in metals produces vibrations of the activated electrons. The activated electrons interact with the lattice by collisions and then their energy is transmitted though the structure by diffusion processes. Vibrations in the structure are detected as heat. If sufficient energy is absorbed then vibrations becomes so intense that the molecular bonding is stretched so far that it is no longer capable of exhibiting mechanical strength and the material is said to have melted. On further heating, the binding is further loosened due to strong

molecular vibrations and the material is said to have evaporated. The vapour is still capable of absorbing the radiation but only slightly since it will only have bound electrons; the exception occurs if the gas is sufficiently hot that electrons are liberated and the gas is then said to be plasma. Plasmas can be strongly absorbing if their free electron density is high enough. According to the model of Cobine *et al.* [79], temperatures of the order of 10000 – 30000 °C are required for significant absorption.

At very high photon fluxes (high laser fluences), the electric field is sufficient to strip electrons from the atoms which become charged and then repel each other. With femtosecond pulses (10^{-15} s) there is no time for thermal driven energy exchange or to form thermal equilibrium (the mean free time between collisions of electrons in a conductor is calculated to be 10^{-13} s [72], therefore the pulse time is about 100 times faster than the electrons impeding them to conduct to energy through thermal collisions.

In the following subsections, the effects of the pulse time, and the laser energy are discussed for the femtosecond (10^{-15} s), picosecond (10^{-12} s) and nanosecond (10^{-9} s) pulsed-lasers.

### 3.4.2.1 - Femtosecond laser pulses

Material processing by femtosecond laser pulses has attracted considerable interest [80], as metals and semi-conductors can be drilled with high precision [81-83]. In femtosecond ablation, the ablation physics differs drastically from the short pulsed laser ablation (ns and ps pulsed lasers) [84]. Generally, the electron-lattice relaxation time in metals is 1-10 ps [85, 86]. Therefore the mechanism of femtosecond laser ablation is different from that of longer pulsed laser ablation. Thermal ablation occurs when the laser pulsewidth is longer than the electron-lattice relaxation time [84]. In femtosecond laser ablation of materials with high thermal conductivity (like metals), the chemical composition and properties of the ablated area is kept unchanged [87, 88]. Heat effects of metallic bulk crystals of Au, Ag, Cu, and Fe ablated with femtosecond-Ti:sapphire laser pulses were studied in [84]. From these investigations, it was found that the crystal form in the ablated area is *partially* changed into amorphous form, and they have suggested that the formation mechanism would be the same as the melt-quenching generally used as the fabrication method of amorphous metals.

Investigations in pure metals realised in [89] have been used to compare the laser ablation efficiency by femto-, pico- and nanosecond pulses. The investigations

consist on the production of micro-craters with focused laser beams. The craters obtained (diameter of the crater ~ 20 µm) with femtosecond pulses where found to be similar as in the experiment reported by [90] in silicon. These craters present a rectangular-like profile (Fig. 3.6b) and an oxide free surface. These can be explained because in this case the ultra-short pulses causes a direct solid-vapour transition at sufficient intensities and therefore, the collateral damage is minimised [91].

Metal	*Ablation threshold fluence, ϕ_{TH}. (mJ/cm^2)*
Stainless Steel	160.0
Copper	352.9
Niobium	146.0
Titanium	102.1

Table 3.1. *Ablation threshold values using 150 fs laser pulses at a wavelength of 775 nm in air under atmospheric pressure* [91].
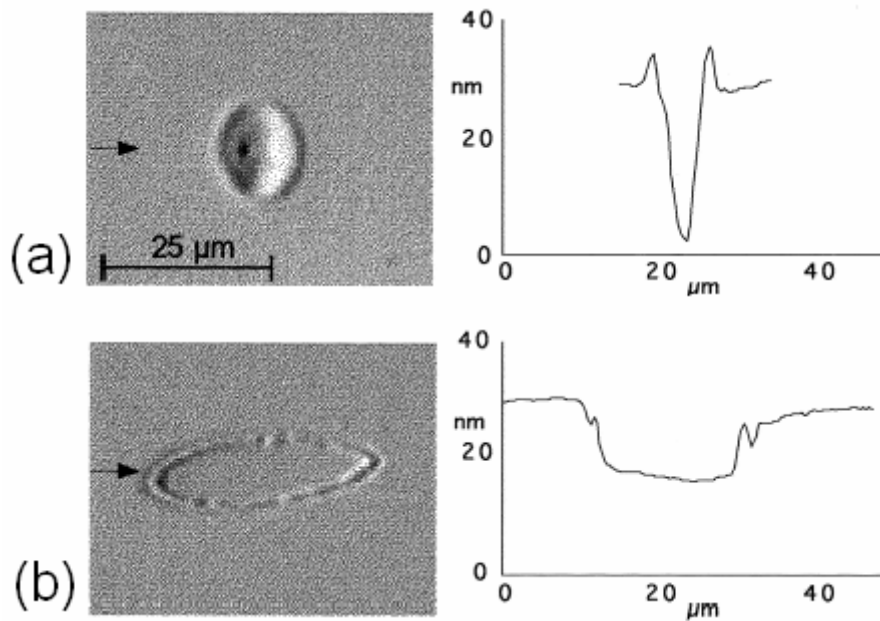
Figure 3.6. Light microscope interference contrast images of final structures in laser-pulsed Si, with the surface profile along the arrow. (a) Si with oxide after 8 ns (3 J/cm²) laser pulse. (b) Si without oxide after a 100 fs (0.5 J/cm²) laser pulse [90].

In the work of Mannion *et al.*, the ablation in metal targets in air with femtosecond laser pulses was studied [91]. The ablation threshold fluences obtained for multi-shot ablation were found to be between 352 and 102 mJ/cm² for the metals indicated in Table 3.1. These laser fluences threshold values are higher than those in pico- or nano- second lasers, and can be explained by the different mechanisms which take place [89].

3.4.2.2 - Nano- and picosecond laser pulses

If nano and picosecond laser pulses are used to produce micro-craters on metals [89] and semi-conductors [90, 92], the formation of a "corona" (thin molten rim at the edges of the craters [93]) is observed along the crater boundary (see Fig.3.6a). The height of the craters depends on the target matter, the laser fluence and number of pulses. The craters present a smooth structure which is produced by thermo- and chemocapillary flow of the melt in an in-plane thermal gradient. Therefore, the crater "corona" is the result of liquid phase expulsion, and also by the plasma particle re-condensation [94].

The corona provides evidence of the different ablation phenomena which take place in pico- and nanosecond pulses from one side, and femtosecond pulse laser on the other side.

<div align="right">

Chapter 4

</div>

<div align="right">

Interference theory, inverse problem and thermal simulation

</div>

In this chapter, three different theoretical aspects which are essential in this PhD thesis are presented. Firstly, the interference principle for *n*-laser beams is introduced. After that, an approximation to resolve the so-called inverse problem is described. Its task is to establish a configuration of electromagnetic waves that reproduces a known and desired interference pattern. Finally, a thermal simulation model, which was developed in this thesis and also used in thermal calculations in other systems [95] is presented. It considers melting and evaporation of the constitutive metallic layers of the films which will be in the next chapters compared with the experimental results.

4.1- Interference theory

As was already described in chapter 3.2, the simplest form of light is a monochromatic, linearly polarised plane wave. This is a sufficient approximation of a real laser beam (see Eq. 3.1).

Under the assumption of plane waves, the total field (*E*) of the interference pattern can be obtained by the superposition of each individual "*j*" beam:

$$E = \sum_{j=1}^{n} E_j = \sum_{j=1}^{n} E_{j0} \, e^{i\left(\bar{k}\,r - \omega t\right)}. \tag{4.1}$$

The product between the vectors $\bar{k}$ and *r* can be written in terms of α_j and β_j which are the angles of the beams respected to the interference-plane (Fig. 4.1):
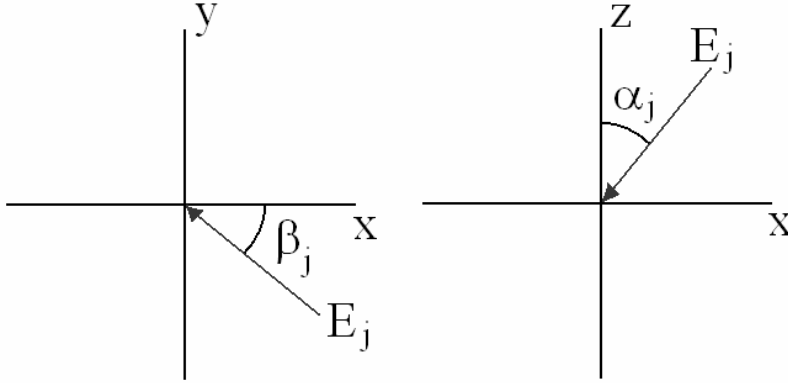
$$\bar{k} \cdot r = \begin{pmatrix} k \cdot \sin\alpha_j \cdot \cos\beta_j \\ k \cdot \sin\alpha_j \cdot \sin\beta_j \\ k \cdot \cos\alpha_j \end{pmatrix} \cdot \begin{pmatrix} x \\ y \\ z \end{pmatrix}. \tag{4.2}$$

where *k* is the wave-number:

$$k = \frac{2\pi}{\lambda},$$

(4.3)

Rewriting 4.1 in terms of α_j, β_j, x, y and considering $\omega=0$ we obtain:

$$E = \sum_{j=1}^{n} E_j = \sum_{j=1}^{n} E_{j0}\, e^{-ik\sin\alpha_j\left(x\cos\beta_j - y\sin\beta_j\right)}.$$

(4.4)

Figure 4.1. *Representation of an electromagnetic wave in 3D. The sample is located at z = 0, i.e. in x,y plane.*

Eq. (4.4) can be rewritten as:

$$E = \sum_{j=1}^{n} E_{j0} \begin{bmatrix} \cos\left(-k\sin\alpha_j\left(x\cos\beta_j - y\sin\beta_j\right)\right)+ \\ i\sin\left(-k\sin\alpha_j\left(x\cos\beta_j - y\sin\beta_j\right)\right) \end{bmatrix}.$$

(4.5)

The spatial intensity distribution is given by:

$$I = \frac{c\varepsilon_0}{2}|E|^2.$$

(4.6)

Two-beam interference (n = 2) produces a two-dimensional linear pattern. Assuming that:

$$E_{01} = E_{02} = E_0 \; ; \; \alpha_1 = \alpha_2 = \alpha \; ; \; \beta_1 = 0\, , \beta_2 = \pi$$

(4.7)

the intensity *I(x)* can be expressed as:

$$I = 2c\varepsilon_0 E_0^{\,2}\cos\left(kx\sin\alpha\right)^2.$$

(4.8)

The calculated line pattern is shown in Fig. 4.2a. The period of the structure (*d*) is given by:

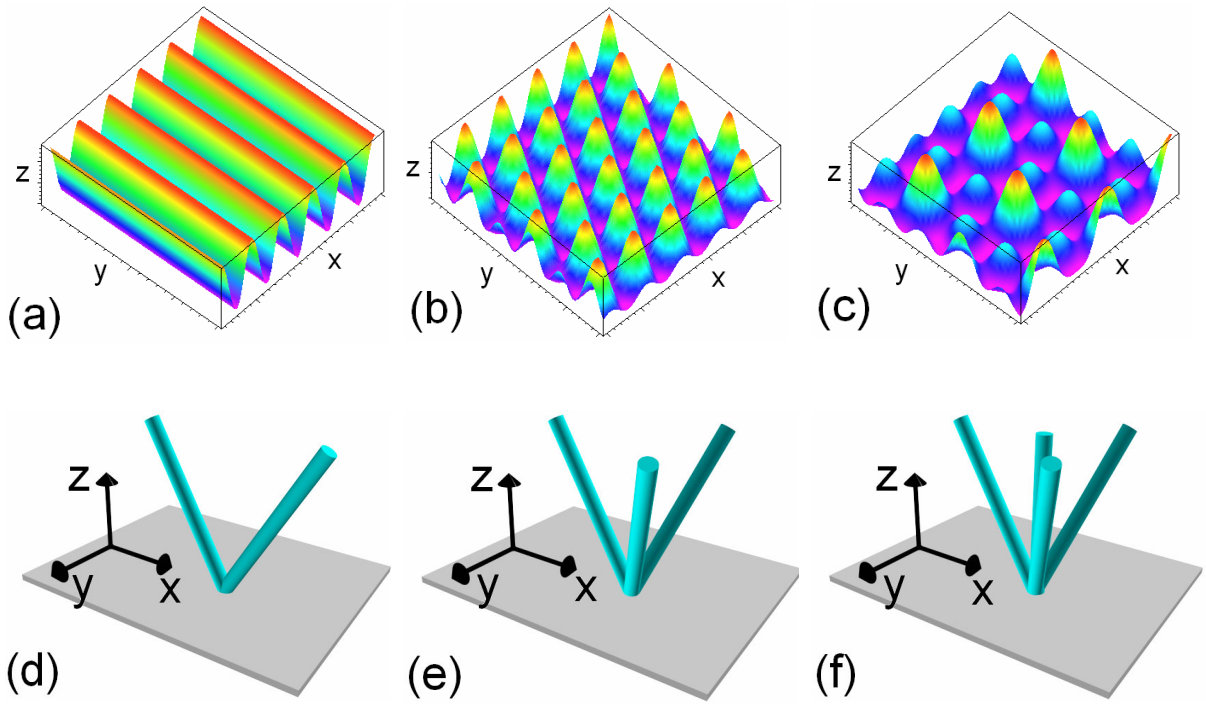$$d = \frac{\lambda}{2\sin\alpha},$$

(4.9)

where 2α is the angle between the laser beams.

Three-beam interference (n = 3) produces different 2-D arrays depending on the magnitude of the electric-field of each beam and the geometric configuration. For symmetric configuration (4.10), the intensity distribution *I(x,y)* is given by Eq. (4.11).

$$E_{01} = E_{02} = E_{03} = E_0 \,;\; \alpha_1 = \alpha_2 = \alpha_3 = \alpha \,;\; \beta_1 = 0 \,,\; \beta_2 = \frac{2}{3}\pi \,,\; \beta_3 = -\frac{2}{3}\pi \qquad (4.10)$$

$$I = \frac{9}{2}c\varepsilon_0 E_0{}^2 \left[\begin{array}{l} \left(-\cos(kx\sin\alpha) - \cos\left(k\sin\alpha\left(-\frac{x}{2} - y\frac{\sqrt{3}}{2} \right) \right) - \cos\left(k\sin\alpha\left(-\frac{x}{2} + y\frac{\sqrt{3}}{2} \right) \right) \right)^2 \\[4mm] + \left(-\sin(kx\sin\alpha) + \sin\left(k\sin\alpha\left(-\frac{x}{2} - y\frac{\sqrt{3}}{2} \right) \right) - \sin\left(k\sin\alpha\left(-\frac{x}{2} + y\frac{\sqrt{3}}{2} \right) \right) \right)^2 \end{array} \right].$$

$$(4.11)$$

(a) (b) (c)

(d) (e) (f)

Figure 4.2 - *Calculated intensity distribution for (a) two-beam interference (d), (b) three-beam interference assuming symmetrical configuration (e), and (c) four-beam interference under the conditions shown in (f), eq. 4.13 .*

Under these conditions, the periodic dot pattern shown in Fig. 4.2b is obtained.

If a fourth beam is added, and considering (4.12), the periodic pattern shown in Fig. 4.2c can be calculated. The intensity distribution shows a high intensity central peak surrounded by 6 peaks with lower intensity arranged in a hexagonal form.

$$E_{01} = E_{02} = E_{03} = E_{04} = E_0 \,;\; \alpha_1 = \alpha_2 = \alpha_3 = \alpha, \, \alpha_4 = 0$$

$$\beta_1 = \beta_4 = 0 \; , \; \beta_2 = \frac{2}{3}\pi \; , \; \beta_3 = -\frac{2}{3}\pi \tag{4.12}$$

In appendix 1, several laser beam arrangements as well as the calculated interference patterns are shown indicating the potential of the method.

4.2 – Inverse Problem

In order to apply the laser interference structuring method, the configuration of laser beams that produce desired interference pattern and hence energy distribution on the surface of the sample has to be calculated prior to the experiment. Calculating the configuration of electromagnetic waves that reproduce a desired interference pattern has been called inverse problem [96] and its solution is not known in general. The task here is to establish a configuration of electromagnetic waves that reproduces $I(x,y)$ or at least gives an approximation $\tilde{I}(x,y)$ for a known and desired pattern $I(x,y)$. In the general case, Eq. 4.1 can be rewritten in terms of intensity distribution:

$$I(x) = I(x,y) = I_0 \left| \sum_{i=1}^{n} c_j \; e^{-i(k_j r)} \right|. \tag{4.13}$$

with $\sum_{i=1}^{n} c_j = 1$ (4.14)

The coefficients c_j describe the amplitude and phase of the electric field of each laser beam. They are complex since the phase can be regarded as a complex factor $e^{i\phi}$. For the laser configuration used in the present study, all laser beams are in phase and have the same angular frequency. In this case, the coefficients c_j are dimensionless and can be directly related to the partial intensity of each partial beam, similar to Eq. 4.4.

Each laser beam "j" with wave vector k_j adds a new degree of freedom to the interference pattern. With relatively few laser beams, the pattern and its symmetries remain simple and are easily recognised [97, 98]. More complicated structures will in general require more generating laser beams for the construction of the interference pattern.

In [96], a mathematical model with a corresponding numerical simulation of the inverse problem was presented. From the mathematical point of view, the problem is a highly nonlinear system. The results have shown to be appropriate to reconstruct very complex interference patterns with a limitation in the number of laser beams but

after hard mathematical computation. Nevertheless, due to the characteristics of the laser beams used in this work, the mathematical procedure of solving the inverse problem can be simplified as follows.

Since the pattern is delivered in terms of individual beams with wave vectors k_j, it is natural to investigate the pattern formed in *k-space*. Periodic structures must show translational invariance and point symmetry [96]. Such crystallographic aspects of interfering light fields have been also investigated in the related subject of optical lattices [99] and have also been extended to quasi-periodic structures [100].
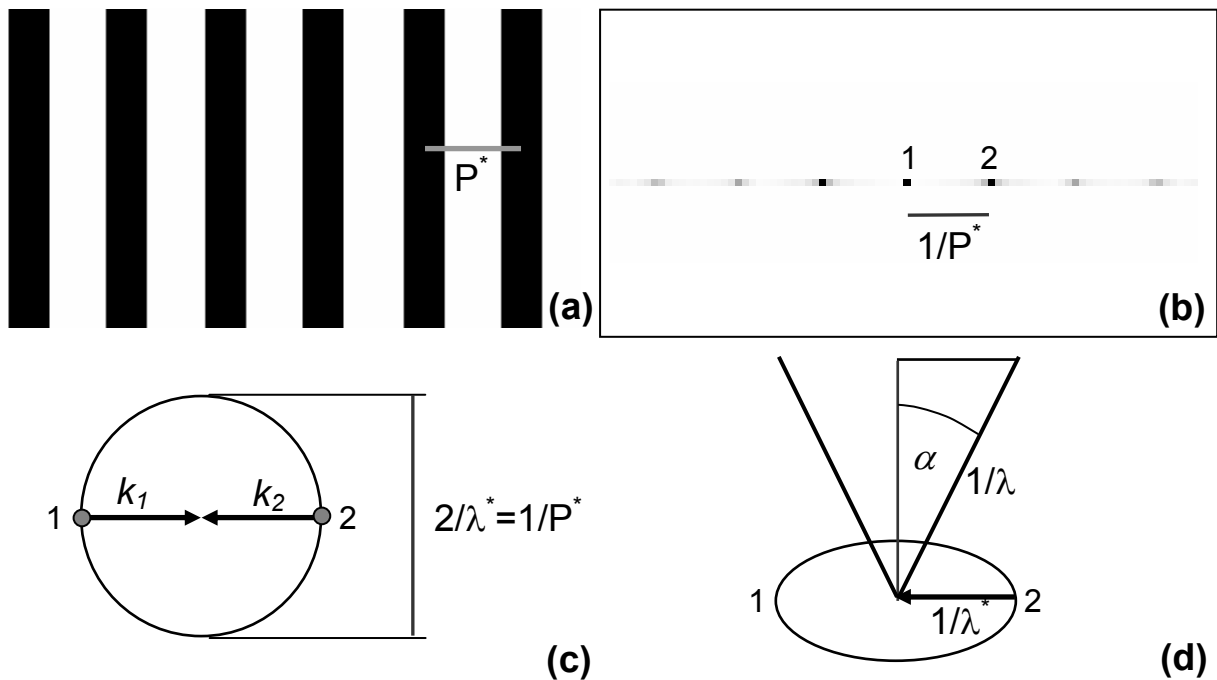
Figure 4.3 *– (a) Desired interference pattern and (b) discrete Fourier transform of (a). The most relevant points of the FT are indicated with 1 and 2. (c) Two-dimensional Ewald sphere construction. (d) Reconstruction of (c) adequate for the laser interference experiments.*

Let's consider for example, the periodical line-type structure of Fig. 4.3a. The first step to resolve the inverse problem is to apply the discrete Fourier transform (FT) to the desired interference pattern $I(x,y)$ (Fig. 4.3b). To reproduce the target pattern $I(x,y)$, the most significant points (vectors k_j) in Fourier space must be used. These vectors contain all the information which is necessary to reproduce the pattern and can be confined in the Ewald-sphere [96, 101]. In the example of Fig. 4.3, the vectors are indicated with the numbers 1 and 2 (Fig. 4.3b). The centre of the sphere is given by the coordinate $(\bar{k}_X, \bar{k}_Y)$ which is the mean value of the k_{xi} and k_{yi} coordinates of all the k-vectors:

$$\bar{k}_x = \frac{\sum\limits_{j=1}^{n} k_{xj}}{n}; \bar{k}_y = \frac{\sum\limits_{j=1}^{n} k_{yj}}{n}.$$

(4.15)

In reciprocal space, the parallel lines are represented by spots which have a distance of $1/P^*$, being P^* the period of the desired pattern (Fig. 4.3). In the 2 dimensional construction of the Ewald-sphere indicated in Fig. 4.3c, the incident vector k_1 is diffracted by the periodic structure obtaining the vector k_2. However, in the inverse problem, both incident and diffracted beams must be considered to reconstruct the desired interference pattern [96]. The radius of the Ewald-sphere is $1/\lambda^*$. Thus, to obtain the period P^*, the wavelength of the incident beam must be:

$$2 \cdot (1/\lambda^*) = 1/P^* \quad => \quad \lambda^* = 2P^*$$

(4.16)

This means that in 2D, the period of the periodical pattern depends on the incident wavelength λ^*.

In our experimental setup the laser beams are not confined to 2D-space, but strike the target with a certain angle α_i (Fig. 4.3d). The projection of the wave vector with wavelength λ onto the diffraction plane must then be equal to the wave vector with wavelength λ^* in 2D-space given in Fig. 4.3d. This constraint defines the values of the angles α_j between the normal to the interference plane. In addition, the angles α_j of the beams are related to each other by:

$$\alpha_j = \cos^{-1}\left(\cos \alpha_i \frac{\sqrt{(k_{xj} - \bar{k}_x)^2 + (k_{yj} - \bar{k}_y)^2}}{\sqrt{(k_{xi} - \bar{k}_x)^2 + (k_{yi} - \bar{k}_y)^2}} \right)$$

(4.17)

The wavelengths λ and λ^* are related by:

$$\frac{(1/\lambda)}{(1/\lambda^*)} = \sin(\alpha).$$

(4.18)

Replacing Eq. 4.18, in 4.16 we obtain:

$$P^* = \frac{\lambda}{2\sin(\alpha)},$$

(4.19)

which is the well known formula to calculate the period of the line-type periodical pattern described by two laser beams with wavelength λ and an angle between the laser beams of 2α (see Eq. 4.9). Moreover, it can be demonstrated that independently of the α angles, the shape of the interference pattern in all cases is the same (with exception of $\alpha = 0$ where the interference pattern vanishes).

Other example of a periodical interference pattern is presented in Fig. 4.4 with its correspondent 2D-FT. The most relevant points are indicated with the numbers 1, 2, and 3. The other points are the periodic extension of the principal ones. The angles β_j of each partial beam to be introduced in Eq. 4.6 can be directly determined as shown in Fig. 4.5.

In a similar manner like the previous case, the period of the structure can be explained in terms of the wavelength and the α angle of one of the wave vectors (which are symmetrical) obtaining:
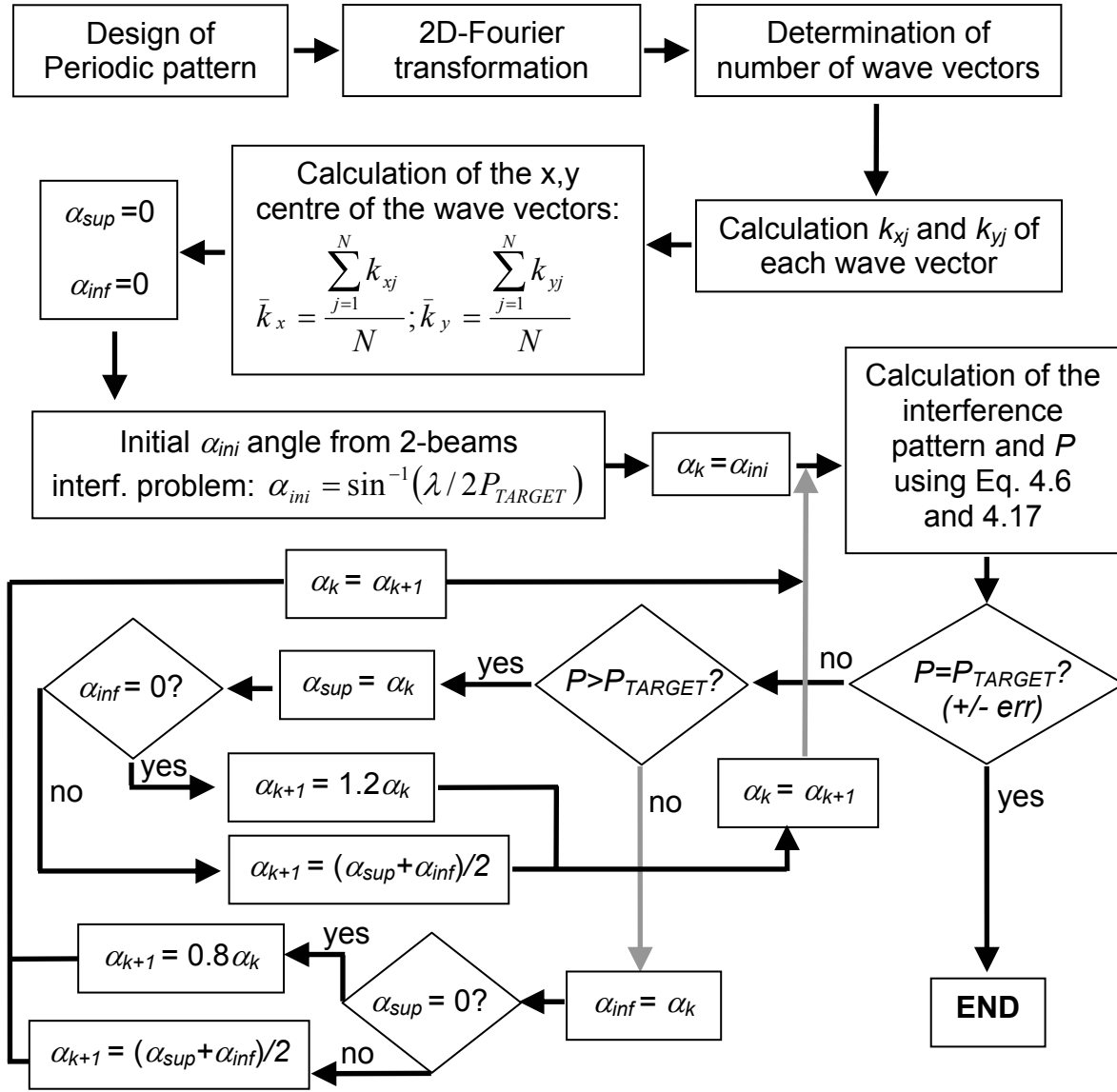
$$P^* = \frac{\lambda}{\sqrt{3}\sin(\alpha)}. \tag{4.20}$$

(a) **(b)**
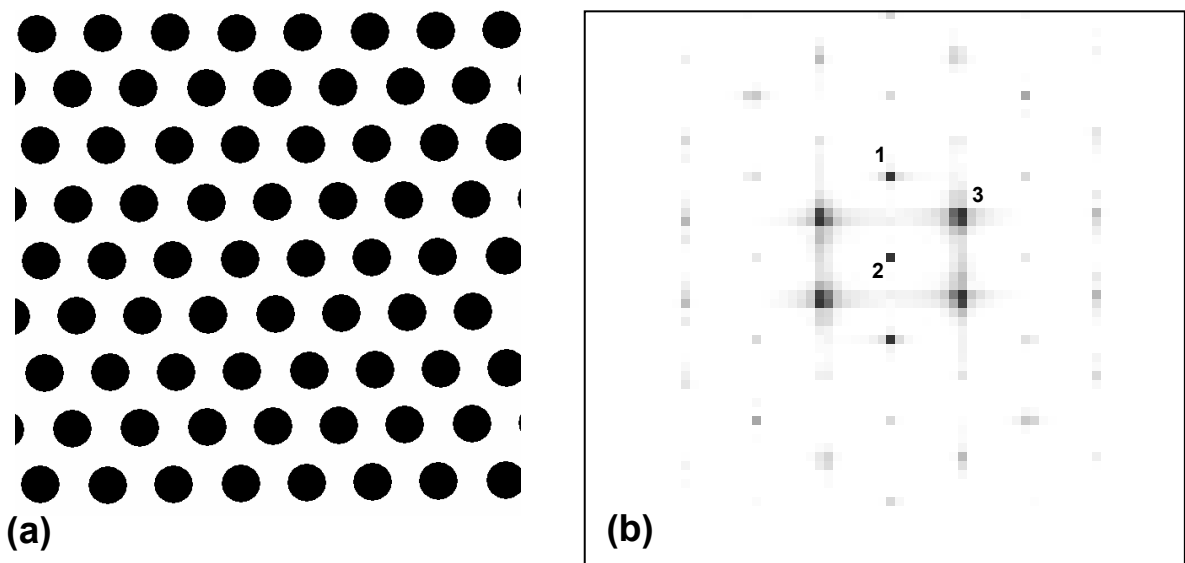
Figure 4.4. (a) Desired interference pattern and (b) discrete Fourier transform of (a). The most relevant points of the FFT are indicated with 1, 2 and 3.
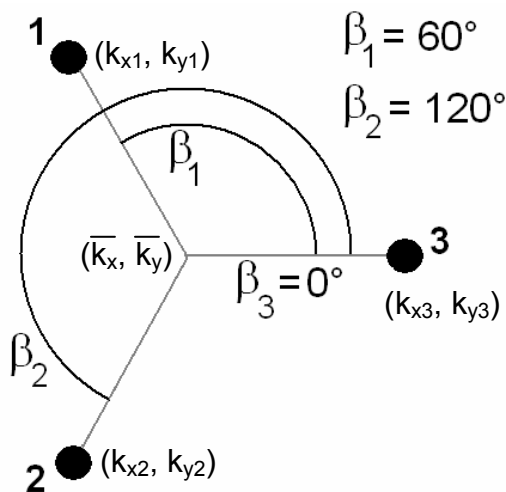
Figure 4.5. Calculation of the β_j angle of each partial beam from the Fourier transformation of Fig. 4.4.

Figure 4.6. *Schematic procedure to calculate the α_j angle of each partial beam: α_{inf} and α_{sup} are the angles related to the maximal and minimal period P respectively obtained during the iteration process.*

In the general case, the angles α_j given in Eq. 4.17 can be calculated iteratively in order to obtain a specific period. As starting value, α_{ini} for the line type pattern case with:

$$\alpha_{ini} = \sin^{-1}\left(\lambda/2P_{TARGET}\right), \tag{4.21}$$

where P_{TARGET} is the desired period. Depending on whether the period of the interference pattern calculated using Eq. 4.6 is larger or smaller than the target period (P_{TARGET}), α_{ini} must be increased or reduced, respectively. This procedure is schematically illustrated in Fig. 4.6. However, the principal shape in *x,y*-coordinates

of the intensity distribution of the desired interference pattern is defined by the angles β_j independently of the α_j.

Another example of a more complex periodical pattern is shown in Fig. 4.7. In Fig. 4.7a, the desired interference pattern is shown together with the identified wave vectors (Fig. 4.7b), and the laser beam configuration required to reproduce the pattern (Fig. 4.7c). The calculated interference pattern using this 4-beams arrangement is given in (Fig. 4.7c). More details about other possible periodical structures and their calculated interference pattern are given in appendix 2.

(a)

(b)

(c)
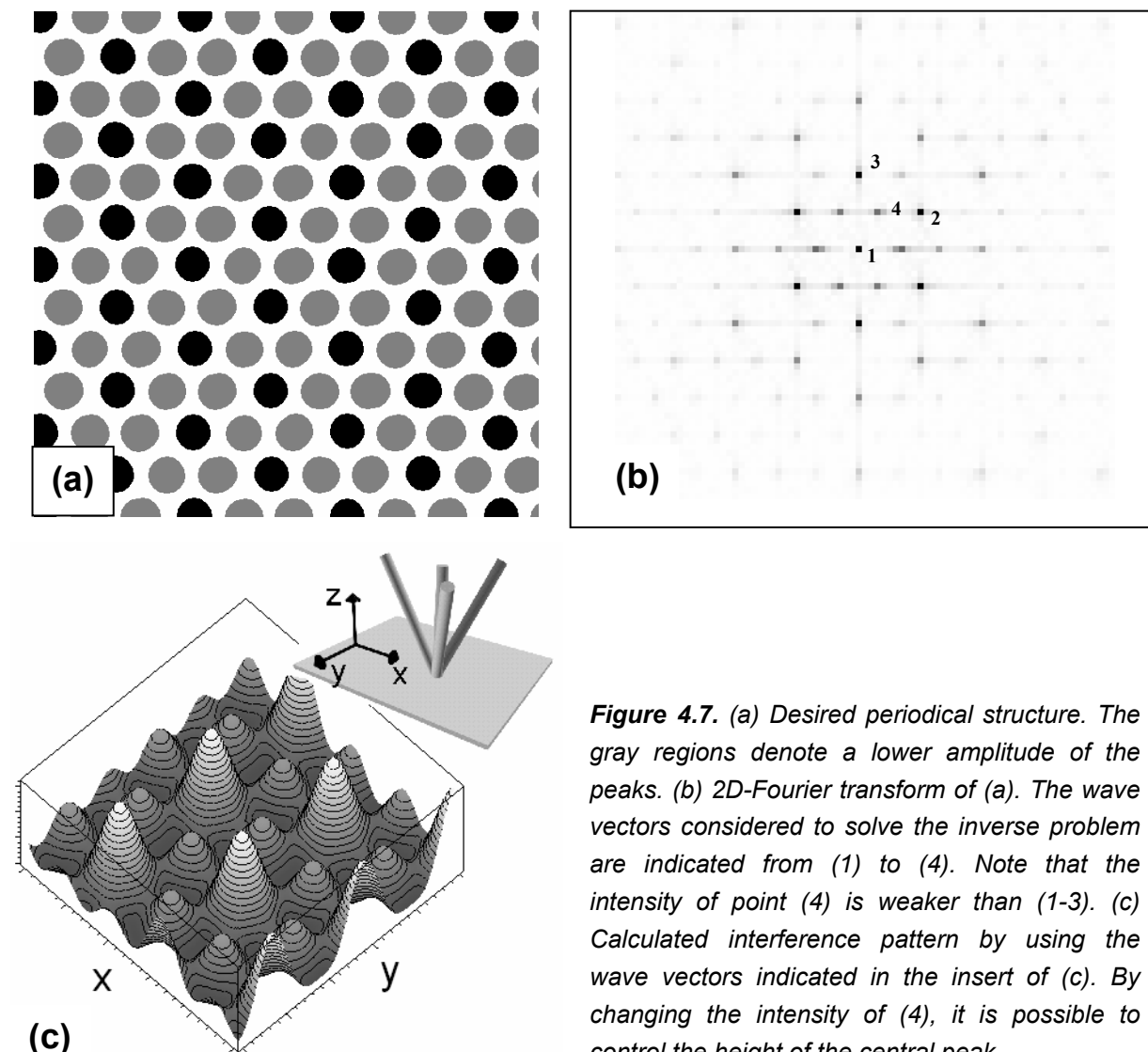
Figure 4.7. *(a) Desired periodical structure. The gray regions denote a lower amplitude of the peaks. (b) 2D-Fourier transform of (a). The wave vectors considered to solve the inverse problem are indicated from (1) to (4). Note that the intensity of point (4) is weaker than (1-3). (c) Calculated interference pattern by using the wave vectors indicated in the insert of (c). By changing the intensity of (4), it is possible to control the height of the central peak.*

4.3 - Thermal simulation

The thermal simulation was carried out by using the FlexPDE® software [102]. This software expands defined parameters and relations, performs spatial differentiation, and symbolically applies integration by parts to reduce second order terms to create symbolic Galerkin equations. It then differentiates these equations to form the Jacobian coupling matrix. The mesh is generated by a mesh generation module which constructs triangular finite elements over the two-dimensional problem domain.

The thermal simulation is based on the heat diffusion equation:

$$\rho\, c_p\, \frac{\partial T}{\partial t} = q_a - q_m - q_b + \nabla\!\left(k_T \nabla T\right), \tag{4.22}$$

where $T = T(x, z, t)$ is the temperature at the position (x, z) at time t, q_a is the power per unit of volume added, q_m and q_b are the powers per unit volume required to melt and vaporize the material, respectively, c_p is the specific heat, k_T is the thermal conductivity, and ρ is the density.

This equation allows us to estimate the temperature distribution in the metallic-films samples as well as the shape, size and volume of the molten and vaporised material produced by the heat source from the laser beam.

For the analysis of the problem, the following conditions are assumed:

- no radiation is lost from the surface,

- when the material melts, there is no convection due to gravitational or electromagnetic effects,

- the intensity of the laser is considered as ten periods of the intensity distribution of a line-type pattern (Eq. 4.23) with a Gaussian shape in the time scale,

$$I(x) = 2I_0 \cos\!\left(k\,x\sin\alpha\right)^2 \tag{4.23}$$

  I_0 is the fluence of the laser (this equation is similar to Eq. 4.8 but rewritten in terms of laser fluence),

- the heat conduction problem includes solid-liquid, and liquid-vapor transitions, considering the energy required for melting and vaporising both metals.

48

The boundary conditions are as follows (see Fig. 4.8):

$$T_{x=0} = T_0 \ ; \ T_{x=b} = T_0 \ ; \ \frac{dT}{dz}\bigg|_{z=0} = 0 \ ; \ T_{z=l} = T_0 \tag{4.24}$$

If the derivative term is *0*, there is no heat conduction through the boundary (no radiation from surface; no heat transmission to the surrounding gas). The values of *l* and *b* (see Fig. 4.8) were 100 and 39 µm respectively.

The power of the laser is absorbed into the material following an interference pattern given by Eq. 4.25 and 4.26:

$$q_a = \alpha \frac{I(x)}{\sigma\sqrt{2\pi}} \exp\left(-\frac{(t-t_p)^2}{2\sigma^2}\right)(1-R)\exp(-\alpha z), \tag{4.25}$$

$$\sigma = \frac{\tau_p}{2\sqrt{2\ln 2}}, \tag{4.26}$$

where α is the absorption coefficient, *t* is the time, t_p is the pulse time, τ_p is the pulse duration (FWHM), *R* is the reflectivity of the surface, and *I(x)* is the intensity of the interference pattern described by Eq. 4.23.
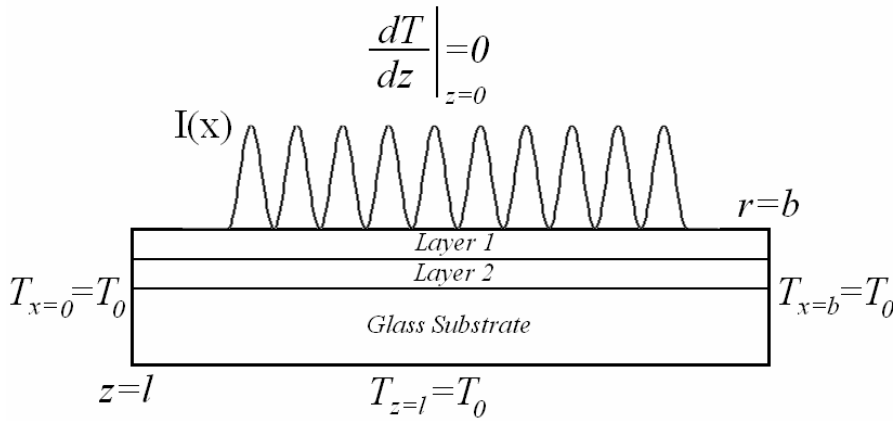
Figure 4.8. Schematic diagram of heat input and boundary conditions

Experimental observations have shown that if the initial reflectivity of a metal is large at the given wavelength, its decrease due to the temperature rise can in response significantly accelerate the heating rate. If, however, the initial reflectivity is sufficiently small, even large variations of the reflectivity affect negligibly the heating rate [73-76] (see chapter 3.3). In the case of the metals which were simulated in this thesis (with the exception of Al), at a wavelength of 266 or 355 nm the reflectivity values are lower than 0.6 [71]. It means that for these metals, the reflectivity during the laser heating can be considered as a constant value (see chapter 3.3). In the case of aluminium, according to [103], the reflectivity decreases about 30% at the

melting point. Consequently, the following equation which describes the reflectivity of aluminium as function of temperature was used:

$$r(T) = \begin{cases} R_0 - k_r\,(T - 300) & ; \quad T < T_m \\ R_{T_m} & ; \quad T > T_m \end{cases},$$

(4.27)

with T_m being the melting temperature (933 K), R_0 = 0.935 (at 266 nm of wavelength), and k_r = 4.48·10^{-4}.

During the process of melting, there is a fraction of material in the solid state and a fraction in the liquid state in each node. The solid fraction is represented by the variable f_{SL}. For $f_{SL}=1$ the metal is in the solid state and for $f_{SL}=0$ it is completely molten (Fig. 4.9) [104].

The fraction f_{SL} changes as a function of temperature as shown in Eq. 4.28:

$$f_{SL} - 1.7 \cdot 10^{-12}\, \nabla \cdot \left(\nabla f_{SL}\right) = 0.5\, erfc\left(\frac{T - T_m}{\Delta T_{0m}}\right),$$

(4.28)

where ΔT_{0m} is a temperature range, over which the melting transition occurs and the term $1.7 \cdot 10^{-12}\, \nabla \cdot (\nabla f_{SL})$ is a diffusion term with a small coefficient that acts as a noise filter, and $erfc$ is the complementary error function ($erfc = 1 - erf$).
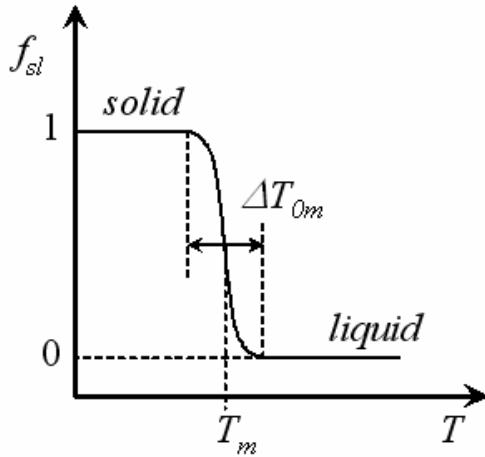
Figure 4.9: *Graph of the variable f_{sl} as function of the temperature T for the phase transition solid – liquid. For f_{sl} = 1 the material is in the solid state; for f_{sl} = 0 the material is in the liquid state. The same scheme is applicable for the phase transition liquid – gaseous.*

For pure metals, the solidification and melting processes occur at constant temperature. Nevertheless, the temperature range ΔT_{0m} must be defined to allow the computation to add the latent heat during the phase transition [105]. For the simulation ΔT_{0m} was selected to be 50 K. The results obtained with ΔT_{0m} = 10 or 1 K do not differ considerably (a difference smaller than 1 % was observed in the last case), but the computation time is much longer.

The latent heat of fusion is the amount of heat absorbed when f_{SL} changes from 1 to 0 (assuming that dH/df_{SL} is constant):

$$L_m = \int_0^1 \frac{dH}{df_{SL}} df_{SL} = \frac{dH}{df_{SL}}, \qquad (4.29)$$

The heat absorbed during the phase transition is:

$$\frac{dH}{dt} = \frac{dH}{df_{SL}} \frac{df_{SL}}{dt} = L_m \frac{df_{SL}}{dt}. \qquad (4.30)$$

Neglecting the filter term of Eq. 4.28, we can write:

$$q_m = L_m \rho \frac{\partial \left[0.5\, erfc \left(\dfrac{T - T_m}{\Delta T_{0m}} \right) \right]}{\partial t}. \qquad (4.31)$$

The liquid-vapour transition was considered in the same way using the boiling temperature T_b, the latent heat of vaporisation L_b, the variable f_{LV}, and the temperature range ΔT_{0b} obtaining:

$$q_b = L_b \rho \frac{\partial \left[0.5\, erfc \left(\dfrac{T - T_b}{\Delta T_{0b}} \right) \right]}{\partial t}. \qquad (4.32)$$

The material properties used in the simulation were taken from [71, 106] and are shown in appendix 3. The specific heat, thermal conductivity, and the density were considered as a function of the temperature.

Chapter 5

Experimental procedure

Thin metallic films, investigated in this thesis, were produced by physical vapour deposition (PVD). Transformations of the specimens under study were induced under different laser irradiation conditions. Sample parameters as thickness and number of layers have also been varied to modify the types of structure that can be obtained. In addition, the heating dynamics upon laser irradiation were followed in-situ by means of real-time electrical conductivity measurements with ns-resolution which were developed in this work. After irradiation, the samples were investigated by different methods including White Light Interferometry (WLI), Scanning Electron Microscopy (SEM), Focus Ion Beam (FIB), Energy Dispersive X-rays (EDX) and Transmission Electron Microscopy (TEM) among others. Measurements of optical properties were conducted to study the diffuse and total reflectance as well as the normal emittance of the structured surfaces. Tribological properties of the structured samples were conducted using a precision nanotribometer.

5.1- Samples preparation

5.1.1- Thin films

Metallic thin films were produced by physical vapour deposition with an Ar–ion gun sputtering facility (Roth & Rau, UniLab) on a glass substrate under a vacuum of 10 Pa. The thickness of the films was monitored in-situ by a microbalance (Tectra, MTM-10). All samples employ glass micro-slides as substrate material.

The thicknesses of the layers as well as the metallic elements used were changed obtaining the samples configuration shown in Table 5.1.

Sample	A	B	C	D	E	F
1ˢᵗ Layer	Fe (30nm)	Fe (30nm)	Fe (30nm)	Cu (30nm)	Cu (30nm)	Cu (30nm)
2ⁿᵈ Layer	Al (30nm)	Al (60nm)	Al (120nm)	Al (30nm)	Al (60nm)	Al (120nm)

Sample	G	H	I	J	K	L
1ˢᵗ Layer	Ni (30nm)	Ni (30nm)	Ni (30nm)	Fe (30nm)	Ni (30nm)	Cu (30nm)
2ⁿᵈ Layer	Al (30nm)	Al (60nm)	Al (120nm)	-	-	-

Sample	M	N	O	P	Q	R
1ˢᵗ Layer	Fe (30nm)	Ti (30nm)	Ti (30nm)	Fe (75nm)	Al (30nm)	Al(30nm)
2ⁿᵈ Layer	Ni (30nm)	Al (30nm)	Ni (30nm)	Cu (30nm)	Fe (120nm)	Ni (120nm)
3ʳᵈ Layer	-	-	-	Al (55nm)	-	

Table 5.1*. Sample configuration: Material and thickness of each layer. In all cases glass was used as substrate.*

5.1.2- Bulk metals

Commercial copper and stainless steel foils (2 mm thick) were prepared metallographically by grinding and polishing with diamond suspension. The final stage of polishing was carried out using diamond particle size of 0.05 µm.

## 5.2- Laser interference structuring system

A high-power pulsed Nd:YAG laser (Quanta-Ray PRO 290, Spectra Physics) was employed for the laser interference experiments. The fundamental wavelength of the Nd:YAG laser is 1064 nm from which shorter wavelengths (532, 355 and 266 nm) can be generated by second-harmonic generation. The samples were irradiated with wavelengths of 266 and 355 nm. The frequency of the laser was 10 Hz. The pulse duration of the 266 and 355 nm radiations were 8 and 10 ns, respectively.

To obtain an interference pattern, a sufficient coherent length (L_c) is necessary, which is characteristic for this type of lasers. The coherence length is defined as the distance over which the output beam maintains a fixed phase relationship (Eq. 5.1):

$$L_C = \frac{c}{\Delta v}$$ (5.1)

where *c* is the speed of light and *Δv* is the line-width.

The line-width of a laser is the width of its power spectral density. In the case of the Nd:YAG laser (Quanta-Ray PRO 290), the line-width is about 1 GHz which produces a coherence length of more than one meter.
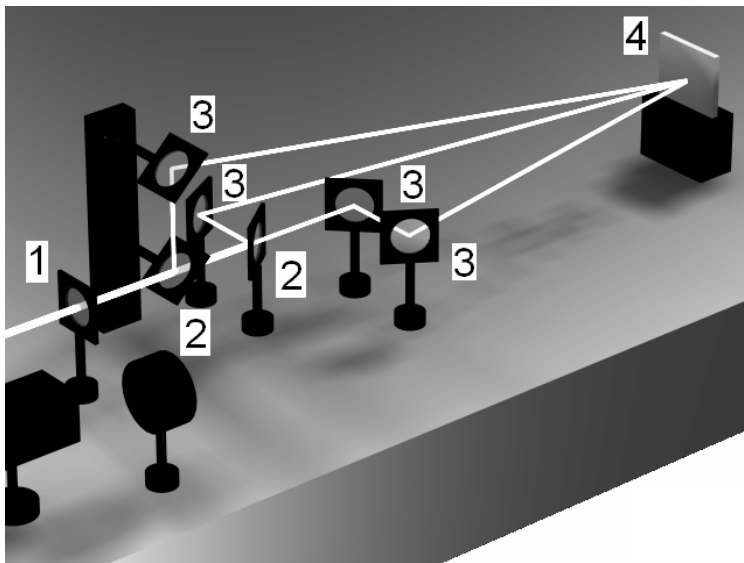
Figure 5.1. Schematic set-up for the laser interference system with the optical elements: (1) lens; (2) beam-splitters; (3) mirrors; (4) sample. Note that the primary beam is divided into 3 sub-beams which are overlapped at the sample surface.

The primary laser beam was split into two or more beams to interfere with each other on the sample surface. By the combination of a polarizer and a half-wave plate one can adjust the intensity impinging on the sample. The intensity can also be adjusted by a mechanical shutter (Uniblitz Electronic VS25S2ZMO) to choose the number of pulses. By a two-lens consisting telescope one can change the diameter of the laser beam and therefore the energy density received on the sample surface. The intensity of each individual beam can be controlled by using suitable lenses and mirrors. To reduce influences from the optical elements, high flatness of the splitters and mirrors are needed to construct the optical system. The energy of each partial beam was measured by using a power meter Power Max® model PM30V1.

The angles in between the laser beams were changed in order to produce different periodical structures. A scheme of the experimental setup is shown in Fig. 5.1.

For optical properties measurements, a square-shape mask was used to obtain a final beam with dimensions of 1.5 x 1.5 mm². Metallic samples with a size of

20 x 20 mm² were structured by using a sample positioning equipment (Kleindieck) controlled by computer micro-positioning stages. These were triggered with the laser.

5.3- In-situ time-resolved electrical resistance measurements

The current transients were measured with a fast oscilloscope LeCroy 9354C (500 MHz) across the 50-Ohm load resistance. A current source Keithley 2400 Digital Source Meter was used to apply a constant current (16 mA). For the experiments, the thin metallic films were sputtered using a rectangle mask over the glass substrate obtaining 1 per 10 mm layers (Fig. 5.2). The current source as well as the oscilloscope were connected at the extremes of the metallic film. The two laser beams were overlapped in the middle of the rectangular shaped film obtaining an interference pattern with the periodical lines perpendicular to the direction of the electric current.
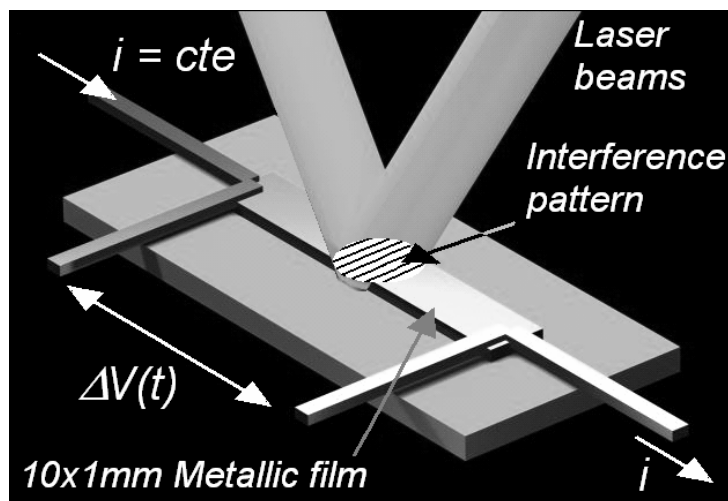
Figure 5.2. Experimental setup for the voltage-time evolution. The characteristic $\Delta V(t)$ was measured with the oscilloscope. The constant current i was provided by the current source.

5.4- Sample characterisation

5.4.1- Topographic characterisation

In order to measure the structure depth defined as the vertical distance between structural minima and maxima, a white light interferometer "Zygo New View 200" equipped with "3D Imaging Surface Structure Analyzer" was used.

Interference microscopes form an interference pattern with light reflected by the sample and a reference surface. If the reference surface is kept in a fixed position, interference fringes of each pixel in the image are formed as the reflecting

sample is moved through focus. The contrast of the interference fringes falls off rapidly as the object is defocused. By electronically processing the stored interference pattern, the envelope of the interference pattern for each pixel is determined to allow measurements of not only the amplitude but also the phase of the reflected light. Since phase can be measured to an accuracy of a few degrees, it is possible to measure height or surface roughness to accuracies of a small fraction of an optical wavelength [107].

The vertical resolution is on the order of 0.3 nm whereas the lateral resolution is between 0.73 and 11.8 µm depending on the used objective [108]. In our case, the periodical structures were measured with 800X zoom objective obtaining the maximal possible lateral resolution.

### 5.4.2- SEM and EDS characterisation

All samples were imaged with a high-resolution scanning electron microscope (SEM) equipped with a field emission gun (FEI Strata DB 235) at 5 kV acceleration voltage. In order to determine the distribution of elements on the structured surfaces, X-ray elemental mapping and line scans were conducted. The measurements were performed by energy dispersive spectroscopy (EDS) with an accelerating voltage of 15 kV using EDAX instruments detector and EDAX Genesis [MR] software. EDS cross sectional analyses in STEM mode were performed at 15-17 kV with a lateral resolution on the order of 100 nm.

5.4.3- Cross-sectional analysis and TEM foil preparation

Thin foils were prepared with the aid of a Dual Beam Workstation (FEI Strata DB 235) using the electron beam for imaging and Pt deposition (Fig. 5.3a) and the focused ion beam (Ga) for milling of the sample (Fig. 5.3b). Initial milling down to a foil thickness of 200 nm was performed utilizing the TEM Wizard provided by the workstation software and ion beam currents between 5000 and 300 pA. The lift-out of the foil was performed in-situ with a micromanipulator Kleindiek (Fig. 5.3c) and the sample was attached with Pt to a half-grid of Cu (Fig. 5.3d). For final thinning small ion beam apertures of 30 and 50 pA at an incident angle between 0.5 and 1.2° were used until the sample thickness was on the order of 70-100 nm. This sample preparation procedure ensures a preservation of the original topography and

provides a homogeneously thinned sample with such different materials as glass and metal [109].

For a first observation of the microstructure, a scanning transmission detector (STEM) was used in the Dual Beam workstation using an acceleration voltage of 15 kV and the ultra-high resolution mode of the electron microscopy.
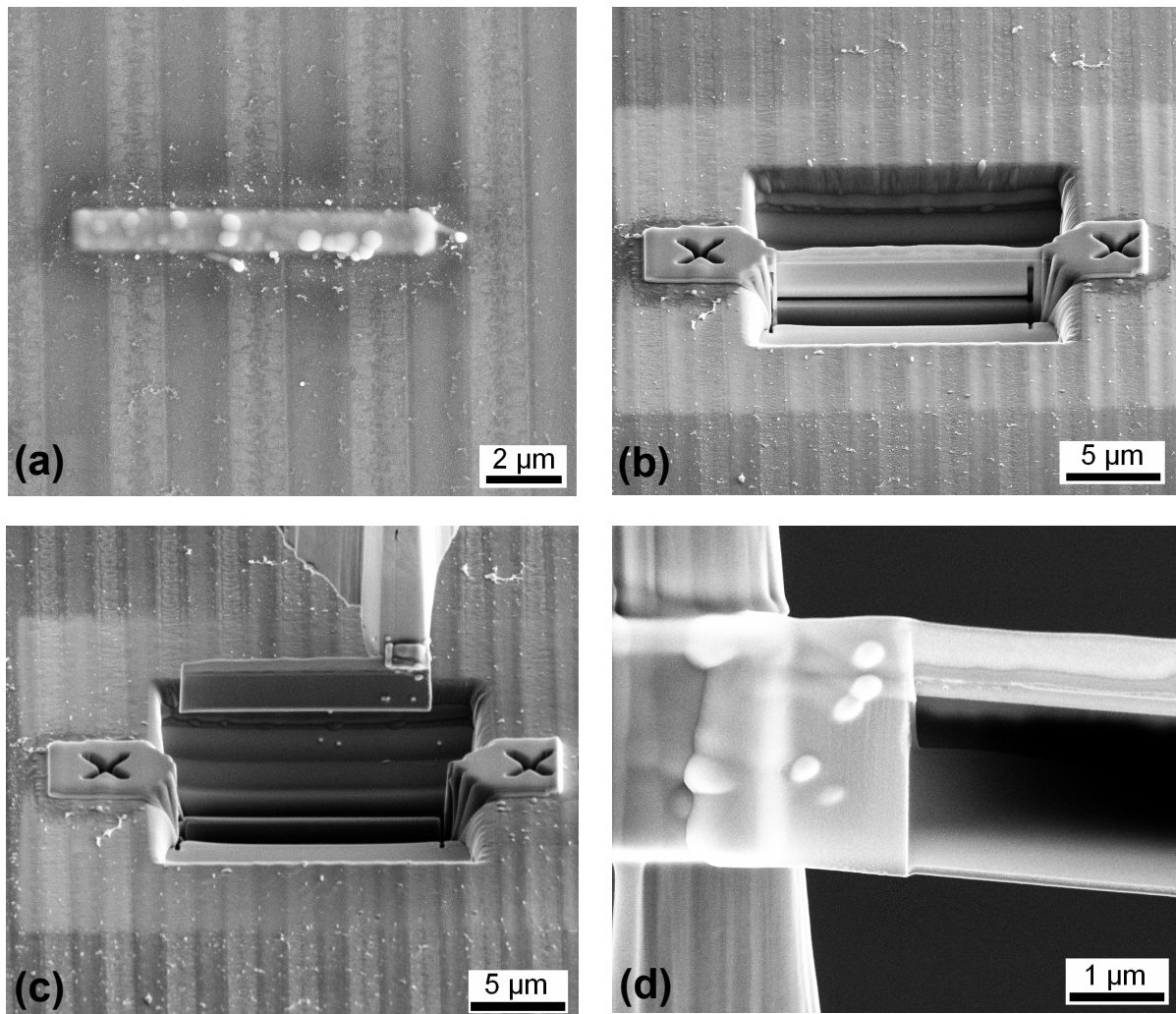
Figure 5.3. Target preparation by focused ion beam: (a) platinum deposition to protect the sample surface; (b) milling process imaged in SEM mode after TEM wizard; (c) lift-out of the foil performed in-situ with a micromanipulator; (d) attachment of the sample to a half-grid of Cu with Pt. (b) and (d): Tilt: 52°.

TEM investigations were carried out with a Jeol JEM 200 CX at an operating voltage of 200 kV. Both direct imaging for elucidation of the microstructure and selected area diffraction for phase identification were used. In addition, EDX (Oxford Isis) analysis was performed in order to identify the chemistry of the different phases.

Cross-sectional investigations were carried out by milling the sample surface with the focused ion beam after Pt deposition to protect the sample. After that, the samples were rotated 52° and imaged with high resolution scanning electron microscope.

5.4.4- High-angle annular dark-field microscopy investigations

For the sample Fe(75nm)/Cu(30nm)/Al(55nm), images and concentration profiles were obtained using a high-resolution analytical TEM (FEI Tecnai F20) operating at 200 kV. For imaging a High-angle annular dark-field (HAADF) detector in the STEM mode was employed. HAADF images are formed by collecting high-angle scattered electrons with an annular dark-field detector. The contrast of HAADF images is:

(a) strongly dependent on the average atomic number of the scattered encountered by the incident probe,

(b) not strongly affected by dynamical diffraction effects,

(c) not strongly affected by defocussing,

(d) and not strongly affected by sample thickness variations.

Therefore, in the case of FIB-lamellae with a relatively uniform thickness, the images mainly show Z-contrast. For concentration profiles line-scans were performed employing an EDX-detector (EDAX).

5.5- Characterisation of optical properties

Optical reflectance measurements were carried out with a Varian Cary 5E UV-Vis-NIR spectrophotometer in the wavelength range from 300 to 2500 nm and with an infrared spectrophotometer Bruker IFS-66V in the range between 1700 and 25000 nm.

Measuring of the total reflectance of laser structured samples was done using an integrated sphere coated with PTFE (polytetrafluoroethylene). The same material (PTFE- Labsphere plate) has been used as reference. Because the utilised FT-IR spectrophotometer was not equipped with a gold integrated sphere for measuring the total hemispherical emittance, only normal emittance was considered.

5.6- Characterisation of tribological properties

In tribometry, a flat or a sphere shaped indenter is loaded on to the test sample with a precisely known Force (Fig. 5.4). A pin is mounted on a stiff lever, designed as a frictionless force transducer. As the sample is either rotating or sliding, resulting frictional forces acting between the pin and the sample are measured by very small deflections of the lever. Wear coefficients for both the sample and material are calculated from the volume of the material lost during a specific friction run.
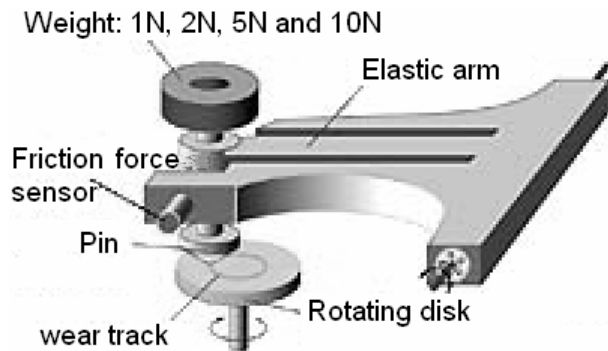

Figure 5.4. Scheme of the operating principle of a tribometer: a force normal to the sample is applied while the sample is rotating. The frictional forces between the sample and the pin are measured with the friction force sensor.

The precision nanotribometer (CSM – Instruments) used in this work consists of three basic units: precision motion mechanisms, force transducer and fibre-optic length detection system [110] (Fig. 5.5). The precision motion mechanisms consist of various drives incorporated within the micro-friction tester for sample positioning, providing normal force adjustment. The sample positioning drives are stepper motors. Coarse normal force adjustment is achieved manually by using a micrometer screw, while fine adjustment is performed using a piezo. A very important element of the system is the force transducer, which is made from photostructurable glass. The force transducer used in the microtribometer is a double leaf spring, shown in the insert in Fig. 5.5. The length of the beam is about 1 cm, while the width of the beams can be varied during fabricating making the double leaf spring suited for measuring either small or medium friction forces. Typically, the width of the beam is set at 100 μm for microtribological applications. With these dimensions, the normal force constant is typically 70 – 100 N/m and the lateral force constant 15 – 50 N/m.

Lateral and normal deflections of the photostructured glass bending element, the back and forth motion of the reciprocating unit as well as the vertical motion of the normal force adjustment drive are all measured using fibre-optic sensors based on the principle of reflection intensity variation. Both lateral as well as normal force constants need to be known to transform the length values read by the fibre-optic sensors to force values. This is performed by placing known precision weights on the

end of the double leaf spring and determining the deflection of the spring. The spring constant is obtained from the linear fit to the data. By rotation of the assembly containing the bending element spring by 90°, the lateral force constant was also determined.
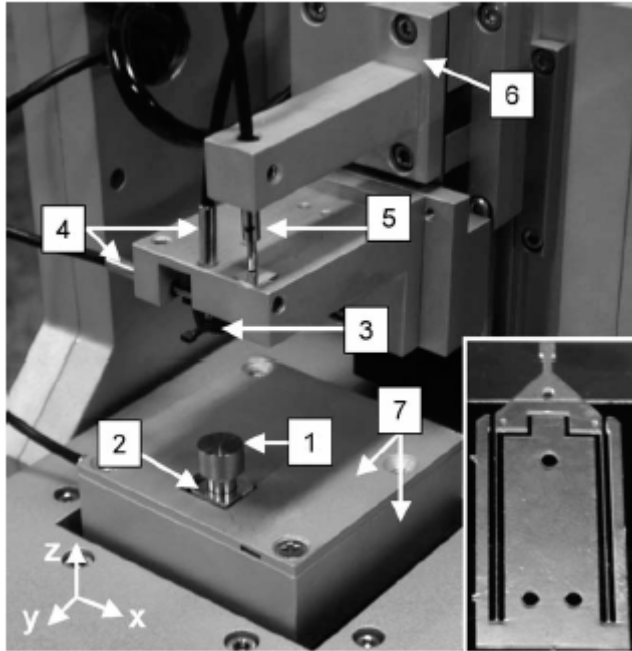
Figure 5.5. Image of the microfriction tester [110]. The main components are marked: (1) sample, (2) reciprocating unit, (3) force transducer, (4) fibre-optic sensors to detect normal and lateral deflections of the force transducer, (5) fibre-optic sensor for normal force adjustment detection, (6) precision drive to adjust normal force and (7) the yz-micropositioning stages powered by stepper motors with an integrated sample tilt adjustment. The inset shows a photo-structured glass spring.

In this study, measurements of the kinetic friction coefficient using the conditions indicated in Table 5.2 were performed. The low applied normal force (1 mN) ensures the preservation of the sample surface because at these conditions wear does not occur [110].

Parameter	Value
Radius	2.00 mm
Linear speed	0.20 cm/s
Normal load	1 mN
Substrate	100Cr6
Cleaning	Iso-propanol
Geometry	Ball
Ball diameter	2.00 mm
Environment	Air
Temperature	24.00 °C
Humidity	32.00 %

Table 5.2. Parameters used during the tribological tests.

Chapter 6

Micro/nano structuring of metallic systems

In this chapter, the structuring of thin metallic films as well as of bulk materials is presented. The first three sections (6.1, 6.2 and 6.3) include the structuring of thin metallic films showing different cases which depend on the number of metallic layers, the relative position of the layers in the film, and its thickness. After that (6.4), the structuring of bulk metals is presented indicating the effect of the laser fluence, the number of laser pulses, and the period of the micro/nano structures. In all the previously mentioned sections, the results are compared with thermal simulations in order to demonstrate the variables which control the structuring processes and the mechanisms involved. After that (6.5), the formation of intermetallic phases and bimetallic alloys is studied for the thin metallic films systems. In section 6.6, the consistence of the thermal simulations is demonstrated via in-situ electrical measurements, which describes the thermal history of the samples with nanosecond resolution. Aditional results about the structuring mechanism in Titania-silica mixed oxides are shown in appendix 4.

6.1- Single-layer systems

### 6.1.1- Structuring regimes

Single-layer thin metallic films were irradiated with interfering laser-beams using different laser fluences. In each experiment, the structure depth (vertical distance between peaks and valleys) was measured. The thin metallic films consist of one metallic layer of 30 nm over glass substrate.

In all cases, depending on the laser fluence, three different topographic regimes can be distinguished. In the first regime R1 (see Figs. 6.1, 6.2 and 6.3), at lower laser fluences, the structure depth is relatively low and the obtained structures are very homogeneous (Fig. 6.4a). In the second regime (R2), the metallic film is removed at the interference maxima positions leading to a rise in the structure depth. Fig. 6.4b shows the characteristic topography of this regime. The dark zones

correspond to the glass substrate. If the fluence of the laser is further increased, the width of the regions where the metallic layer is removed (dark areas) also increases. This indicates a higher removal rate of material. Still higher fluences produce a fall of the structure depth indicating the beginning of the regime 3. The surface of the structured samples reveals droplets of metal at the energy minima positions (Fig. 6.4c) which indicates that the whole metallic layer is practically removed.
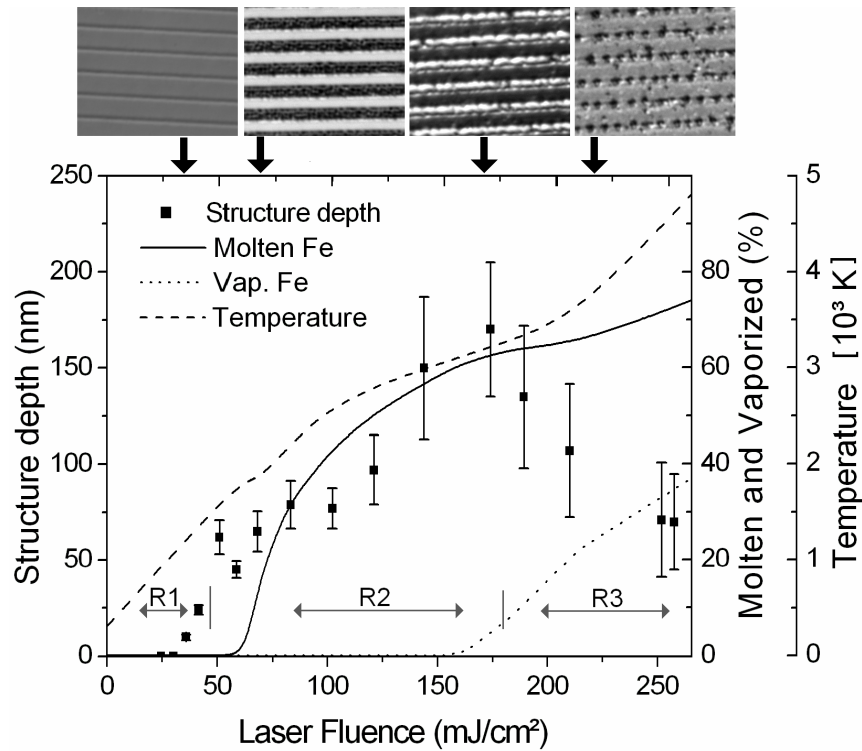

Figure 6.1. Structure depth (experimental), temperature, molten and vaporised material (simulated) depending on the laser fluence for the sample Fe (30 nm). The details above the picture show the type of topography which corresponds to each regime (light microscope images).
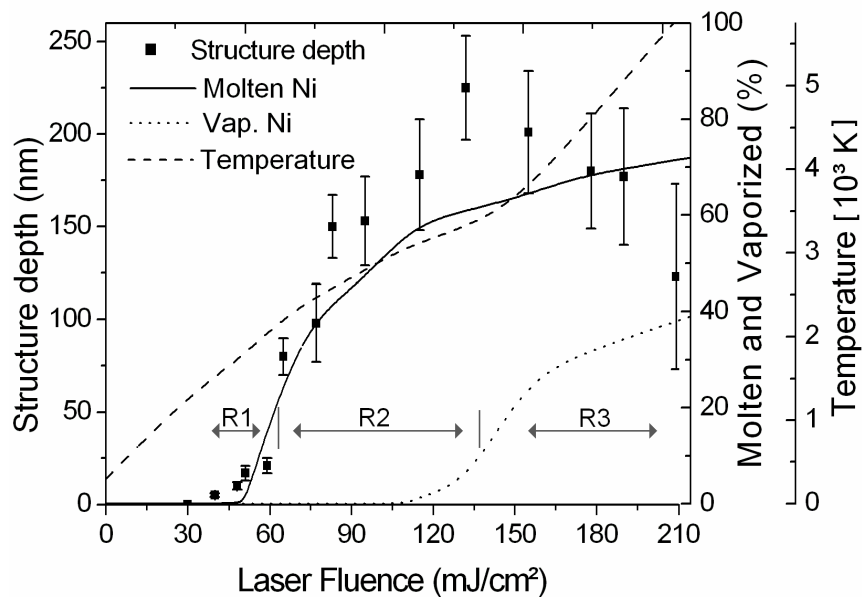
Figure 6.2. Structure depth (experimental), temperature, molten and vaporised material (simulated) depending on the laser fluence for the sample Ni (30 nm).
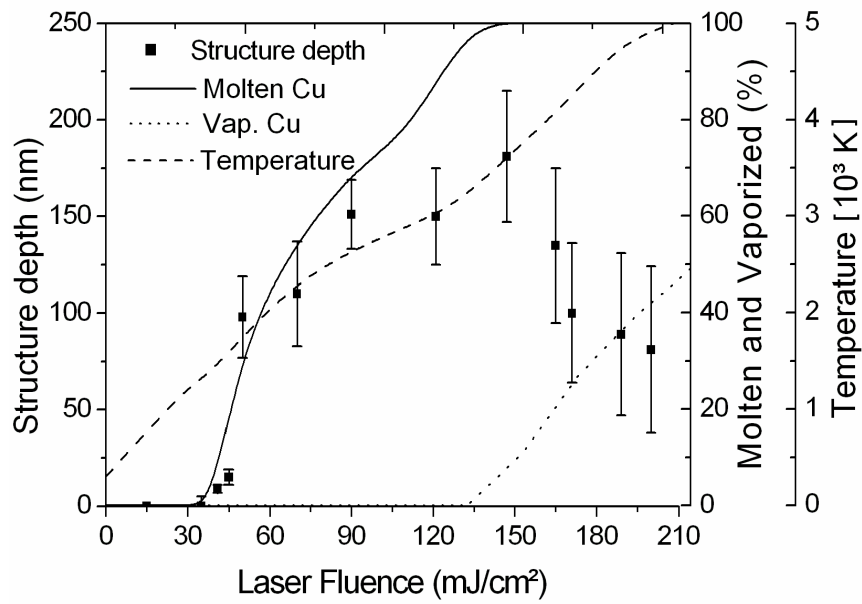
Figure 6.3. Structure depth (experimental), temperature, molten and vaporised material (simulated) depending on the laser fluence for the sample Cu (30 nm).
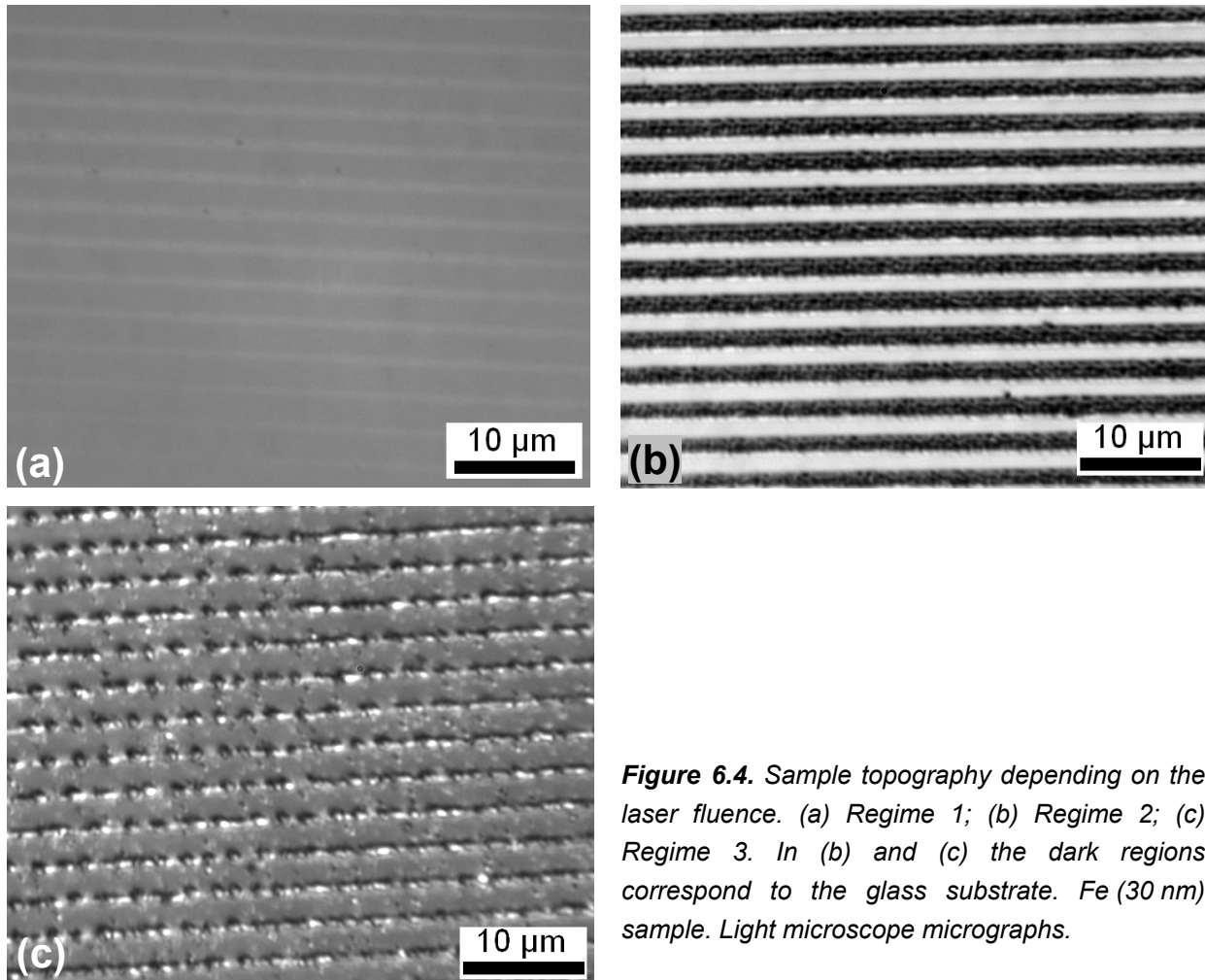

Figure 6.4. Sample topography depending on the laser fluence. (a) Regime 1; (b) Regime 2; (c) Regime 3. In (b) and (c) the dark regions correspond to the glass substrate. Fe (30 nm) sample. Light microscope micrographs.

65

6.1.2- Thermal simulation

The thermal simulation by finite element method was used to calculate the molten and vaporised metallic regions as a function of the laser fluence.

As an example for the calculation method, the simulation of a Fe (30 nm) sample using a laser fluence of 210 mJ/cm² is presented (Fig. 6.5). An angle of 5.05° in between the laser-beams generates a line like interference pattern with a period of 3.02 µm. Due to the high laser fluence, the Fe-film is partially molten (Fig. 6.5a) and even evaporated (Fig. 6.5b) at the interference maxima positions. At the interference minima positions on the other hand, the material remains in the solid state. That can be explained through a difference of approximately 2880 K, which is observed between both positions (Fig. 6.6). Due to the nanometric thickness of the film (30 nm), the temperature along the z-axis is constant, which is in accordance with [74]. Thus, rectangular molten and vaporised regions are calculated (Fig. 6.5).
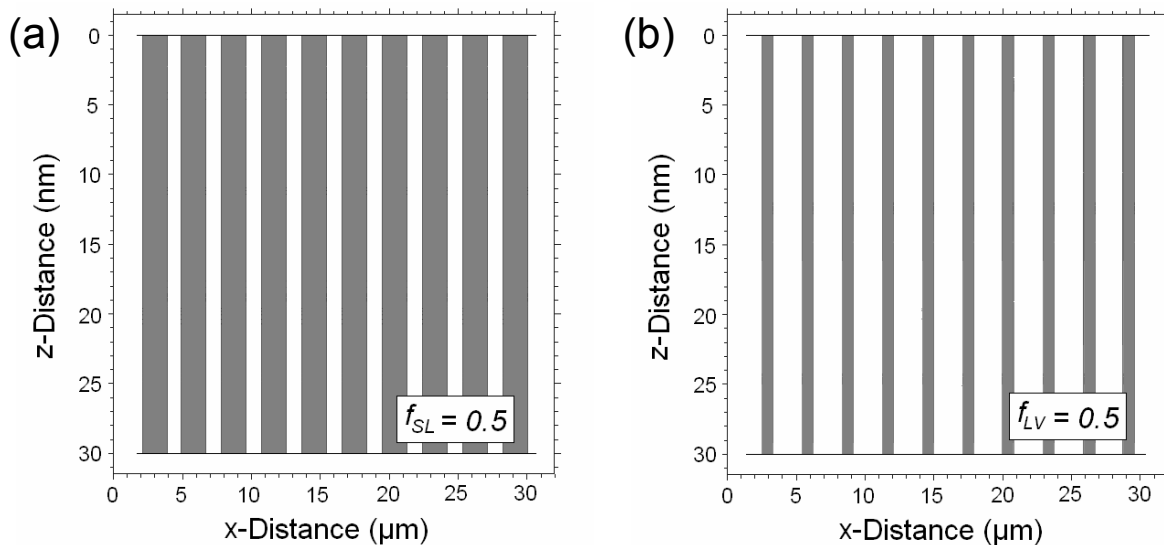
Figure 6.5. *Simulated (a) molten and (b) vaporised regions of a 30 nm Fe-film. The grey colour represents the molten (a) or the vaporised (b) material taking as reference a value of 0.5 for the variable f_{SL} and f_{LV}, respectively. The molten region in (a) represents the 65% of the Fe-metallic layer. The vaporised metal in (b) represents 22% of the Fe-layer. Laser fluence = 210 mJ/cm².*

The dependence of the laser fluence on the structure depth (experimental) together with the simulated percentages of the molten and vaporised regions, and the temperature at the interference maxima is presented in Fig. 6.1, 6.2 and 6.3 for the metallic films Fe, Ni and Cu, respectively. The molten and vaporised fractions at each laser fluence value were calculated by measuring the grey areas indicated in Fig. 6.5 and comparing them with the total area of the metallic film.
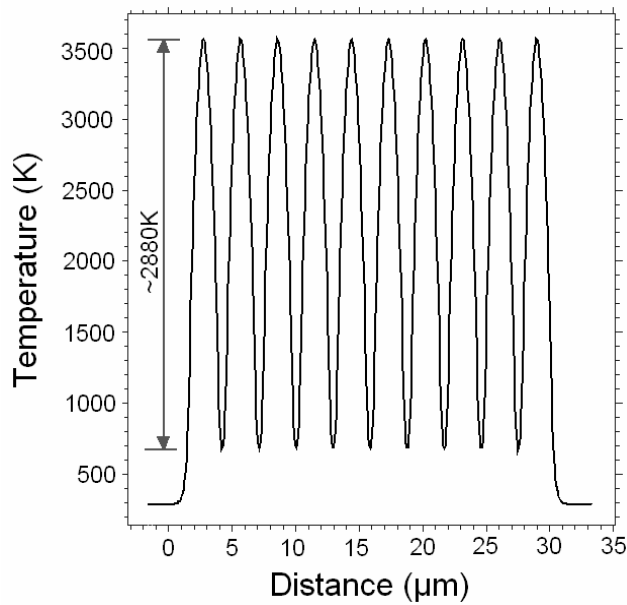
Figure 6.6. *Lateral temperature profile of a 10 peaks interference pattern of a 30 nm-Fe film over glass substrate. A difference of about 2880 K between the interference maxima and minima positions was calculated.*

6.1.3- Discussion

Three different topographic regimes were observed depending on the laser fluence. The structuring mechanism for this layer configuration is shown in Fig. 6.7. In the first regime (R1), at low laser fluences, the structuring process is conducted without removal of material at the interference maxima positions (Fig. 6.4a). The high temperature at the interference maxima (Fig. 6.7a) produces the thermal dilatation of the metal. The dilatation causes permanent deformation of the metallic layer at the interference maxima and therefore the structuring can be conducted without melting (Fig. 6.7b). In the second regime, the metallic layer is partially molten at the interference maxima (Fig. 6.4b). The molten material flows towards the interference minima producing non-homogenous structures (Fig. 6.7c). The term non-homogenous indicates that along the symmetrical axis of the periodical pattern, the maximum height is not constant. That explains why it is possible to obtain structure depths even larger than the thickness of the film (see transition in the structure depth from R1 to R2 in Fig. 6.1, 6.2 and 6.3). The size of the removed area can be controlled increasing or decreasing the laser fluence (Fig. 6.7d). If the laser fluence is still higher, the structure depth decreases (Fig. 6.7e). At this laser fluence value, the energy density is high enough to locally vaporise the metal at the interference maxima positions and thus enter to the ablation regime (R3) with high removal rates of material (see Fig. 6.4c). This fact is also suggested by the thermal simulation because at these laser fluences vaporised metal is observed.

Two different threshold values related to the energy per unit area required to change from one to other structuring regime can be defined according to the laser fluences which correspond to an abrupt rise or fall in the structure depth. The first threshold laser fluence is related to the energy necessary to change from the first to the second regime (F_{R1-2}). According to the thermal simulation, this fluence represents the energy necessary to start to melt the metallic layer. In a similar manner, the second threshold value is related to the energy required to change from the second to the third regime (F_{R2-3}) and can be defined as the energy necessary to vaporise the metallic layer. The threshold laser fluences from both the experimental results and the thermal simulation are presented in Table 6.1. A maximum difference of 24.6% was observed between the experiments and the simulation.
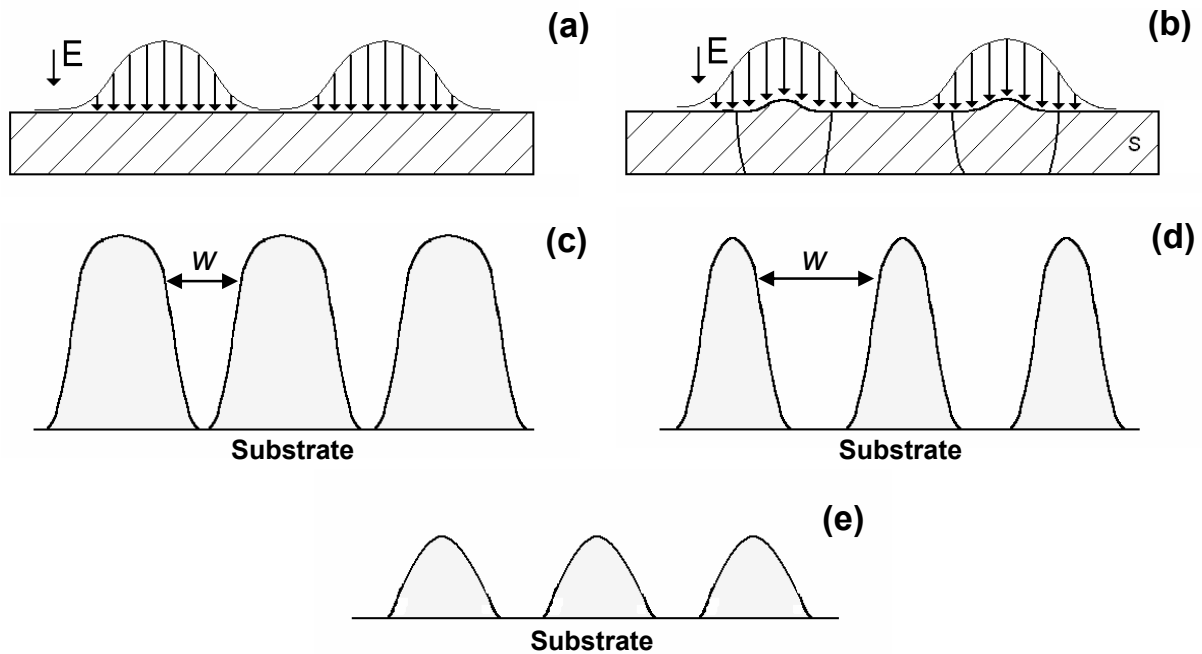
Figure 6.7. Micro/nano structuring schema of the one-layer case (a) The laser interference pattern acts over the surface of the metal; (b) permanent deformation of the layer is induced by thermal dilatation of the metal; (c) the layer is molten at the interference maxima; (d) by increasing the laser fluence, the width (w) of the removed area also increases; (e) ablation regime with a high removal rate of material which results in flatter structures.

	Threshold	Exp. (mJ/cm²)	Sim. (mJ/cm²)	err %
Fe	F_{R1-R2}	46	61	24.6
	F_{R2-R3}	172	156	10.3
Ni	F_{R1-R2}	62	50	24.0
	F_{R2-R3}	132	110	20.0
Cu	F_{R1-R2}	45	47	4.3
	F_{R2-R3}	147	141	4.3

Table 6.1. Threshold laser fluence values for single-layer metallic systems.
*Exp: experimental; Sim: simulated.*

6.2- Two layer systems - Case A: Metal with the higher melting point on top

### 6.2.1- Structuring regimes

The influence of the laser fluence on the sample topography was studied. All investigated metallic systems present the same characteristics in the observed topographic types. Two different structuring regimes were distinguished. In the first one, the structuring is conducted without removal of material at the interference maxima. As example, the topography of the system Fe(30 nm)/Al(120 nm) structured with a low laser fluence is shown in Fig. 6.8a. Higher fluences produce an abrupt change of the topography as shown in Fig. 6.8b (sample Cu(30 nm)/Al(120 nm)). The dark lines in Fig. 6.8b correspond to the substrate because at these positions the metallic layers were locally and periodically removed.

The effect of the period on the quality of the periodical structures was also studied. Samples irradiated with an interference pattern of a large period indicate to be very uniform. This means that the peaks and valleys of the periodical structures can be clearly distinguished (Fig. 6.8). Interference patterns with periods smaller than about 2 µm produce structures with a low quality. Moreover, in some cases the periodical structures can not be differentiated.
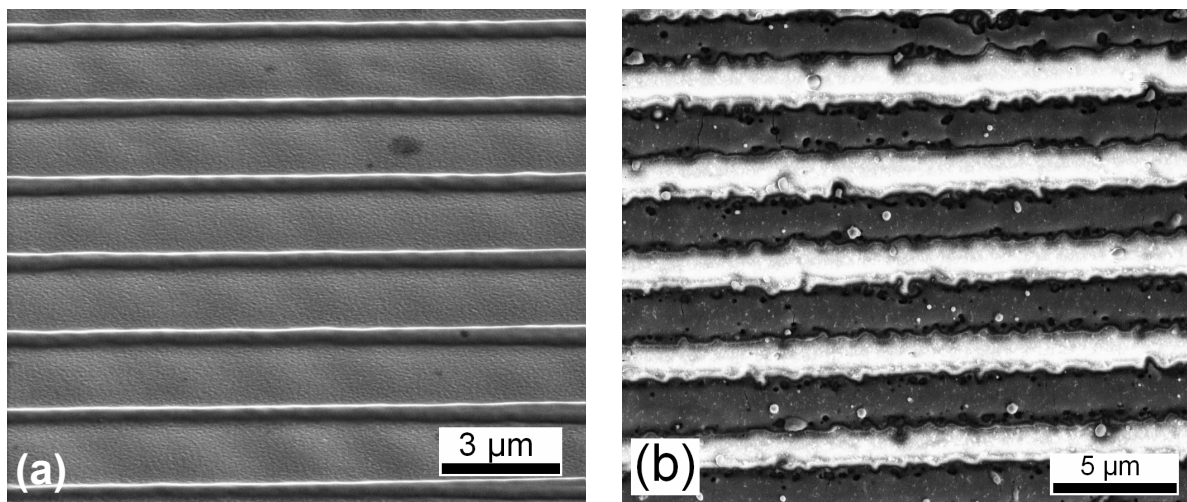
Figure 6.8*. Topography of the sample after structuring using (a) a low (sample Fe(50 nm)/Al(120 nm)/Glass, Tilt: 52°) and (b) high laser fluences (sample Cu(30 nm)Al(30 nm), Tilt: 0°). Note that the thin lines in (a) are above the general surface level. The dark lines in (b) correspond to substrate because the metallic layer was removed. SEM Images.*

The laser fluence value at which the topographic type changes was also studied in relation to the period of the interference pattern. For the sample Fe(30 nm)/Al(30 nm) these values are 40 and 51 mJ/cm² for periods of 4.35 and 3.01 µm, respectively.
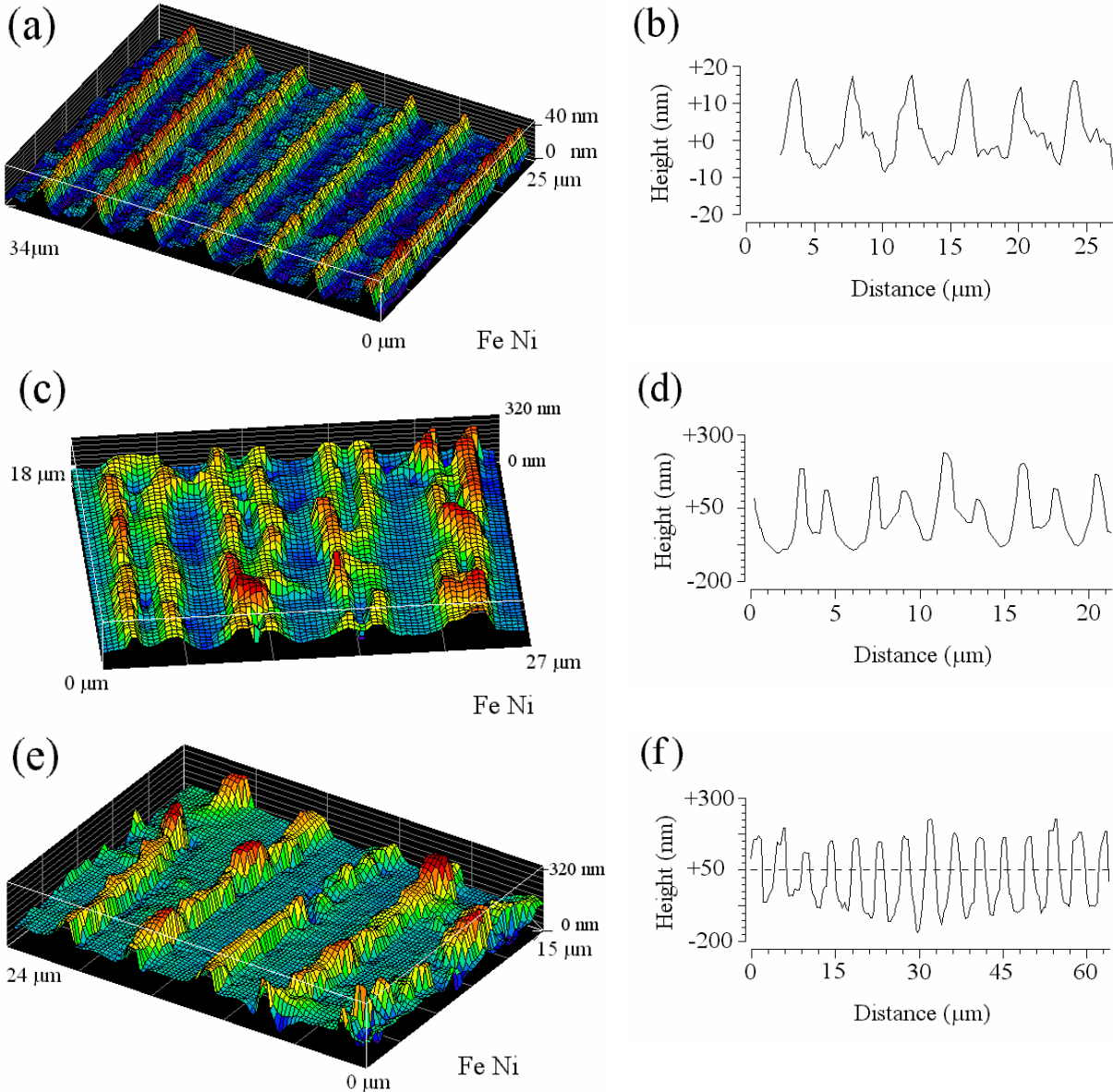
Figure 6.9. *Sample Fe(30 nm)/Ni(30 nm)/Glass. 3D-Topography and lateral profile for a laser fluence of: (a, b) 192 mJ/cm² (value between F_{R1} and F_{R1-2}); (c, d) 210 mJ/cm² (laser fluence value above F_{R1-2}), the lateral profile shows a large depression and next two consecutive peaks of material; and (e, f) 215 mJ/cm². White light interferometry (WLI) images. Period = 4.35 µm.*

Fig. 6.9a and 6.9b show the topography and the lateral profile of a Fe(30 nm)/Ni(30 nm) sample after irradiation with a laser fluence of 192 mJ/cm² (low energy regime). The period of the structures was 4.35 µm. From this figure, it is possible to note that the thin lines are above the general surface level. Fig. 6.9c and

d show the topography and the lateral profile of the same system after structuring with a laser fluence of 210 mJ/cm². In this case, the lateral profile shows a large depression and next two consecutive peaks (Fig 6.9d). Fig. 6.9e and 6.9f show the topography and the lateral profile of the same sample at a laser fluence value of 215 mJ/cm². A periodic peak-valley pattern with a higher structure depth in comparison to the pattern shown in Fig. 6.9b can be observed. In Figs. 6.9c and 6.9e the metal was removed at the interference maxima positions.

6.2.2- Thermal simulation

Unlike in single-layer systems, depending on the fluence of the laser, one or both metallic layers can be molten or even vaporised at the interference maxima positions of the interference pattern. Also, in this case, because of the nanometric thickness of the layers, the film temperature along the z-axis was found to be constant. Several metallic samples were studied obtaining similar results.

As example, the thermal simulation of the sample Cu(30 nm)/Al(30 nm) is presented. Two different fluences were simulated (70 and 120 mJ/cm²) indicating the temperature evolution and the fractions of molten material in each layer (this last calculated at the time at which the maximum temperature is reached at the interference maxima positions). In the first case (Fig. 6.10), the maximum temperature reached during the laser pulse (1040 K) is not high enough to melt the upper copper layer (T_m = 1358 K). The maximum temperature difference between the interference maxima and minima occurs 4.0 ns after the laser pulse and reaches about 450 K. In the second case (Fig. 6.11), the laser fluence (120 mJ/cm²) is high enough to melt both layers. The maximum temperature difference between interference maxima and minima takes place 4.2 ns after the laser pulse in this case is of 740 K.

The dependence of the structure depth on the laser fluence together with the simulated percentages of the molten and vaporised regions, and the temperature at the interference maxima and minima is presented in Figs. 6.12 to 6.17 for several metallic systems. In all cases, the thickness of each individual layer was 30 nm (the total thickness of the metallic film was 60 nm).
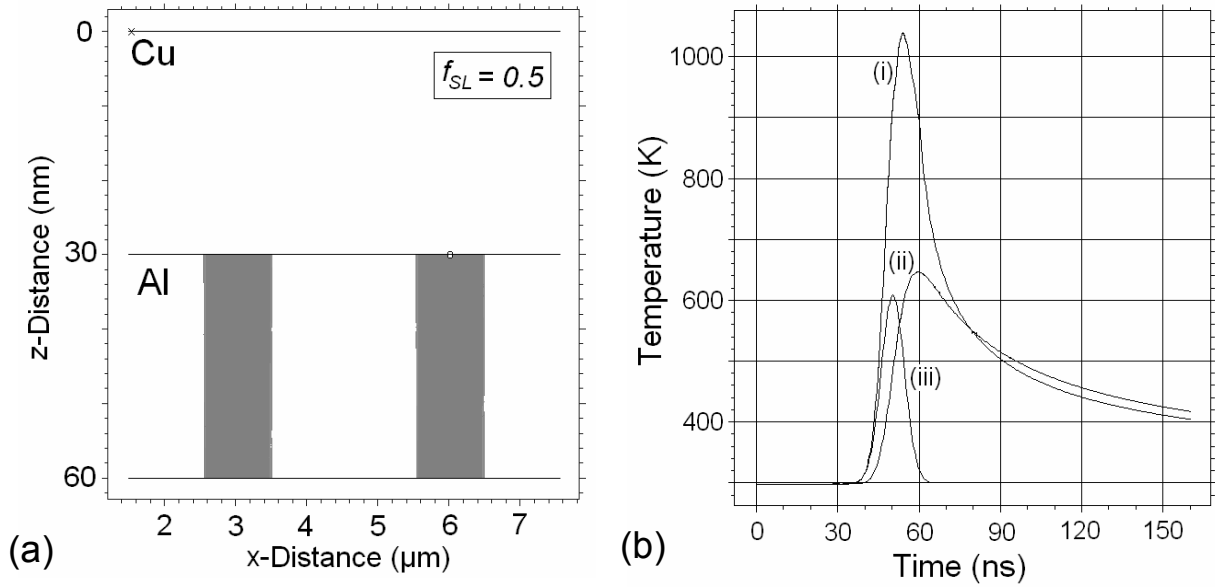
***Figure 6.10**. (a) Simulated molten regions of a Cu(30 nm)/Al(30 nm) sample at 70 mJ/cm² of laser fluence. The grey colour represents the molten material taking as reference a value of 0.5 for the variable f_{SL} to define the solid-liquid frontier. (b) Temperature evolution at interference maxima (i) and minima (ii). (iii) Laser pulse (arbitrary units). The temperature at the interference maxima is high enough to melt the aluminium layer but not the copper layer (melting point: 1358 K).*
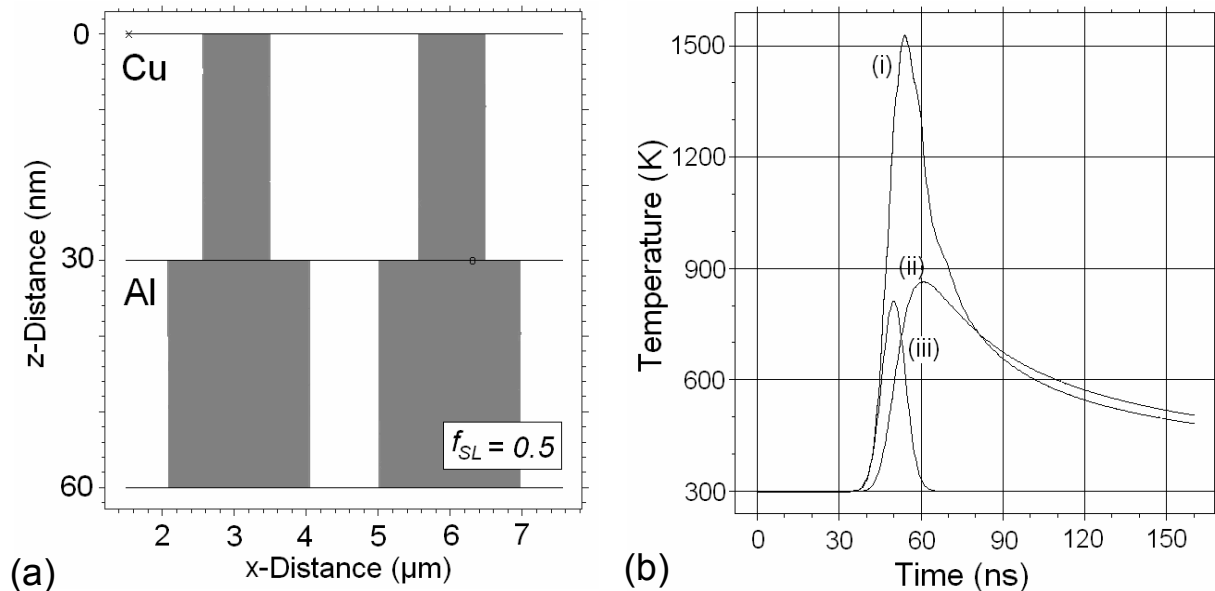
***Figure 6.11**. (a) Simulated molten regions of a Cu(30 nm)/Al(30 nm) sample at 120 mJ/cm² of laser fluence. The grey colour represents the molten material taking as reference a value of 0.5 for the variable f_{SL} to define the solid-liquid frontier. (b) Temperature evolution at interference maxima (i) and minima (ii). (iii) Laser pulse (arbitrary units). The temperature at the interference maxima is high enough to melt both the aluminium and the copper layer.*

72
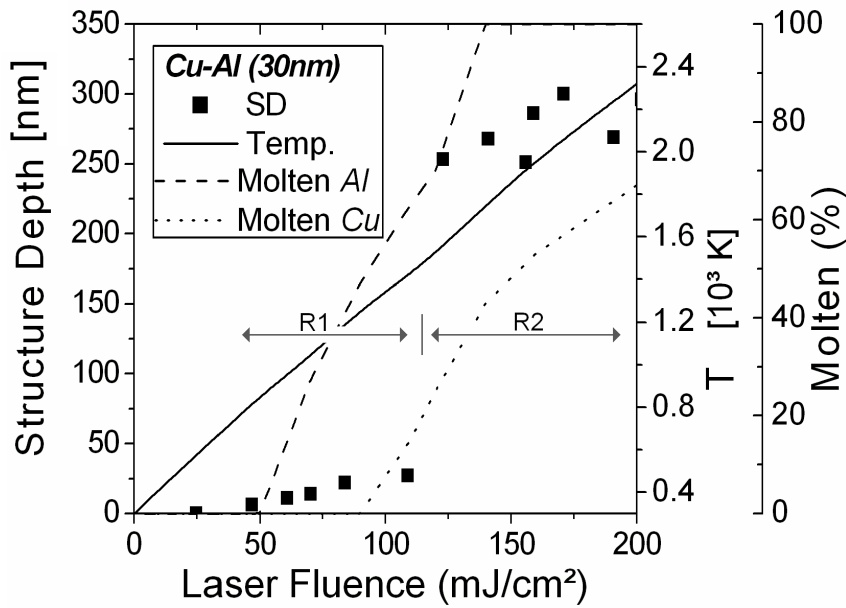
Figure 6.12. *Structure depth (experimental), maximum temperature at the interference maxima, molten and vaporised material (simulated) depending on the laser fluence for a Cu(30 nm)/Al(30 nm) sample.*
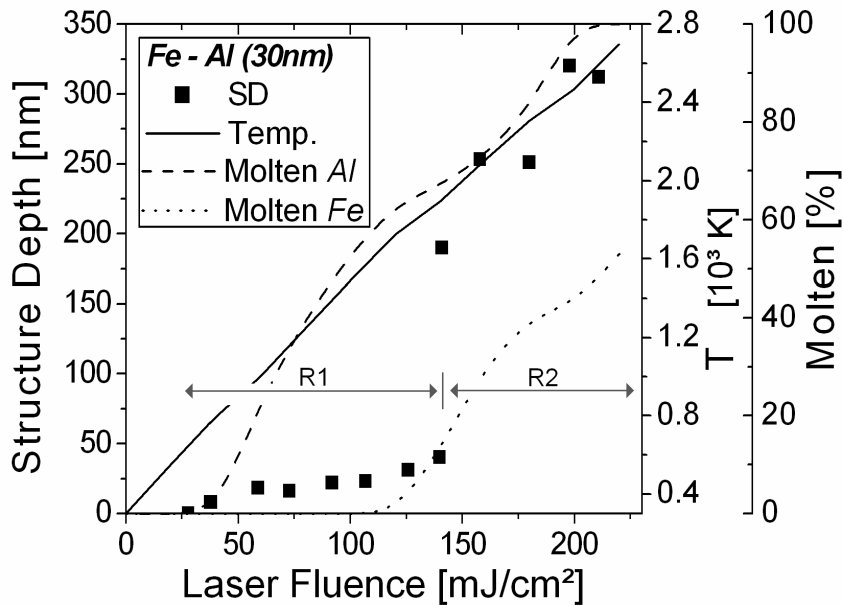
Figure 6.13. *Structure depth (experimental), maximum temperature at the interference maxima, molten and vaporised material (simulated) depending on the laser fluence for a Fe(30 nm)/Al(30 nm) sample.*
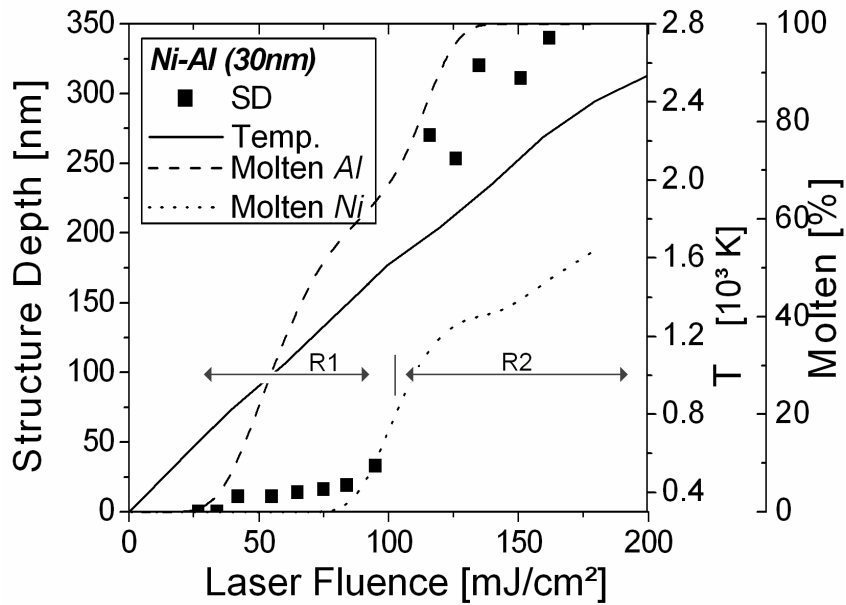
Figure 6.14. *Structure depth (experimental), maximum temperature at the interference maxima, molten and vaporised material (simulated) depending on the laser fluence for a Ni(30 nm)/Al(30 nm) sample.*

Figure 6.15. *Structure depth (experimental), maximum temperature at the interference maxima, molten and vaporised material (simulated) depending on the laser fluence for a Fe(30 nm)/Ni(30 nm) sample.*

Figure 6.16. Structure depth (experimental), maximum temperature at the interference maxima, molten and vaporised material (simulated) depending on the laser fluence for a Ti(30 nm)/Al(30 nm) sample.
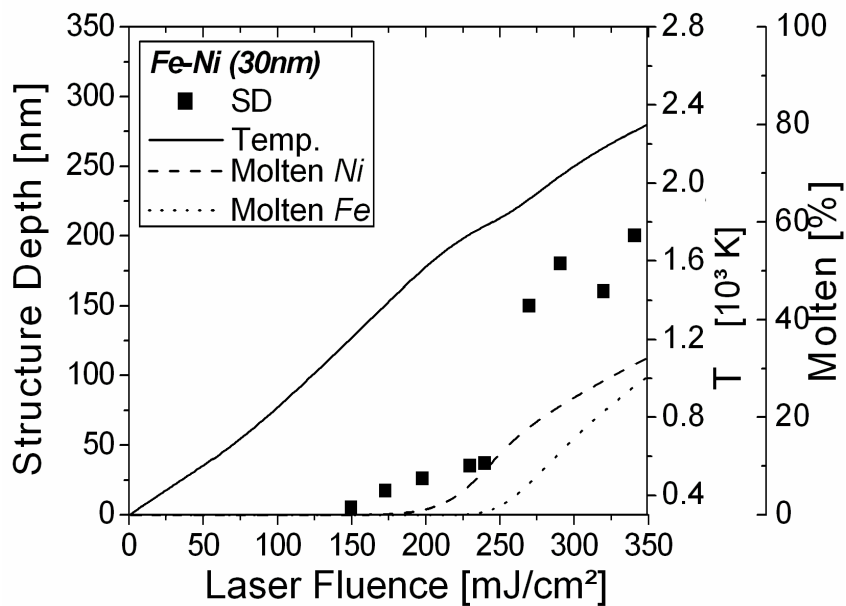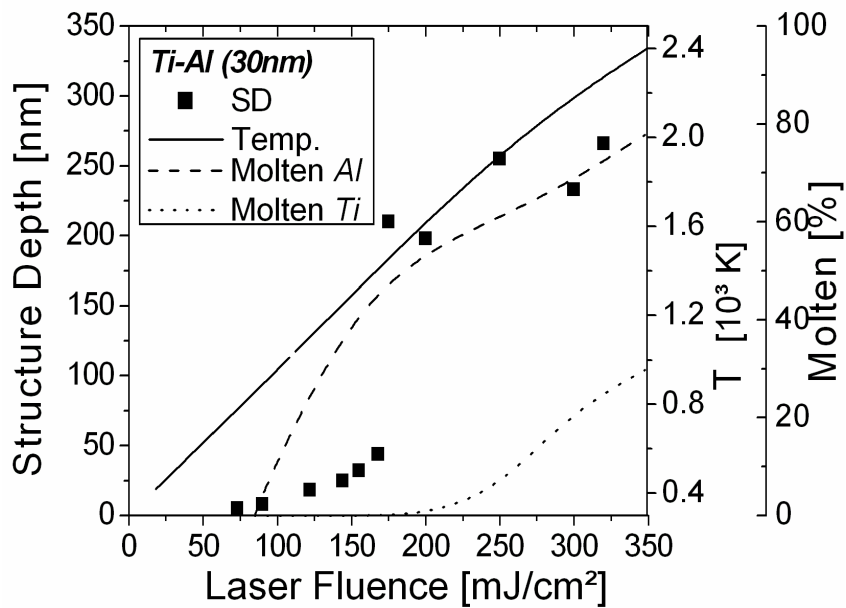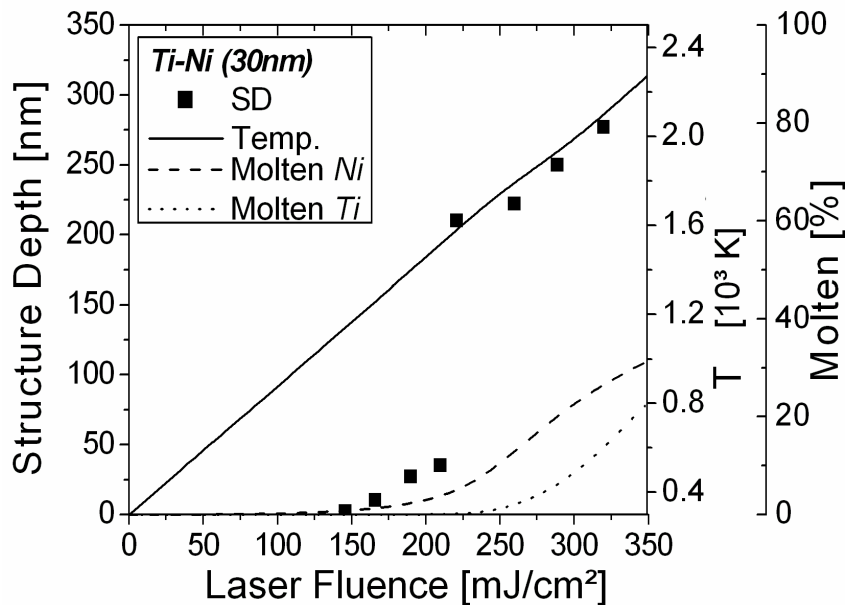

Figure 6.17. Structure depth (experimental), maximum temperature at the interference maxima, molten and vaporised material (simulated) depending on the laser fluence for a Ti(30 nm)/Ni(30 nm) sample.

The effect of the period of the interference pattern on the difference in temperature between the interference maxima and minima was studied. Fig. 6.18 indicates the temperatures at the interference maxima and minima positions as well as its quotient obtained during the laser-pulse evolution simulated for a Fe(30 nm)/Al(120 nm) sample at a laser fluence of 110 mJ/cm². For a period of 3 μm the temperature at the interference maxima and minima are 1701 and 764 K while for 1.5 μm the calculation reveals 1391 and 902 K, respectively.
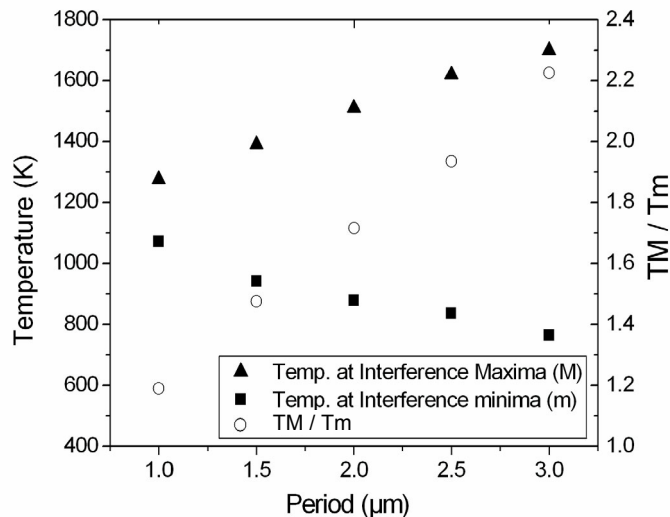
Figure 6.18. Temperatures at the interference minima (Tm) and maxima (TM) and its quotient (TM / Tm) simulated for a Fe(30 nm)/ Al(120 nm) sample at a laser fluence of 110 mJ/cm².

6.2.3- Multi-beam experiments

Different geometrical configurations including 3 beams laser interference experiments as well different laser fluences were used. The samples Cu(30 nm)/Al(120 nm) and Fe(30 nm)/Al(120 nm) were investigated.
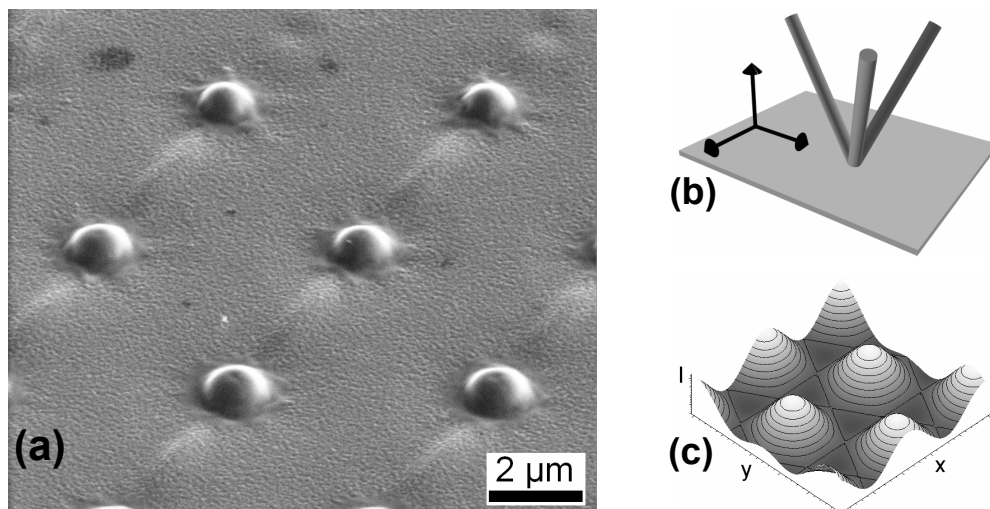
Figure 6.19. (a) Periodical dot-type structure on a Fe(30 nm)/Al(120 nm) sample obtained by using three laser-beams. (b) Laser-beam configuration; the relative size of the beams indicates the magnitude of the partial beams intensity (see Table 6.2). (c) Calculated interference pattern considering (b).

76

Three laser-beam interference experiments include identical and dissimilar energies for each laser-beam as described in chapter 4.1. Different examples of the produced periodical structures are shown in Figs. 6.19 to 6.23 including a scheme of the laser-beam configuration used as well as the calculated interference pattern. Table 6.2 shows both the angles and the partial energies of the beams employed in each experiment.
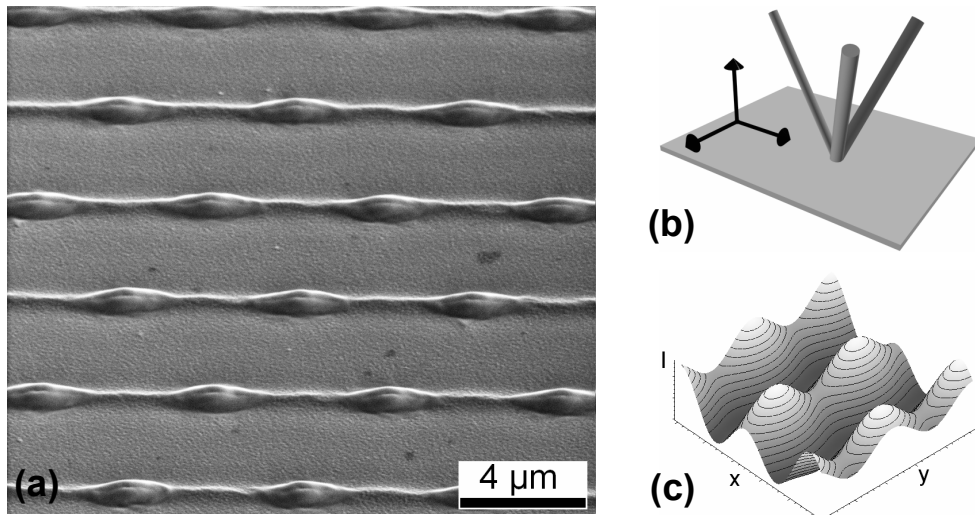
Figure 6.20. *(a) Periodical dot/line-type structure on a Fe(30 nm)/Al(120 nm) sample obtained by using three laser-beams. (b) Laser-beam configuration (c) Calculated interference pattern considering (b).*

Figure 6.21. *(a) Oval-type periodical structure on a Cu(30 nm)/Al(120 nm) sample obtained by using three laser-beams. (b) Laser-beam configuration indicating the relative intensity of the partial beams (see Table 6.2). (c) Calculated interference pattern considering (b).*
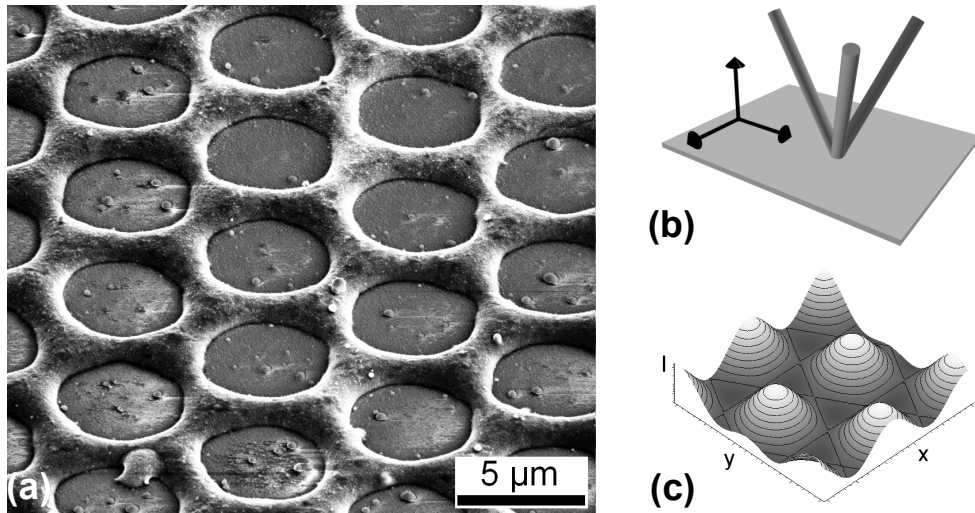
Figure 6.22. *(a) Crater type periodical structure on a Cu(30 nm)/Al(120 nm) sample obtained by using three laser-beams and symmetrical configuration. (b) Laser-beams arrangem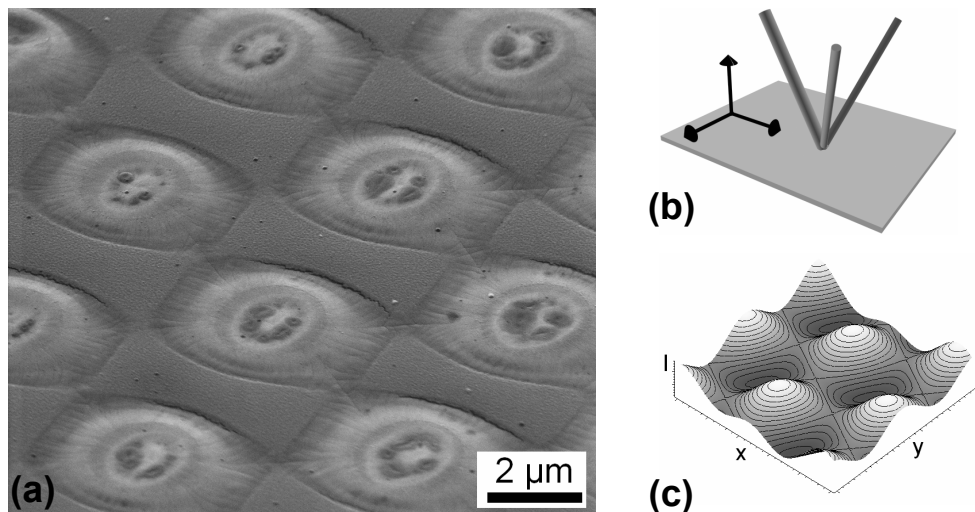ent; the partial intensity of each laser-beam was the same. (see Table 6.2). (c) Calculated interference pattern considering (b). The metallic layer at the interference maxima positions was removed because of the high laser fluence.*
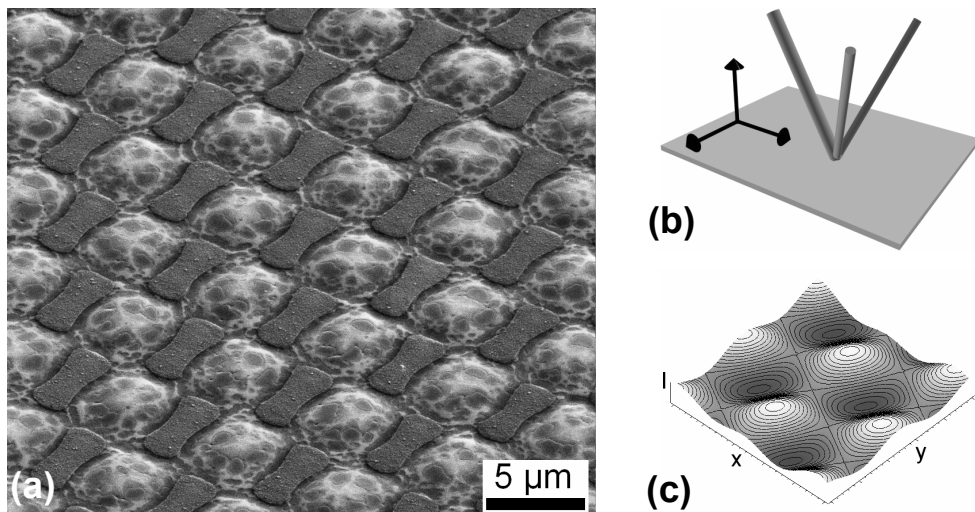
Figure 6.23. *(a) Square periodical type structure on a Cu(30 nm)/Al(120 nm) sample obtained by using three laser-beams and non-symmetrical configuration. (b) Laser-beams arrangement; the relative size of the beams indicates the magnitude of the partial beam intensities (see Table 6.2). (c) Calculated interference pattern considering (b).*

Sample	Fluence (mJ/cm²)	α_1 (grad)	α_2 (grad)	α_3 (grad)	$E_1\%$ [*]	$E_2\%$ [*]	$E_3\%$ [*]	Figure
Fe/Al	70	1.71	1.71	1.70	33.3	33.3	33.4	6.18
Fe/Al	89	1.71	1.71	1.71	43.0	43.0	14.0	6.19
Cu/Al	78	1.60	1.60	1.60	60.2	19.9	19.9	6.20
Cu/Al	121	1.60	1.60	1.60	33.3	33.3	33.4	6.21
Cu/Al	81	1.60	1.60	1.60	66.6	16.7	16.7	6.22

Table 6.2. Laser parameters employed to produce the two dimensional periodical structures shown in Figs. 6.18 to 6.22. In all cases, the angle in between the laser-beams parallel to the surface sample was 120° (symmetrical geometrical configuration). (*) $E_1\%$, $E_2\%$ and $E_3\%$ represent the percentage of the intensity of each laser-beam (E1% + E1% + E1% =100%).
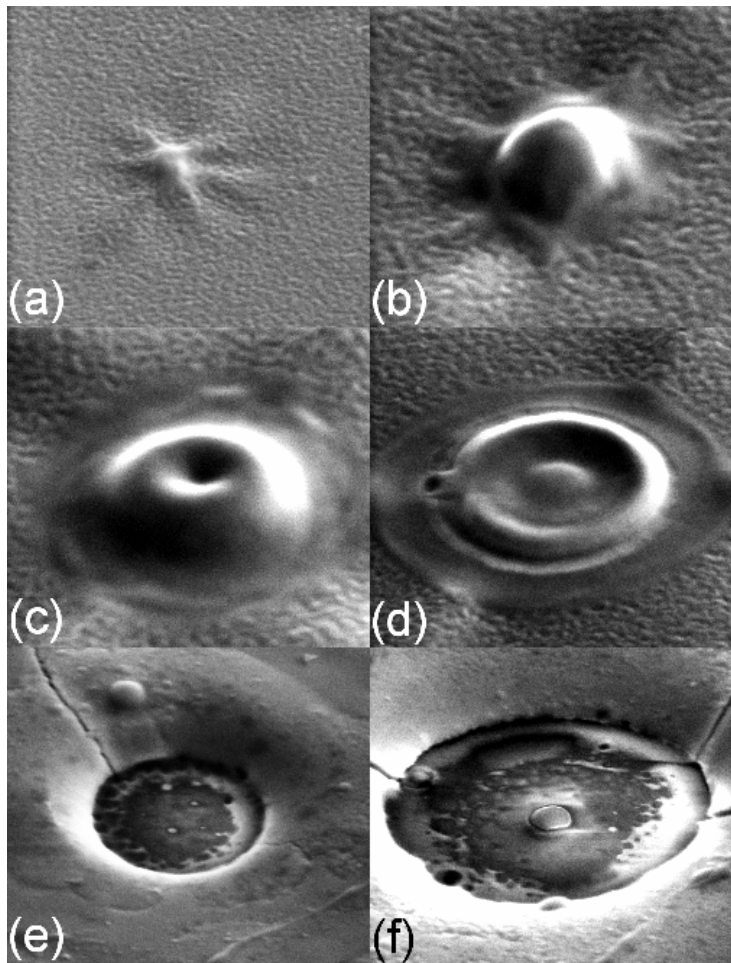
Figure 6.24. View of the structure transition generated with 3 symmetrical nanosecond laser-beams. (a) and (b) semi- spherical structures generated with a laser fluence of 25 and 65 mJ/cm². (c) A depression in the middle of the semi-sphere is generated and increases while the laser fluence also increases (d). Crater type structure obtained at (e) 91 and (f) 124 mJ/cm² of laser fluence.

Different dot-type periodical structures which were produced using symmetrical configuration and identical partial beam energy are shown in Fig. 6.24. The structures are ordered according to the laser fluence utilised in the experiments

having the lowest value in Fig. 6.24a and the highest in Fig. 6.24f. Depending on the laser fluence, different dot structures were observed. At laser fluences below 72 mJ/cm², the shape is semi-spherical with a maximum height of 335 nm (Figs. 6.24a and 6.24b). At 72 mJ/cm² (Fig. 6.24c), a small depression in the middle of the semi-sphere develops. While still increasing the laser fluence, the obtained structures are flatter and crater-shaped (Fig. 6.24d) without removing the metallic layers at the interference maxima. At 78 mJ/cm², a central hole starts to form (Fig. 6.24e). Even higher laser fluences produce craters which results from the removal of the metallic layers at the interference maxima positions (Fig. 6.24e and 6.24f). Similar results were observed in the sample Cu(30 nm)/Al(120 nm).
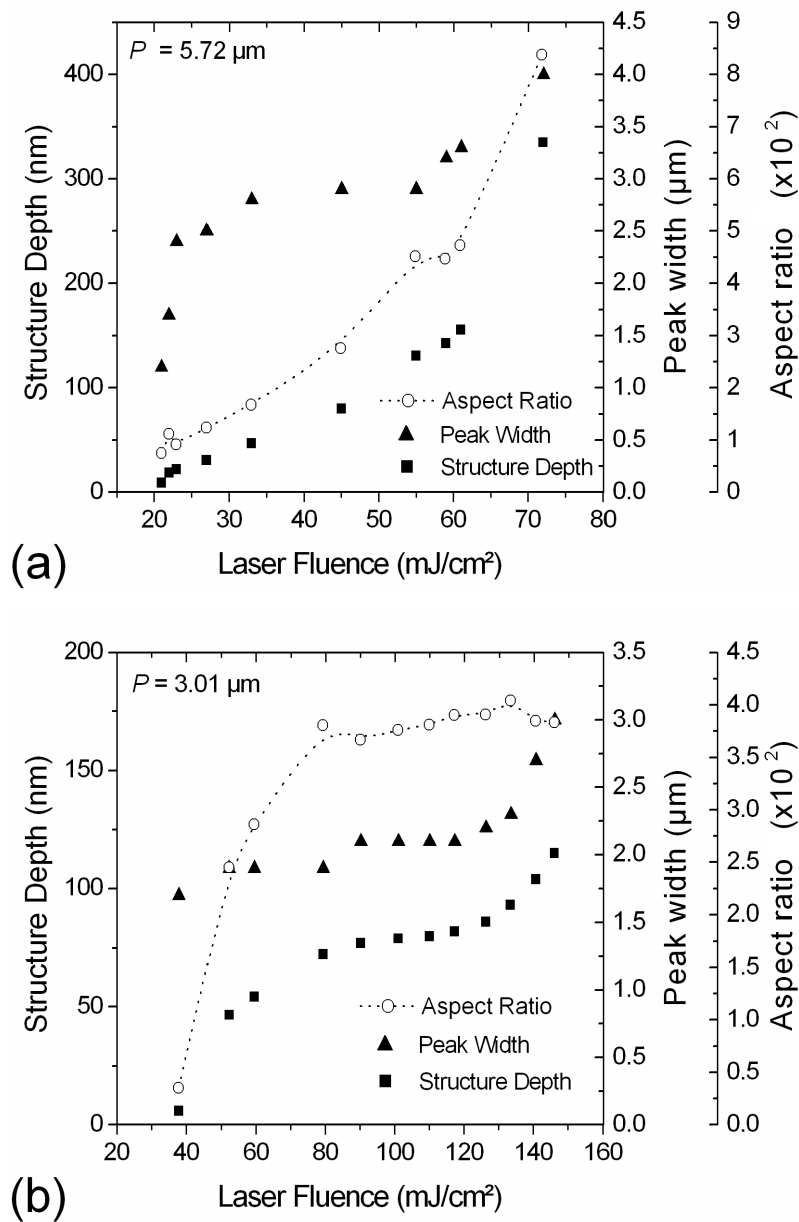
Figure 6.25. Structure depth, width, and aspect ratio of (a) dot-type and (b) line-type periodical structures as function of the laser fluence in the low energy regime. Sample Fe(30 nm)/Al(120 nm).

6.2.4. Aspect ratio of line- and dot-type structures

The structure depth (or structure height), width and aspect ratio (defined as the quotient between height and width of the structures) as function of the laser fluence are shown in Fig. 6.25a for the sample Fe(30 nm)/Al(120 nm). The laser fluence range covers from 0 to 72 mJ/cm² and in all cases the pattern formed corresponds to the structure-type shown in Fig. 6.24b. The maximum aspect ratio obtained in this case was 8.4 %. A similar analysis was carried out for the line-type structures in the low-energy regime. The laser fluence was changed from 0 to 150 mJ/cm². The results are presented in Fig. 6.25b observing a maximum aspect ratio of 4.0 %.

6.2.5- EDS analysis

Several periodical structures as well as different topographic regimes (structuring conducted with or without local and periodical removal of material at the interference maxima) were evaluated. In all cases, the element Si was taken as a reference for the glass substrate.
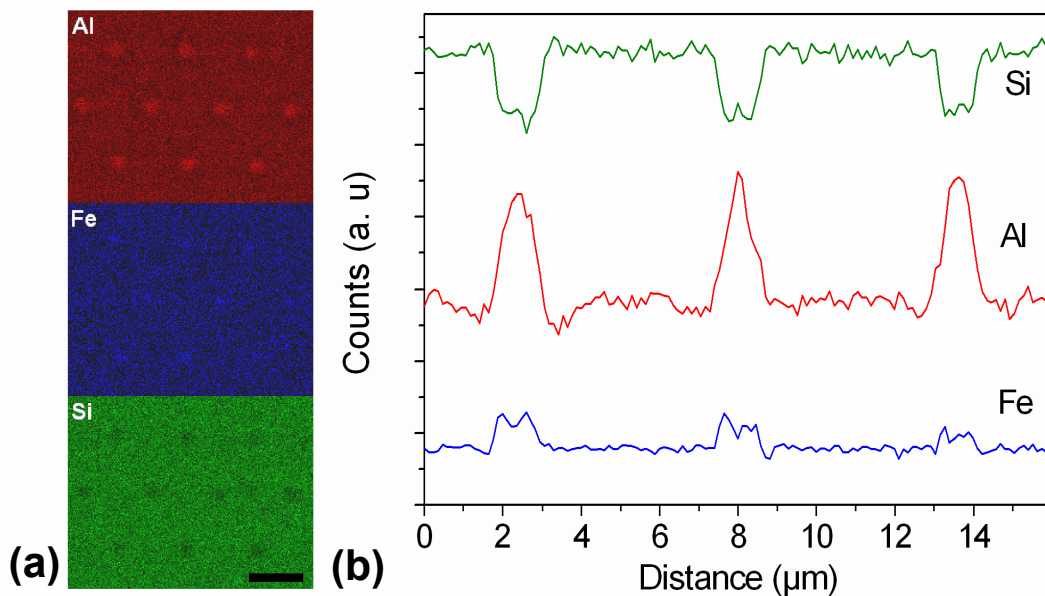
Figure 6.26. *(a) EDS maps of the elements Al, Fe and Si (sample Fe(30 nm)/Al(120 nm)). (b) EDS line-scan of the same sample showing three interference maxima. Dot-type structure; scale bar: 5 µm.*

The sample Fe(30 nm)/Al(120 nm) was irradiated with three laser-beams obtaining a dot-type structure (see Fig 6.19). The structure depth was 268 nm. The

laser fluence used in the laser interference experiment was 65 mJ/cm². The obtained structure corresponds to the low energy regime (structuring without removal of material). The EDS maps of Fig. 6.26a indicate that at the interference maxima positions the intensity of the element Al (lower layer) increases while the intensity of the element Fe (upper layer) practically does not indicate changes. The map of the element Si shows a fall in the intensity at the interference maxima as can be observed in Fig. 6.26a. The line-scan of the same sample (Fig. 6.26b) presents the same characteristics but also a rise in the intensity of the element Fe can be distinguished at the interference maxima.
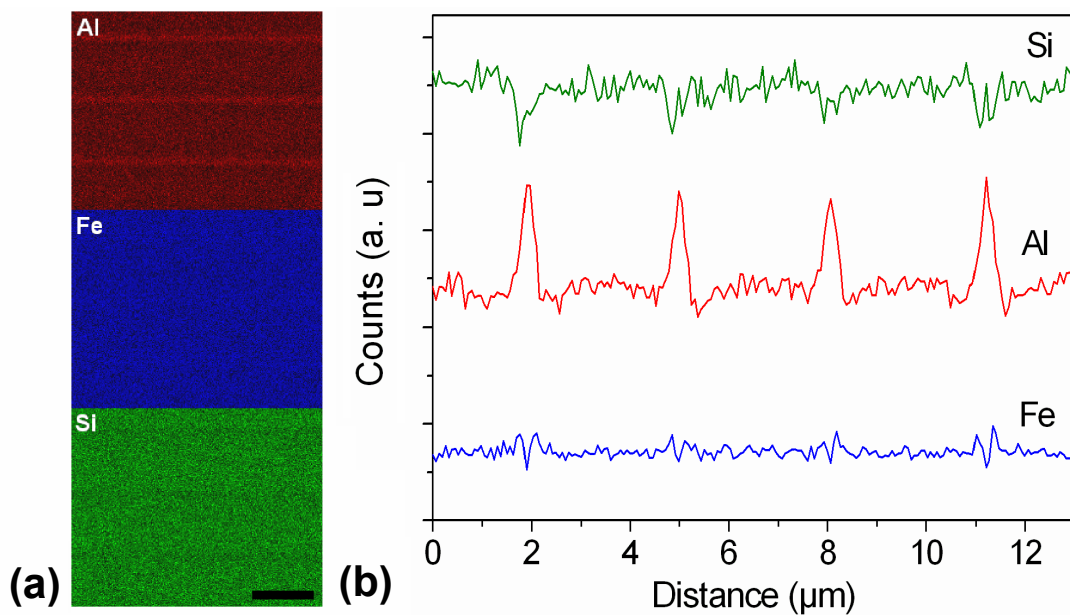
Figure 6.27. *(a) EDS maps of the elements Al, Fe and Si (sample Fe(30 nm)/Al(120 nm)). (b) EDS line-scan of the same sample showing three interference maxima. Line-type structure; scale bar: 3 µm.*

The sample Fe(30 nm)/Al(120 nm)/Glass was also irradiated with two laser-beams obtaining a line-type structure with a period of 3.04 µm. The laser fluence was 39 mJ/cm² and the structure depth was 40 nm. Also in this case, the structuring was conducted without removal of material at the interference maxima positions. The EDS map of the element Al shows higher intensities at the interference maxima (Fig. 6.27a), while the other elements (Si and Fe) do not present important changes. Similar results were observed in the line-scan shown in Fig. 6.27b which indicates four interference maxima.

Figure 6.28. *(a) EDS maps of the elements Al, Cu and Si (sample Cu(30 nm)/Al(120 nm)). (b)EDS line-scan of the same sample showing four interference maxima. The structuring was conducted with removal of material. Line-type structure; scale bar: 3 μm.*

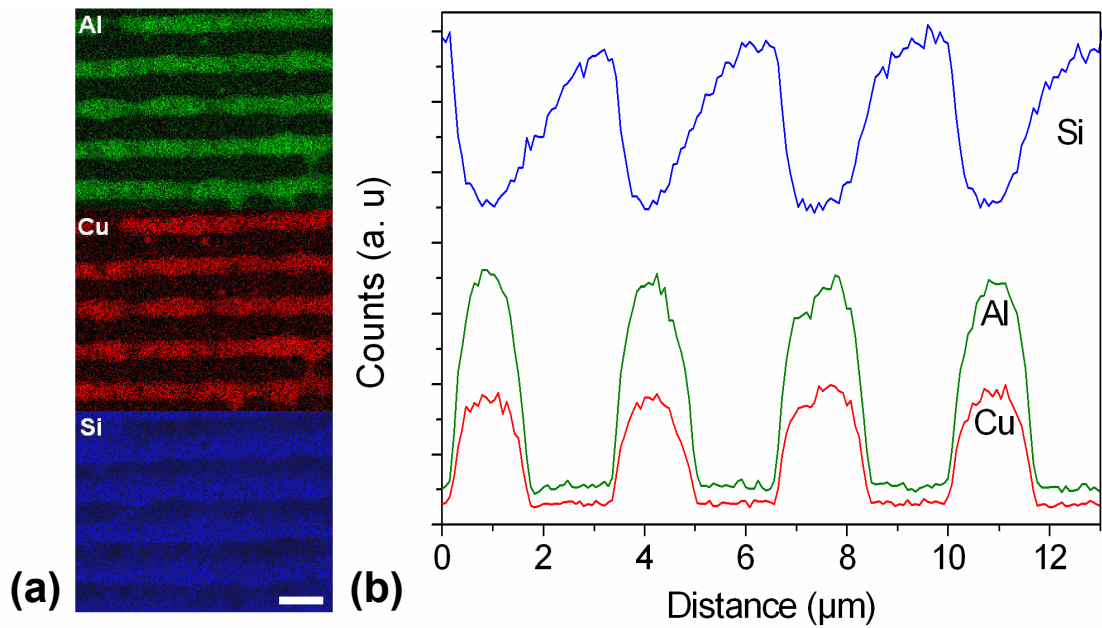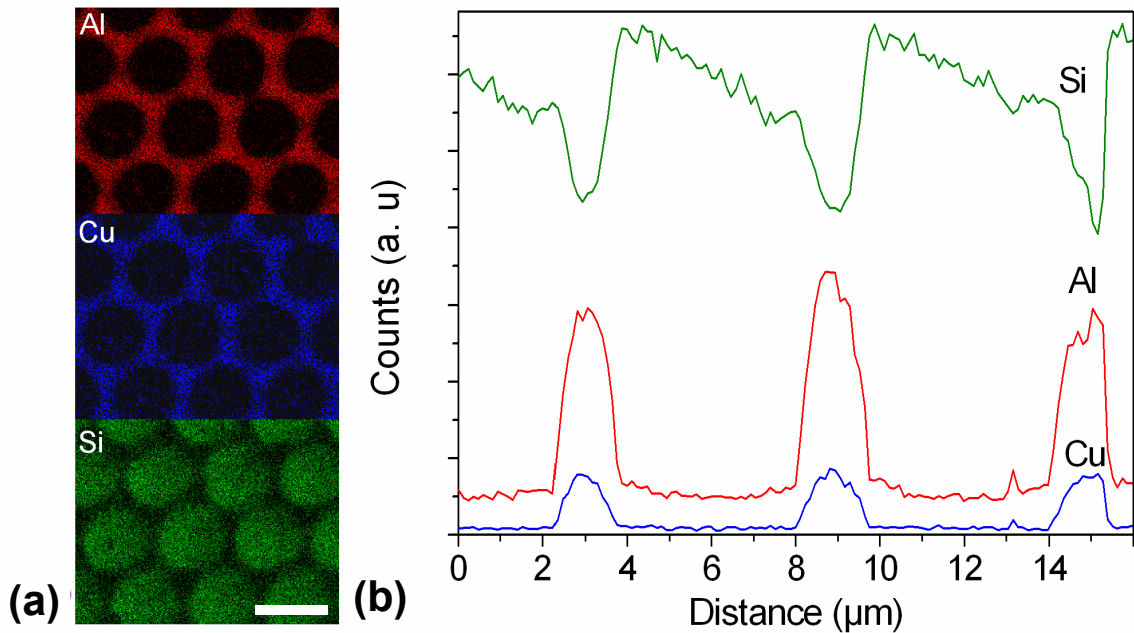***Figure 6.29.*** *(a) EDS maps of the elements Al, Cu and Si (sample Cu(30 nm)/Al(120 nm)). (b) EDS line-scan of the same sample showing four interference maxima. The structuring was conducted with removal of material. Crater-type structure; scale bar: 5 μm.*

The Cu(30 nm)/Al(120 nm) sample was irradiated with laser fluences of 147 and 121 mJ/cm² for two and three laser-beams interference experiments, respectively. These values are high enough to remove both metallic layers at the interference maxima (high energy regime). In the first case (line-type interference

83

pattern) the angle in between the laser-beams was 4.82° obtaining a period of 3.16 μm. For 3 laser-beams experiments, the configuration indicated in Table 6.2 (Fig. 6.22) was employed obtaining a symmetrical period of 5.58 μm. The EDS scans of the elements Cu (upper layer), Al (lower layer) and Si (glass substrate) are presented in Fig. 6.28a and 6.29a. The EDS maps of the elements Cu and Al indicate high contrast regions showing a low number of counts at the interference maxima sites. On the other side, the EDS map of the element Si shows an important rise in the intensity at the interference maxima positions. Similar results are observed in the EDS line-scan shown in Fig. 6.28b and 6.29b presenting four and three interference maxima for the line- and the crater-type patterns, respectively.

6.2.6- Cross-sectional analysis

Cross-sectional analyses of the dot- and line-type periodical structures are shown in Fig. 6.30 and 6.31, respectively. The examined samples correspond to a Fe(30 nm)/Al(120 nm) sample irradiated with 3 laser-beams (Fig. 6.30), and a Cu(30 nm)/Al(120 nm) which was structured with 2 beams (Fig. 6.31). The figures show the morphology of both metallic layers. In both cases, the structures correspond to the low energy regime where the upper layer is not molten as indicated by the fact that the thickness of the upper layer remained continuous preserving the original thickness of the unstructured layers. The platinum layer was added to protect the structure during milling (see chapter 5.4.3).

The cross-sectional profile of Fig. 6.30a and b corresponds to the 3 laser interference periodical structures shown in Fig. 6.24c and 6.24b, respectively. The cross-section shown in Fig. 6.30a and 6.30b indicates between the interference maxima and the middle-distance between two maxima (half period of the structure) a small depression. The initial height of the lower film (before structuring) is indicated in Fig. 6.30c by the dot-line. The period was 5.72 μm.

A similar analysis was carried out for the line type pattern (sample Cu(30 nm)/Al(120 nm)). Also in this case, between the peaks of the structure a small depression indicated in Fig. 6.31b by ΔA can be observed.

In both cases, the thickness of the upper layer indicates any substantial changes in comparison to the aluminium layer (lower layer).
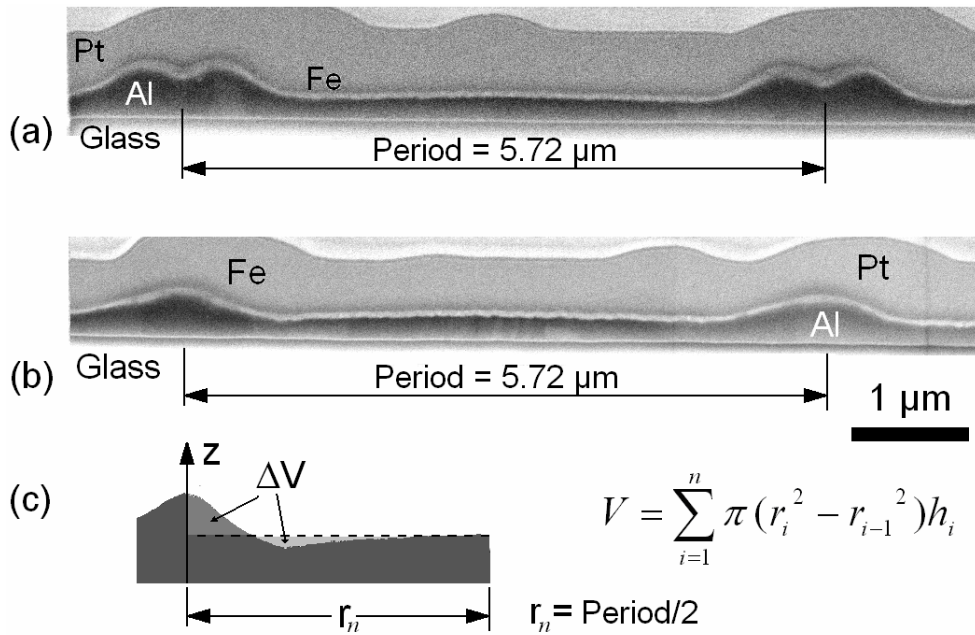
Figure 6.30. *(a) Cross-section of the dot type-periodical structure shown in Fig. 6.23c and (b) Fig. 6.23b. (c) Digitalisation of the profile shown in (b) to calculate the volume of the unstructured and structured aluminium layer. ΔV denotes the volume of molten Al which has flown to the interference maxima.*
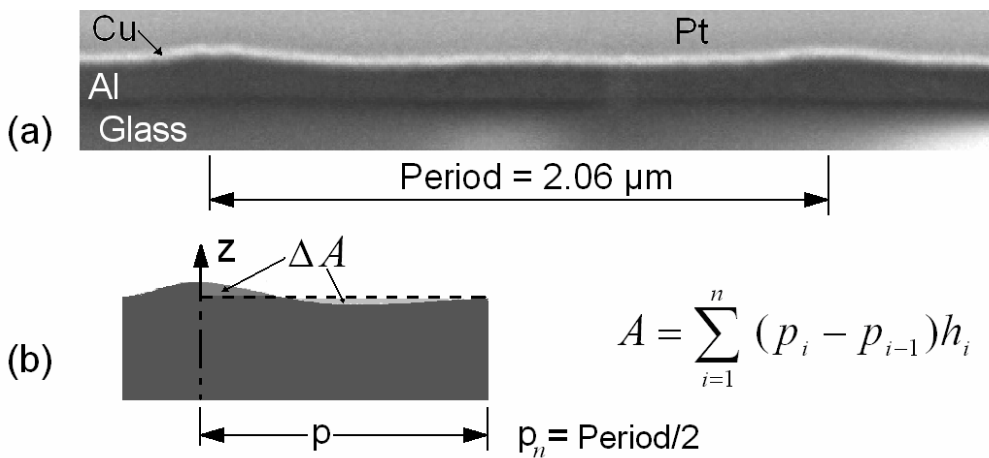
Figure 6.31. *(a) Cross-section of the line type-periodical structures of a Cu(30 nm)/Al(120 nm) sample. (b) Digitalisation of the profile shown in b) to calculate the volume of the unstructured and structured aluminium layer. ΔV denotes the volume of molten Al which has flown to the interference maxima positions.*

6.2.7- Effect of the layer thickness on the structure depth

The effect of the layer thickness on the structure depth in the low energy regime was studied. The maximum structure depth (SD) in this regime was reached at the threshold value before the topographic type changes. Table 6.3 shows the

maximum structure depth for the systems Cu/Al, Ni/Al and Fe/Al obtained with different thicknesses of the second metallic layer. In all cases, the aluminium layer was placed over the glass substrate. Fig. 6.32a shows the topographic profile of Fe/Al samples with different aluminium layer thickness. The period of the periodical structures was 3.01 µm. The surface profiles indicate a high homogeneity of the obtained periodical structures. Fig. 6.32.b shows the topography of a Fe(30 nm)/Al(120 nm) sample structured in the low energy regime (structure depth: 77 nm) with a laser fluence of 90.1 mJ/cm².

Al-LT [(1)] *(nm)*		*30*	*60*	*120*
	Fe	*40*	*72*	*115*
1st LM [(2)]	*Ni*	*33*	*59*	*100*
	Cu	*27*	*33*	*56*

Table 6.3. *Maximum structure depth in the low energy regime for two-layer samples (in nm).*
[(1)] *Al-LT: Aluminium layer thickness.* [(2)] *1st LM: First layer material.*
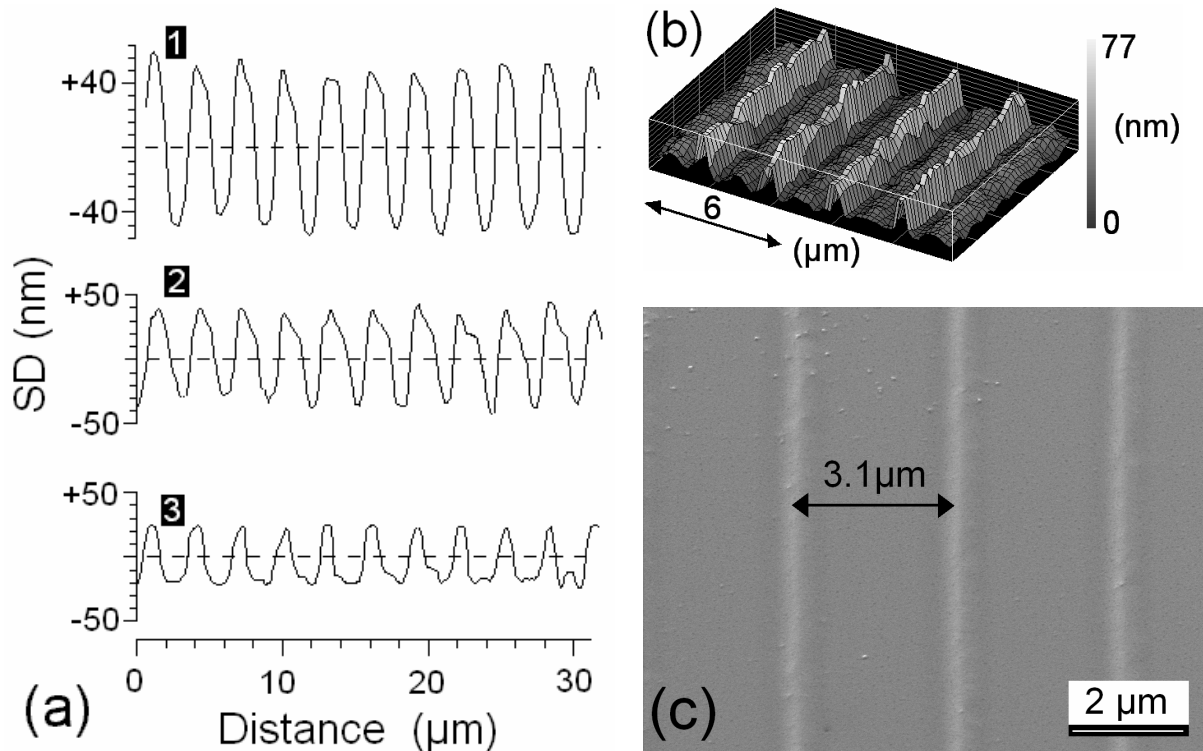
Figure 6.32. *(a) Maximum structure depth (SD) in the low energy regime of Fe/Al samples with an aluminium layer thickness of (1) 120, (2) 60, and (3) 30 nm, respectively (WLI Images); (b) 3D image of a Fe(30 nm)/Al(120 nm) sample structured in the low energy regime with a SD of 77 nm (WLI Image); (c) Ni(30 nm)/Al(120 nm) sample showing a structure period of 3.1 µm (SEM Image).*

6.2.8- Nanohardness investigations

Nanohardness investigations were carried out at different positions of the sample Fe(30 nm)Al(120 nm) which was structured with a three laser-beam interference pattern (dot-type structure with a structure depth of 210 nm) by means of nano-indentational atomic force microscopy. The nano-indentation force was chosen to be represented by a trapezoid with maximum loads of 300, 400 and 500 µN. On the measured material, this corresponds to a maximum indentation depth of about 55 nm. However, due to the small thickness of the metallic film, the substrate could influence the measurements. Nevertheless, these investigations permit to compare the relative hardness of the film at the different positions.
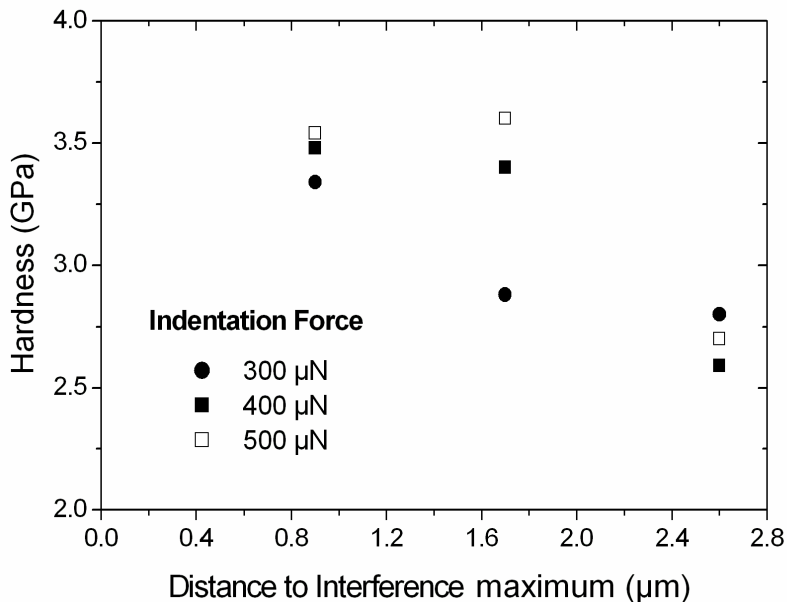
Figure 6.33. Gradient of nano-hardness over half period of laser interference irradiation.

Fig. 6.33 shows the gradient of nanohardness over half period of laser interference irradiation. Due to the similar curvature of the nanoindenter and the structures at the interference maxima position, nanohardness in this region is greatly influenced by topographic effects [111]. These measurements were therefore not considered. The nanohardness increases from 2.7 up to 3.5 GPa from the interference minima to the regions near the interference maxima where the curvature of the structures are smaller than the nanoindenter itself. Similar results were found in [112] for a Ni/Al multi-layered sample, but due to the small structure depth of the periodical structures (about 9 nm), the nanoindentation experiments were also conducted at the interference maxima positions.

6.2.9- Discussion

6.2.9.1- Line-type structures

The studied metallic systems are characterised by having similar thermal properties with the exception of the melting and boiling point. For example, the systems Fe/Al and Ti/Al present a difference of 878 K and 1007 K in the melting point respectively, while in the systems Fe-Ni and Ti-Ni this difference is only 83 K and 213 K, respectively. The thermal simulation has shown that if the difference in the melting point of the materials of the sample is very different, the metal with the lower melting point starts to melt at lower laser fluence values.

	Threshold	Exp. (mJ/cm²)	Sim. (mJ/cm²)	err %
Fe(30 nm)/Al(30 nm)	F_{R1}	40	38	5.3
	F_{R1-R2}	144	121	19.0
Ni(30 nm)/Al(120 nm)	F_{R1}	33	22	50.0
	F_{R1-R2}	92	78	17.9
Fe(30 nm)/Ni(30 nm)	F_{R1}	151	202	25.2
	F_{R1-R2}	230	251	8.4
Ti(30 nm)/Al(30 nm)	F_{R1}	81	87	6.9
	F_{R1-R2}	168	176	4.5
Ti(30 nm)/Ni(30 nm)	F_{R1}	146	151	3.3
	F_{R1-R2}	221	233	5.2

Table 6.4. *Threshold laser fluence values for two-layer metallic systems.*
Exp: experimental; Sim: simulated.

Like in section 6.1.3, two different threshold values related to the laser fluences required to change from one to another structuring regime can be defined. The first threshold value is defined as the fluence necessary to initiate the structuring of the metallic samples (F_{R1}). Comparing this value in the studied systems, it is possible to see for example, that the systems Fe/Al and Ti/Al start to structure at 40 and 81 mJ/cm², respectively. At these laser fluences, the systems Fe/Ni and Ti/Ni (studied systems with the lower difference in the melting point) did not present any structuring. According to the thermal simulation, at these laser fluences, the aluminium layer is partially molten in both Fe/Al and Ti/Al systems, whereas in the systems Fe/Ni and Ti/Ni the second layer (Ni) remains in the solid state (Figs. 6.15 and 6.17). As the laser fluence is increased, more metal is molten and a higher structure depth is obtained. Therefore, the laser fluence F_{R1} can be defined as the energy necessary to melt the lower layer. The threshold laser fluences calculated

from both the experimental results and the thermal simulation are presented in Table 6.4.

Although the minimal period which can be theoretically obtained for the 2 beams interference case (calculated using Eq. 4.9 with $\alpha = 2\pi$) is half of the wave length, in all studied cases the minimal achieved period (with relative well defined structures) was only of about 2 μm. The equation which governs the dissipation of heat in the structuring process is the heat diffusion equation (Eq. 4.22) as was indicated in chapter 4. Thus, materials with high thermal conductivity dissipate the heat much faster from the interference maxima towards the minima. For metals, the thermal conductivity is quite high because the heat can be conducted by two primary mechanisms, atomic vibrations and conduction by free electrons [113]. The thermal simulation indicates that the smaller the period of the interference pattern, the smaller the temperature difference between the interference maxima and minima (Fig. 6.18). Therefore, for small periods the low thermal gradient is not high enough to produce the periodical structure. The smallest period that can be achieved in metals can be related with the thermal diffusion length with values of about 1 and 2 μm for iron and copper, respectively. These dimensions fit well with the experimental observations. Larger periods at fixed laser fluence permit to achieve higher temperatures at the interference maxima positions. This explains the reason for which lower laser fluences are required to produce the transition from the structuring with removal of material to the structuring without removal of material for large periods.

Energy dispersive spectroscopy (EDS) measurements as well as cross-sectional analysis in the low energy regime (without removal of material) provides important information to understand the structuring mechanism. EDS maps carried out on a Fe(30 nm)/Al(120 nm) sample indicates that the intensity of the element Al increases at the interference maxima positions (see Fig. 6.26 and 6.27). The cross-sectional analysis of these structures (Fig. 6.30) shows that at the interference maxima the thickness of the aluminium layer is larger than at the interference minima, which correlates well with the EDS measurements. If the structure depth is low, no substantial variation in the intensity of elements of the upper layer (in this case iron) and the glass substrate are observed (Fig. 6.27). Nevertheless, if the structure depth increases, variations in the intensity of the elements in the upper layer and the glass substrate can be also observed (Fig. 6.26). The intensity of the element Si decreases at the interference maxima due to the thicker layer compared with the interference minima and consequently the x-rays emitted from the glass substrate are stronger attenuated. The intensity of the element Fe (upper metallic layer) increases at the interference maxima but forms a double peak pattern. This pattern can be explained as follows. Fig. 6.34a shows the scheme of the Fe layer at one interference maximum considering that the thickness of the iron layer is constant

(see t'_1 and t'_2 in Fig. 6.34a). According to the *z*-axis, the thickness of the layer along the *x*-axis is not constant (see t_1 and t_2). If the structure depth is still higher, a larger difference between t_1 and t_2 can be calculated. This diagram is very similar to the Fe intensity profile at the interference maxima (Fig. 6.34b), but the relative minimum has not the same height. The lateral resolution of the EDS measurements in thin-metallic films is about 100 to 300 nm [114]. Therefore, by calculating the FFT filtering of the curve *thickness* vs. *x-position* (Fig. 6.34b) with a window of 300 nm, the curve shown in Fig. 6.34c is obtained. This curve correlates well with the experimental results. Important to remark at this point is the symmetry of the periodical structure, which means that the position of the detector during the measurements does not affect the obtained results (the analysis was carried out with the dot-type periodical structures indicated in Fig. 6.19).
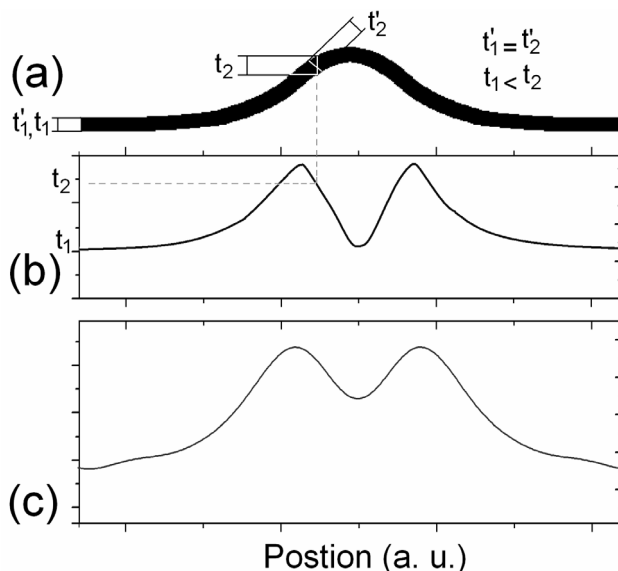
Figure 6.34. *(a) Interference maximum schema of the upper layer. (b) Calculated thickness of the upper layer along the x-axis from (a). (c) FTT filtering of curve (b) with a window of 300 nm.*

Cross-sectional analysis in the low energy topographic regime indicates that between the interference maxima and the middle-distance between two maxima (half period of the structure) a small depression is to be found. The initial height of the film (before structuring) can be considered as shown in Fig. 6.31b by the dashed line. At low laser fluences, the periodical interference pattern, which can be assumed as a periodical heat source, melts locally the lower metallic layer at the interference maxima, but the upper layer remains in the solid state. The molten layer expands because of the lower density of the liquid which results in the high speed deformation of the upper layer at interference maxima positions [115]. Due to volume decrease during resolidification of the molten metal and the hardened upper metallic layer (as demonstrated in section 6.2.8), molten aluminium (metal of the lower layer) must flow

90

towards the interference maxima induced by a pressure gradient. Important to mention at this point is that if the temperature at the maxima positions reaches values near the melting point, then the hardness of the deformed layer decreases [116]. This can lead to a new deformation of the layer, but in the opposite direction as shown in Fig. 6.30a (this will be explained in section 6.2.9.2).

The flow of molten metal from the interference minima towards the interference maxima can be demonstrated as follows. Because of the geometry of the thermal gradient, linear coordinates can be assumed to describe the problem of the line-type structures. In addition, due to symmetry reasons, only the areas in the cross-section must be considered. The initial area with the width of half a period of the unstructured aluminium layer is given by (Fig. 6.31b):

$$A_0 = (p/2)h_0.$$

<div align="right">(6.1)</div>

where p is the period of the structure, and h_0 the initial thickness of the Al-layer.

The corresponding area after the structuring is represented by the sum of the rectangular elements along x, with height h_i and width x_i-x_{i-1} (see Fig. 6.31b):

$$A = \sum_{i=1}^{n} A_i = \sum_{i=1}^{n} (x_i - x_{i-1})h_i.$$

<div align="right">(6.2)</div>

The areas calculated by Eq. (6.1) and (6.2) differ by 4.24 % for the case studied in Fig. 6.31a (see Table 6.5). The error of the area determination is of the order of 5% estimated by error propagation. Therefore, the two areas are the same within the uncertainty of the measurement. Hence it is proven that the molten aluminium has flown from the regions that surround the interference maxima positions following the thermal gradient. The area of the molten metal related to the flow towards the interference minima is equal to the regions indicated as ΔA in Fig. 6.31b. This result implies that no evaporation of material occurred. Thus, for line-type interference patterns a one-dimensional flow of aluminum from the interference minima to the interference maxima can be demonstrated without any loss of material.

Area integral	Area (µm²)	Err (%)[i]
(us); Initial area [(p/2).h]	0.118	-
Low energy: 75 mJ/cm²	0.123	4.24

Table 6.5. Area calculation of the unstructured (us) and structured line-type patterns assuming linear coordinates; h = 0.120 µm; p = 2.06 µm. (i) The error was calculated taking as reference the unstructured sample.

According to the results shown in section 6.2.7, the thickness of the second metallic layer plays an important role on the structure depth. From Table 6.3 and Fig. 6.32 it can be seen that as the thickness of the second layer increases, the structure depth also increases. This result is observed in Fe/Al, Ni/Al, and Cu/Al samples. Nevertheless, this effect is not so strong in the system Cu/Al. From the thermal simulation it can be seen that at the laser fluence value at which the *Cu*-layer is heated up to the melting point, the Al-layer is molten about 43%. In the systems Fe/Al and Ni/Al, these values are 64 and 59%, respectively. This observation indicates that the larger the volume of molten aluminium, the higher the structure depth. The same conclusion can be obtained if the cross-sectional analysis described above is considered. More molten aluminium implies more aluminium available to flow to the interference minima.

The percentages of molten aluminium (or the molten metal in the second layer) can be directly related to the aluminium melting range (*Al-MR*) which is defined by the difference between the laser fluence values at which the second and the first metallic layers start to melt. According to the thermal simulation, in the system Cu/Al the *Al-MR* is only about 50mJ/cm² while in the systems Ni/Al and Fe/Al is 70 and 79 mJ/cm², respectively. Therefore in those systems with higher *Al-MR*, a higher structure depth is expected (Fig. 6.35). The *Al-MR* can be also related to the difference between the melting points of both metallic layers. Thus, when this difference is higher, a larger structure depth can be obtained in the low energy regime (Fig. 6.35).
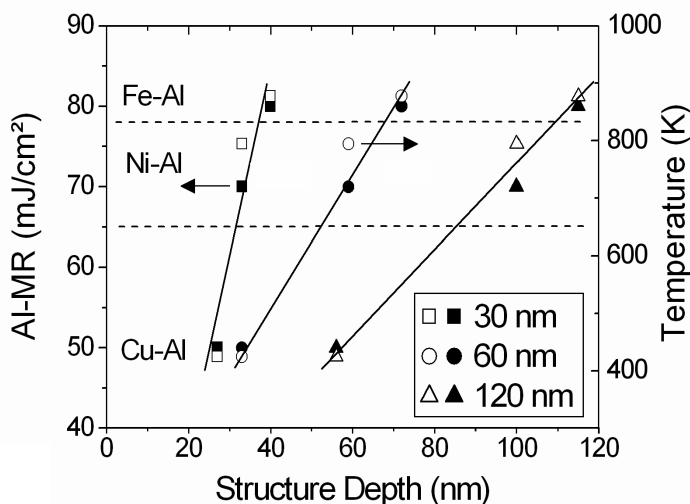
Figure 6.35*. Structure depth vs. the Al-MR (black symbols) and the difference of the melting points between the first and the second metallic layer (white symbols). The thickness of the aluminium layer is indicated inside the rectangle. The lines were included for a better understanding of the figure.*

If the laser fluence is still higher, a second topographic type is observed being the structuring conducted with local and periodical removal of material at the interference maxima positions. The structures produced at these fluences present a

high structure depth. According to the thermal simulation, in all cases the transition from the low energy regime to the high energy regime occurs when the upper layer is heated up to its melting point (see Fig. 6.12 to 6.17). Therefore, this threshold laser fluence can be defined as the energy necessary to melt the upper metallic layer at the interference maxima (F_{R1-2}). This can be explained because at this temperature the metallic layer is soft enough to be broken by the force produced by the expansion of the molten metal of the lower layer. Table 6.4 shows the F_{R1-2} values calculated using the thermal simulation, the experimental laser fluence at which the topography changes, and the absolute error between the experimental and calculated values indicating a good agreement.

For larger periods, the transition occurs producing a double-peak pattern as indicated in Fig. 6.9d. For higher laser fluence values, more material is molten and the consecutive peaks of Fig. 6.9d develop into one peak as shown in Fig. 6.9f. Nevertheless, if the period is smaller than about 3.5 µm, the transition occurs directly into the form of the pattern shown in Fig. 6.9f.

The EDS maps as well as the line-scan of a sample Cu(30 nm)/Al(120 nm) (Fig. 6.28 and 6.29) show that at the interference maxima the intensity profile of both metallic elements reduces practically to zero while the Si intensity strongly increases. This observation is in agreement with this topographic type at which the metallic layers are removed at the interference maxima.

6.2.9.2- Dot-type structures

The types of topographical regimes, which are obtained using three laser-beams, depending on the laser fluence follow basically the structuring mechanism explained in the previous section.

At low fluences, the structures shown in Fig. 6.24c and 6.24d are similar to those of Fig. 6.24b apart from a central depression which is formed at laser fluences larger than 72 mJ/cm² (sample Fe(30 nm)/Al(120 nm)). Hardness of a metal markedly decreases as the temperature approaches the melting point [116]. Furthermore, interference patterns with larger periods produce a higher thermal gradient or a larger temperature difference between the interference minima and maxima positions (in addition this difference is still larger if interference patterns with more than 2 laser-beams are used). Thus, for large periods and laser fluences near the threshold value at which both metallic layers are removed at the interference maxima, a very local and periodical softening of the upper layer arises explaining the central depression at the interference maxima. This occurs due to the volume decrease of the molten lower

layer during resolidification which results in a pressure gradient. The same effect can be also observed in line-type patterns but for periods larger than 5 μm.

If higher laser fluences are applied in the case of 3-beam interference patterning, the hexagonal lattice structure with defined removal of material at the interference maxima using symmetrical configuration shown in Figs. 6.24e and 6.22 is obtained. These structures are similar to the periodical arrays obtained by Nakata *et al.* [117] in 50 nm gold thin films using femtosecond laser pulses. However, because of the different interaction between nano- and femtosecond lasers with metals [84], at lower laser fluences no evidence of molten metal was found in the last case. The electron lattice relaxation time in metals is between 1 and 10 picoseconds [85, 86] and thus the metals are directly evaporated in the case of femtosecond pulsed laser. With nanosecond pulses, the metal has enough time to melt since the electron lattice relaxation time is much smaller than the pulse duration [84].

Similar to line-type patterning, the cross-sectional analysis in the low energy regime can bring information about the structuring mechanism. Because of the geometry of the thermal gradient, cylindrical coordinates must be used in this case. The initial volume (V_0) of the unstructured aluminium cylinder with its centre at the interference maxima, (see Fig. 6.30c) is given by:

$$V_0 = \pi (p/2)^2 h_0.$$ (6.3)

The volume of the final structured aluminium layer can be calculated by the sum of the cylindrical-rings with height h_i and thickness $r_i - r_{i-1}$:

$$V = \sum_{i=1}^{n} \pi (r_i^2 - r_{i-1}^2) h_i.$$ (6.4)

The volumes calculated by Eq. (6.3) and (6.4) differ by 1.48 and 1.40 % in the cases studied in Fig. 6.30a and b, respectively (see Table 6.6). Like in the line-type case, only an insignificant difference between both calculations was found. Thus, for dot-type interference patterns a two-dimensional flux of aluminium from the interference minima to the interference maxima can be demonstrated.

| Cylindrical integral	Volume (μm³)	Err (%)[i]
(us); Cylinder volume [π.(p/2)².h]	*2.936*	*-*
Low energy: 65 mJ/cm²	*2,979*	*1.48*
Medium energy: 72 mJ/cm²	*2,895*	*1.40*

Table 6.6. Volume calculation of the unstructured (us) and structured dot-type patterns assuming cylindrical coordinates. h = 0.122 μm, p = 5.52 μm. (i) The error was calculated taking as reference the unstructured sample.

Comparing the geometrical parameters (structure depth, width and aspect ratio) of the line- and dot type periodical structures (Fig. 6.25), a higher structure depth as well as aspect ratio can be obtained in the last case. This can be explained because as it was demonstrated above, the flow of aluminium (or metal of the lower layer) occurs from the surroundings of the interference maxima (2D flow) in the case of dot-type structures, while in the line-type case the flow is one dimensional. Thus a smaller amount of molten metal contributes to the structuring.

EDS analysis indicates similar results like in the line-type patterns. Higher structure depth produces a larger contrast in the intensity of the element of the second metallic layer which can be directly connected to the relative thickness of the layer (Fig. 6.26). In the high energy regime, the removal of material is also confirmed by a high rise of the intensity of the element Si of the glass substrate (Fig. 6.29).

6.2.9.3 – General structuring mechanism

According to sections 6.2.9.1 and 6.2.9.2, for bi-layered systems with two different metals (A and B in Fig. 6.36) where the metal of the top-layer (metal A) has the higher melting point, the following structuring mechanism is suggested:
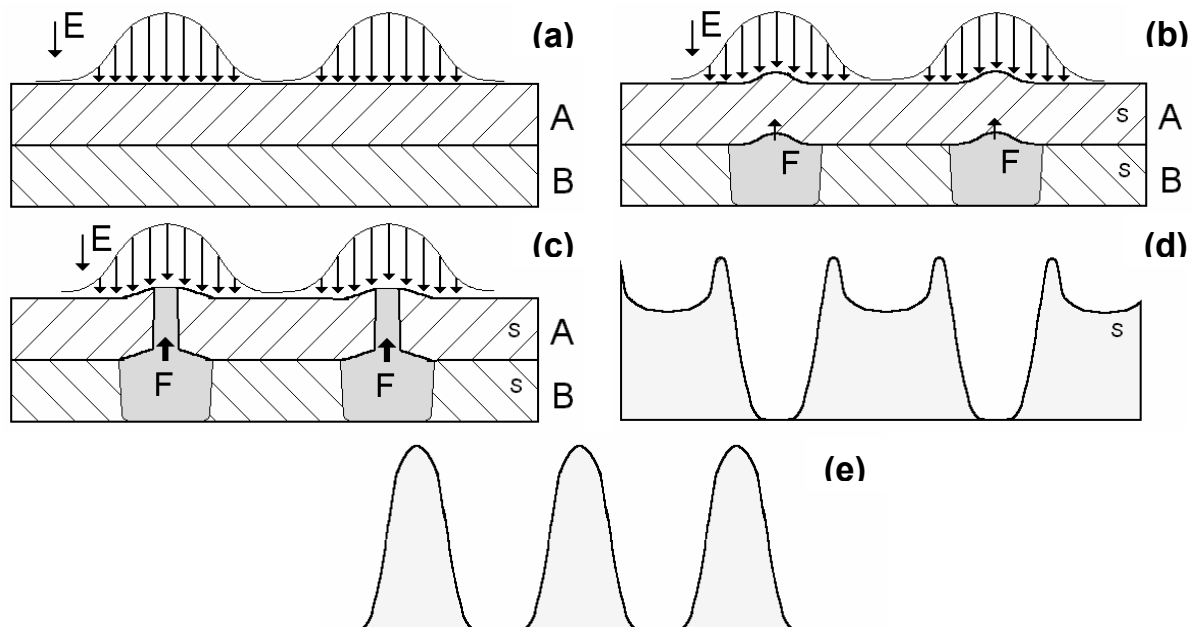
Figure 6.36*. Micro/nano structuring schema of the two-layer case. The melting point of A is higher than B. (a) The laser interference pattern acts over the surface of the metal A; (b) deformation of the layer A caused by the high pressure of molten B; (c) the layer A is broken; (d) periodical pattern obtained for interference patterns with larger periods; (e) periodical pattern obtained for larger values of the laser fluence and small periods.*

The laser interference pattern acts over the surface of the metal *A* as shown in Fig 6.36a. Because of the thin layers, the temperature along with the z-axis can be assumed to be constant obtaining rectangular molten regions. Due to the lower melting point of *B*, it is molten before *A*. Later on, more molten *B* increases the pressure until it is released by outward deformation of layer *A* (Fig 6.36b). Therefore, in this regime, the structuring is conducted by the expansion of the molten lower layer at the interference maxima positions. In addition, if the thickness of the lower layer and the difference between the melting points of the metallic layers increases, the maximum structure height which can be obtained in this regime also increases. The analysis of one- and two dimensional periodical structures permits to confirm this statement. The aspect ratio of the two-dimensional structures was found to be larger than the case of one-dimensional periodical structures. Cross-sectional analysis using a dual-beam work station of the line- and dot-type structures has demonstrated that molten aluminium flows from the regions near the interference maxima towards the interference maxima following a linear or a cylindrical geometry for the one- and two-dimensional cases, respectively. This depends on the shape of the induced thermal gradient. Consequently, for the cylindrical geometry more molten metal is available for the structuring process and thus the aspect ratio is larger in comparison to the line-type periodical patterns.

For higher laser fluence values, the pressure is increased above the threshold value at which the upper layer is heated up to its melting point and breaks the layer *A* (Fig 6.36c) obtaining the pattern shown in Fig 6.36d. or Fig. 6.36e. The first pattern (Fig 6.36d) is obtained only for laser fluences near the laser fluence threshold value at which the topography type changes and also depends on the period of the periodical structure being more feasible for larger periods. If the laser fluence value is even higher (or the period smaller), more metal is molten and the second pattern is obtained (Fig. 6.36e). The maximum structure depth in the lower energy regime is obtained at the threshold laser fluence value where the topography type changes.

6.3- Two layer systems - case B: Metal with the higher melting point at the bottom

6.3.1- Structuring regimes

The systems Al(30 nm)/Fe(120 nm) and Al(30 nm)/Ni(120 nm) were irradiated using laser fluences from 10 to 900 mJ/cm². These relatively high values have been

used due to the high reflectivity of the aluminium layer at the used wavelength (R = 0.935 at λ = 266 nm [106]).
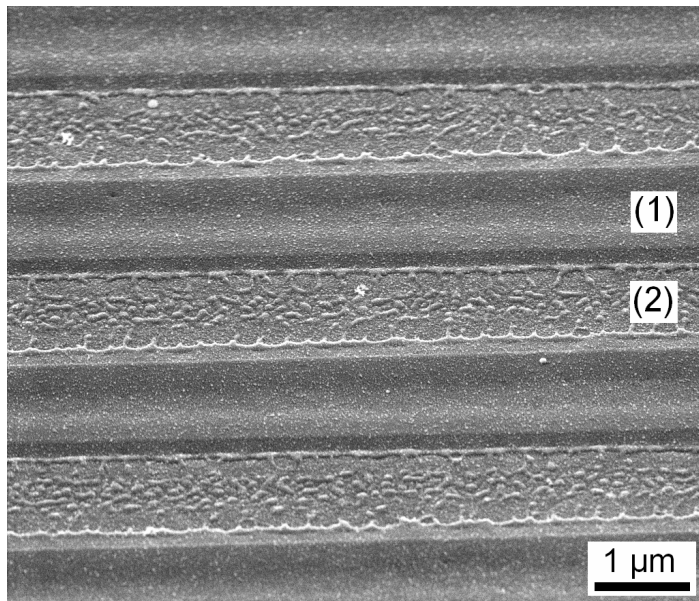
Figure 6.37. Al-Fe micro pattern obtained by local periodic removal of the upper layer (Al) at the interference maxima positions. Period of the pattern: 3.08 µm. Sample Al(30 nm)/Fe(120 nm); (1) Interference minimum; (2) interference minimum.

Three different structuring regimes were distinguished for these systems. In the first regime (R1), the structuring is conducted without removal of material at the interference maxima. Like in the single-layer case (section 6.1), the structure depth is relatively low and the obtained structures are quite homogeneous. In the second regime (R2), the first metallic layer at the interference maxima positions is removed and consequently a higher structure depth is obtained. Fig. 6.37 shows an *Al-Fe* micro pattern obtained by local periodic removal of the upper layer (Al) at the interference maxima positions. In addition, droplets of the melt of aluminium can be observed which have flown across the neighbouring lines. The resulting line structure presents a period of 3.08 µm. At higher laser fluences, both layers are removed and thus a third topographic regime is observed (R3) (Fig. 6.38).

6.3.2- Thermal Simulation

Like in previous sections, the experimental results were compared to the fraction of molten material of each metallic layer calculated by the thermal simulation. Depending on the fluence of the laser, one or both metallic layers can be molten. Also in this case, because of the nanometric thickness of the layers, the film temperature along the z-axis was found to be constant. The evolution of the molten fractions of both metallic layers depending on the fluence of the laser is shown in Fig. 6.38.
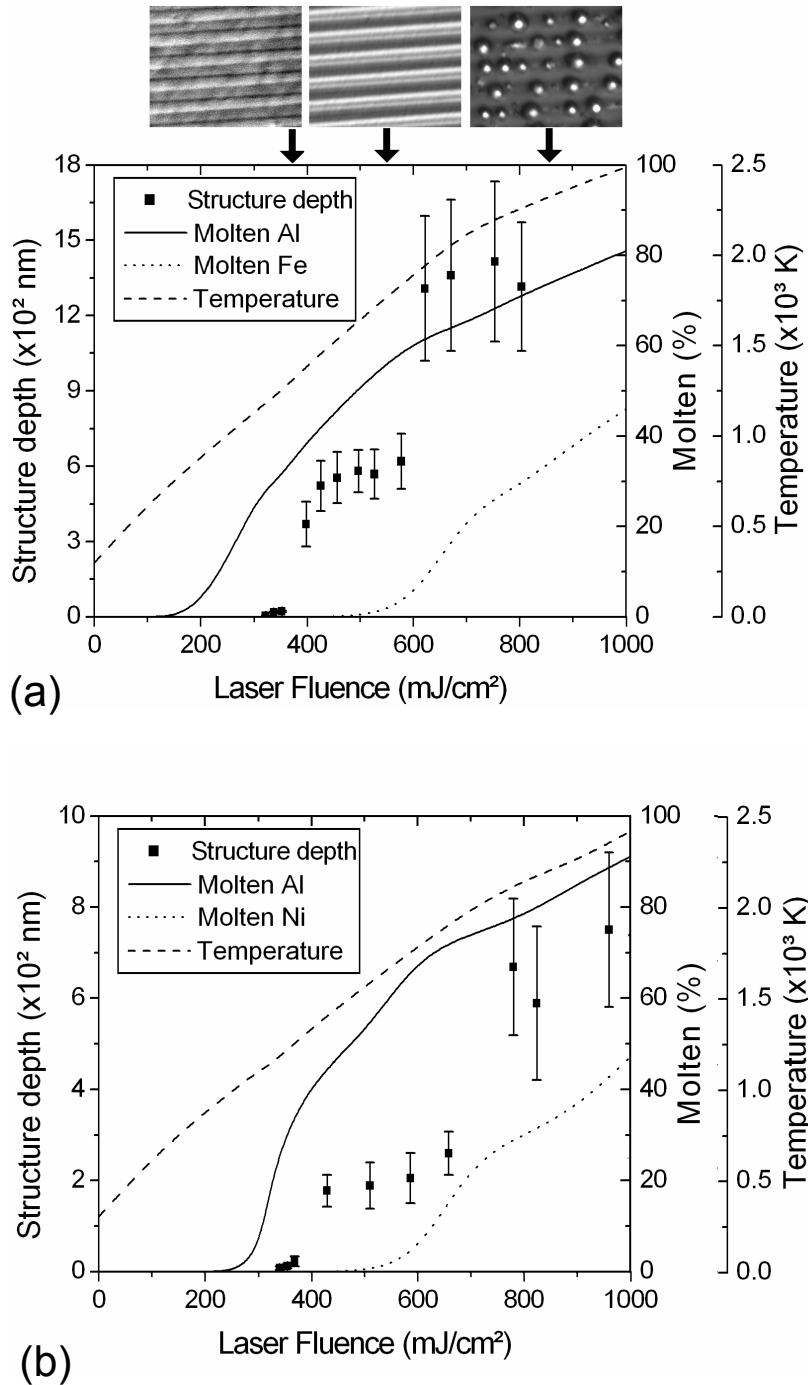
Figure 6.38. *Structure depth (experimental), temperature, molten and vaporised material (simulated) as a function of the laser fluence for (a) Al(30 nm)/Fe(120 nm), and (b) Al(30 nm)/Ni(120 nm) samples. The details in (a) show the topographic types obtained in each regime (optical micrographs).*

Fig. 6.38a reveals that between 400 and 590 mJ/cm² only the aluminium layer is molten at the interference maxima (system Al(30 nm)/Fe(120 nm)). This situation is illustrated in Fig. 6.39 indicating the calculated molten regions at a laser fluence of 500 mJ/cm². A difference of about 1270 K can be observed between the interference maxima and minima positions. Laser fluences larger than 590 mJ/cm² permit to partially melt both layers at the interference maxima as indicated in Fig. 6.40a. The

simulation corresponds to a laser fluence of 800 mJ/cm². The thermal history at the interference maxima and minima positions is indicated in Fig. 6.40b.
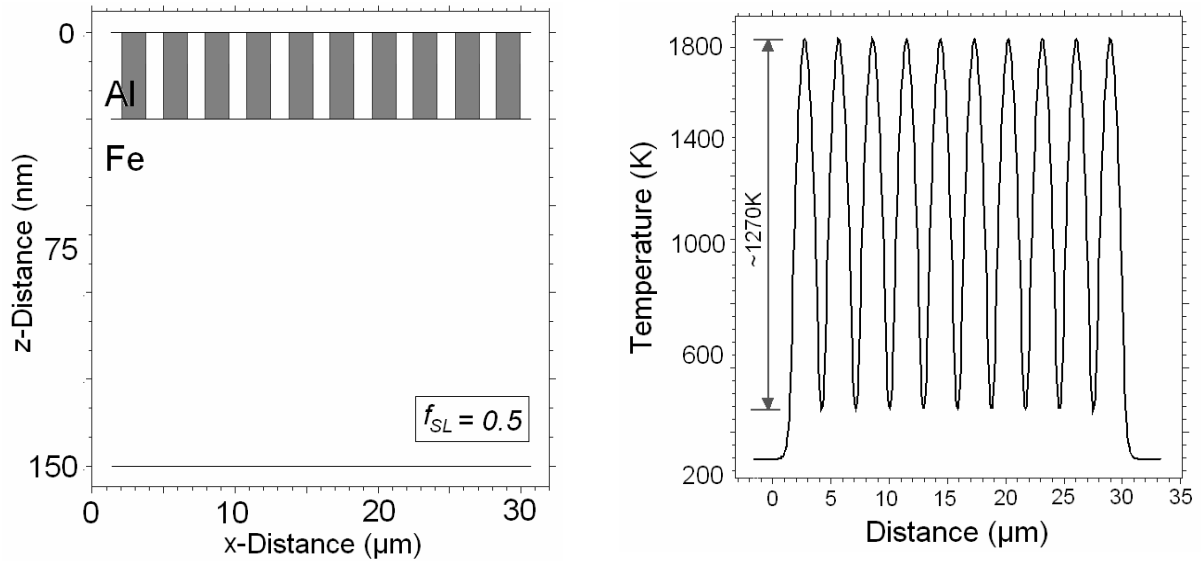
Figure 6.39. (a) Simulated molten regions of a Al(30 nm)/Fe(120 nm)/Glass sample irradiated with 500 mJ/cm² of laser fluence. The grey colour represents the molten material taking as reference a value of 0.5 for the variable f_{SL} to define the solid-liquid frontier. Only the Al-layer (upper layer) is molten. (b) Lateral temperature profile of a 10 peaks interference. Note that the difference in temperature between the maxima and minima of the interference pattern is about 1270 K.
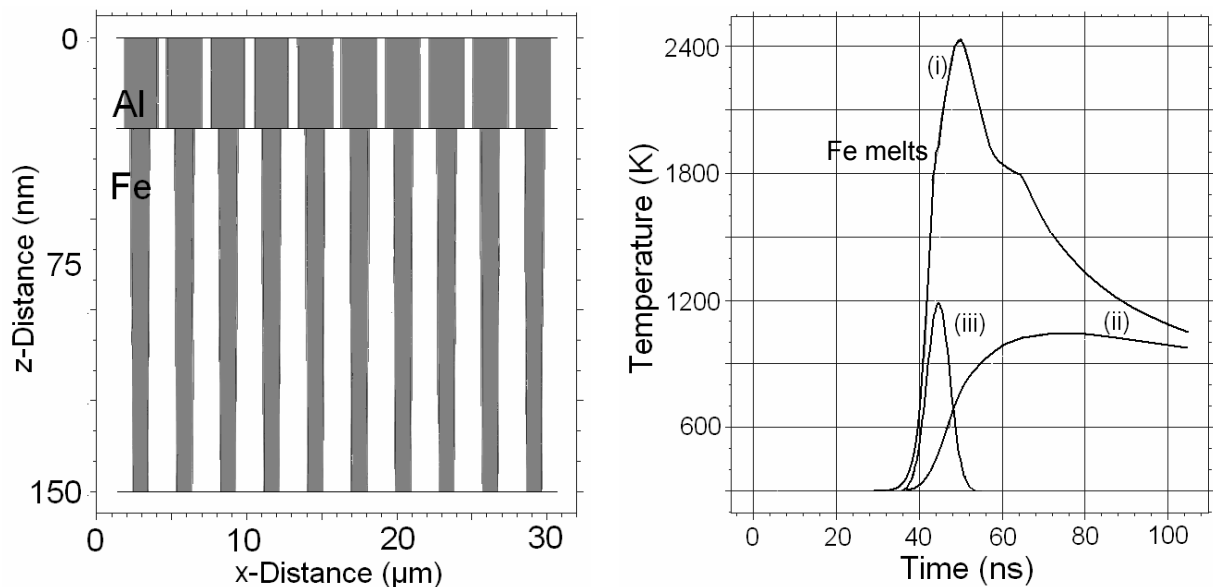
Figure 6.40. (a) Simulated molten regions of a Al(30 nm)/Fe(120 nm)/Glass sample irradiated with 800 mJ/cm² of laser fluence. The grey colour represents the molten material taking as reference a value of 0.5 for the variable f_{SL} to define the solid-liquid frontier. (b) Temperature evolution at interference (i) maxima and (ii) minima. (iii) Laser pulse (arbitrary units). The temperature at the interference maxima is high enough to melt both the aluminium and the iron layer.

6.3.3- EDS and cross-sectional analyses

Similar to section 6.2, the structured metallic samples were analysed by means of EDS in order to investigate the layer structure. The sample Al(30 nm)/Fe(120 nm) was irradiated with 533 mJ/cm² obtaining a typical periodic structure of the second regime with a period of 3.08 µm (see section 6.3.1). Silicon was taken as reference for the glass substrate. The EDS line-scan across three interference maxima indicates that at the interference maxima the intensity of the element aluminium (lower layer) decreases while the intensity of the element iron (upper layer) practically does not present any changes (see Fig. 6.41).
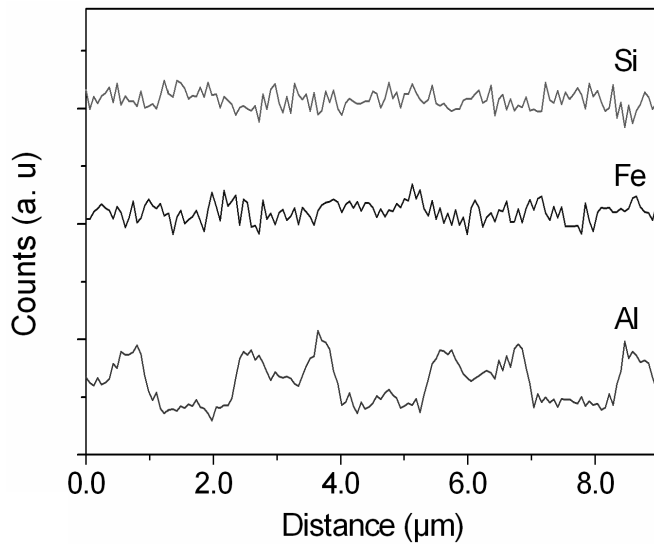
Figure 6.41. EDS line-scan of the sample Al(30 nm)/Fe(120 nm) indicating three interference maxima. The structuring was conducted in the second regime with removal of the upper Al-Layer. Line-type structure.
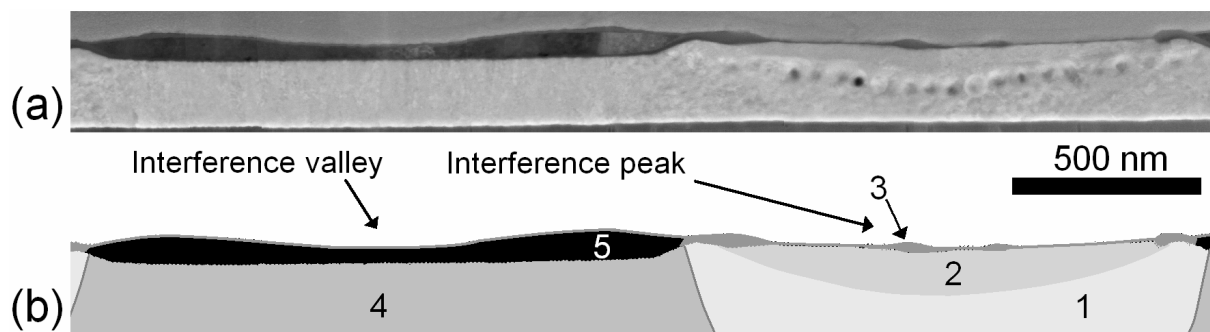
Figure 6.42. Sample Al(30 nm)/Fe(120 nm). (a) TEM foil prepared by the procedure outlined in chapter 5.4.3 with a total thickness of 83 nm. The foil shows one interference maxima (interference peak) and one laser interference minima (interference valley) (STEM mode image at 17 kV). (b) Schematic description of 5 different microstructural regions.

The cross-sectional profile of the same sample structured in the second topographic regime is shown in Fig. 6.42. The figure shows the morphology of both metallic layers. The platinum layer was added to protect the structure during the preparation of the TEM foil (see chapter 5.4.3). The cross-section shows that at the interference maxima the Al-layer (dark colour) was removed while at the interference minima a "double" peak structure is observed.

The EDS line-scan of the TEM foil as shown in Fig. 6.43 reveals two nano-layers of Al_2O_3; one between the Al and Fe layer, and the other over the Al layer. To normalise the intensity of each element, the element Mg was utilised (the element Mg was not in the sample and thus can it be used as reference of the background signal).
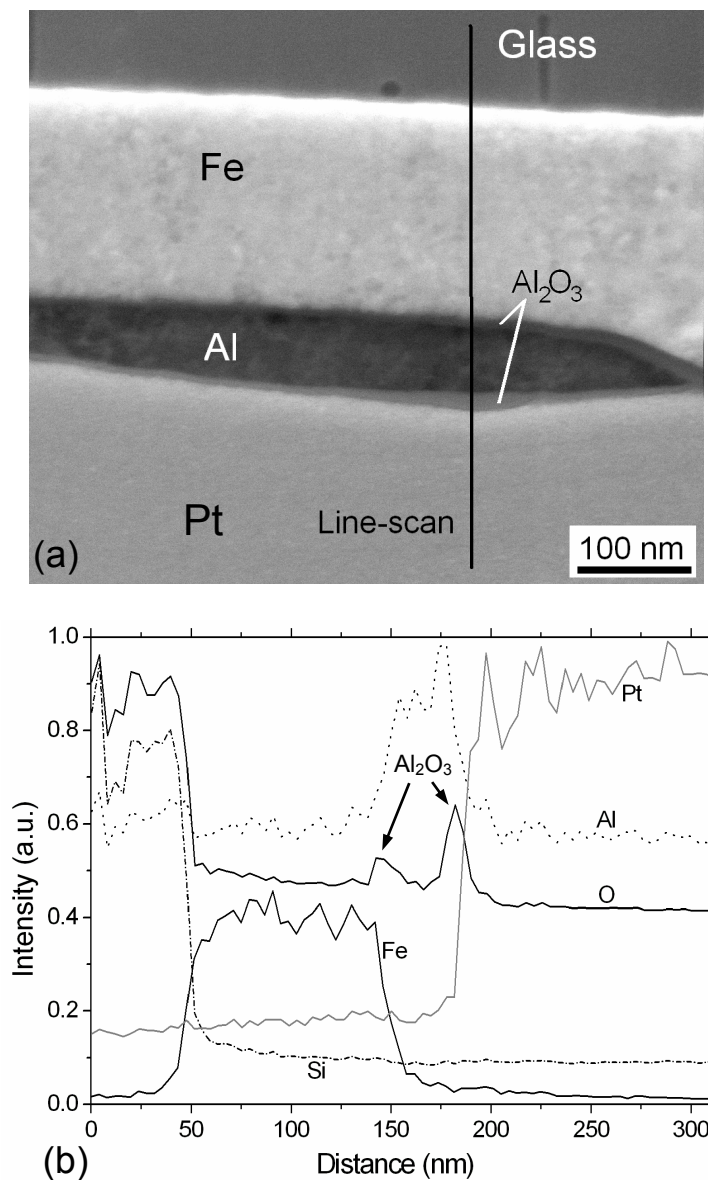
Figure 6.43. (a) Cross-section of the line type-periodical structure of a Al(30 nm)/Fe(120 nm) sample at one interference minima. (b) EDS Line-scan of the TEM foil as indicated in (a) revealing two nano-layers of Al_2O_3.

6.3.4- Discussion

In Fig. 6.38, three different topographic regimes are presented depending on the laser fluence. The first topographic type occurs without removal of material at the interference peaks. The depth of this structure is very low compared to the other topographic regimes. Similar to single-layer systems, the structuring can be explained because of the thermal dilatation which causes permanent deformation of the metallic layer at the interference maxima and therefore the structuring is conducted without melting. If the laser fluence is high enough so that the Al-layer is heated up to its melting point, the first transition in topographic regime occurs. On the high fluence side of the transition, the Al at the interference maxima is removed but the second layer remains in the solid state. The rise in the structure depth can be explained by lateral displacement of molten aluminium caused by the high pressure of the plasma and the gradient in the surface tension of the molten metal [118]. At higher laser fluences, also the second layer is molten resulting in a second transition (see details Fig. 6.38a). This transition can be observed in the "structure depth vs. laser fluence" diagram by the second discontinuity in the structure depth which correlates well with the onset of melting of material in the second layer calculated by the thermal simulation.

The EDS line-scan of Fig. 6.41 of the sample Al(30 nm)/Fe(120 nm) shows that the counts of Al decreases at the maxima of energy. This can be explained by the reason that at this laser fluence value the structuring is conducted removing the upper layer with the lower melting point (Al layer) at the interference maxima positions. The comparison between the cross-section of the sample and the EDS line-scan shows that the intensity of Al follows the thickness of the Al-layer (Fig 6.42). The formation of the Al_2O_3 layers is produced during the re-solidification process of the Al-layer after the laser pulse (Fig 6.43). This is not observed for metallic systems were the metal with the higher melting point is on the top of the sample if only the lower layer is molten.

Taking into account the discussion above, the following structuring mechanism is suggested in the case of two-layer systems, where the metal with the lower melting point is placed at the top of the sample:

At low laser fluences, similar to the single-layer case (section 6.1), the structuring is conducted without melting by the thermal dilatation of the layer (Fig. 6.44a). If the laser fluence is increased, the upper layer with the lower melting point (*B*) is molten and it is removed at the interference maxima due to two cooperative mechanisms which are firstly the local plasma pressure and secondly the surface tension gradient induced by the temperature difference between the interference maxima and minima.

However, the lower layer *A* remains in the solid state (Fig. 6.44b). Higher fluences permit to melt more metal at the interference maxima and consequently the width of the removed areas increases (Fig. 6.44c). At still higher laser fluences, also the second layer (*A*) is molten resulting in a second transition, and the metallic film is completely removed at the interference maxima due to the reasons mentioned above (Fig. 6.44d).
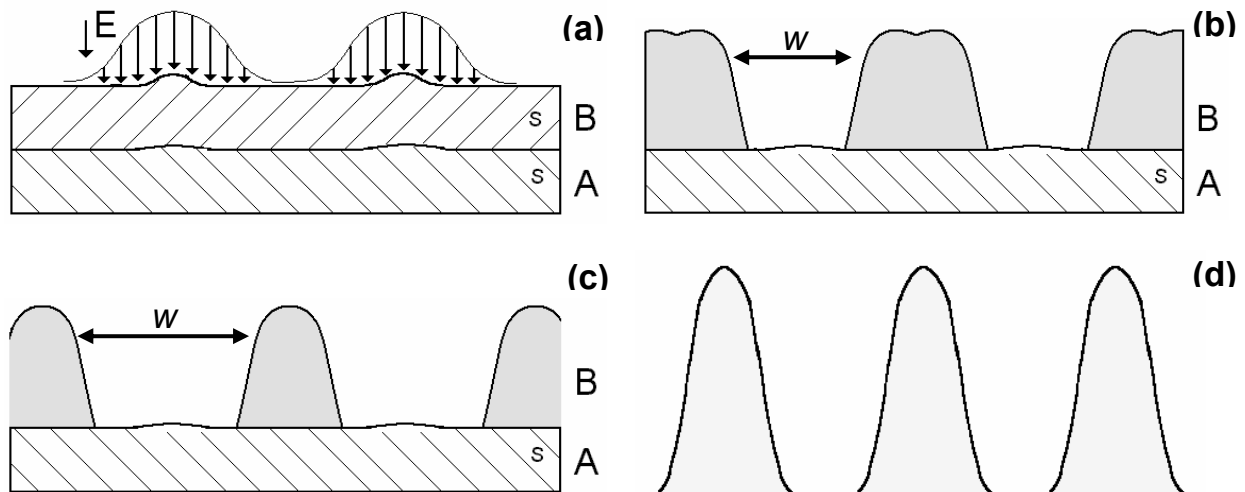
Figure 6.44. *Micro/nano structuring schema of the two-layer case. The melting point of A is higher than B. (a) The laser interference pattern acts over the surface of the film inducing thermal dilatation of the layer; (b) The layer B is molten and higher fluences increases the width (w) of the removed areas (c). (d) Both metallic layers are molten and removed at the interference maxima.*

6.4- Structuring of bulk materials

Different conditions including number of pulses, periods and laser fluences were used for the laser interference experiments. The above mentioned conditions determine the topographical characteristics of the structured samples which basically are: (1) the structure depth, (2) the aspect ratio, and (3) the homogeneity of the structured samples (this last term being connected to the quality of the shape of the periodical pattern). Following, different periodical structures in stainless steel and copper are presented.

6.4.1- Effect of period

In Fig. 6.45, different periodical structures irradiated with a line-type interference pattern with periods between 2 and 7 µm are shown. The results indicate

that interference patterns with relatively large periods (> 3 µm) produce more homogeneous structures with a characteristic peak valley profile (see Figs. 6.45 and 6.46). For small periods, the structures are less homogeneous and present discontinuities in the lateral profile as indicated in Fig. 6.46 (note the differences in the structure depth along the crest of the periodical gratings).
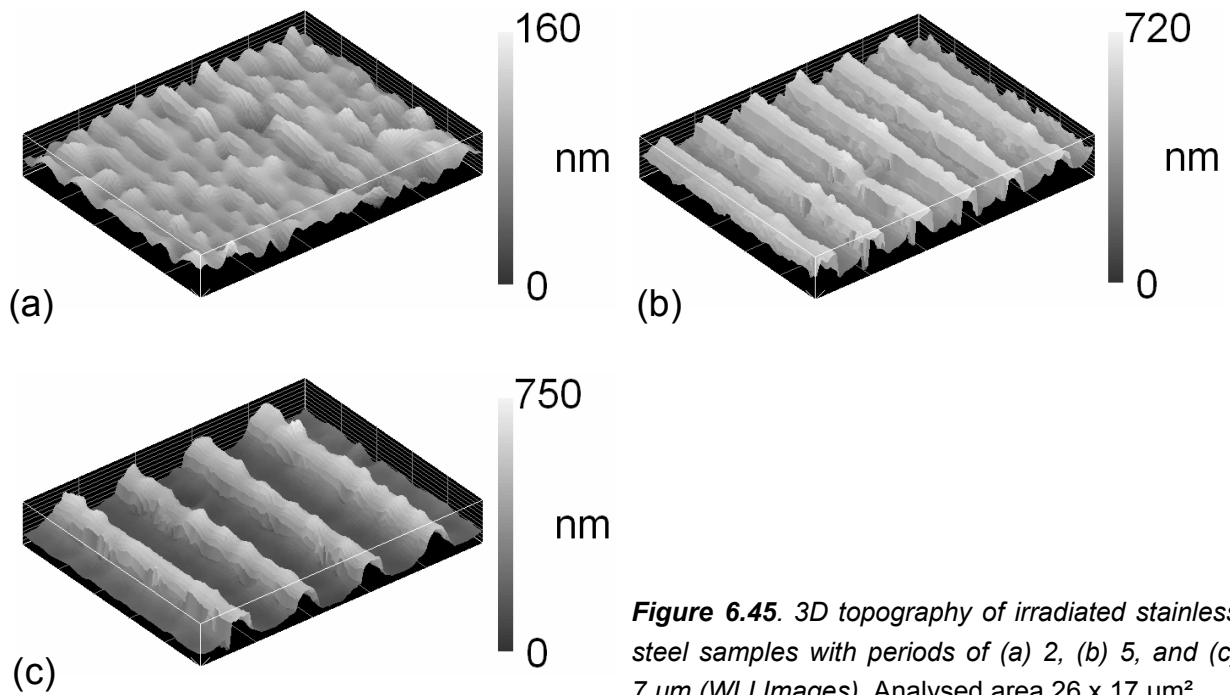
Figure 6.45. *3D topography of irradiated stainless steel samples with periods of (a) 2, (b) 5, and (c) 7 µm (WLI Images).* Analysed area 26 x 17 µm².
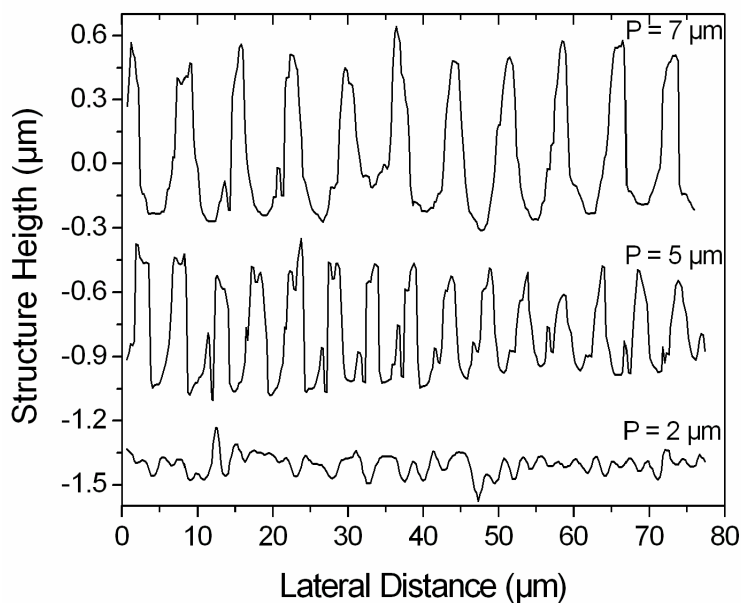
Figure 6.46. *Lateral profile of structured samples in stainless steel with periods of 2, 5, and 7 µm.*

Pulse number LF(mJ/cm²)	*1 Pulse*	*5 Pulses*	*10 Pulses*
975	(a) Int. Maximum Int. minimum	(f)	(k)
1296	(b)	(g)	(l)
1580	(c)	(h)	(m)
1843	(d)	(i)	(n)
2506	(e)	(j)	(o)
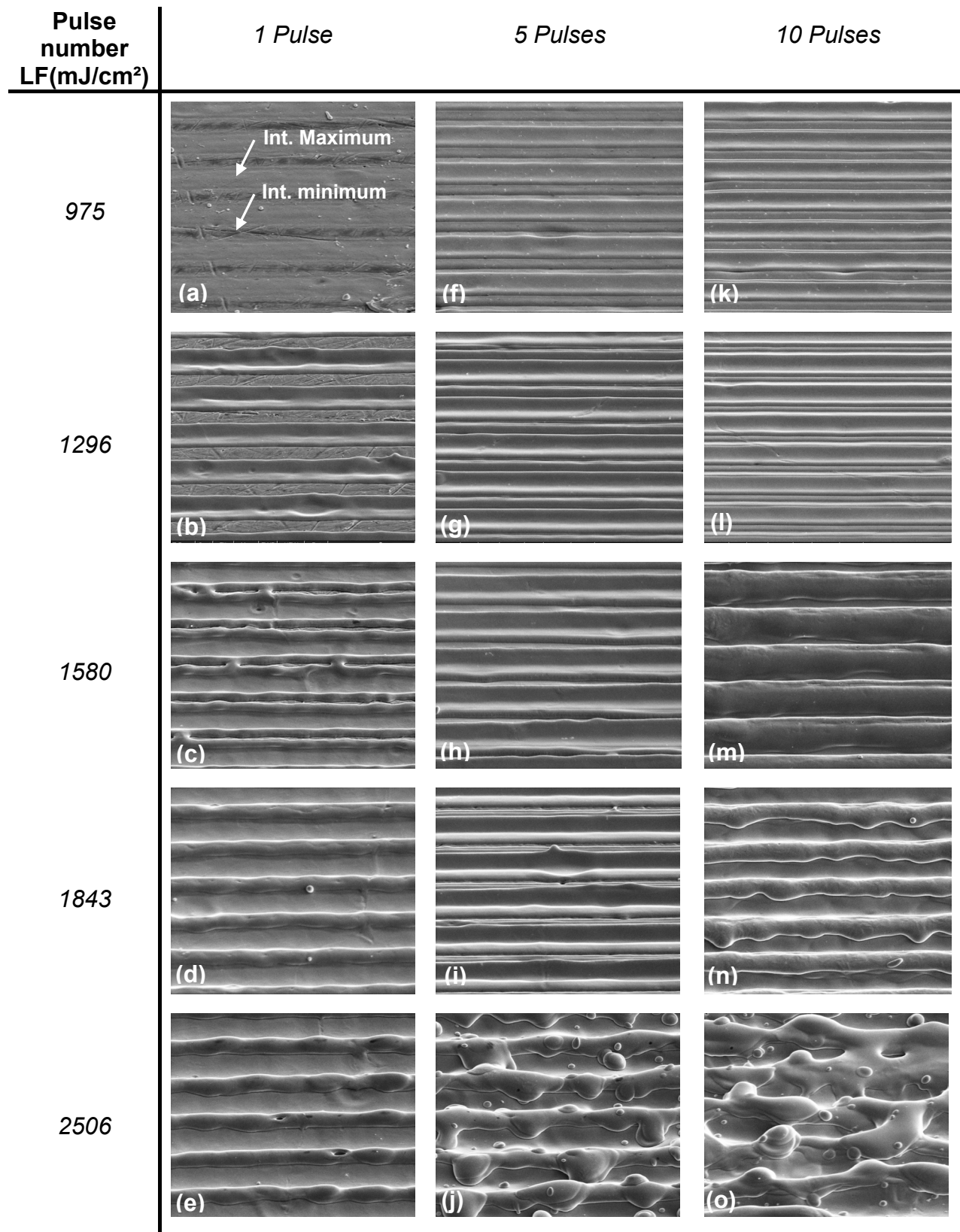
Figure 6.47*. Irradiated stainless steel samples using different laser fluences and number of pulses. Tilt: 52°.*

6.4.2- Effect of laser fluence

It is common knowledge of laser processing techniques (i.e. laser welding, cutting, drilling) that laser fluence plays an important role in the quantity of metal that can be molten or evaporated [119-121]. At relatively low fluences, the metallic surface is molten at the interference maxima positions producing flatter regions in comparison with the polished surface (see arrows in Fig. 6.47a). Higher energy densities produce quite homogeneous structures with a well-defined periodical shape which follows a double peak pattern (Fig. 6.47b and c). An increment in the laser fluence results in a rise of the structure depth (Fig. 6.47d) and the double peak structures transform themselves into a sinusoidal shaped profile (Fig. 6.47e). If even higher fluences are used, less homogeneous structures with metallic particles over the surface are obtained. These structures are similar to those indicated in (Fig 6.47j). A larger number of metallic particles were observed in the copper samples compared with the stainless steel surfaces.

The cross-section of a stainless steel sample irradiated with a line-type interference pattern with period of 4 µm and a laser fluence of 2506 mJ/cm² is shown in Fig. 6.48. The figure reveals the re-crystallised grains after the laser structuring.
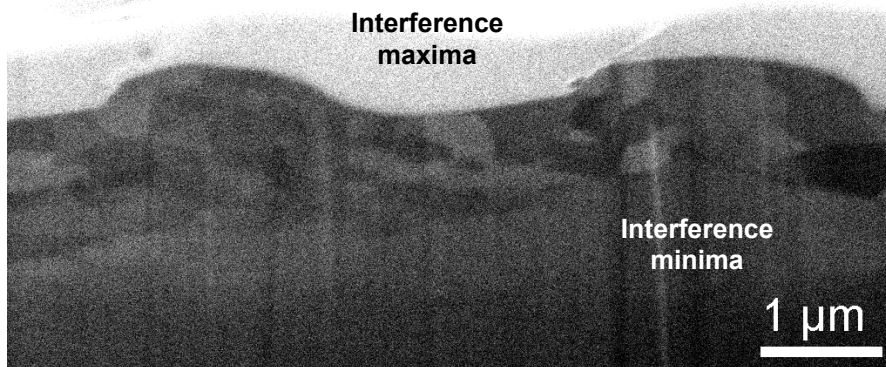
Figure 6.48. SEM cross-section of a stainless steel sample irradiated with one laser pulse and 2506 mJ/cm² of laser fluence; period = 4 µm; Tilt: 52°.

6.4.3- Effect of number of pulses

The number of laser pulses was changed from 1 to 10 for different laser fluences between 975 to 2506 mJ/cm² (Fig. 6.47). The results indicate that a large number of laser pulses produce less homogeneous structures similar to those which are obtained using high laser fluences. However, if low fluences are used, the

number of laser pulses can be increased up to about 10 pulses obtaining periodical structures with a well-defined peak-valley shape (Figs. 6.47n and m).

6.4.4- Discussion

Independently of the metal employed in the experiments, similar characteristics in the topography of the structured samples were observed. These characteristics basically depend on the period of the interference pattern, the number of laser pulses, and the fluence of the laser.

As was demonstrated in section 6.2.2 for bi-layered thin metallic films, the smaller the period of the interference pattern the smaller the temperature difference between the interference maxima and minima positions. Thus, for small periods (2 µm), the low gradient in the temperature between the maxima and minima positions is not able to conduct to the formation of a periodical structure (Fig. 6.45a).

Few laser pulses and medium laser fluences produce more homogeneous structures. By increasing the laser fluence, more metal is molten at the interference maxima positions. Similar to the transition between the structuring conducted without removal of material and the structuring conducted with removal of material in thin metallic films, the plasma and the gradient in the surface tension of the liquid metal shifts the molten metal towards the interference minima positions [118] (cold regions) (see Fig. 6.47b). This occurs until the molten metal which flows from two consecutive interference maxima perpendicular to the thermal gradient crash into each other at the interference minima. After that, the metal resolidifies at a relatively high cooling rate obtaining small grains with a size between 500 and 800 nm (Fig. 6.48). The micrograph in Fig. 6.48 clearly permits to recognise the depth of the molten region which is larger at the interference maxima positions. Still larger laser fluences (or a larger number of laser pulses) permit to melt more and more metal. Therefore, due to the large volume of liquid metal, the resulting structures are less homogeneous. In metals with a low surface tension (i.e. copper), the surface of the molten areas is not able to retain the liquid metal, and thus particles are ejected.

Based on these observations, the following structuring mechanism is suggested:

In Fig. 6.49a, the interference pattern melts locally and periodically the surface of the metal. Due to the pressure of the plasma and the gradient in the surface tension generated by the thermal gradient, the molten metal is shifted from the hot regions (interference maxima) towards the interference minima (Fig 6.49b). Higher laser fluences or a larger number of laser pulses permits to melt more metal, and a

stronger lateral shift occurs which results in the formation of structures with a larger structure height. Moreover, metals with a lower surface tension generate less homogeneous structures.
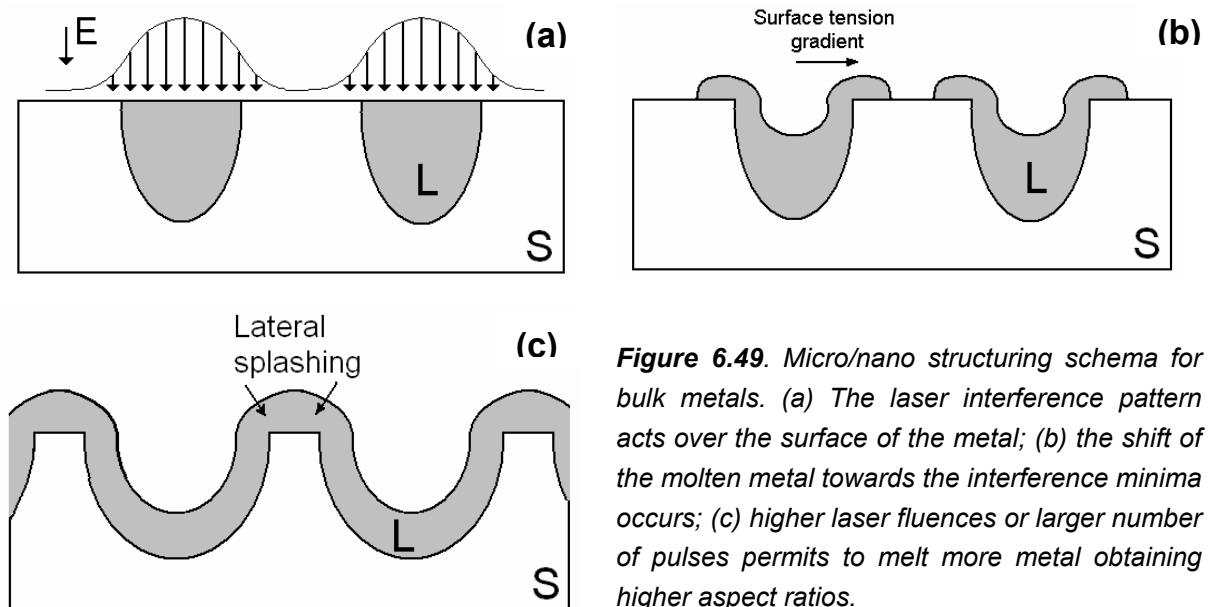
Figure 6.49. Micro/nano structuring schema for bulk metals. (a) The laser interference pattern acts over the surface of the metal; (b) the shift of the molten metal towards the interference minima occurs; (c) higher laser fluences or larger number of pulses permits to melt more metal obtaining higher aspect ratios.

6.5- Long-range formation of intermetallic pattern

Due to the large temperature gradient across the interference pattern, the process of laser interference structuring can be used for local phase changes. In the following subsections, the formation of intermetallic compounds in the samples Fe(30 nm)/Al(120 nm) and Al(30 nm)/Fe(120 nm) and Fe(75 nm)/Cu(30 nm)/Al(55 nm) is presented.

6.5.1- Sample Fe(30 nm)/Al(120 nm)

In order to investigate the possibility of the formation of intermetallic phases at high laser fluence values, the sample Fe(30 nm)/Al(120 nm) was structured with three laser-beams in a symmetrical configuration using a laser fluence of 89 mJ/cm² (Fig. 6.50).
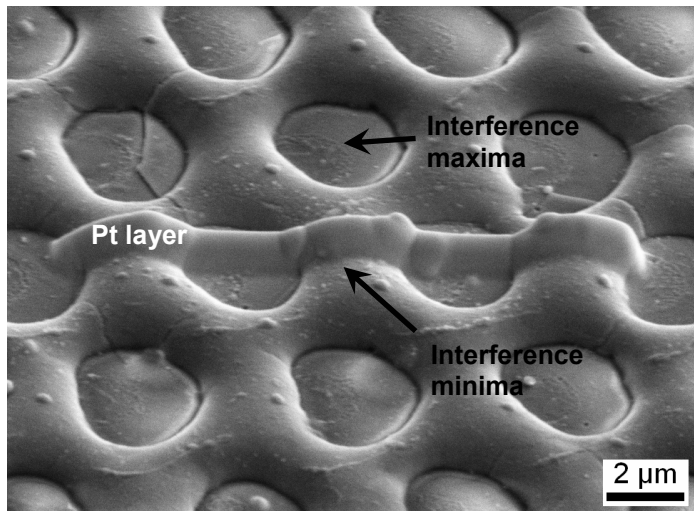
Figure 6.50. Sample Fe(30 nm)/ Al(120 nm) after deposition of Pt for the TEM foil preparation. The craters correspond to the interference maxima positions (see indication in the figure). SEM Image, Tilt: 52°.
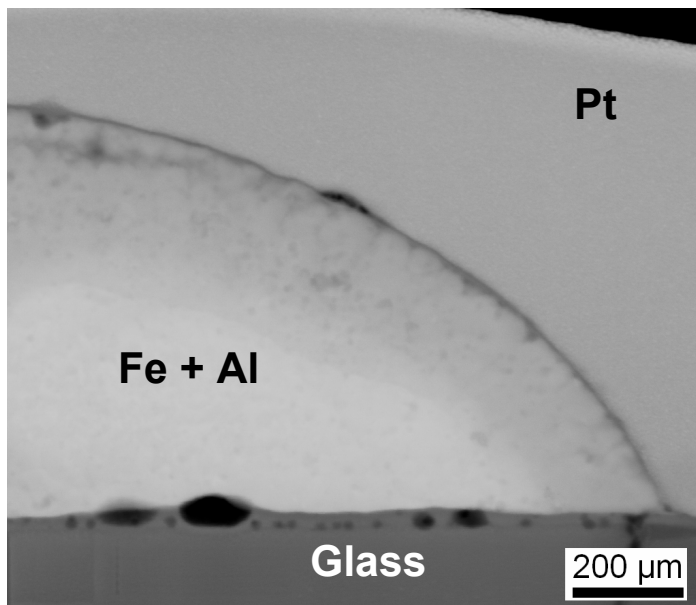
Figure 6.51. Sample Fe(30 nm)/ Al(120 nm). The TEM foil was prepared by the procedure outlined in chapter 5.4.3 with a total thickness of 91 nm. The image corresponds to a half interference minimum. STEM mode image at 15 kV.

A TEM foil was prepared following the procedure outlined in chapter 5.4.3. Fig. 6.51 shows a half-interference minimum in STEM mode. The figure distinguishes principally three regions connected to the Pt layer (added to protect the layer during the TEM foil preparation), the re-solidified mixture of Al and Fe after laser structuring, and the glass substrate.

The selected area electron diffraction pattern of Fig. 6.52a reveals ordered intermetallic compounds. Because of the close lying reflexes it cannot unambiguously be determined if the intermetallics are $FeAl_2$, Fe_2Al_5 or a mixture of both [122]. The formation of such intermetallic phases can be explained as follows. Due to the high laser fluence, the metallic layers at the interference maxima are molten and removed from the interference maxima. The flux of the metal permits convective mechanism mixing both components and consequently, allowing the formation of intermetallic

compounds. According to the thickness of the layers (30 nm of Fe and 120 nm of Al) an atomic ratio of 1:2.839 for iron and aluminium can be calculated. The intermetallic compounds $FeAl_2$ and Fe_2Al_5 possess an atomic ratio of 1:2 and 1:2.5 for Fe and Al, respectively. Therefore, its formation is more feasible than other intermetallic compounds like Fe_3Al (atomic ratio 1:0.333) or FeAl (atomic ratio 1:1).
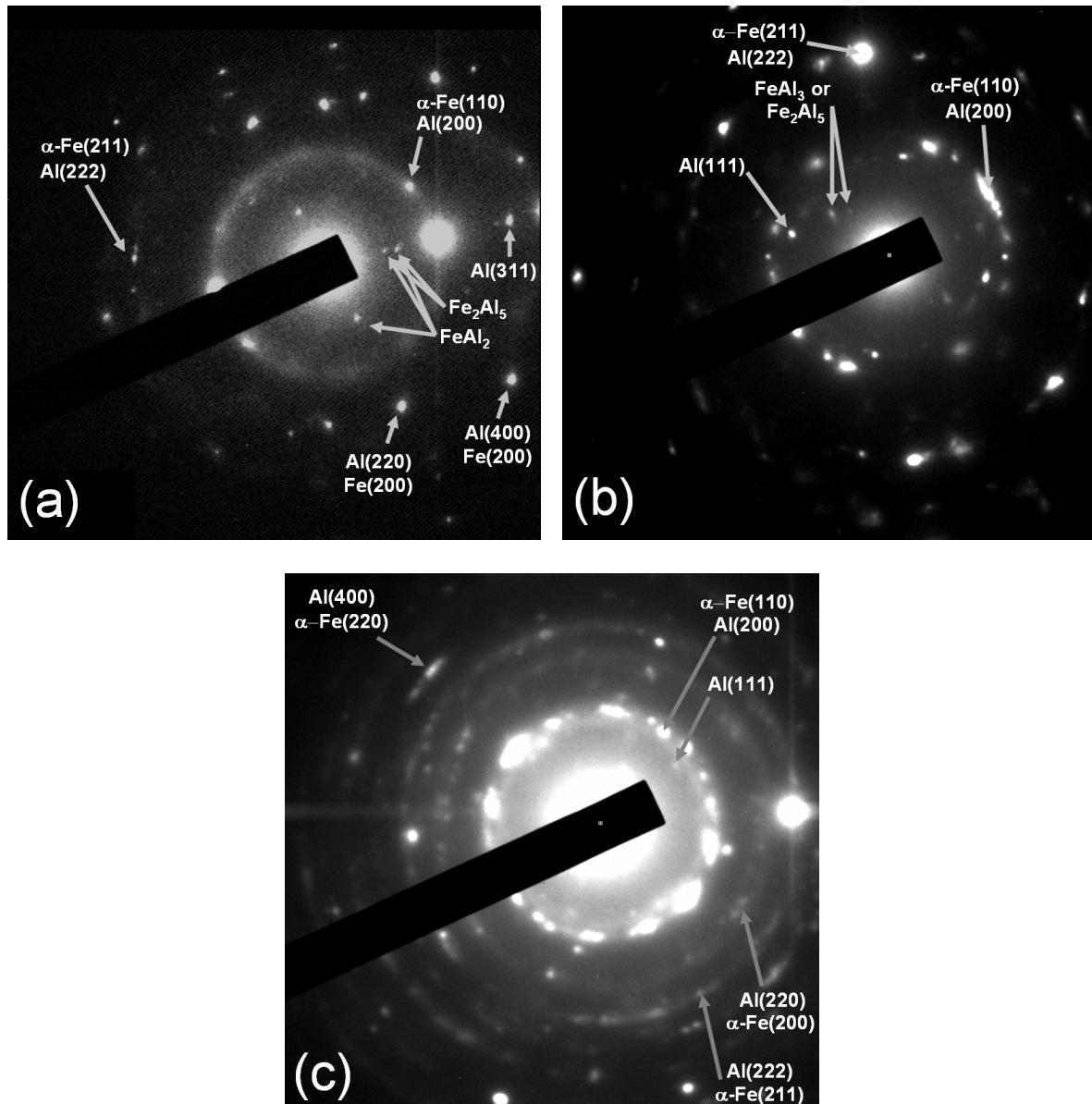
Figure 6.52. *Selected area electron diffraction patterns of: (a) irradiated layers with ordered intermetallics' reflexes of $FeAl_2$ or Fe_2Al_5 (sample Fe(30 nm)/Al(120 nm)); (b) region 2 of Fig. 6.42b indicating ordered intermetallics' reflexes of $FeAl_3$ or Fe_2Al_5 (c) region 5 of Fig. 6.42b without ordered intermetallics' reflexes. (b) and (c) correspond to the sample Al(30 nm)/Fe(120 nm).*

6.5.2- Sample Al(30 nm)/Fe(120 nm)

The sample Al(30 nm)/Fe(120 nm) belongs to the case explained in section 6.3 where the metal with the lower melting point is located at the top of the sample. A laser fluence of 590 mJ/cm² was employed to produce the periodical structuring. This value corresponds to the regime at which the aluminium layer is removed at the interference maxima (see Fig. 6.37).

Fig. 6.42 shows the TEM foil (STEM image at 17 KV) of the sample Al(30 nm)/Fe(120 nm). The thickness of the foil was 83 nm. The foil shows one laser interference maximum and one laser interference minimum. Fig. 6.42b indicates schematically 5 different microstructure regions of different grain size and composition. The grain size was determined by dark field images.

Regions 4 and 1 (Fig. 6.42b) correspond to pure iron (determined by EDS) with an average grain size between 6 and 15 nm for region 4, and 15 and 25 nm for region 1. The difference in grain size can be explained by the high input of energy at the interference maxima. Thus, the temperature of the film in region 4 reached values near the melting point leading to recrystallisation with an increase in the grain size.

An EDS analysis (in TEM) of region 2 indicates the presence of iron and aluminium. The TEM diffraction image (Fig. 6.52b) of the same selected area indicates reflexes of ordered intermetallics, either $FeAl_3$, Fe_2Al_5 or a mixture of both [122]. In [123], the kinetic interaction between solid iron and liquid aluminium was studied. They have reported the formation of a $FeAl_3$ layer near the Al layer next to a layer of Fe_2Al_5. Between regions 1 and 2, several ordered pores produced at the interference peaks are observed. The formation of pores was also observed by [123] and explained by the diffusion of Al in the intermetallic compound formed. The grain size in this region was found to be between 1 and 6 nm.

The EDS analysis of region 5 indicates only the presence of aluminium. The grain size according to the TEM images was found to be smaller than 3 nm. The small grain size of the aluminium in this region can be explained by the high cooling rate (calculated from the thermal simulation) which occurs at the surface of the sample (10^{10} K/s). Such low grain sizes are also indicated by the ring pattern shown in Fig. 6.52c as compared with Fig. 6.52b. In this case, no intermetallic compounds were detected.

In region 3 of Fig. 6.42b, aluminium as well as oxygen were detected by EDS. This observation indicates that the remaining molten aluminium at the interference maxima oxidises forming an Al_2O_3 layer after the laser pulse. Moreover, a layer of Al_2O_3 can be observed over the region 5 of Fig. 6.42b. This effect is not observed for

metallic systems where the metal with the higher melting point is on the top of the sample and only the lower layer is molten.

6.5.3- Sample Fe(75 nm)/Cu(30 nm)/Al(55 nm)

The sample Fe(75 nm)/Cu(30 nm)/Al(55 nm) was irradiated using two laser-beams and a laser fluence of 91 mJ/cm². A line-type interference pattern with period of 5.81 µm was obtained (Fig. 6.53). According to Fig. 6.53a, the structuring at this laser fluence was conducted without removing the metallic layer at the interference maxima. However, from the thermal simulation, this laser fluence should be enough to melt the copper and the aluminium layers at the interference maxima (see Fig. 6.53b).
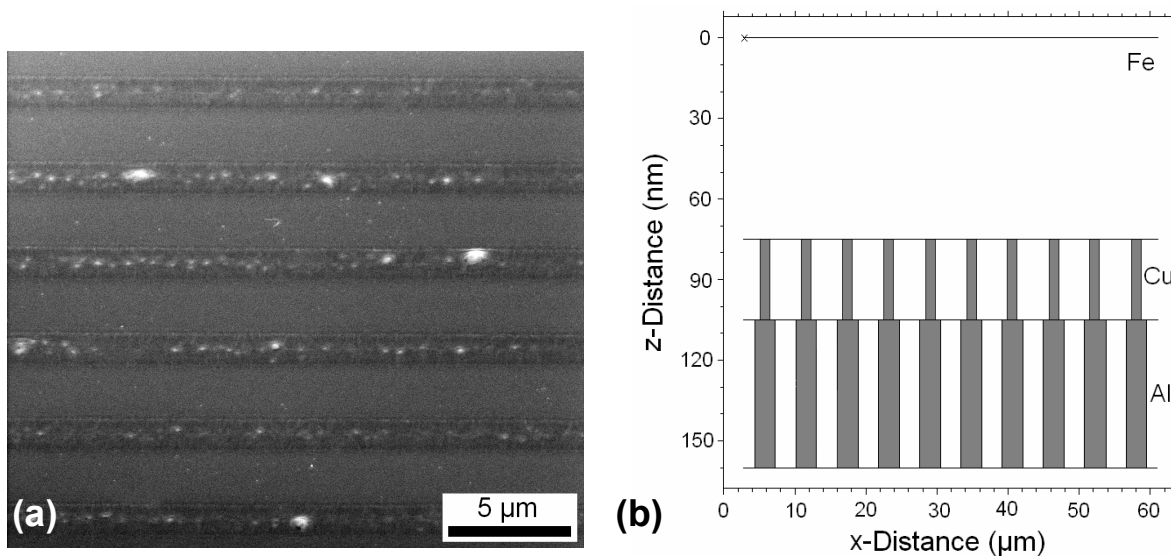
Figure 6.53. *(a) Laser interference micro/nano structuring of the Fe/Cu/Al sample with two interfering laser-beams and a laser fluence of 91 mJ/cm². Only one pulse was used for the experiments. Period = 5.81 µm. (b) Thermal simulation of the three layer system indicating the solid (white) and molten (grey) regions. Ten interference maxima are simulated. Both the lower copper and aluminium layers are molten at the interference maxima.*

The cross-sectional analysis of the sample using the structuring conditions described above clearly indicates two microstructural zones (Fig. 6.54). At the interference minima, three different metallic layers can be recognised (Fig. 6.55a) which correspond to Fe, Cu, Al from top to bottom (the Pt layer was used to protect the sample during milling in the TEM foil preparation procedure). However, given the fact that Cu and Al can react at relatively low temperature, interdiffusion and reaction

might have occurred during the process of sample preparation [124] obtaining an interdiffusion zone as indicated in Fig. 6.55a (*I-Zone*). This is also suggested by the EDX STEM line-scan conducted at the same position (Pos 1, Fig. 6.54) where a significant change in the slope of the composition-position profile of the elements Cu and Al is observed at the Cu/Al intersurface (Fig. 6.56a).

Interference maximum   **Interference minima**
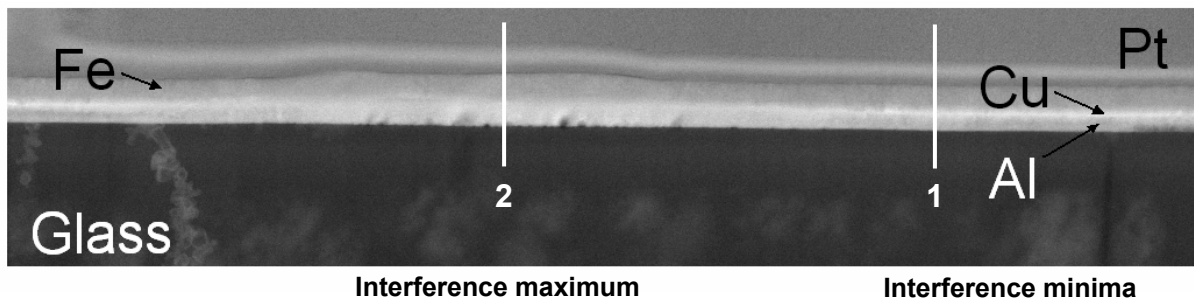
Figure 6.54. FIB-prepared cross-section of the structured sample with 91 mJ/cm² showing one interference maximum and minimum (STEM image at 15 kV).
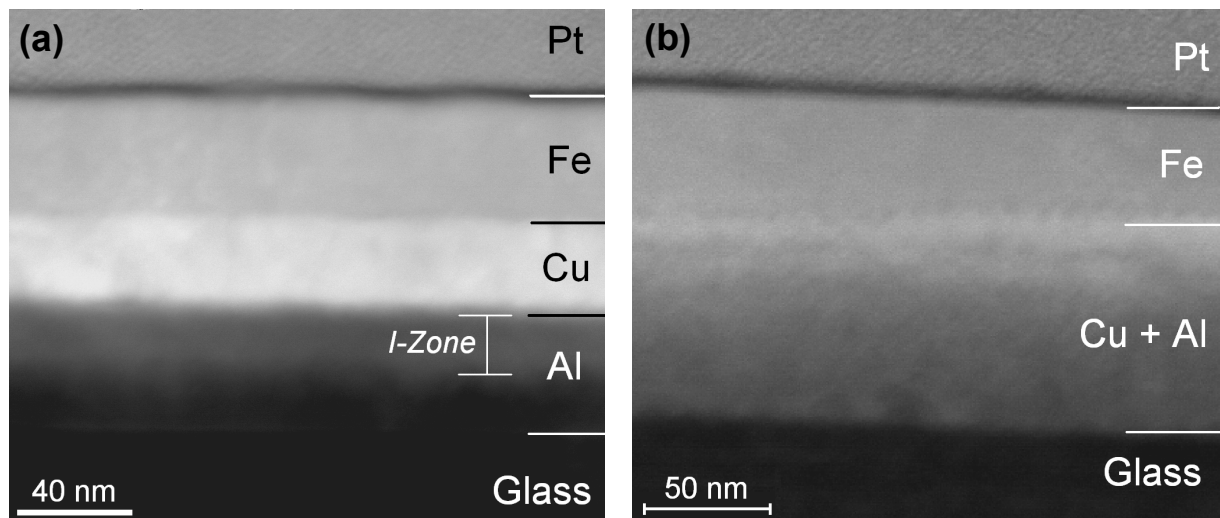
Figure 6.55. (a) HAADF micrographs at: (a) interference minima and (b) maxima positions. The contrast is strongly dependent on the average atomic number. Note in (b) that in the Cu/Al mixed layer the contrast varies gradually form light grey (Cu) to dark grey (Al).

At the interference maxima positions (Pos 1, Fig. 6.54), on the other hand, only two metallic layers can be distinguished (Fig. 6.55b). From the EDX STEM line-scan, the sharp changes in the composition profiles of the elements Fe and Cu indicate that the metals are not mixed. On the other side, the Cu and Al layers strongly interact due to diffusion and convective processes in liquid state during the laser pulse obtaining very strong changes in the composition profiles (Fig. 6.56b).

This observation proofs that a laser fluence of 91 mJ/cm² is adequate to melt only the lower metallic layers leaving the Fe-layer in the solid state.
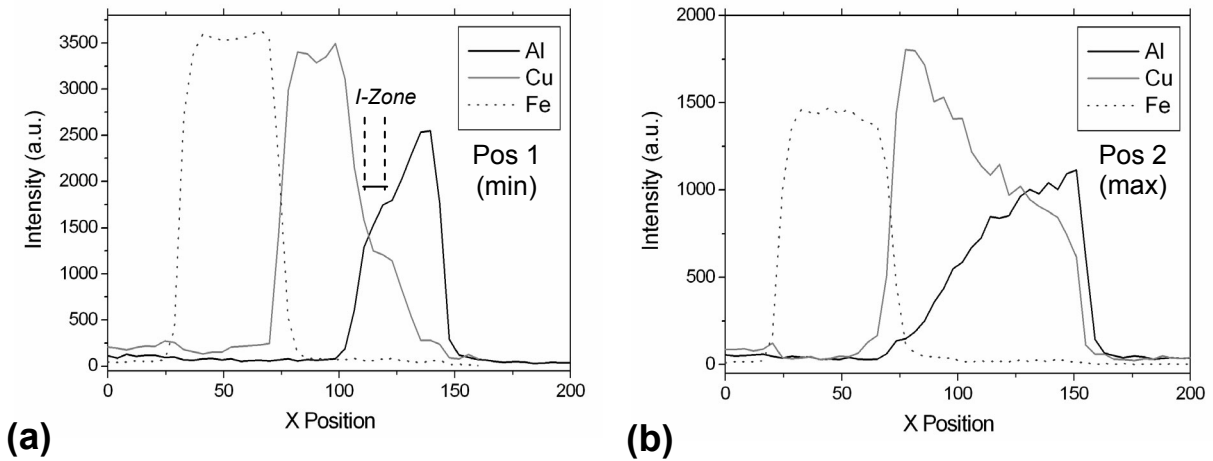
Figure 6.56. *EDX HAADF line-scans at the positions indicated in Fig. 6.50; (a) Interference minimum; (b) Interference maximum.*
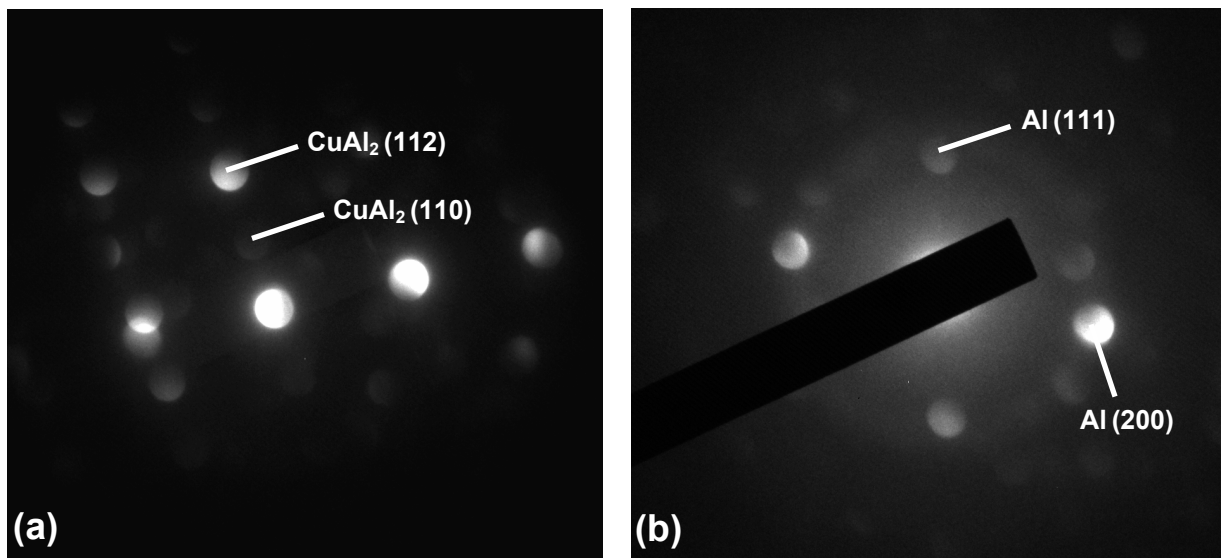
Fig. 6.57. *Convergent beam electron patterns (CBED) of (a) interdiffusion-zone (b) Al layer, both at the interference minima positions.*

TEM investigations of the irradiated sample provide important information about microstructural details as well as about phase formation due to the high temperature induced by the laser irradiation. Convergent beam electron diffraction investigations (CBED) carried out at the position of the interdiffusion zone at the interference minima (see Fig. 6.55a) indicate ordered reflexes of the intermetallic phase $CuAl_2$ (Fig. 6.58a). As mentioned above, this phase could be produced during

the sputtering process [124]. Below this layer only reflexes of Al are observed (Fig. 6.57b).

The cooling rate at a single point of the sample after heating depends on the lateral and vertical coordinate and hence, the grain size is changing according to these positions. Similar to [55, 112], at the unmodified regions, which correspond to the interference minima positions, a ring diffraction pattern is obtained using a 200 nm SAD (selective angle diffraction) aperture due to the polycrystalline structure of the layers with grain sizes from 15 to 50 nm (Fig. 6.58a). On the other side, the layer structure of the film is changed significantly at the position of the laser maximum. During the resolidification process, the maximum cooling rate is obtained at the interference maxima on the top of the upper layer (6.10^{10} K/s). However, in this case, the upper iron layer is not molten because of the relatively low laser fluence. Below the iron layer and at the interference maxima positions, the cooling rate decreases to 1.10^{10} K/s producing larger grains. Moreover, in Fig. 6.58b, the ring pattern related to the copper and aluminium layers vanishes resulting in a typical dot pattern which can be explained by the larger grains formed during the resolidification process.
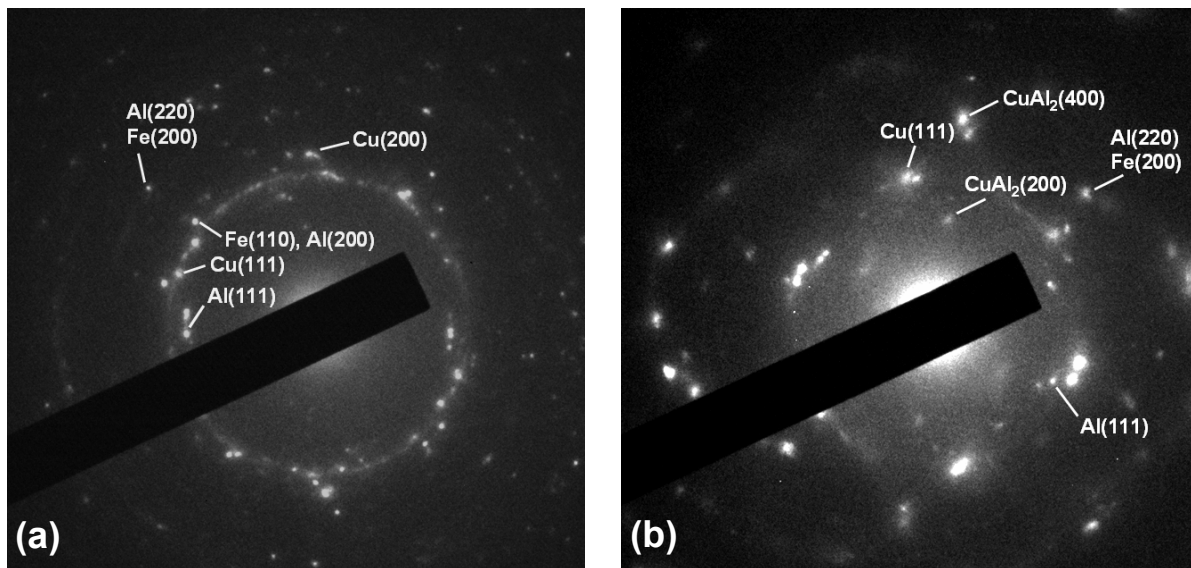
Figure 6.58. *Selected area electron diffraction patterns of irradiated Fe(75 nm)/Cu(30 nm)/Al(55 nm) sample at (a) interference minima, and (b) interference maxima positions.*

The TEM diffraction image of Fig. 6.58b also indicates reflexes of ordered intermetallic of $CuAl_2$ which is formed at relatively low temperatures [124]. In addition, the atomic ratio between Cu and Al in the film is 1 to 5.25 which is favourable for the formation of an intermetallic phase with a high atomic content of aluminium (taking into account the possible intermetallic phases that Al and Cu can

form: Cu_9Al_4, Cu_3Al_2, AlCu and $CuAl_2$ [125]). Therefore, this intermetallic phase can be formed at the interference maxima positions.

6.6- Time - resolved electrical resistance measurements

Time-resolved electrical resistance measurements with nanosecond resolution were carried out on Fe(30 nm)/Al(120 nm) and Fe(30 nm)/Cu(60 nm) samples in order to demonstrate the consistence of the thermal simulations in the time scale. The measurements were compared with both the temperature and electrical resistance history of the layers calculated using the thermal simulation. In all cases, the obtained structures are typical of the low energy regime (R1, see section 6.4.2).

For the sample Fe(30 nm)/Al(120 nm), two different laser fluences were simulated: 61 and 130 mJ/cm².

At 61 mJ/cm², the thermal simulation shows that only the Al-layer is molten at this fluence value. This effect strongly increases the electrical resistance of the aluminium layer as indicated by the simulated electrical resistance history (Fig 6.59a). The voltage-time evolution measured during the laser interference experiments shows an abrupt rise in the electrical resistance which can be connected to the melting and heating processes. After the cooling of the film, the voltage falls to a constant voltage, but still larger than the initial value (about 1.9 %). Consequently the electrical resistance of the structured sample is larger than that of the unstructured sample.

In the case of the sample irradiated with 130 mJ/cm² of laser fluence, a difference of 6.0% was found between the initial and final voltage values during the laser interaction. It means that if the structure depth is even larger, a higher difference in the electrical resistance between the structured and the unstructured sample is observed (Fig. 6.59b) Similar results were observed by [126] during time-resolved electrical resistance measurements in diamond carbon layers during pulsed laser irradiation. The results were explained by melting and internal graphitisation of the films. In metals, the increase of the electrical resistance after structuring can be explained by changes in the topography and by the formation of defects induced by the local heating [127-129]. Both simulated fluences show a good agreement in the period of time at which the heating and cooling processes occur (400 and 600 ns for 61 and 130 mJ/cm², respectively).
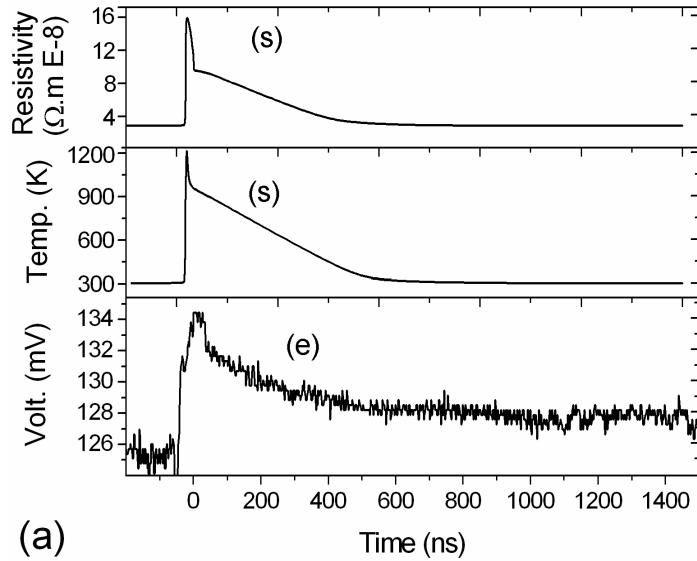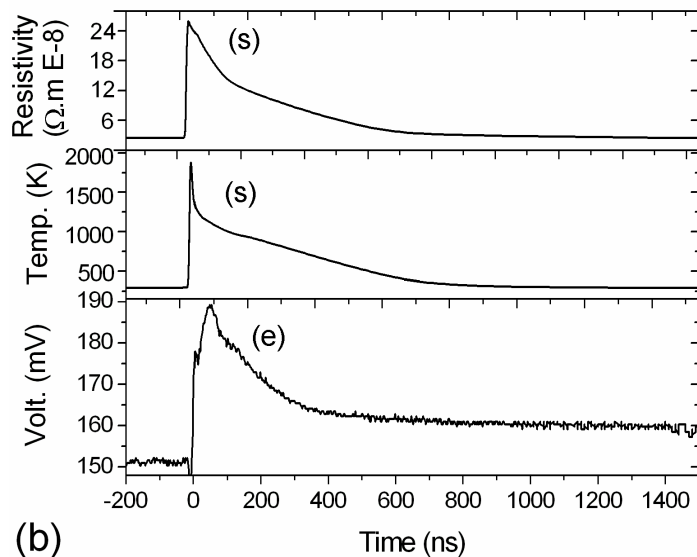
Figure 6.59. History of the electrical resistance of the Al-layer (simulated), the temperature at the interference maxima (simulated), and the voltage evolution (experimental) during a 8 ns laser pulse on a Fe(30 nm)/Al(120 nm) sample. (s) Simulated; (e) experimental. The laser fluence was: (a) 61 mW/cm²; (b) 130 mJ/cm².

Figures 6.60 and 6.61 show the voltage-time evolution during the laser interference irradiation experiments of the samples Fe(30 nm)/Al(120 nm) and Fe(30 nm)/Cu(60 nm). Al curves correspond to the low energy regime. The higher the laser fluence, the higher the difference in the electrical resistance between the initial value before the laser pulse and the maximum value measured during the heating process (for example 7.2 and 25.2 % for the laser fluences 61 and 130 mJ/cm² respectively, sample Fe(30 nm)/Al(120 nm)). This effect can be explained by the increase of the temperature and the volume of molten metal which is produced when the laser fluence is increased. Thus, a higher electrical resistance is obtained during the laser irradiation.
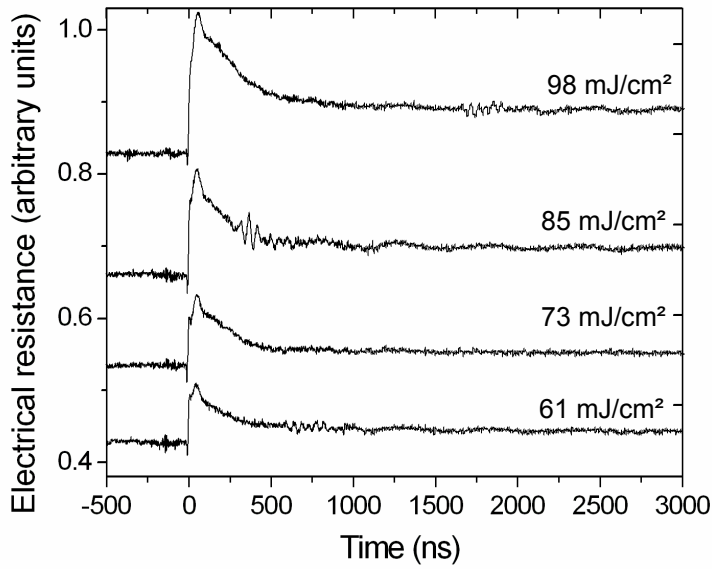
Figure 6.60. Time-resolved electrical resistance measurements of the sample Fe(30 nm)(Al(120 nm) at 98, 85, 73, and 61 mJ/cm². All the laser fluences correspond to the low energy regime.
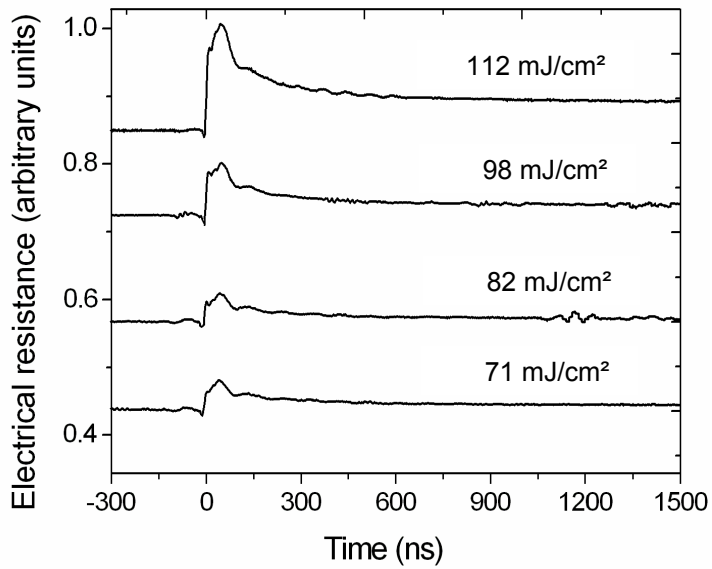
Figure 6.61. Time-resolved electrical resistance measurements of the sample Fe(30 nm)(Cu(60 nm) at 112, 98, 82, and 71 mJ/cm². All the laser fluences correspond to the low energy regime.

Chapter 7

Modulation of optical and tribological properties

7.1- Optical properties

The major requirement for solar selective surfaces is high absorbance in the solar spectrum (0.3-2.5 μm) but low thermal emittance at the operating temperatures. The production process should be simple and inexpensive and the materials used should not be toxic. Among the variety of fabrication methods (i.e. CVD [130], PVD [131], chemical conversion [132]) and various coating designs (i.e. multilayer [133, 134], cermets [135], semiconductors [136, 137]), metal surfaces with a particulate microstructure (dendritic, porous or granular) on the same scale as the wavelength of the incident radiation reveal simply both spectral and directional selectivity.

Surface structuring of low thermal emittance metals brings the desired spectral selectivity in a simple and inexpensive manner, without the difficulty of controlling both thickness and composition of conventional coatings. Furthermore, these surfaces are not very sensitive to environmentally induced structural modifications, which are generally responsible for the rapid deterioration of the optical properties in conventional selective coatings [138]. In addition, surface irregularities such as grooves and pores with dimensions comparable to the cut-off wavelength (maximum wavelength to be absorbed) simply increase the solar absorbance and to a lesser extent, the infrared emittance by multiple reflections [139]. Therefore, texturing of low emittance metals can be considered as valuable candidates for photo-thermal conversion surfaces.

Roughening the surface of a single material can be done by reactive etching, sputter etching and electrochemical process. Photo-thermal conversion using just morphology effects of metal substrates without any extra absorber layer has been investigated in [140] for Cr and Ni. There, periodic surfaces were produced by holographic technique on photo-resist film and then coated with a metallic layer by evaporation. However, these surfaces are not suitable for high temperature applications due to the deterioration of the polymer which constitutes the under-layer.

119

Sai *et. al.* [141] have introduced a sequential method to produce solar selective absorbers based on two-dimensional tungsten surface gratings called fast atom beam (FAB) etching. The disadvantages of this method are the use of sequential steps as well as a mask to produce such periodical structures.

Because of the advantages of the Laser Interference Metallurgy (i.e. no secondary step is required) the direct processing of metallic surfaces for solar absorbers is presented as alternative to [140, 141]. In this thesis, different periodic structures were produced in copper and stainless steel. Measurements of total and diffuse reflectance as well as normal emittance demonstrate the viability of the new method.

Measurements of optical properties were also conducted in bi-metallic thin films. In this case, the possibility to mix the optical properties of both metals was studied. These results are presented in section 7.2.

7.1.1- Optical properties of structured bulk materials

7.1.1.1- Experimental Results

Solar absorbance (α) and thermal emittance (ε) were calculated from the reflection data in solar and thermal infrared wavelengths, using solar spectral radiance in air mass (AM) 2 and black body radiation at 300 K [142] using the following relations:

$$\alpha = \frac{\int_0^\infty A(\lambda)\left[1 - R(\lambda)\right]d\lambda}{\int_0^\infty A(\lambda)d\lambda}$$

(7.1)

$$\varepsilon(\theta, T) = \frac{\int_0^\infty E(T,\lambda)\left[1 - R(\theta,\lambda)\right]d\lambda}{\int_0^\infty E(T,\lambda)d\lambda}$$

(7.2)

where *A(λ)* is the solar spectral radiance, *E(T,λ)* the spectral blackbody emissive power and *R(θ,λ)* and *R(λ)* are the angle dependent spectral reflectance and total reflectance, respectively.

Normal emittance at room temperature is obtained considering *ε(θ=0, T=300K)* (see Eq. 7.2).

Fig. 7.1 and 7.2 show both the total and diffuse reflection of the structured and unstructured stainless steel and copper surfaces. The curves indicate how the total and diffuse reflection of the metallic surfaces can be changed when the period and the structure depth of the samples is changed (see Table 7.1).
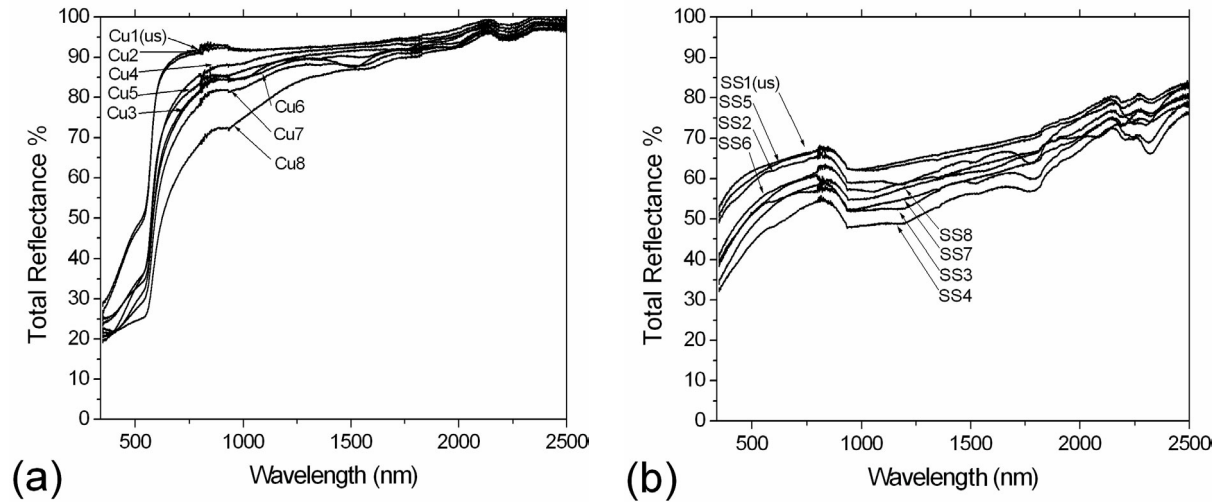
Figure 7.1. *Total spectral reflectance for (a) copper and (b) stainless steel samples structured with different periods and structure depth. (us): unstructured. For legend see Table 7.1 (A. Lasagni, M. R. Nejati, R. Clasen, F. Mücklich, Adv. Eng. Mat. 8 (2006), 580-584).*
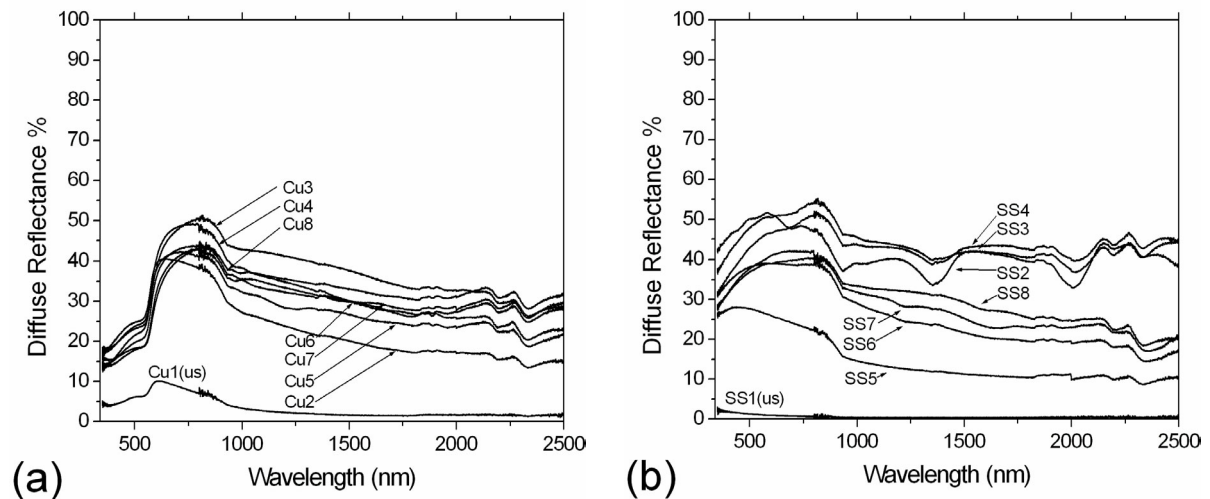
Figure 7.2. *Diffuse spectral reflectance for (a) copper and (b) stainless steel samples structured with different periods and structure depth. (us): unstructured. For legend see Table 7.1 (A. Lasagni, M. R. Nejati, R. Clasen, F. Mücklich, Adv. Eng. Mat. 8 (2006), 580-584).*

The dependence of the total absorbance (calculated using Eq. 7.1) for both stainless steel and copper samples as a function of the aspect ratio is shown in Fig. 7.3a. This last figure indicates that the higher the aspect ratio, the better the total absorptance.

Measurements of thermal emittance at room temperature for the different aspect ratios are shown in Fig. 7.3b. In this case it can be clearly seen that the thermal emmitance has not an important dependency on aspect ratio of the structured samples.

Sample name	Near normal absorbance from total reflectance	Emittance at (300 K)	Period (µm)	Structure depth (µm)	Aspect ratio	Pulse number
Cu1(us)	0.156	0.010	-	0	0.000	0
Cu2	0.150	0.044	2.00	0.282	0.140	1
Cu3	0.250	0.029	2.00	0.490	0.245	10
Cu4	0.223	0.022	2.00	0.442	0.221	4
Cu5	0.242	0.035	3.59	0.627	0.175	1
Cu6	0.261	0.048	3.59	1.030	0.287	3
Cu7	0.288	0.038	3.59	1.307	0.364	6
Cu8	0.352	0.040	3.59	1.601	0.446	10
SS1(us)	0.349	0.076	-	0	0.00	0
SS2	0.410	0.093	4.01	0.593	0.148	1
SS3	0.450	0.111	4.01	0.982	0.245	5
SS4	0.498	0.093	4.01	1.335	0.333	10
SS5	0.343	0.107	2.00	0.078	0.039	1
SS6	0.411	0.087	2.00	0.344	0.172	5
SS7	0.451	0.097	2.00	0.410	0.205	10
SS8	0.425	0.098	3.01	0.753	0.250	10

Table 7.1. Normal absorbance from total reflection, thermal emittance at 300 K, structure depth, period and aspect ratio of both copper and stainless steel samples. (us): unstructured.
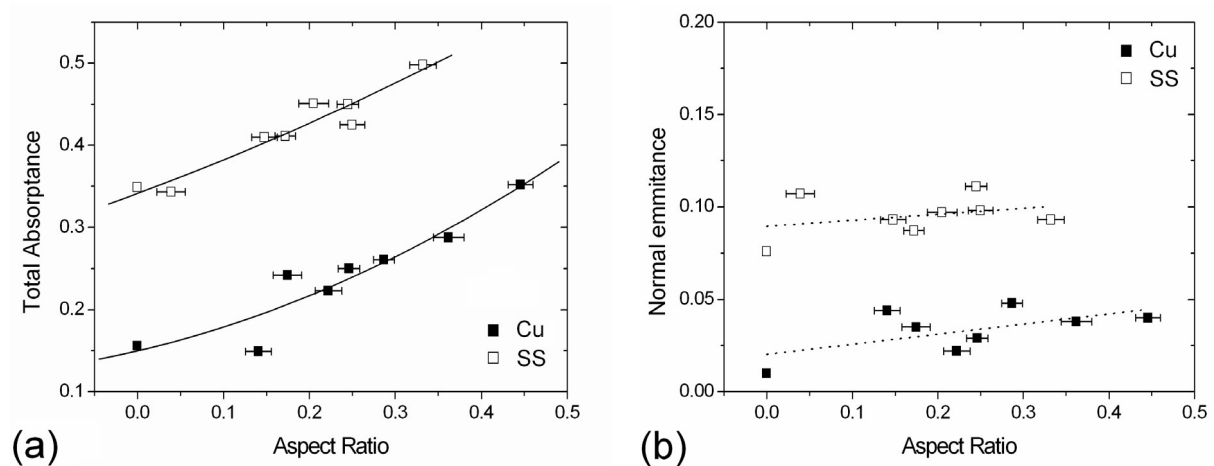
Figure 7.3. (a) Total absorbance and (b) thermal emittance as function of the aspect ratio for copper and stainless steel structured samples (A. Lasagni, M. R. Nejati, R. Clasen, F. Mücklich, Adv. Eng. Mat. 8 (2006), 580-584).

7.1.1.2 Numerical calculations

Numerical calculations of total reflectance were carried out using the software PCGrate-S(x) v. 6.1 Demo [143]. This software can simulate effects of micro-roughness, model gratings covered with very thin or thick layers of arbitrary shape, it can rigorously calculate spherical gratings, and it can also work with conical mountings and non-planar incident waves as well as with a general polarisation state [143]. The optical properties of the surfaces are calculated by means of the integral method [144]. Any optical system can be correctly described by the corresponding Maxwell equations with appropriate boundary conditions which take into consideration both characteristic properties of the radiation source and discontinuities of the electromagnetic field at the interfaces between media components in the system of interest. Then one should remember that physical characteristics (and, in particular, the refractive index) are continuous inside each medium, while at the interfaces sharp changes of these characteristics may occur.
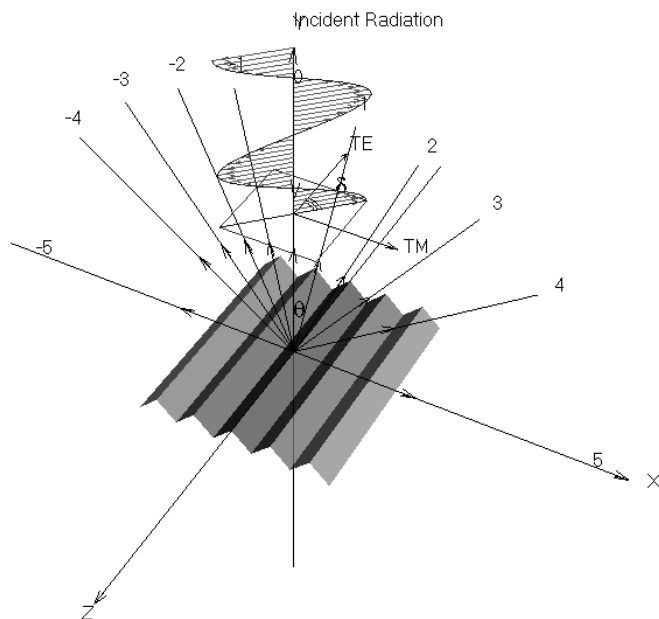
Figure 7.4. *Geometrical characteristics of both the surfaces as well as the incident radiation employed in the numerical calculations.*

Different periods as well as structure depths were evaluated for pure-copper. For the calculation, as input the complex refractive index as function of the wavelength is required. Due to the different composition of the cooper samples used in the experiments (see section 7.1.1.1), the experimental results could not be directly compared with the numerical calculations. Nevertheless, the calculations of the total reflectance as function of the wavelength for different periodical structures will bring important information to understand the described problem.

Fig. 7.4 shows a schema with geometrical characteristics of both the surfaces as well as the incident radiation employed in the numerical calculations. The incident radiation was perpendicular to the surface and no polarised light was used.

The simulated total reflectance in relation to the wavelength of the incident light is shown in Fig. 7.5a. Four different aspect ratios were simulated (0.125, 0.250, 0.375 and 0.500). For the 0.5 aspect ratio case, two different periods (2 and 4 µm) were simulated (Fig. 7.5b). No important differences were observed in the total reflectance for the last two described cases.

(a)

(b)
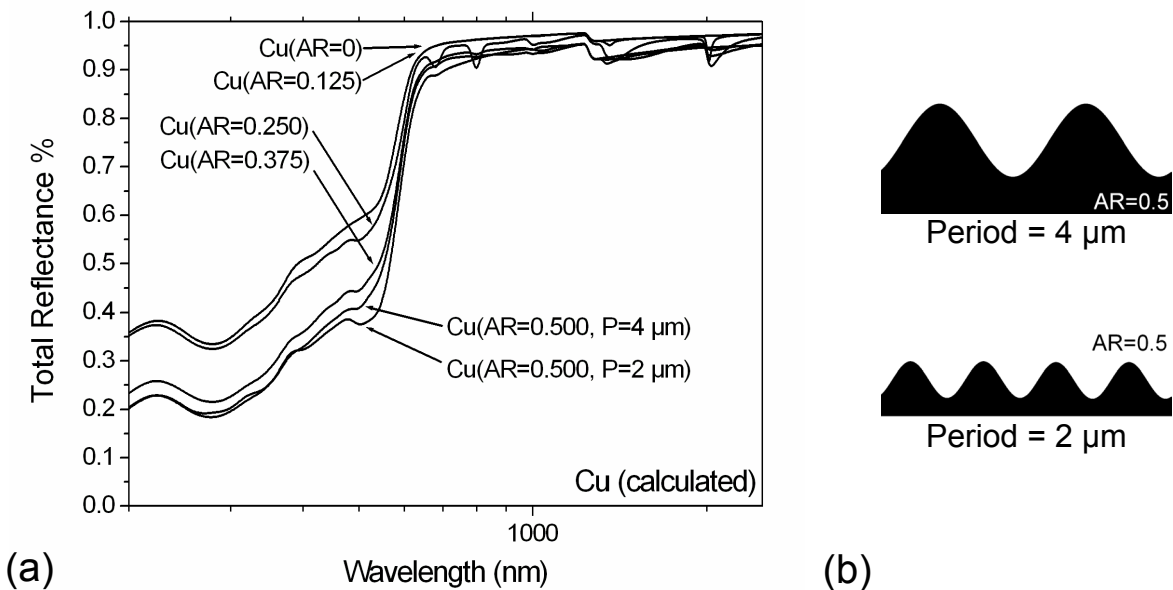
Figure 7.5. *(a) Total spectral reflectance depending on the wave length for different periods and aspect-ratios. (b) Simulated profile with an aspect ratio of 0.5 for periods of 4 and 2 µm. AR: Aspect ratio; P = Period)*

7.1.1.3 Discussion

Measurements carried out on different metals show that the absorbance depends on the structure depth, period and optical properties of the metal.

For example, in Fig. 7.1a it can be seen that the sample Cu2 with a low structure depth (282 nm) does not increase significantly the total absorbance but the diffuse reflectance (Fig. 7.2a). Moreover, although the sample SS2 has practically a two times higher structure depth than the sample SS6 (593 and 344 nm, respectively) the total absorbance is practically the same (see Table 7.1).

It means that the total absorbance of the structured samples does not depend individually upon their periods or structure depth. Similar to [140], it is possible to

define one parameter which resumes both above mentioned characteristic to describe the structured surfaces: the *aspect ratio*.

Comparing the total solar absorbance of the unstructured and the structured samples with the largest aspect ratio in both studied metals, an improvement of about 20 and 15% can be observed in copper and stainless steel, respectively. In the case of multi-pulse experiments, for a fixed period the higher the number of laser pulses, the higher the structure depth. Consequently larger aspect ratios are obtained and thus the total spectral absorbance is increased (see for example samples Cu2, Cu3 and Cu4 in Table 7.1).

The numerical calculations of total reflectance are also in accordance with the experimental observations (Fig. 7.5): the higher the aspect ratio, the better solar absorptance. Moreover, simulated optical properties of copper surfaces, with different periods but the same aspect ratio, show practically the same total solar absorptance.

Spectral properties of line-type periodical structures can be explained by the graded refractive index model [145, 146] as shown in Fig. 7.6. Fresnel reflection is generated mainly by the sharp change of the refractive index at the boundary between the material and its surrounding medium. Therefore, the reflectivity becomes low by changing the effective refractive index gradually.
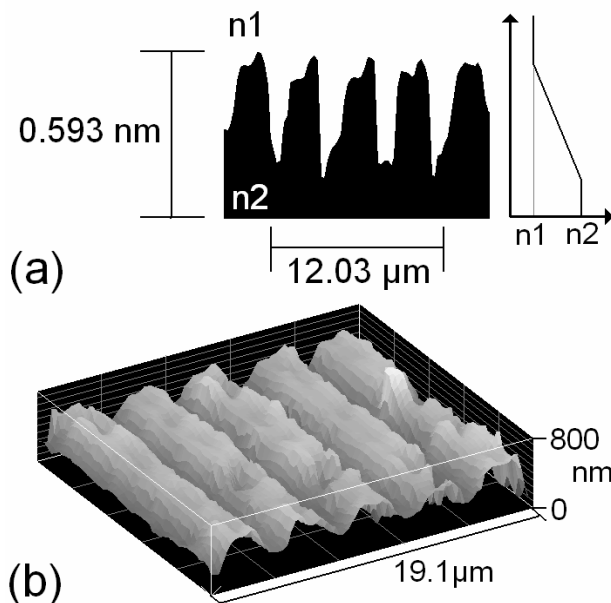
Figure 7.6. (a) Cross-section of sample SS2 (stainless steel) indicating a structure depth of 0.593 μm and a period of 4.01 μm. The refraction index of both metal and air are indicated with n2 and n1, respectively. Because of the periodical structure, the refraction index changes gradually. (b) 2D topography of SS2 sample (White Light Interferometer images).

Measured thermal emittance at room temperature, as shown in Fig. 7.3b, has no important dependence on the aspect ratio of the structured samples. This different optical behaviour is explained by "wave-front discrimination" effect. For visible wavelengths, which are small compared to the actual irregularities, the surface

appears rough and radiation may be trapped trough multiple forward reflection and partial absorption in the micro-cavities. For the thermal infrared radiation, however, the wavelength is larger than the dimension of the surface roughness and the surface will therefore appear smooth and mirror-like and radiates as a flat surface in the long-wave spectrum. Thus, the metal will show its bulk properties of low infrared emittance.

7.1.2 Optical reflectance of structured bi-metallic thin films

A bi-layered Cu(30 nm)/Al(120 nm) sample was irradiated with two laser-beams obtaining a line-type periodical pattern with a grating distance (period) of 2.01 µm. The laser fluence utilised in the interference experiments was 107 mJ/cm² and the structuring process was conducted with local and periodical removal of material at the interference maxima positions (see chapter 6.2).
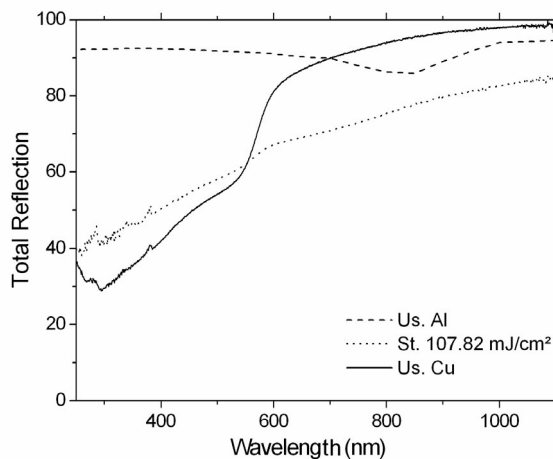
Figure 7.7 *Total reflectance as a function of the wavelength for the structured Cu/Al bi layered sample, and non-irradiated Cu and Al thin metallic films. (Us): unstructured, (St): structured.*

Fig. 7.7 shows the dependence of the total reflectance as function of the wavelength for the studied thin metallic film sample together with the optical characteristics of non-irradiated copper and aluminium film samples. The total reflectance of aluminium is much higher than that of copper principally at wavelength values smaller than 690 nm. The structured sample indicates that at wavelengths smaller than 550 nm, the total reflectance increases compared with the copper sample. For larger wavelengths, the total reflectance of the structured Cu/Al samples is lower than both copper and aluminium film samples. As was mentioned above, the structuring of this sample was conducted with removal of material at the interference maxima. In this topographic regime, the first metallic layer (copper) reaches its melting point resulting in a completely molten bi-layer at the interference maxima.

126

Then, the molten metal moves laterally from the interference maxima towards the minima. Therefore, the new surface of the sample is constituted by a mixture of aluminium, copper and areas without metallic components (the substrate of the sample was glass). Consequently, the observed increase in the total reflectance can be explained as the result of the contribution of both metallic elements (in particular by the aluminium layer with a very high optical reflectance), while the significant drop at wavelength larger than 550 nm can be explained due to the removal of the metallic layer at the interference maxima positions.

7.2. Tribological performance of structured bulk materials

Tribological properties of a system are very important for saving energy or increasing service life as is necessary in automotive industry. It is known that the topography of a solid surface has a significant influence on the friction behaviour and the wear resistance. The performance of a tribological system can be improved by using optimised surface design instead of a perfectly smooth surface [147, 148, 149]. Mate *et.al.* [150] reported on the correlations between topography and friction of lubricated and unlubricated carbon films finding a strong correlation between both parameters. Different texturing processes have been used in the past to produce structured surfaces. These methods consist basically on mechanical processes (polishing, grinding, ultrasonic, machining, etc.) and laser micro-patterning techniques. Particularly, texturing by laser radiation has attracted much interest because laser processing allows producing topographical features on almost any material [149]. The textured surfaces basically consisted of an array of lines or dots with periods between 20 and 200 µm [149, 151-153]. These surfaces were produced with nano- or femtosecond lasers using the direct laser writing technique (see section 2.6). Due to the characteristics of the laser writing method, about 56 h are required for example to produce a line-type structured surface with a period of 10 µm in a surface of 3 x 3 mm² if a beam scanning speed of 30 µm/s is used (this scan speed was taken from [152]). This represents a fundamental disadvantage of the direct laser writing technique compared to laser interference metallurgy (In LIMET 10^{-8} s are required to produce the same periodical structure (see section 2.8)). Due to this reason and based on recent results of tribological test on periodical patterned surfaces [149, 151-154], laser interference metallurgy offers the optimal characteristics to improve the tribological performance of metallic surfaces.

In the following section, preliminary results from ball-on-disk against a steel ball without lubricant are described as example of application.

7.2.1 Results and discussion

In nanotribometry, a flat, a pin or a sphere is loaded onto the test sample with a precisely known force. The pin is mounted on a stiff lever, designed as a frictionless force transducer. The friction coefficient is determined during the test by measuring the deflection of the elastic arm (for further details see section 5.6). The reason for using the nanotribometer tester was that friction measurements performed at low loads are made under wear-less or negligible wear conditions.

Fig. 7.8 shows the frictional performance of the polished and structured stainless steel samples without lubricant. It is obvious, that the structured surfaces by far provide the best performance, i.e. the lowest and constant friction coefficient. Table 7.2 lists the roughness of both the structured and unstructured samples measured using a White Light Interferometer (WLI). Both the three structured samples have similar roughnesses which are extremely large compared to the polished sample. Similar to [155], the reduction in microfriction of the microstructured samples can be explained by the reduction of the true contact area between the surface and the sphere of the tester with increasing the surface roughness. This produces a drop of the friction force and consequently the friction coefficient diminishes.
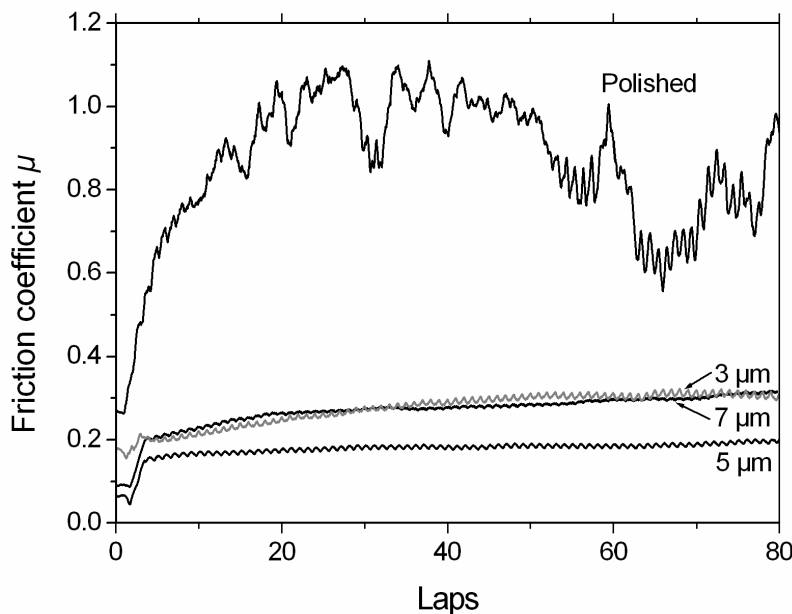
Figure 7.8. *Frictional performance of the polished and the line-type structured surfaces with periods of 3, 7 and 5µm.*

Sample	Roughness rms (µm)	Roughness Ra (µm)
polished	0.031	0.023
3 µm	0.159	0.135
5 µm	0.251	0.217
7 µm	0.240	0.197

Table 7.2. Roughness of the structured and unstructured samples measured using a White Light Interferometer (WLI).

However, it is not clear why the difference between the friction coefficient of the samples structured with 7 and 5 µm of period is produced. Both mentioned samples have a similar surface roughness although the sample structured with 5 µm shows a better performance. One possible explanation could be that independent of the roughness value, the true contact area of the sample structured with 7 µm of period (about 3 µm) is larger than the sample structured with 5 µm as illustrated in Fig. 7.9. Therefore, this would result in a small friction force explaining the experimental results. In the future, a detailed quantitative analysis would be necessary to clarify this result.
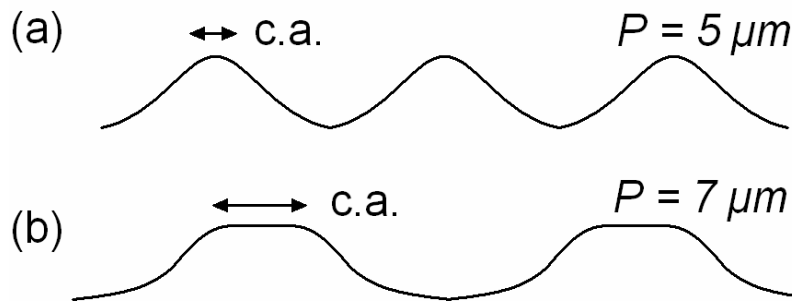
Figure 7.9. *True contact area (c.a.) schema for the case of the samples structured with 5 and 7 µm, respectively.*

Chapter 8

Conclusions and outlook

The laser interference structuring method shows optimal characteristics for the direct processing of various materials. Since plane laser waves are applied, this structuring can proceed for the macroscopic diameters of the laser-beam (mm - cm) and consequently it should allow a fast functionalisation of surfaces with dimensions of technical relevance.

In the present work, different aspects of the "Laser Interference Metallurgy" method were studied.

a) With the aid of the interference theory it was demonstrated that depending on the number of laser-beams, the geometrical arrangement of the beams, and their intensity, many different periodical patterns can be created. For example, two laser-beams produce a line-type pattern while three laser-beams arranged in symmetrical configuration produce a dot-type pattern.

b) The design of advanced patterns has been carried out calculating the solution of the inverse problem. This means that, for a desired periodical pattern, it is possible to establish a configuration of electromagnetic waves that reproduces or at least gives an approximation of the pattern.

c) Due to the photo-thermal interaction of laser light with metals, the produced and calculated interference patterns can be replicated on metallic surfaces obtaining several kinds of surface arrays with a well-defined long-range order. Two situations related to the energy per unit area of the laser-beams can be distinguished. In the first case the relative height of the structure increases at the interference maxima positions. In the second case the opposite is true; at the interference maxima positions the relative height of the structures decreases.

d) Since the behaviour of laser light with metals is relatively well-known, quantitative thermal simulations of the laser interference experiments were developed. In the case of thin metallic film systems, the changes in the topographical types can be explained in terms of the laser fluence which is required to melt or vaporise one or

more of the layers of the film. In the same way such simulations give the opportunity for efficient research of laser interference metallurgy in the future.

e) The in-situ electrical measurements, which describe the thermal history of the samples during the laser-pulse interaction, demonstrated the consistency of the thermal simulations. For metallic thin films, the duration of the whole structuring process is between 400 and 600 ns according to both experimental measurements and the numerical calculations.

Furthermore, the structuring mechanisms in the different studied cases is described. For metallic thin film systems, different configurations related to the number of metallic layers and their relative position in the film were studied.

f) *Single-layer* system: at low laser fluences the structuring mechanism is produced by the permanent deformation of the metallic layer at the interference maxima induced by the local thermal expansion (without melting). Higher laser fluences lead to the melting of the metal and it is removed from the interference maxima positions. The width of the removed areas can be controlled by increasing or decreasing the laser fluence. If the laser fluence is still higher, the metal can be evaporated with a higher removal rate.

For *bi-layered* systems, two different structuring mechanisms were observed depending on the layer configuration.

g) *Bi-layered* systems: metal with the lower melting point at the top: at low laser fluences, the structuring is produced without melting due to permanent deformation of the metallic layer at the interference maxima positions induced by the local thermal expansion. If the laser fluence is increased, the upper layer with the lower melting point is molten and it is removed at the interference maxima due to two cooperative mechanisms which are the local plasma pressure and the surface tension gradient induced by the temperature difference between the interference maxima and minima. However, the lower layer remains in the solid state. Higher fluences permit to melt more metal at the interference maxima and consequently the width of the removed areas increases. At still higher laser fluences, also the second layer is molten resulting in a second transition. In the latter case, the metallic film is completely removed at the interference maxima positions.

h) *Bi-layered* systems: metal with the lower melting point at the bottom: due to the lower melting point of the lower layer, this layer can be molten before the upper one at relative low laser fluences. The molten metal at the interference maxima positions, with a lower density and consequently with a larger volume compared to the metal in the solid state, increases the pressure over the top-layer until it is released by outward deformation. Therefore, in this regime, the structuring is conducted by the

expansion of the molten lower layer at the interference maxima positions. In addition, if the thickness of the lower layer and the difference between the melting points of the metallic layers increases, the maximal structure height which can be obtained in this regime also increases. Moreover, the maximum aspect ratio of the two-dimensional structures (dot-type) was found to be larger than the case of one-dimensional periodical structures and explained due to either two- or one-dimensional flow of molten metal induced by the pressure gradient, respectively.

For higher laser fluence values, the upper layer is heated up to its melting point resulting in a completely molten bi-layer. After that, the molten metal is removed from the interference maxima positions due to the local plasma pressure and the surface tension gradient.

i) The same structuring mechanism could be extended to *multi-layered* samples consisting of more than two different metals located over the substrate according to their melting points (the metal with the lowest melting point is located directly over the substrate, the metal with the second lowest over the previous layer and so on). For a determined laser fluence, this configuration permits to melt both the two lower layers with the lower melting points remaining the upper one in the solid state. Consequently, convective and diffusional processes without removing the metals at the interference maxima positions are possible.

j) EDS analyses of the structured samples have brought valuable information for the interpretation of the layered structure. They permitted the study of the constitutive elements of the film indicating that the intensity of the respective elements of the layer follows their relative thicknesses.

k) In several cases it was demonstrated that the local and periodical heat of the interference pattern can successfully serve to create a phase array in a microstructural scale. In this way, it is possible to transform unordered metallic alloys or films into patterns of intermetallic compounds and a lateral intermetallic-metallic composite. The mixing of the metals which forms the intermetallic phase was in some cases conducted by diffusion processes of liquid in the solid metal. For two-layer systems structured with an energy per unit are sufficient to melt both metallic layers, it was also possible to obtain ordered intermetallic phases but in this case the metal at the interference maxima positions was removed. However, if a third metallic layer is added, this last retains the both lower molten layers at their original position permitting a better local and periodical mixing of the layers due to diffusion and convective processes in the liquid state.

l) The special characteristic of the structuring of bulk materials should be mentioned. In general, few laser pulses and large periods produce more homogeneous structures with characteristic peak-valley topography. For small periods, due to the

large thermal diffusivity of metals, the heat is easier evacuated from the interference maxima toward the interference minima and thus the difference in temperature between this both regions is low. This effect makes difficult to melt the metal only at the interference maxima positions (the same effect is produced in thin metallic film samples) and thus the obtained structures are less homogeneous. Metals with a lower surface tension generate less homogeneous structures at high laser fluences and in some cases particles of molten metal are formed.

Concerning the potential applications of patterned metallic surfaces, two different cases were studied.

m) *Photo-thermal solar absorbers*: spectral properties of the structured samples indicate that the larger the aspect ratio, the better the solar absorbance. Moreover, due to the increase of the surface roughness, the diffuse reflectance also increases, which means that the still retained reflectance is much more diffuse than specular. Due to the small period of the structures, thermal emittance does not increase considerably at room temperature. These observations were also confirmed by numerical calculations based on the Maxwell equations. To increase absorbance to values up to 40-50 %, larger aspect ratios must be achieved and also different pattern-shapes (i.e. periodical dots arrays or nets) should be evaluated. Moreover, the structuring of other low emittance metals like molybdenum or tungsten, which are more stable at higher temperatures and show good intrinsic selectivity, would cause the highest spectral selectivity which tolerates degradation at high temperature. For thin metallic film samples, it was demonstrated that for laser fluence conditions at which both layers are molten and mixed, the optical reflectance at small wavelengths (< 600 nm) is in between the reflectance of both metals. However, at large wavelengths the total reflectance is lower than that of both unstructured metals due to the removal of the metallic layers at the interference maxima positions and the small contribution of the glass substrate.

n) *Tribological properties of line-like periodical structures*: it was verified that surface texturing by laser interference metallurgy is an effective key to friction reduction. The reduction of the friction coefficient is due to the lower true contact area of the patterned surface. Moreover, thanks to the very short time which is required for the surface processing in comparison with other techniques like direct laser writing, the laser interference metallurgy presents ideal characteristic for industrial applications. However, other effects like friction and wear in lubricated surfaces, as well as effect of humidity should be investigated in the future.

List of publications

The following publications were realised in the frame of this PhD thesis.

Publications in refereed journals:

1. A. Lasagni, M. R. Nejati, R. Clasen, F. Mücklich, Periodical surface structuring of metals by Laser Interference Metallurgy as a new fabrication method of textured solar selective absorbers; Adv. Eng. Mat. 8 (2006), 580-584.

2. A. Lasagni, C. Holzapfel, F. Mücklich: Production of two-dimensional periodical structures by laser interference irradiation on metallic thin films, Appl. Surf. Sci. 253 (2006), 1555-1560.

3. A. Lasagni, F. Mücklich: Analysis of Periodical Structures produced by Laser Interference Structuring by Energy Dispersive X-ray Spectrometry; Pract. Met. 43 (2006), 16-29.

4. F. Mücklich, A. Lasagni, C. Daniel: Laser Interference Metallurgy - using interference as a tool for micro/nano structuring; International Journal of Materials Research, 97 (2006), 1337-1344.

5. A. Lasagni, C. Holzapfel, F. Mücklich: Periodic pattern formation of intermetallic phases with long range order by Laser Interference Metallurgy; Adv. Eng. Mater. 7 (2005), 487-492.

6. A. Lasagni, F. Mücklich: Structuring of Metallic bi- and three-Nano Layer Films by laser interference irradiation; Control of the Structure Depth; Appl. Surf. Sci. 247 (2005), 32-37.

7. A. Lasagni, F. Mücklich: Study of the multilayer metallic films topography modified by laser interference irradiation; Appl. Surf. Sci. 240 (2005), 214-221.

8. A. Lasagni, M. Seyler, C. Holzapfel, W. Maier, F. Mücklich: Periodical gratings in mixed oxide films by laser interference irradiation; Adv. Mater. 17 (2005), 2228-2232.

9. F. Mücklich, A. Lasagni, C. Daniel: Laser Interference Metallurgy – Periodic Surface Patterning and Formation of Intermetallics; Intermetallics; 13 (2005), 437-442.

10. C. Daniel, A. Lasagni, F. Mücklich: Stress and texture evolution of Ni/Al multi-film by laser interference irradiation; Surface and Coatings Technology 180 –181 (2004), 478–482.

11. A. Lasagni, C. Holzapfel, T. Weirich, F. Mücklich: Laser Interference Metallurgy: a new method for periodic surface microstructure design on multilayered metallic thin films; Appl. Surf. Sci. (accepted).

12. C. Petersen, A. Lasagni, C. Holzapfel, C. Daniel, F. Mücklich, M. Veith: SEM/TEM characterization of periodical novel amorphous/nanocrystalline micro-composites

obtained by laser interference structuring: The system HAlO-Al·Al$_2$O$_3$; App. Surf. Sci. (accepted).

13. A. Lasagni, D. Acevedo, C. Barbero, F. Mücklich (2006): One-step production of organized surface architectures on polymeric materials by direct laser interference patterning, Advanced Engineering Materials (accepted)

14. D. Acevedo, A. Lasagni, C. Barbero, F. Mücklich (2006): Simple Fabrication Method of Conductive Polymeric Arrays using Direct Laser Interference micro/nano Patterning, Advanced Materials (accepted)

15. A. Lasagni, F. Mücklich: FEM Simulation of periodical local heating caused by Laser Interference Metallurgy; Journal of Materials Processing Technology (submitted).

Publications in other journals and proceedings:

16. A. Lasagni, C. Holzapfel, F. Mücklich: Design and calculation of advanced microstructural patterns by laser interference metallurgy, Proc. Mat. Res. Soc. Symp. 890-Y04, (2006) 02.1-6

17. A. Lasagni, F. Mücklich: Periodical 3-Beams Interference Micro-Structuring of Multilayer Metallic Thin Films; in WDS'04 Proceedings of Contributed Papers: Part III - Physics [f-3], Prague, Matfyzpress (2006), 480-485.

18. A. Lasagni, F. Mücklich: Laser Interference Metallurgy: New Surface properties through advanced microstructure design; in Proceedings of the Junior Scientist Conference, Vienna, Austria, (2006), 151-152.

19. A. Lasagni, F. Mücklich: Structuring of thin metallic films by means of interfering laser beams; in Proceedings of the Jornadas SAM/CONAMET/MEMAT 2005, Mar del Plata, Argentina (2005), ISBN 987-22443-0-8.

20. A. Lasagni, F. Mücklich: Art and science of micro-patterning; In "Revista SAM", ISSN 1668-4788, 1 (2005) 1-17.

21. F. Mücklich, A. Lasagni, C. Daniel: Micro/Nanostructuring with Laser Interference Metallurgy; in: G. Kneringer, P. Rödhammer, H. Wildner (Eds.), Proceedings of the 16th Int. Plansee Seminar (2005), Vol. 2, 144-158.

22. F. Mücklich, C. Daniel, A. Lasagni, Yu F.: Direct Surface Patterning induced by Interfering Laser Beams, Mat. Res. Soc. Symp. Proc. Vol. EXS-2 (2003) M11.1.1.

23. C. Daniel, A. Lasagni, F. Mücklich: Microstructure – Mechanical Properties Relationship of Laser Interference Irradiated Ni/Al Multi-Film; Mat. Res. Soc. Symp. Proc. Vol. 795 (2003) U10.4.1.

References

[1] 506 MRS Bulletin/July 2001.

[2]. X. Xia, Adv. Mater. 16 (2004), 1245.

[3] M. Geissler, X. Xia, Adv. Mater. 16 (2004), 1249.

[4] P. E. J. Legierse, J. H. T. Pasman, in: Polymers in Information Storage Technology, Plenum, New York, 1989, 155.

[5] P. Hoyer, N. Baba, H. Masuda, Appl. Phys. Lett. 66 (1995), 2700.

[6] H. W. Lehmann, R. Widmer, M. Ebnoether, A. Wokaun, M. Meier, S. K. Miller, J. Vac. Sci. Technol. B 1 (1983), 1207.

[7] S. Y. Chou, P. R. Krauss, P. J. Renstrom, Appl. Phys. Lett. 67 (1995), 3114.

[8] H. C. Haverkorn van Rijsewijk, P. E. J. Legierse, G. E. Thomas, Philips Tech. Rev. 40 (1982), 287.

[9] B. D. Terris, H. J. Mamin, M. E. Best, J. A. Logan, D. Rugar, Appl. Phys. Lett. 69 (1996), 4262.

[10] U. Reblan, H. Endert, G. Zaal, Laser Focus World 30 (1994), 91.

[11] D. Kim, S. K. Tripathy, L. Li, J. Kumar, Appl. Phys. Lett, 66 (1995), 1166.

[12] N. L. Abbott, A. Kumar, G. M. Whitesides, Chem. Mater. 6 (1994), 596.

[13] T. J. Hirsch, R. F. Miracky, C. Lin, Appl. Phys. Lett. 57 (1990), 1357.

[14] M. Datta, J. Electrochem. Soc. 142 (1995), 3801.

[15] H. Tabei, S. Nara, K. Matsuyama, J. Electrochem. Soc. 121 (1974), 67.

[16] S. Leppäyuori, J. Väänänen, M. Lothi, J. Remes, A. Uusimäki, Sens. Actuators A 41/42 (1994), 593.

[17] H. Moilanen, J. Lappalainen, S. Leppävuori, Sens. Actuators A 43 (1994), 357.

[18] M. Döring, Philips Tech. Rev. 40 (1982), 192.

[19] A. P. Blanchard, R. J. Kaiser, L. E. Hood, Biosens. Bioelectron. 11 (1996), 687.

[20] M. Stolka, Chemtech 19 (1989), 487.

[21] T. M. Bloomstein,D. J. Ehrlich, Appl. Phys. Lett. 61 (1992), 708.

[22] A. Kumar, G.M. Witesides, Appl. Phys. Lett. 63 (1993), 2002.

[23] Y. Xia, E. Kim, X.-M. Zhao, J. A. Rogers, M. Prentiss, G. M. Whitesides, Science, 273 (1996), 347.

[24] X.-M. Zhao, Y. Xia, G. M. Whitesides, Adv. Mater. 8 (1996), 837.

[25] E. Kim, Y. Xia, G. M. Whitesides, Nature 376 (1995), 581.

[26] E. Kim, Y. Xia, X.-M. Zhao, G. M. Whitesides, Adv. Mater. 9 (1997), 651.

[27] M. Dekker, Microlithography – Science and Technology, Eds: J. R. Sheats, B. W. Smith, New York, 1998.

[28] A. N. Boto, P. Kok, D. S. Abrams, S. L. Braunstein, C. P. Williams, J. P. Dowling, Phys. Rev. Lett. 85 (2000), 2733.

[29] L. Geppert, IEEE Spectrum, 33 (1996), 33.

[30] C. David and A. Souvorov, Review of Scientific Instruments 70 (1999), 4168.

[31] D. Bäuerle, Laser processing and chemistry, second edition, Springer Verlag, Berlin, 1996.

[32] F. Gaboriau, M-C. Peignon, A. Barreau, G. Turban, Ch. Cardinaud, K. Pfeiffer, G. Bleidissel, G. Grützner, Microelectronic Engineering 53 (2000), 501.

[33] S. Chou, P. Krauss, P. J. Renstrom, J. Vac. Sci. Technol. B 14 (1996), 4129.

[34] H. Tan, A. Gilberston, S. Y. Chou, J. Vac. Sci. Technol., B 16 (1998), 3926.

[35] Y. Xia, G. M. Whitesides, Angew. Chem., 37 (1998), 550.

[36] Y. N. Xia, G. M. Whitesides, Annu. Rev. Mater.Sci., 28 (1998), 153.

[37] B. H. Cumpston, S. P. Ananthavel, S. Barlow, D. L. Dyer, J. E. Ehrlich, L. L. Erskine, A. A. Heikal, S. M. Kuebler, I.-Y. S. Lee, D. McCord-Maughon, J. Qin, H. Rockel, M. Rumi, X.-Li Wu, S. R. Marder, J. W. Perry, Nature 398 (1999), 51.

[38] Rachel Jakubiak, Timothy J. Bunning, Richard A. Vaia, Nanotechnology E-Bulletin, 1.1 (2004), 3.

[39] P. Hariharan, Optical Holography: Principles, Techniques, and Applications, 2nd ed., Cambridge University, New York 1996.

[40] I.B. Divliansky, A. Shishido, I. Khoo, T.S. Mayer, D. Pena, S. Nishimura, C.D. Keating, T.E. Mallouk, Appl. Phys. Lett., 79 (2001), 3392.

[41] M. Mützel, S. Tandler, D. Haubrich, D. Meschede, K. Peithmann, M. Flaspöhler, K. Buse, Phys. Rev. Lett, 88 (2002), 083601-1.

[42] J. Hendrik, K. Wielea, P. Simon, Appl. Phys. Lett, 83 (2003), 4707.

[43] A. Shishido, I. B. Diviliansky, I. C. Khoo, T.S. Mayer, S. Nishimura, G.L. Egan, T.E. Mallouk, Appl. Phys. Lett, 79 (2001), 3332.

[44] H. H. Solak, C. David, J. Gobrecht, L. Wang, F. Cerrina, J. Vac. Sci. Technol. B20 (2002), 2844.

[45] Z. Weihua , Z. Gaoyang, C. Zhiming, Materials Science and Engineering B99 (2003), 168.

[46] Y. Ono, K. Ikemoto, Lasers and Electro-Optics, 2001. CLEO/Pacific Rim 2001. The 4th Pacific Rim Conference. vol.2 (2001), II-348.

[47] M. Campell, D. N. Sharp, M. T. Harrison, R. G. Denning, A. J. Turberfield, Nature 404 (2000), 53.

[48] F. Mücklich, A. Lasagni, C. Daniel, Intermetallics 13 (2005), 437.

[49] C. Daniel, F. Mücklich, Wear 257 (2004), 266.

[50] E. Favret, N.O. Fuentes, F. Yu, App. Surf. Sci. 230 (2004), 60.

[51] T. Recktenwald, F. Mücklich, Pract. Met. 40 (2003), 614.

[52] C. Daniel, F. Mücklich, Z. Liu, App. Surf. Sci. 208-209 (2003), 317.

[53] Z. Liu, X.K. Meng, T. Recktenwald, F. Mücklich, Mat. Sci. & Eng. A 342 (2003), 101.

[54] T. Recktenwald, Z. Liu, T. Laurent, F. Mücklich, Pract. Met. 40 (2003), 6, 287.

[55] C. Daniel, F. Mücklich, Appl. Surf. Sci. 242 (2005), 140.

[56] M. Veith, K. Andres, C. Petersen, C. Daniel, C. Holzapfel, F. Mücklich, Adv. Eng. Mat. 7 (2005), 27.

[57] B. Tan, N.R. Sivakumar, K. Venkatakrishnan, J. Opt. A: Pure Appl. Opt. 7 (2005), 169.

[58] M. von Allmen, A. Blatter, Laser-Beam Interactions with Materials, second ed. Springer, Berlin, Germany, 1995.

[59] M.K. Kelly, J. Rogg, C.E. Nebel, M. Stutzmann, Sz. Kátai, Phys. Stat. Sol., 166 (1998), 651.

[60] J. F. Ready, Handbook of Laser Materials Processing, Magnolia Publishing, Inc., Orlando, USA, 2001, pp. 91, 93, 94, 106.

[61] K. Kawamura, T. Ogawa, N. Sarukura, M. Hirano, H. Hosono, Appl. Phys. B 71 (2000), 119.

[62] K. Kawamura, N. Sarukura, M. Hirano, H. Hosono, Japan. J. Appl. Phys. 39 (2000), L767.

[63] K. Venkatakrishnan, N.R. Sivakumar, B. Tan, Appl. Phys. A 76 (2003), 143.

[64] M.K. Kelly, O. Ambacher, B. Dahlheimer, G. Groos, R. Dimitrov, H. Angerer, M. Stutzmann, Appl. Phys. Lett. 69 (1996), 1749.

[65] F. Yu, P. Li, H. Shen, S. Mathur, C.M. Lehr, U. Bokowsky, F. Mücklich, Biomat. 26 (2005), 2307.

[66] P. Li, U. Bakowsky, F. Yu, C. Loehbach, F. Mücklich, and C. M. Lehr, IEEE Trans. on Nanobiosci. 2 (2003), 138.

[67] S. Lazare, R. Srinivasam, J. Phys. Chem. 90 (1986), 2124.

[68] M. Allmen, A. Blatter, Laser-Beam Interactions with Materials, second edition, Springer-Verlag Berlin, Germany, 1998.

[69] P. Drude, Theory of optics, Longmass, Green & Co. Inc, New York, 1922.

[70] F. Wooten, Optical Properties of Solids, Academic Press, New York, 1972.

[71] M. F. Modest, in: J. F. Ready, D. F. Farson (Ed), Handbook of Laser Materials Processing, Magnolia Publishing, Inc., Orlando, USA, 2001, 175.

[72] W. M. Steen, Laser Material Processing, third edition, Springer London Limited, USA, 2003.

[73] T. E. Zavecz, M. A. Saifi, Appl. Phys. Lett. 26 (4), 1975, 165.

[74] S. M. Metev, V. P. Veiko, Laser-Assisted Micro-Technology, second edition, Springer Berlin, Germany, 1998.

[75] J. F. Ready, IEEE J. Quantum Electron 137 (1976), QE-12.

[76] Bergmann, Schaefer: Lehrbuch der Experimentalphysik, Bd. 3 Optik, Ed. Walter de Gruyter, Berlin, 1993.

[77] L. Ang, Y. Lau, R. Gilgenbach, H. Spindler, App. Phys. Lett. 70 (1996), 696.

[78] J. Jackson, Classical Electrodynamics, Wiley, New York, 1990.

[79] J. Cobine, Gaseous conductors, McGrow-Hill, New York, 1941.

[80] Femtosekeunden Technologie, VDI-Technologiezentrum Physikalische Technologien, Düsseldorf, Germany, 1997.

[81] J. Krüger, W. Kautek, Proc. SPIE 2403 (1995), 436.

[82] S. Preuss, A. Demchuk, M. Stuke, Appl. Phys. Lett. A 61 (1995), 436.

[83] B. N. Chickov, C. Momma, S. Nolte, F. von Alvensleben, A. Tünnermann, Appl. Phys. A 63 (1996), 109.

[84] Y. Hirayama, M. Obara, Appl. Surf. Sci. 197-198 (2002), 741.

[85] S. D. Bronson, A. Kazeroonian, J. S. Mooderak, D. W. Face, T. K. Cheng, Phys. Rev. Lett. 64 (1990), 2172.

[86] G. L. Eeslay, Phys. Rev. B, 33 (1986), 2144.

[87] Y. Hiriyama, H. Yabe, M. Obara, J. Appl. Phys. 89 (2001), 2943.

[88] K. Ozono, M. Obara, A. Usui, H. Sunakawa, Opt. Commun. 181 (2001), 103.

[89] A. Semerok, C. Chaléard, V. Detalle, J.-L. Lacour, P. Mauchien, P. Meynadier, C. Nouvellon, B. Sallé, P. Palianov, M. Perdrix, G. Petite, Appl. Surf. Sci. 138-139 (1999), 311.

[90] M. Weingärtner, R. Elschner, O. Bostanjoglo, Appl. Surf. Sci. 138-139 (1998), 449.

[91] P. Mannion., J. Magee, E. Coyne, G. M. O'Connor, Proceedings of SPIE Vol. 4876 (2003), 470.

[92] R.F.W. Hermman, J. Gerlach, E.E.B. Campbell, Appl. Phys. A 66 (1998), 35.

[93] J. Jandeleit, A. Horn, R. Weichenhain, E.W. Kreutz, R. Poprawe, Appl. Surf. Sci. 127-129 (1998), 885.

[94] R. Kelly, A. Miotello, Nucl. Instr. Meth. Phys. Res. B 91 (1994), 682.

[95] C. Daniel, A. Lasagni, F. Mücklich, Surf. and Coat. Technol. 180-181 (2004), 478-482.

[96] M. Mützel, U. Rasbach, D. Meschede, C. Burstedde, J. Braun, A. Kunoth, K. Peithmann, K. Buse, Appl. Phys. B 77 (2003), 1.

[97] U. Drodofsky, J. Stuhler, T. Schulze, M. Drewsen, B. Brezger, T. Pfau, J. Mlynek, Appl. Phys. B 65 (1997), 755.

[98] M. Mützel, D. Meschede, Las. Phys. 15 (2005) 1, 95.

[99] K.J. Petsas, A.B. Coates, G. Grynberg, Phys. Rev. A 50 (1994), 5173.

[100] L. Guidoni, C. Triché, P. Verkerk, G. Grynberg, Phys. Rev. Lett. 79 (1997), 3363.

[101] S. Lipson, H. Lipson, D. Tannhauser, Optik, 3rd edition, Springer, Germnay, 1997, 171.

[102] Flex PDE ^{TM}: "A Flexible solution system for Partial Differential Equations". 1996-2005 PDE Solutions Inc, http://*www.flexpde.com*

[103] S.R. Franklin, R.K. Thareja, Appl. Surf. Sci. 222 (2004), 293.

[104] F. Soldera, A. Lasagni, F. Muecklich, T. Kaiser, K. Hrastnik, Comp. Mater. Sci. 32 (2005), 123.

[105] Gunnar Bäckström, Fields of Physics by Finite Element Analysis, GB Publishing, Malmö, Sweden, 2004.

[106] D. R. Linde (Ed), CRC Handbook of Chemistry and Physics, 74th Edition, CRC Press, Boca Raton, 1993.

[107] T. R. Corle, G. S. Kino: Confocal Scanning Optical Microscopy and Related Imaging Systems, Academic Press, 1996.

[108] Zygo Coorporation Technical Report, http://www.zygo.com

[109] A. Barna, B. Pecz, Ultramicroscopy 70, 1998. Technology, Plenum, New York, 1989, 155.

[110] S.I.-U Ahmed, G. Bregliozzi, H. Haefke, Wear 254 (2003), 1076.

[111] Y. Wei, X. Wang, M. Zhao, J. Mater. Res., 19 (2004), 208.

[112] C. Daniel, A. Lasagni, F. Mücklich, Mater. Res. Soc. Symp. 795 (2004) U10.4.

[113] J.F. Shackelford, Materials Science for Engineers, sixth edition, Person Education International, USA, 2005.

[114] A.D. Romig, in: American Society for Metals, Volume 10, 9th edition, ASM International editorial, USA, 1998, 432.

[115] S. Tamirisakandala, P.V.R.K. Yellapregada, S.C. Medeiros, W.G. Frazier, J.C. Malas, B. Dutta, Adv. Eng. Mater. 5 (2003), 667.

[116] J.H. Westbrook, H. Conrad, The Science of Hardness Testing and Its Research Applications, ASM, Metals Park, Ohio, 1973.

[117] Y. Nakata, T. Okada, M. Maeda, Jpn. J. Appl. Phys. 42 (2003), L1452.

[118] T.R. Anthony, H.E. Cline, J. of App. Phys. 48 (1977), 3888.

[119] S. Yokoya, A. Matsunawa, Trans. JWRI, 16 (1983), 1.

[120] Y. Arata, H. Maruo, I. Miyamoto, S. Tekeuchi, Trans. JWRI 8 (1979), 15.

[121] A. Ruf, D. Breitling, C. Föhl, J. Radtke, F. Dausinger, H. Hügel, T. Kononenko, S. Klimentov, S. Garnov, V. Konov, J. Suzuki, 1st WLT Conference of Laser Man. Proc., Munich (2001), 214.

[122] International Center for Diffraction Data, PDF-No. Al [04-0787], Fe [06-0696], FeAl2 [34-0570], Fe2Al5 [47-1435], Powder Diffraction File, 1998.

[123] A. Bouyad, Ch. Gerometta, A. Belkebir, A. Ambari, Mat. Sci. and Eng. A 363 (2003), 53.

[124] H.G. Jiang, J.Y. Dai, H.Y. Tong, B.Z. Ding, Q.H. Song, Z.Q. Hu, J. Appl. Phys. 74 (1993), 6165.

[125] R. Hultgren, P.D. Desai, D.T. Hawkins, M. Gleiser, K.K. Kelley, Selected values of the thermodynamic properties of binary alloys, first edition, American Society for Metals, Ohio, USA, 1973.

[126] S.M. Pimenov, V.V. Kononenko, E.V. Zavedeev, V.I. Konov, Proceedings of the Sixth Applied Diamond Conference (ADC/FCT 2001), Editors Y. Tzeng, K. Miyoshi, M. Yoshikawa, M. Murakawa, Y. Koga, K. Kobashi, G.A.J. Amaratunga, NASA/CP – 2001-210948, 370.

[127] M. Kass, C.R. Brooks, D. Falcon and D. Basak, Intermetallics, 10 (2002), 951.

[128] E. Stach, V. Radmilovic, D. Deshpande, A. Malshe, D. Alexander, D. Doerr, Appl. Phys. Lett. 83 (2003), 4420.

[129] D. Vouagner, Cs. Beleznaïa, J.P. Girardeau-Montauta, Appl. Surf. Sci. 71 (2001), 288.

[130] D. P. Grimmer, K. C. Kerr and W. J. McCreary, J. Vac. Sci. Technol. 15 (1978) 59.

[131] A. Glen, A. Nyberg, H. G. Craighead, R. A. Buhrman, Thin solid films 96 (1982), 185.

[132] D. M. Mattox, R. R. Sowell, J. Vac. Sci. Technol., 11 (1974), 793.

[133] R. E. Peterson, J. W. Ramsey, J. Vac. Sci. Technol. 12 (1975), 174.

[134] R.T. Kivaisi, L.E. Folrdal, Solar Energy Mater. 2 (1980), 403.

[135] Q. C. Zahng, D. R. Mills, Sol. Ener. Mat. Sol. Cells 27(1992), 723.

[136] B. O. Seraphin, Thin Solid Films 39 (1976), 86.

[137] B. O. Seraphin, Thin Solid Films, 57 (1979), 293.

[138] G. Pellegrini, Sol. Ener. Mater. 3 (1980), 391.

[139] K. G. T. Hollands, Sol. Ener. 7 (1963), 108.

[140] R. T. Kivaisi, L. Stensland, Appl. Phys. A 27 (1982), 233.

[141] H. Sai, H. Yugami, Y. Kanamori, K. Hane, Sol. Ener. Mat. Sol. Cells, 79 (2003), 35.

[142] J. A. Duffie, W. A. Beckman, Solar Engineering of Thermal Processes, second ed., Wiley, London, 1991.

[143] http://www.pcgrate.com/

[144] R. Petit, Electromagnetic Theory of Gratings, Springer, Berlin, 1980.

[145] Y. Kanamori, K-I Kobayashi, H. Yugami, K. Hane, Jpn. J. Appl. Phys. 42 (2003), 4020.

[146] S. J. Wilson, M. C. Hutley, Opt. Acta 29 (1982), 993.

[147] F. Klocke, O. Auer, A. Zaboklicki, VDI (ed.), VDI-Report 1331, Düsseldorf, 1997, 343.

[148] A. Hopperman, M. Kordt, Oellhydraulik und Pneumatik 46 (2002), 560.

[149] S. Schreck, K.-H. Zum Gahr, App. Surf. Sci. 247, (2005), 616.

[150] C.M. Mate, Surf. Coat. Technol. 62 (1993), 373.

[151] G. Dumitru, V. Romano, Y. Gerbig, H.P. Weber, H. Haefke, Appl. Phys. A 80 (2005), 283.

[152] A. Blatter, M. Maillat, S.M. Pimenov, G.A. Shafeev, A.V. Simakin, Trib. Lett., 4 (1998), 237.

[153] A. Kovalchenko, O. Ajayi, A. Erdemir, G. Fenske, I. Etsion, Trib. International 38 (2005), 219.

[154] A. Erdemir, Trib. International, 38 (2005), 249.

[155] W. Hild, G. Hungenbach, J.A. Schaefer, M. Fischer, S. I.-U. Ahmed, M. Scherge, Mat.-wiss. U. Werkstofftech, 35 (2004), 626.

[156] Righini, G.C., Opelli, S., Journal Sol-Gel Sci. and Technol. 8 (1997), 991.

[157] M. He, X.-C. Yuan, N. Q. Ngo, N. Q., J. Bu, S. H. Tao, Journal of Optics A: Pure and Appl. Optics 6 (2004), 94.

[158] K. Jähnisch, V. Hessel, H. Löwe, M. Baerns, Angew. Chem. 116 (2004), 410.

[159] S. Thybo, S. Jensen, J. Johansen, T. Johannessen, O. Hansen, U. J. Quaade, .J. Catal. 223 (2004), 271.

[160] E. W. Bohannan, X. Gao, K.R. Gaston, C.D. Doss, C. Sotiriou-Leventis, N. Leventis, J. Sol-Gel Sci. Technol. 23 (2002), 235.

[161] S. Ono, S. Hirano, J. Am. Ceram. Soc. 80 (1997), 2533.

[162] D. Blanc, S. Pelissier, Thin Solid Films 384 (2001), 251.

[163] Z. Jiwei, Z., Z. Liangying, Y. Xi, S. N. Hodgson, Surf. Coat. Technol. 138 (2001), 135.

[164] K. J. Ilcisin, R. Fedosejevs, Appl. Opt., 1987, 26, 396.

[165] H. M. Phillips, D. L. Callahan, R. Sauerbrey, G. Szabó, Z. Bor, Appl. Phys. Lett. 58 (1991), 2761.

[166] H. Fukumura, H. Uji-i, H. Banjo, H. Masuhara, D. M. Karnakis, N. Ichinose, S. Kawanishi, K. Uchida, M. Irie, Appl. Surf. Sci. 127 (1998), 761.

[167] S. Shoji, S. Kawata, Appl. Phys. Lett. 76 (2004), 2668.

[168] W. Yu, X.-C Yuan, Optics Express 11 (2003), 1925.

[169] S. Klein, S. Thorimbert, W.F. Maier, J. Catal. 163 (1996), 476.

[170] Y. Deng, W. F. Maier, J. Catal. 199 (2001), 115.

[171] International Center for Diffraction Data, PDF-No. TiO_2 [84-1284], SiO_2 [83-0541], Powder Diffraction File, 1998.

Appendix 1

Examples of possible interference patterns

The orientation and intensity of each partial beam is considered as it was explained in chapter 4 (Eq. 4.1, 4.2, and Fig. 4.1). Following, different interference patterns for 3 and 4 beams are calculated.

A1.1- Three laser beams

Case A1.1.1

$E_{10} = E_{20} = 1$; $E_{30} = 0.5$

$\alpha_1 = \alpha_2 = \alpha_3 = 0.05$ rad

$\lambda = 266$ nm

$\beta_1 = 0$; $\beta_2 = 2\pi/3$; $\beta_3 = -2\pi/3$
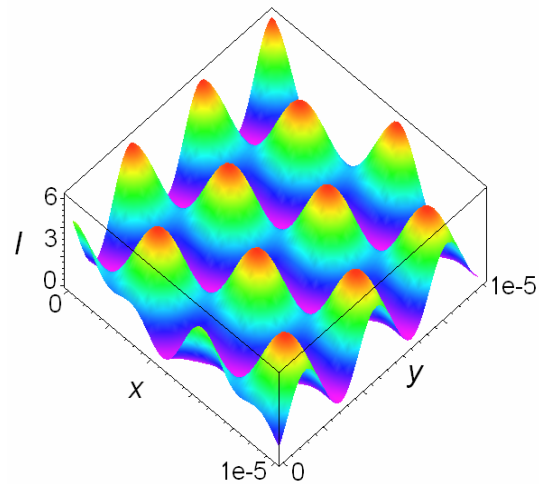
Case A1.1.2

$E_{10} = E_{20} = 1$; $E_{30} = 0.2$

$\alpha_1 = \alpha_2 = \alpha_3 = 0.05$ rad

$\lambda = 266$ nm

$\beta_1 = 0$; $\beta_2 = 2\pi/3$; $\beta_3 = -2\pi/3$

Case A1.1.3

$E_{10} = E_{20} = E_{30} = 1$

$\alpha_1 = \alpha_2 = \alpha_3 = 0.05$ rad

$\lambda = 266$ nm

$\beta_1 = 0$; $\beta_2 = \pi/2$; $\beta_3 = -\pi/2$

Case A1.1.4

$E_{10} = E_{20} = E_{30} = 1$

$\alpha_1 = \alpha_2 = \alpha_3 = 0.05$ rad
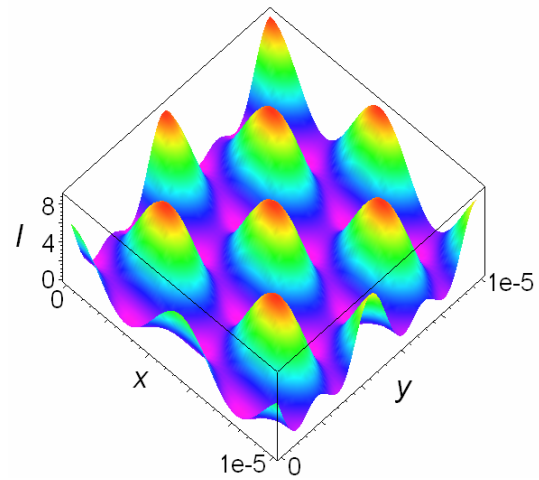
$\lambda = 266$ nm

$\beta_1 = 0$; $\beta_2 = \pi/2$; $\beta_3 = -\pi$

Case A1.1.5

$E_{10} = E_{20} = E_{30} = 1$

$\alpha_1 = \alpha_2 = \alpha_3 = 0.08$ rad

$\lambda = 266$ nm

$\beta_1 = 0$; $\beta_2 = 2\pi/3$; $\beta_3 = \pi/2$
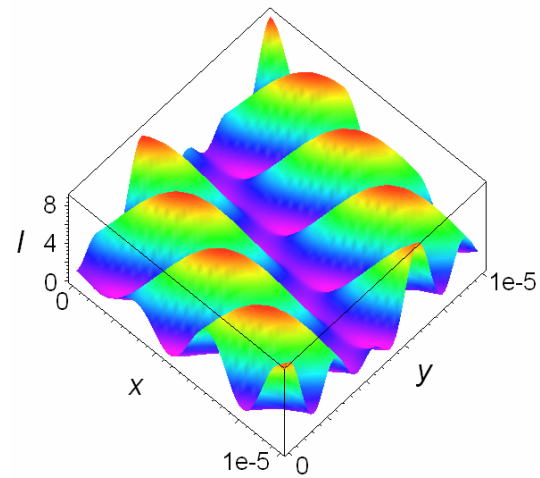
A1.2- Four laser beams
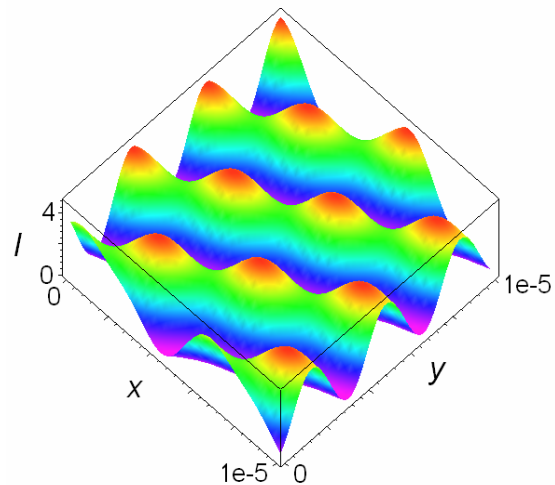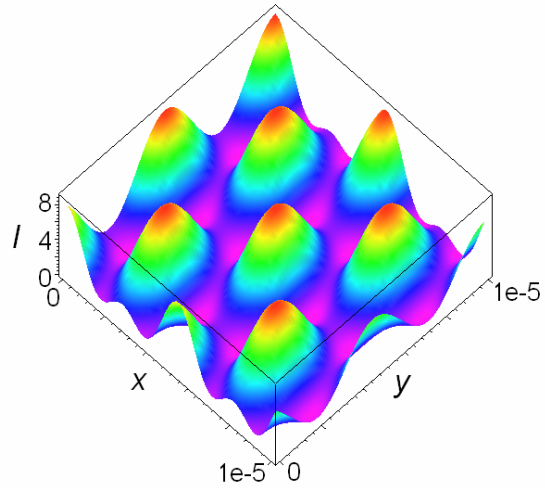
Case A1.2.1

$E_{10} = E_{20} = E_{30} = E_{40} = 1$

$\alpha_1 = \alpha_2 = \alpha_3 = \alpha_4 = 0.05$ rad

$\lambda = 266$ nm

$\beta_1 = 0$; $\beta_2 = \pi/2$; $\beta_3 = \pi$; $\beta_4 = 3\pi/2$

Case A1.2.2

$E_{10} = 0.5$; $E_{20} = E_{30} = E_{40} = 1$

$\alpha_1 = \alpha_2 = \alpha_3 = \alpha_4 = 0.05$ rad

$\lambda = 266$ nm

$\beta_1 = 0$; $\beta_2 = 2\pi/3$; $\beta_3 = -2\pi/3$; $\beta_4 = 0$
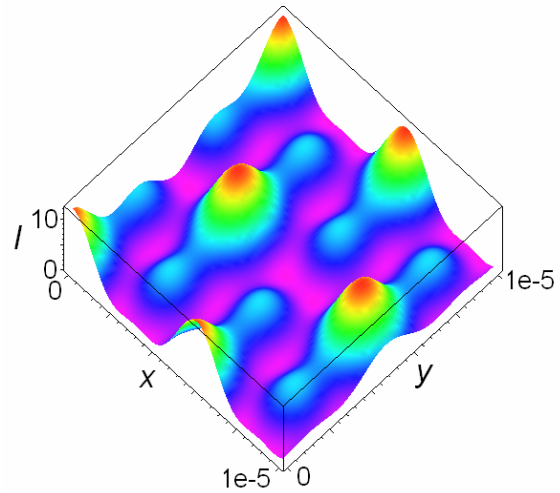
Case A1.2.3

$E_{10} = E_{20} = E_{30} = E_{40} = 1$

$\alpha_1 = \alpha_2 = \alpha_3 = \alpha_4 = 0.05$ rad

$\lambda = 266$ nm

$\beta_1 = 0$; $\beta_2 = 2\pi/3$; $\beta_3 = -2\pi/3$; $\beta_4 = -\pi$
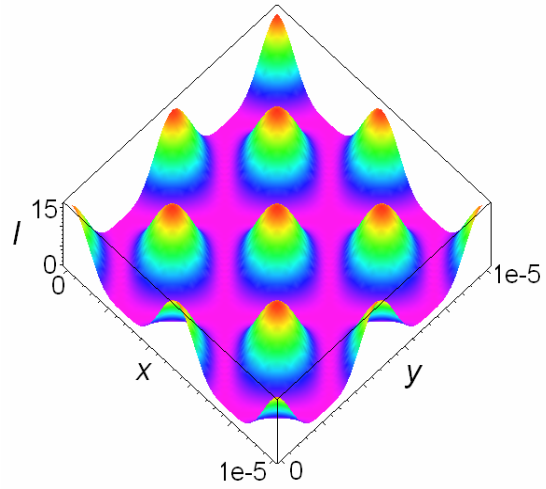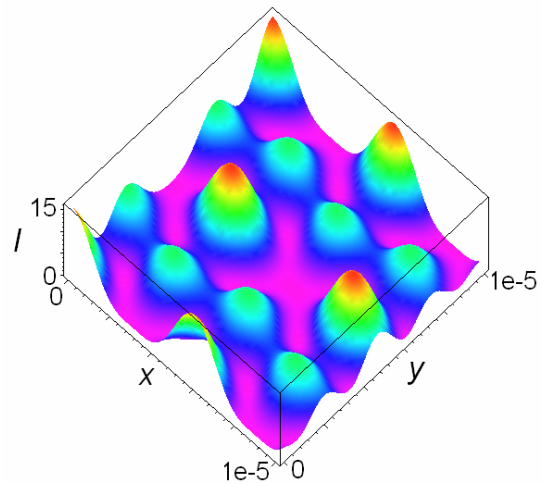
Appendix 2

The inverse problem

Different examples of the solution of the inverse problem are given in this appendix. Each example presents the desired periodical structure, the two-dimensional Fourier transform, the calculated wave-vectors and its correspondent interference pattern.

(a)

(b)

Desired period: 2 µm
Required laser beams: 2
Wavelength (λ): 266 nm

Calculated Angles (rad):

$\beta_1 = \pi$
$\beta_2 = 0$
$\alpha_1 = 0.064$
$\alpha_2 = 0.064$

(c)
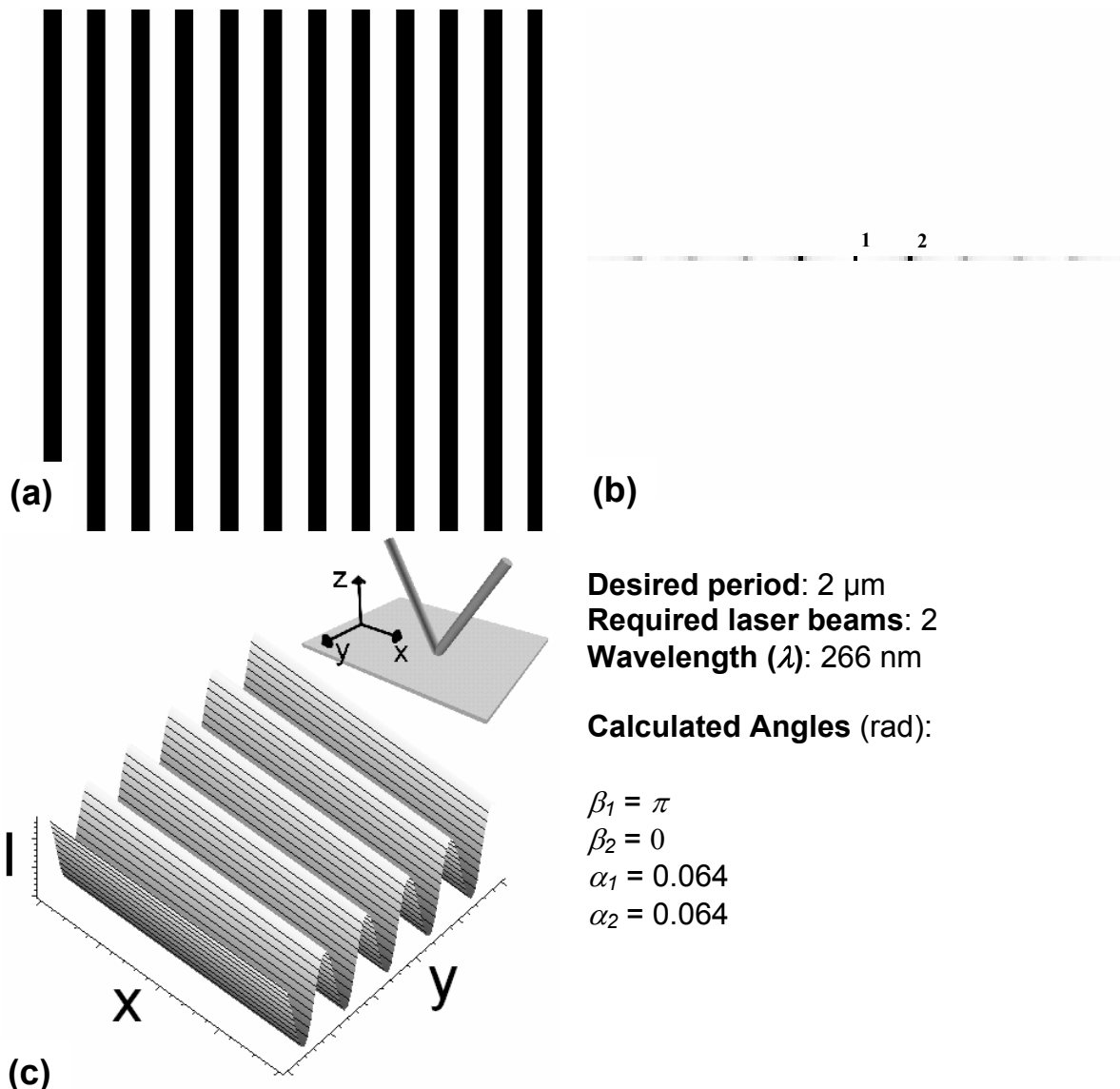
Figure A.3.1 *(a) Desired periodical structure. (b) 2D-Fourier transformation of (a). The wave vectors considered to solve the inverse problem are indicated with the numbers 1 and 2. (c) Calculated interference pattern by using the wave vectors shown in the insert of (c).*

Desired period: 7 μm
Required laser beams: 3
Wavelength (λ): 266 nm

Calculated Angles (rad):

β_1 = -2/3 π
β_2 = 0
β_3 = 2/3 π
α_1 = 0.025
α_2 = 0.025
α_3 = 0.025
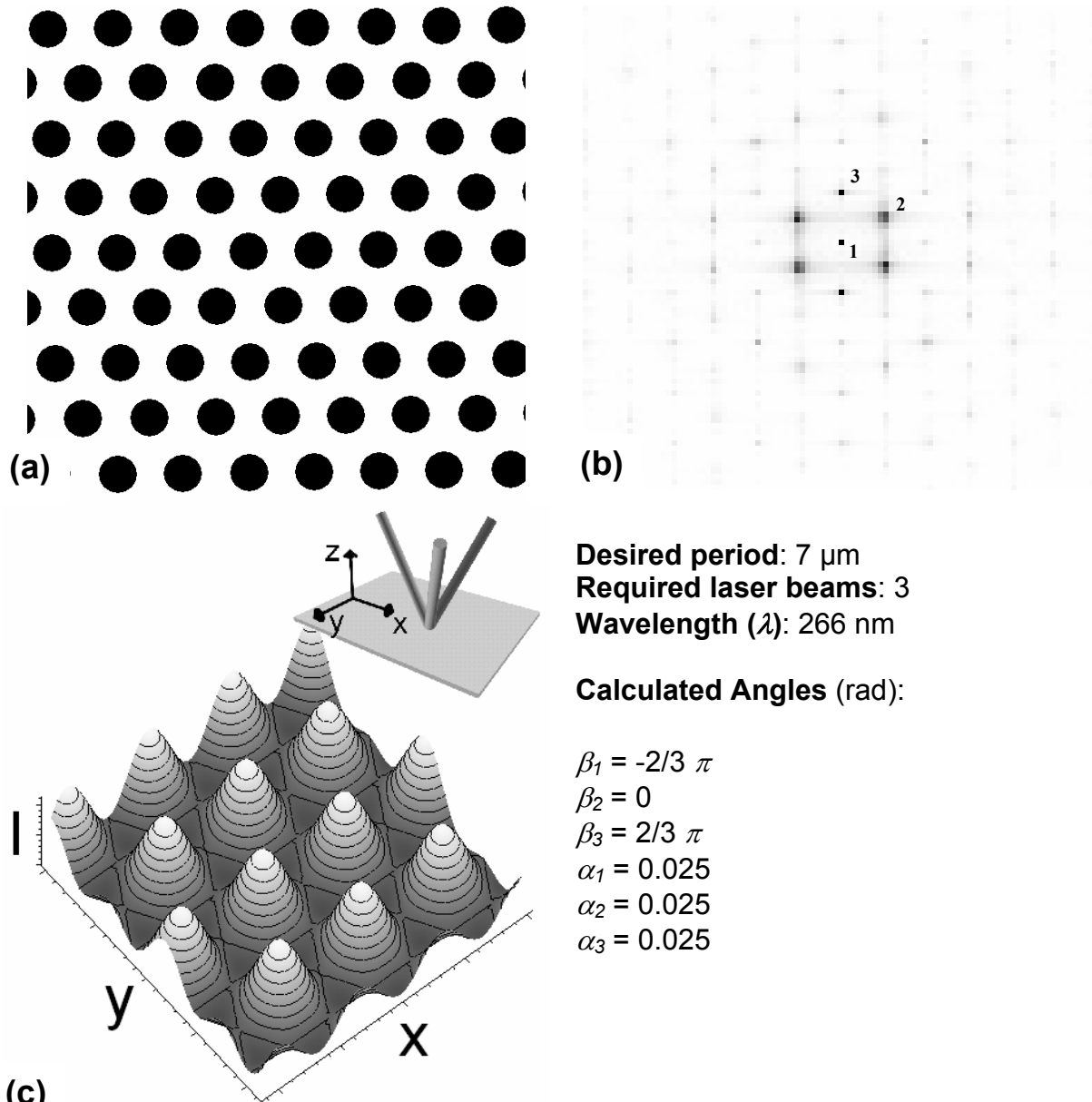
Figure A.3.2 (a) Desired periodical structure. (b) 2D-Fourier transform of (a). The wave-vectors considered to solve the inverse problem are indicated with the numbers 1, 2 and 3. (c) Calculated interference pattern by using the wave-vectors shown in the insert of (c).

(a)

(b)

Desired period: 4 µm
Required laser beams: 4
Wavelength (λ): 266 nm

Calculated Angles (rad):

β_1 = -3/4 π
β_2 = -1/4 π
β_3 = 1/4 π
β_4 = 3/4 π
α_1 = 0.047
α_2 = 0.047
α_3 = 0.047
α_4 = 0.047

(c)
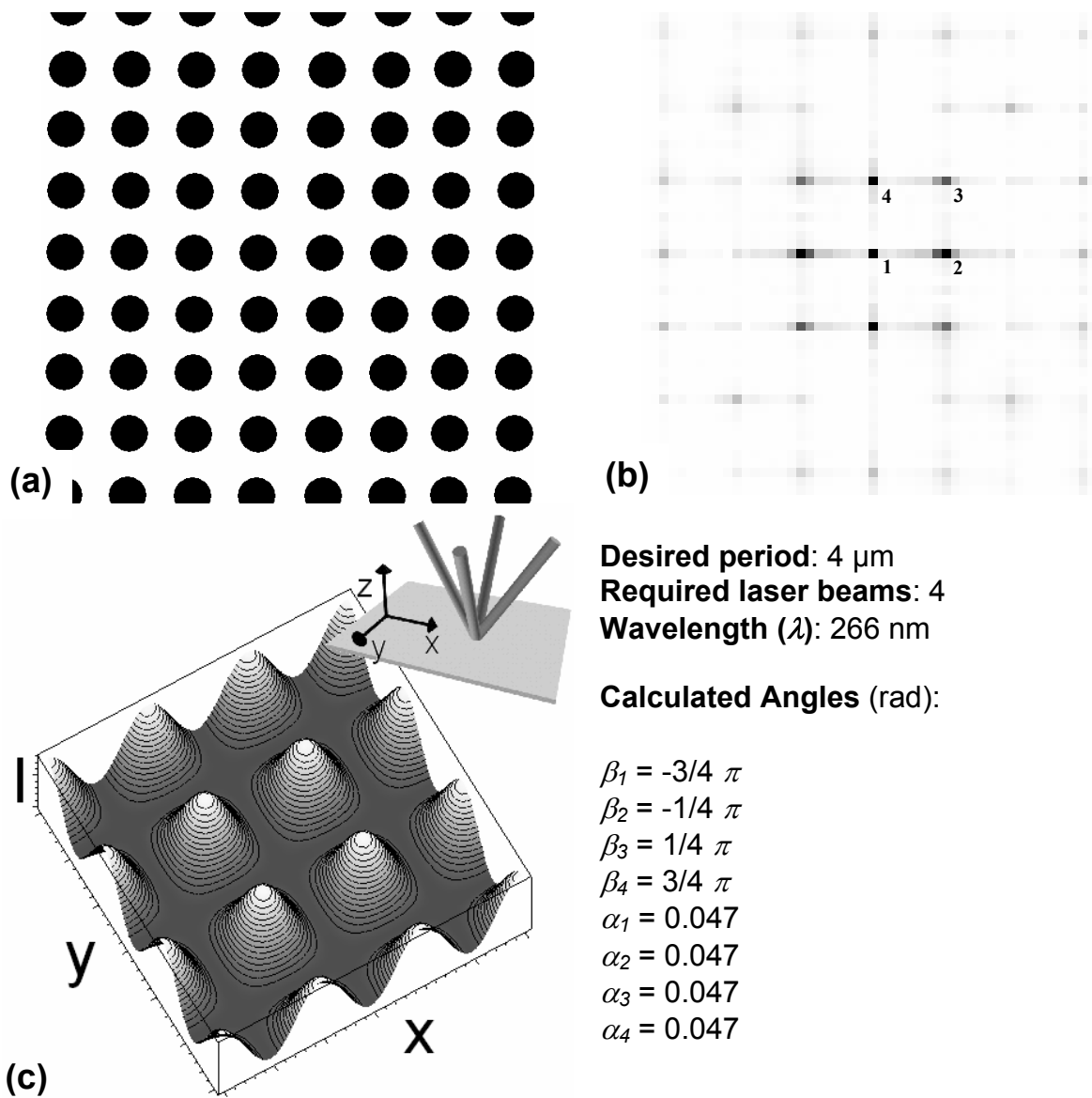
Figure A.3.3 *(a) Desired periodical structure. (b) 2D-Fourier transform of (a). The wave-vectors considered to solve the inverse problem are indicated with the numbers 1, 2, 3 and 4. (c) Calculated interference pattern by using the wave-vectors indicated in the insert of (c).*

153

(a)

(b)

(c)

Desired period: 5 µm
Required laser beams: 4
Wavelength (λ): 266 nm

Calculated Angles (rad):

$\beta_1 = 0$
$\beta_2 = -2/3\ \pi$
$\beta_3 = 2/3\ \pi$
$\beta_4 = 0$
$\alpha_1 = 0.060$
$\alpha_2 = 0.060$
$\alpha_3 = 0.060$
$\alpha_4 = 0$

Figure A.3.4 *(a) Desired periodical structure.(b) 2D-Fourier transform of (a). The wave-vectors considered to solve the inverse problem are indicated with the numbers 1, 2, 3 and 4.Note that the intensity of point (4) is weaker than (1-3). (c) Calculated interference pattern by using the wave-vectors indicated in the insert of (c). By changing the intensity of (4) it is possible to control the height of the central peak.*

Desired period: 5 µm
Required laser beams: 5
Wavelength (λ): 266 nm

Calculated Angles (rad):
β_1 = -3/4 π
β_2 = -1/4 π
β_3 = 1/4 π
β_4 = 2/4 π
β_5 = 0
α_1 = 0.076
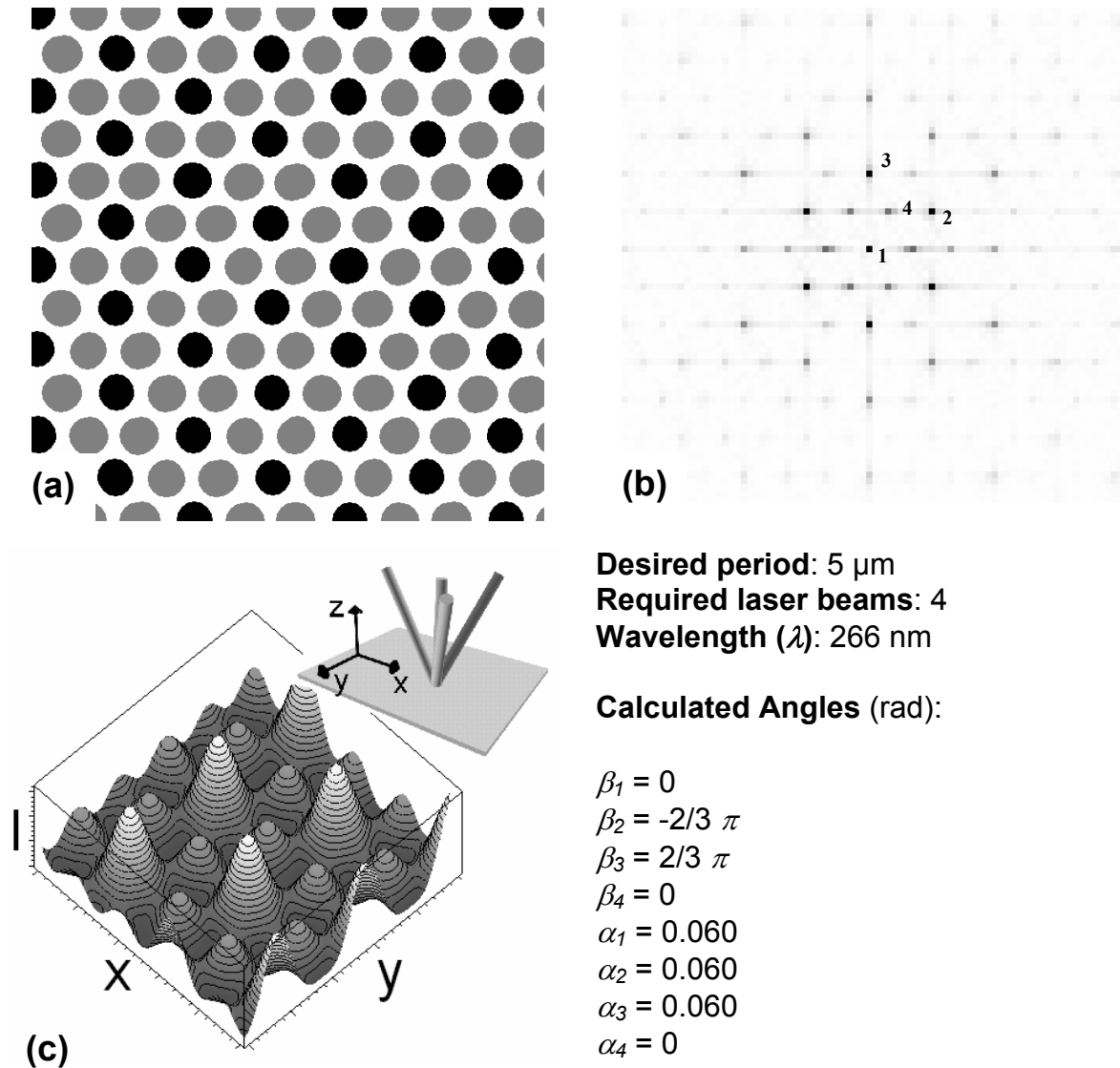α_2 = 0.076
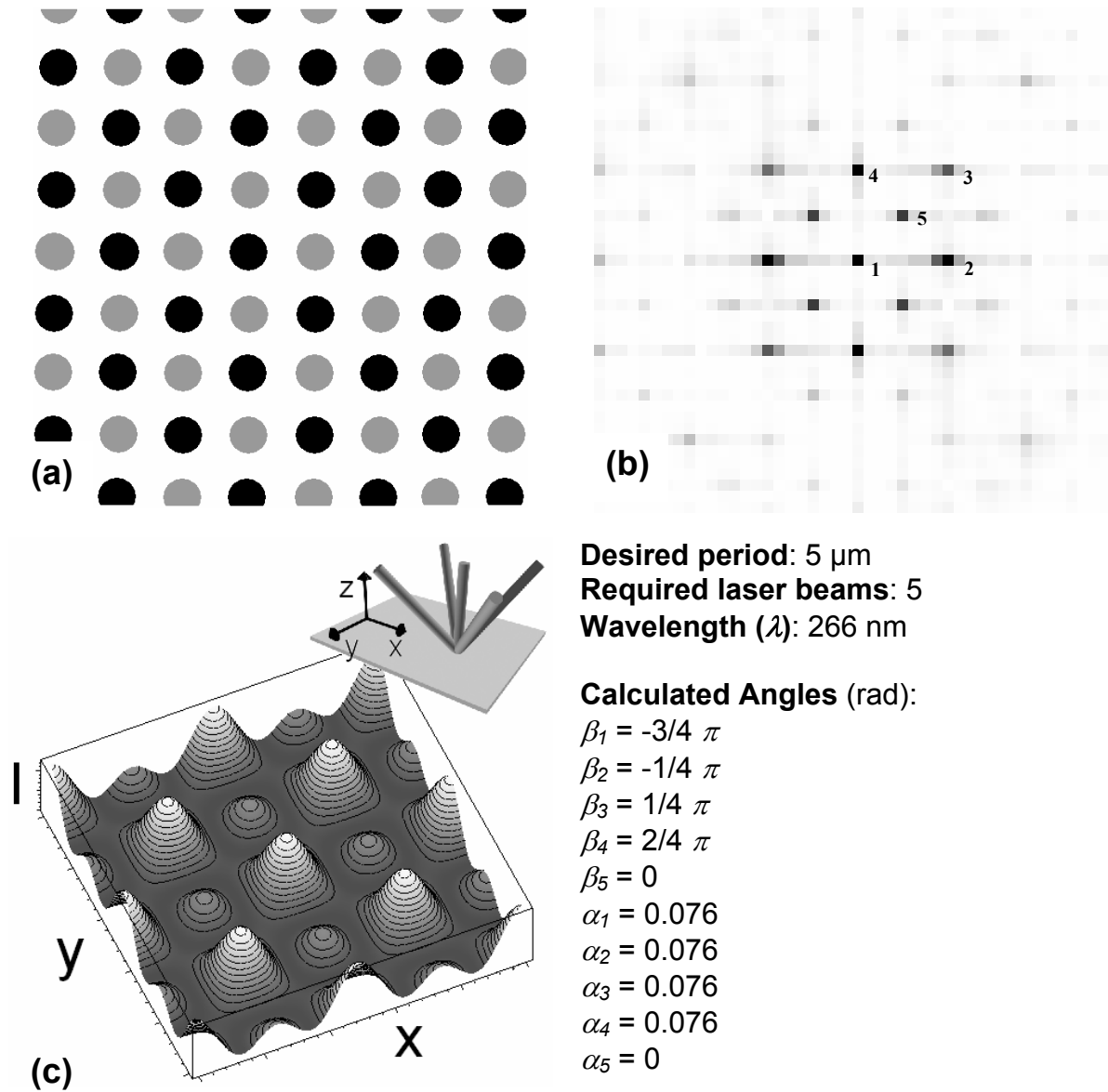α_3 = 0.076
α_4 = 0.076
α_5 = 0

Figure A.3.5 *(a) Desired periodical structure.(b) 2D-Fourier transform of (a). The wave-vectors considered to solve the inverse problem are indicated with the numbers 1, 2, 3, 4 and 5. (c) Calculated interference pattern by using the wave-vectors indicated in the insert of (c).*

Desired period: 2.5 µm
Required laser beams: 6
Wavelength (λ): 266 nm

Calculated Angles (rad):
$\beta_1 = 4/3\ \pi$
$\beta_2 = -1/3\ \pi$
$\beta_3 = -1/2\ \pi$
$\beta_4 = 1/2\ \pi$
$\beta_5 = 1/3\ \pi$
$\beta_6 = 2/3\ \pi$
$\alpha_1 = 0.043$
$\alpha_2 = 0.043$
$\alpha_3 = 0.129$
$\alpha_4 = 0.129$
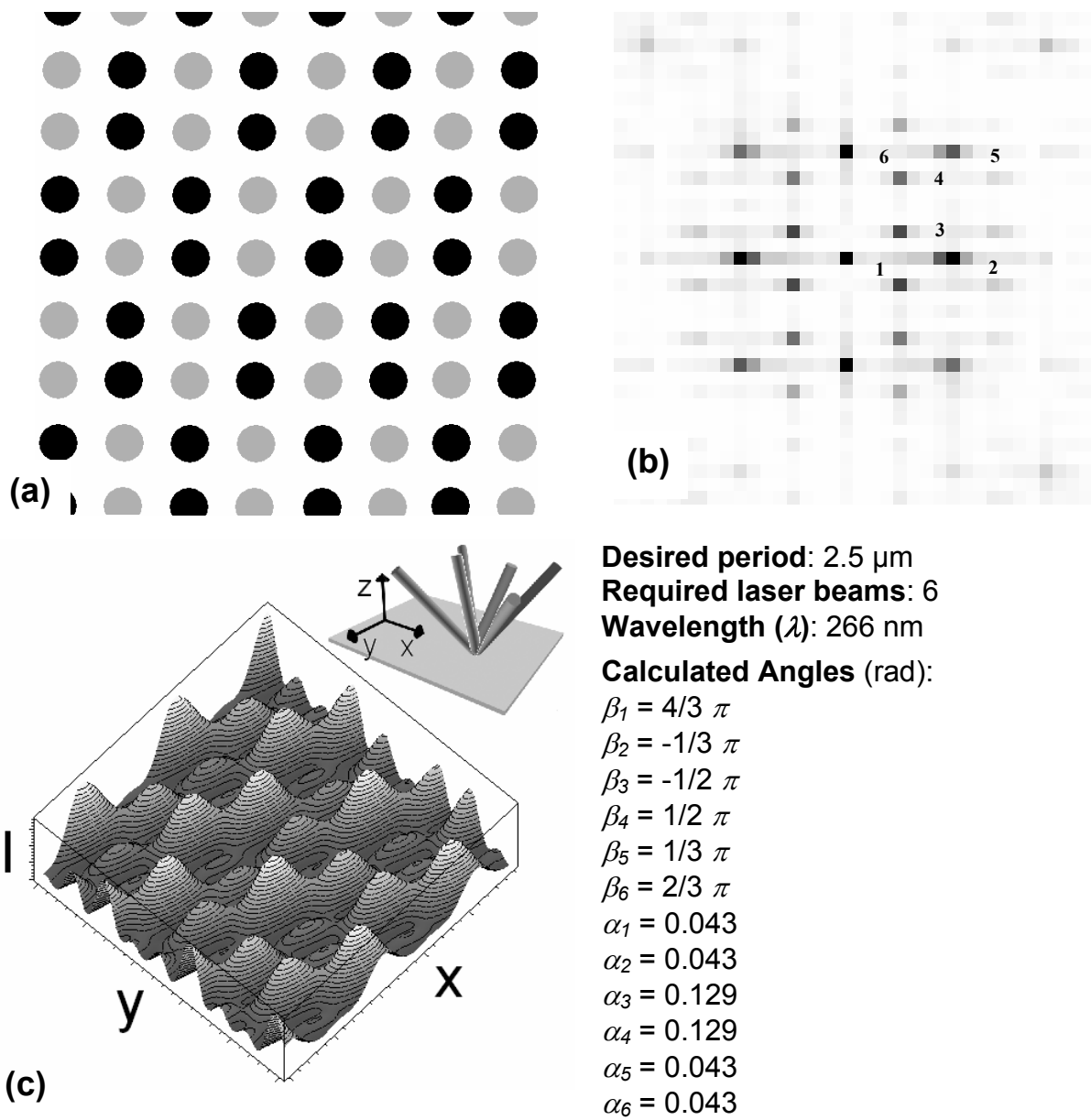$\alpha_5 = 0.043$
$\alpha_6 = 0.043$

Figure A.3.6 *(a) Desired periodical structure.(b) 2D-Fourier transform of (a). The wave-vectors considered to solve the inverse problem are indicated with the numbers 1, 2, 3, 4, 5 and 6. (c) Calculated interference pattern by using the wave-vectors indicated in the insert of (c).*

Appendix 3

Properties of metals

A3.1- Aluminium (Al)

Property		Symbol	Value
Melting Point		T_m (K)	934
Boiling Point		T_b (K)	2792
Latent heat of melting		L_m (J/g)	397
Latent heat of vaporization		L_b (J/g)	10860
Thermal conductivity	(solid)	k (W/mK)	$186.02+0.3271.T-0.0006.T^2+ 3E\text{-}7.T^3$
	(liquid)		237 (at T_m)
Specific heat	(solid)	c_p (J/g.K)	$0.1552.(4.94+2.96E\text{-}3.T)$
	(liquid)		1.086 (at T_m)
Density	(solid)	ρ (g/m³)	2.7E6
	(liquid)		$(2.365-(3.2E\text{-}4).(T-T_m)).1E6$
Reflectivity		r	0.935 (at λ = 266 nm)
			0.9245 (at λ = 355 nm)
Absorption coefficient		α (m^{-1})	1E8 (at λ = 266 nm)
			1.1E8 (at λ = 355 nm)

A3.2- Copper (Cu)

Property		Symbol	Value
Melting Point		T_m (K)	1357
Boiling Point		T_b (K)	2840
Latent heat of melting		L_m (J/g)	208.7
Latent heat of vaporization		L_b (J/g)	4721
Thermal conductivity	(solid)	k (W/mK)	$424.29-0.0801.T+8E\text{-}6.T^2$
	(liquid)		401 (at T_m)
Specific heat	(solid)	c_p (J/g.K)	$0.06589.(5.41+(1.4E\text{-}3).T)$
	(liquid)		0.494 (at T_m)
Density	(solid)	ρ (g/m³)	8.92E6
	(liquid)		$(7.94-(8.05E\text{-}4).(T-T_m)).1E6$
Reflectivity		r	0.334 (at λ = 266 nm)
			0.434 (at λ = 355 nm)
Absorption coefficient		α (m^{-1})	1.2E7 (at λ = 266 nm)
			1.5E7 (at λ = 355 nm)

A3.3- Iron (Fe)

Property		Symbol	Value
Melting Point		T_m (K)	1811
Boiling Point		T_b (K)	3134
Latent heat of melting		L_m (J/g)	247.3
Latent heat of vaporization		L_b (J/g)	6214
Thermal conductivity	(solid)	k (W/mK)	$-0.0000000120.T^3+0.0000823.T^2 - 0.156.T + 120.22$
	(liquid)		80.2 (at T_m)
Specific heat	(solid)	c_p (J/g.K)	$0.0750.(8.873+(1.474E\text{-}3).T -56.92.T^{-0.5})$
	(liquid)		0.750 (at T_m)
Density	(solid)	ρ (g/m³)	7.87E6
	(liquid)		$(7.08-(6.338E\text{-}4).(T\text{-}T_m)).1E6$
Reflectivity		r	0.470 (at λ = 266 nm)
			0.556 (at λ = 355 nm)
Absorption coefficient		α (m^{-1})	0.95E7 (at λ = 266 nm)
			0.97E7 (at λ = 355 nm)

A3.4- Nickel (Ni)

Property		Symbol	Value
Melting Point		T_m (K)	1728
Boiling Point		T_b (K)	3003
Latent heat of melting		L_m (J/g)	298
Latent heat of vaporization		L_b (J/g)	6440
Thermal conductivity	(solid)	k (W/mK)	$0.00008.T^2 - 0.1384.T + 125.78$
	(liquid)		85.0 (at T_m)
Specific heat	(solid)	c_p (J/g.K)	$0.0713.(6+1.8E\text{-}3.T)$
	(liquid)		0.656 (at T_m)
Density	(solid)	ρ (g/m³)	8.91E6
	(liquid)		$(7.81- 8.33E\text{-}4 (T\text{-}T_m)).1E6$
Reflectivity		r	0.421 (at λ = 266 nm)
			0.428 (at λ = 355 nm)
Absorption coefficient		α (m^{-1})	1.0E7 (at λ = 266 nm)
			0.95E7 (at λ = 355 nm)

A3.5- Titanium (Ti)

Property		Symbol	Value
Melting Point		T_m (K)	1941
Boiling Point		T_b (K)	3560
Latent heat of melting		L_m (J/g)	295
Latent heat of vaporization		L_b (J/g)	8895
Thermal conductivity	(solid)	k (W/mK)	$-0.000000081.T^3 + 0.00032.T^2 - 0.33.T + 292.7$
	(liquid)		229 (at T_m)
Specific heat	(solid)	c_p (J/g.K)	$-0.00000011.T^2 + 0.00032.T + 0.441$
	(liquid)		0.52 (at T_m)
Density	(solid)	ρ (g/m³)	4.51E6
	(liquid)		$(4.11 - 6.99E\text{-}4.(T\text{-}T_m)).1E6$
Reflectivity		r	0.265 (at λ = 266 nm)
			0.350 (at λ = 355 nm)
Absorption coefficient		α (m^{-1})	1E7 (at λ = 266 nm)
			1.3E7 (at λ = 355 nm)

Appendix 4

Production of periodical gratings in mixed oxide films

Micro- and submicro-structured mixed oxides are important materials in the fields of optical waveguides [156] and micro-optics elements [157]. In the field of heterogeneous catalysis related to air and exhaust gas cleaning or gas phase reactions, effective mass transport between catalytically active thin films and the fast flowing gas phase in monolithic catalysts is crucial. Micro-structuring of the thin films can significantly improve mass and heat transfer, as already shown in microreaction technology [158]. In these reactors catalysts are usually present as thin films supported on micro-structured modules.

Physical Methods for patterning and structuring materials can be divided into single-step and multi-step techniques. The most well-known multi-step procedures are masking techniques [159] and photolithography [160, 161]. All these methods require the time-consuming fabrication of a hardware mask and thus lack flexibility. Single-Step techniques include direct laser-writing and mask-free structuring of materials by irradiation with interfering laser beams [11] through the interaction of matter with the electromagnetic energy via the photo-thermal, photo-chemical or photo-physical effect [31, 68]. Direct laser writing has found applications in the fabrication of microlens arrays, [157] the production of waveguides and optical gratings [162] and the spatially resolved densification of ceramic materials [163]. Mask-free interference patterning method [11] permits the direct material surface modification in a single step procedure[59, 164-167]. This last technique has been widely used in structuring metals as e.g. to enhance the wear behaviour of electrical contacts [112] or in polymers to induce directional cell growth in patterned collagen coatings [66]. However, only few examples for interference patterning of mixed oxides can be found in the literature. A mixture of organometallic precursors together with polymerisable organic compounds undergoes photopolymerisation initiated by the irradiation with laser interference pattern [43, 168]. After polymerisation, excess monomer solution can be rinsed away to yield the interference pattern.

Here we describe the preparation of mixed titania-silica oxide thin films by a sol-gel process and the direct 2D-micro-structuring of these films by irradiation with

nanosecond laser pulse interference patterns without organic photopolymerisation. The dependence of the resulting structures on the number of pulses and the laser fluence is discussed and a mechanism for the formation of these structures is presented. A Titania-silica mixed oxides has been selected, because this material is easily prepared by sol-gel processes [169] and shows excellent catalytic properties in selective oxidation reactions[170]. In addition, the Ti-ions absorb in the wave length region of the laser used, so sufficient absorbance of the laser energy is achieved.

A4.1- Characterisation of the $Ti_{50}Si$-sol

The absorption characteristics of the wet $Ti_{50}Si_{50}$-film were evaluated by recording UV-VIS spectra in the range of 230 nm to 1100 nm. Quartz slides were coated with the sol, using the same coating conditions as for the samples used in the laser interference experiments. Fig. A4.1 shows the transmission spectrum of the film. The strong absorption of light by the $Ti_{50}Si_{50}$-film below 350 nm clearly indicates the high interaction of the sol-gel material with the laser radiation at 266 nm.
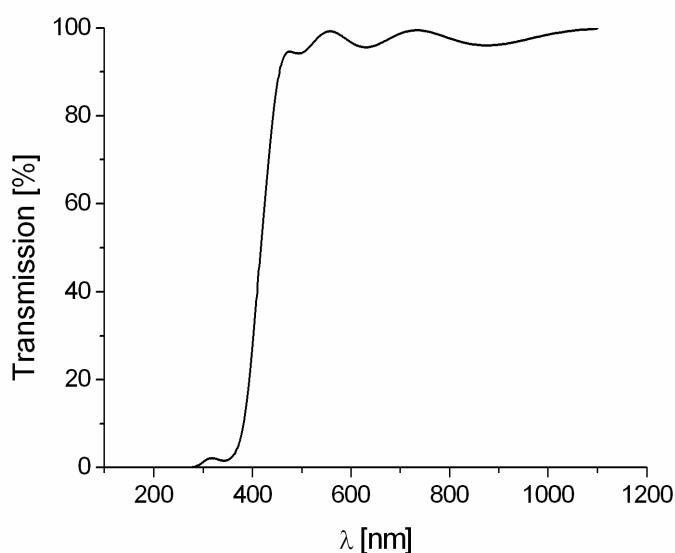
**Figure A4.1** *UV-VIS spectrum of the wet $Ti_{50}Si_{50}$-film*

A4.2- Laser structuring mechanism

Sol-gel films have been irradiated with 3-beam laser interference patterns and their topography has been determined to evaluate whether the direct formation of microstructures in sol-gel films is a destructive or constructive phenomenon. The Intensity distribution of this pattern was calculated by:

162

$$I \alpha E_0{}^2 \left[\left(-\cos(kx\sin\alpha) - \cos\left(k\sin\alpha\left(-\frac{x}{2} - y\frac{\sqrt{3}}{2} \right) \right) - \cos\left(k\sin\alpha\left(-\frac{x}{2} + y\frac{\sqrt{3}}{2} \right) \right) \right)^2 \right. \\ \left. + \left(-\sin(kx\sin\alpha) + \sin\left(k\sin\alpha\left(-\frac{x}{2} - y\frac{\sqrt{3}}{2} \right) \right) - \sin\left(k\sin\alpha\left(-\frac{x}{2} + y\frac{\sqrt{3}}{2} \right) \right) \right)^2 \right] \quad \text{(A4.1)}$$

where E_0 is the amplitude of the electric field; α is the angle between the beam direction and the vertical direction perpendicular to the interference plane, and k is the wave-number.

The surface topography of the irradiated sample is equivalent to the negative pattern of the irradiated laser interference pattern. Maxima of intensity correspond to craters in the $Ti_{50}Si_{50}$-film (Fig. A4.2). This can only be explained by ablation. The high energy of the laser produces extreme temperatures (> 1000 K), which apparently result in instant evaporation and thus supports the observed phenomena. The observation provides no evidence for any shrinkage effect.
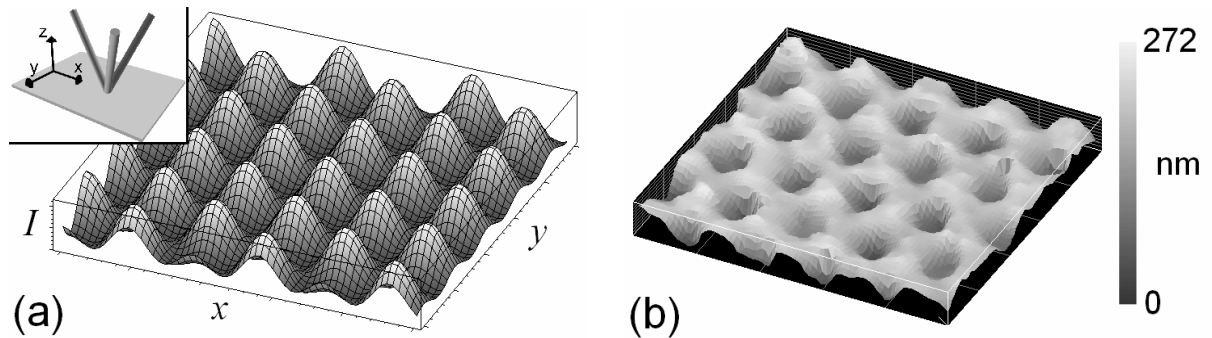

Figure A4.2. *(a) Calculated laser intensity distribution for 3-beam interference pattern using symmetrical configuration, the insert in the picture represents the arrangement of the beams to produce such interference. (b) Topography of the sol-gel film after irradiation measured with White Light Interferometer.*

A4.3 - Structure depth as a function of the laser fluence and the period of the structures using one laser pulse

The structure depth as well as the homogeneity of the structured surfaces was studied as a function of the laser fluence and the period of the structures. The period of the line like interference pattern was 2.85 and 1.00 µm. The laser fluence was systematically varied from 0 to 300 mJ/cm². In the case of a period of 2.85 µm (Fig.

A4.3a and b), the patterned structure presents a good homogeneity while the topography of the structure with a period of 1.00 μm presents large variations in the structure depth. Fig. A4.4a and b show the structure depth as function of the laser fluence for a period of 1.00 and 2.85 μm after and before calcination respectively. The roughness (rms) of the structured structures (period of 2.85 μm, before calcination) increases as the fluence of the laser increases from 0.039 to 0.211 μm for 10 and 190 mJ/cm² respectively. At 310 mJ/cm² the roughness is still higher (0.222 μm) but the structure depth decreases (see Fig. A4.4b).
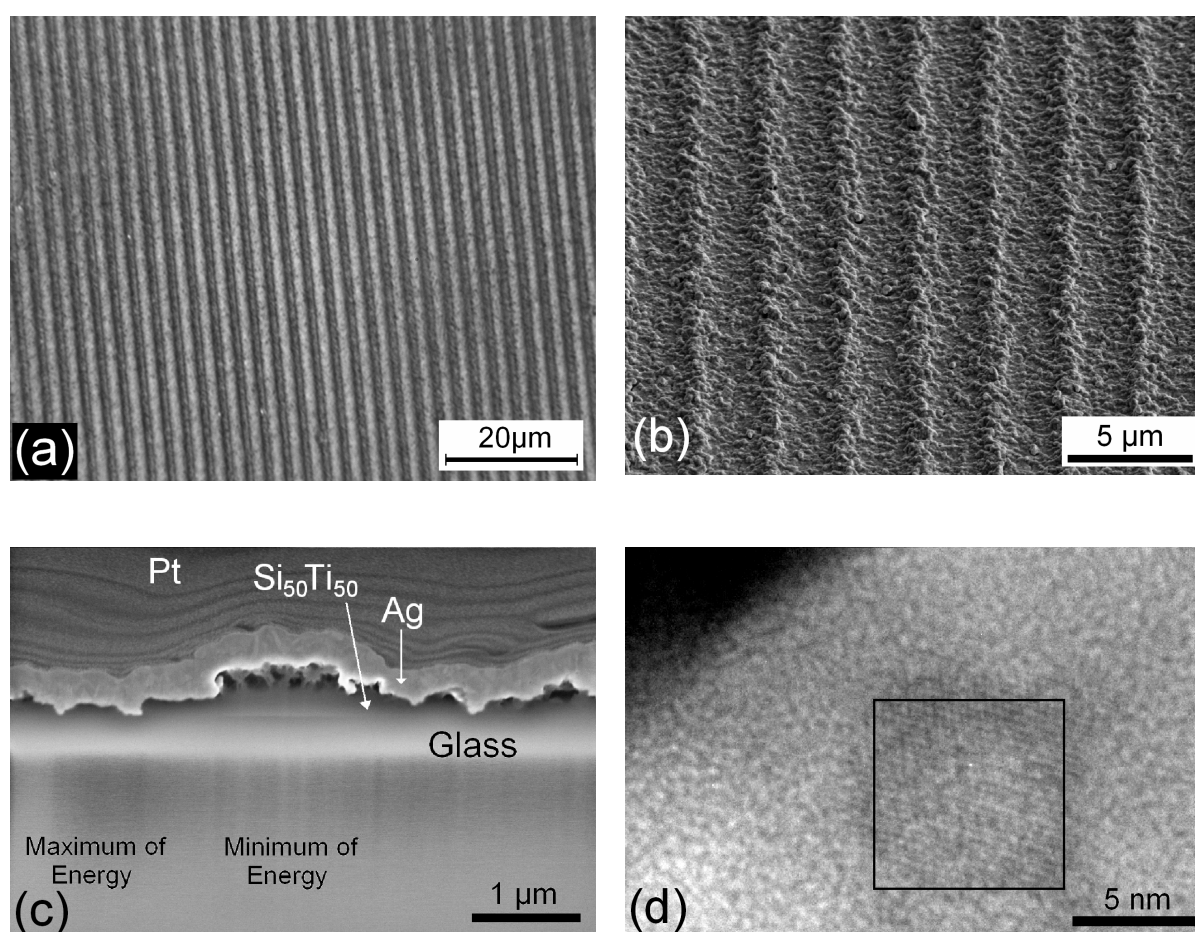
Figure A4.3. *(a) Optical micrograph of the patterned $Ti_{50}Si_{50}$-Sol sample after calcination (period = 2.85 μm). (b) SEM-Image of the microstructured $Ti_{50}Si_{50}$-surface after calcination. (c) Cross sectional SEM image in TLD-S mode of a calcinated $Ti_{50}Si_{50}$-sol showing a maximum and minimum on the structure. Pt: platinum layer from the FIB preparation sample; Ag: silver layer sputtered for the SEM visualization of the sample. (d) TEM image at a maximum of energy showing a crystalline phase (rectangle) with a d-spacing of 0.32 nm.*

A4.4- Structure depth as a function of the number of laser pulses and for different fluences

The structure depth as well as the homogeneity of the structured surfaces was studied as a function of the laser fluence and the number of laser pulses. The period of the line like interference pattern was 4.4 µm. Four different laser fluences were used (5.3, 10.7, 16.0 and 21.4 mJ/cm²) varying the number of pulses (Fig. A4.4c and d). Note that in the case of laser fluence values larger than 10.7 mJ/cm², one pulse is enough to structure the sample whereas in the case of 5.3 mJ/cm² the structuring is produced from 250 pulses.
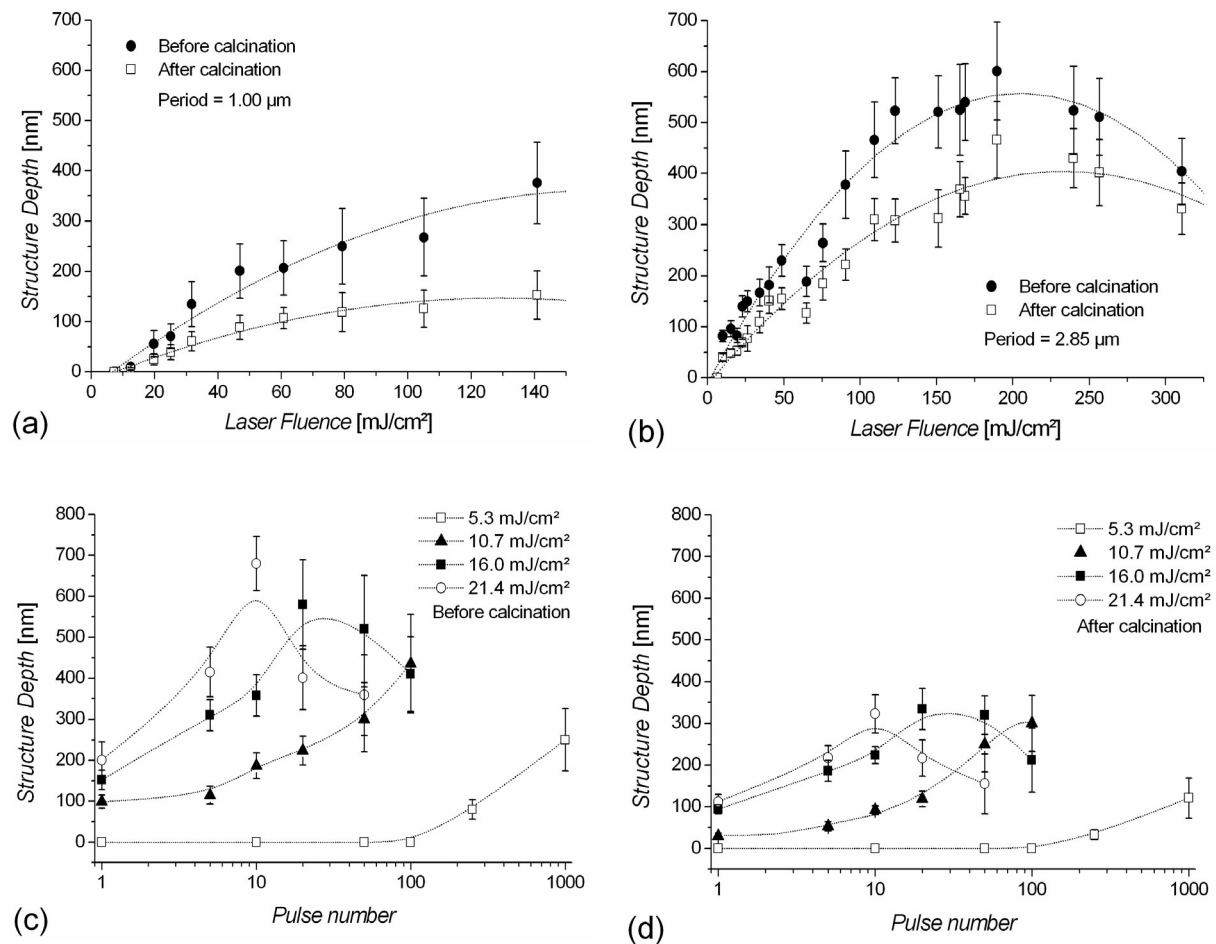
Figure A4.4. *Structure depth as a function of the laser fluence after and before calcination for a period of (a) 1.00 and (b) 2.85µm respectively. Structure depth as a function of the pulse number (c) before and (d) after calcination for laser fluence values of 5.3, 10.7, 16.0, and 21.4mJ/cm² and a period of 4.4 µm.*

Fig. A4.5 shows the 3D topography of the periodical structures obtained after calcination using (a) 1 laser pulse and 21.6 mJ/cm² of laser fluence; and (b) 50 laser pulses and 21.4 mJ/cm² of laser fluence. It can be seen that for a small number of pulses the structures are quite homogeneous, while large pulse numbers result in the formation of significant structural irregularities.

A4.5 - SEM and TEM observation of the structured samples

For verification of the information gathered by WLI measurements, the surface and the cross section of one sample has been investigated by SEM and TEM. Fig. A4.3b shows a SEM image of the sample surface after calcination. This image verifies the wave-like topography with a period of 2.85 µm found by WLI measurements. The cross sectional image (prepared by the FIB method) of the structured $Ti_{50}Si_{50}$-film after calcination is shown in Fig. A4.3c. A TEM image in a region of maximum laser intensity (valley bottom) is shown in Fig. A4.3d. According to electron diffraction images, it was found that the material at minimum laser energy (hill tops) is amorphous whereas at the energy maxima (valley bottoms) a crystalline phase with a d-spacing of 0.32 nm has formed. This plane spacing is similar to the TiO_2 d-spacing (0.32432 nm) of the plane (1 1 0), or the (1 0 1) plane spacing of SiO_2 (0.32060 nm) [171].

A4.6 - Discussion

The variation in the structure depth and homogeneity of the structured films as a function of the number of laser pulses and laser fluence can be summarized as follows:

a) Multiple laser pulse experiments:

With an increasing number of laser pulses the homogeneity of the structures decreases (see Fig. A4.5). Only with few pulses (1 to 10) for all laser fluence values studied (with the exception of 5.3 mJ/cm² where no structuring is obtained until 250 pulses), no large deviations in the structure depth are observed. Each laser pulse produces a nearly perfect periodical structure containing discontinuities because of the plasma pressure over the wet sol-gel-film, which is not observed for other materials like metals or ceramics. Every new laser pulse impacts on this structured surface, and because of the previous irregularities, more discontinuities will be

produced and for large amounts of pulses the quality of the obtained structures will be decreased.

The maximal structure depth reached corresponds to the thickness of the film. This value is achieved with fewer pulses if the laser fluence is increased, and after that, the structure depth decreases (see Fig. A4.4c and d). That occurs because over this value, the laser pulses remove also material at the interference valleys (zones of minimal energy of the interference pattern).

b) <u>Single laser pulse experiments</u>:

In this case, as the laser fluence is increased, the structure depth also increases up to the threshold value. The maximal structure depth is also the thickness of the film. At this point, the maximum increase in geometric surface area is obtained. For a structure depth of 460 nm and a period of 2.85 µm, the increase in geometric surface area is 21 %, assuming an ideal sinus-like wave pattern. After this value, if the laser fluence is still increased, the structure depth decreases (see Fig. A4.4a and b) but the roughness remains practically constant. This effect can be explained in a similar manner like in the multiple laser pulses experiments, but in this situation the additional removal of material at the interference valleys is achieved because of the high energy of the laser, which is also transmitted to the interference valleys zones of the pattern by thermal conduction. The explanation of why the roughness is still higher at larger fluences can be explained because of the irregularities which are produced.
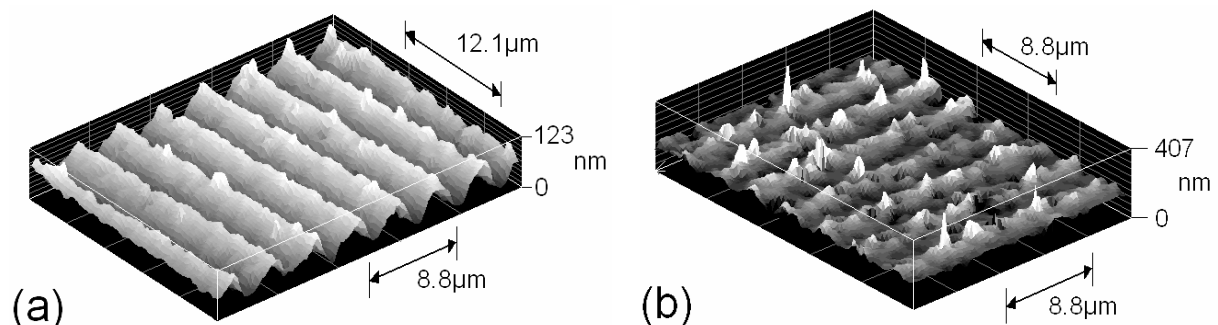

Figure A4.5. *3D topography of Ti$_{50}$Si$_{50}$ sol-gel samples after calcination by using: (a) 1 laser pulse, 21.6 mJ/cm²; and (b) 50 laser pulses, 21.4 mJ/cm² (white light interferometer images)*

The homogeneity of the line-like structures obtained decreases by using laser fluence values larger than the threshold value mentioned above, or by reducing the period of the periodical pattern. This fact can be explained because the large excess of energy of the laser as well as a small period in the structure produces local overheating. High energy of the laser causes high boiling in the still alcohol containing film. This boiling produces bubbles of gaseous alcohol which destroy the structure. As the period decreases, thermal conduction from the maxima of laser

irradiation (high temperature) to the minima of laser pattern (low temperature) decreases, simply because the distance between maxima and minima is shorter and the heat capacity of the smaller hills is smaller resulting in a smaller temperature gradient.

Considering this subjects, the following mechanism concerned to the direct 2D-micro-structuring of absorbing sol-gel thin films is presented.
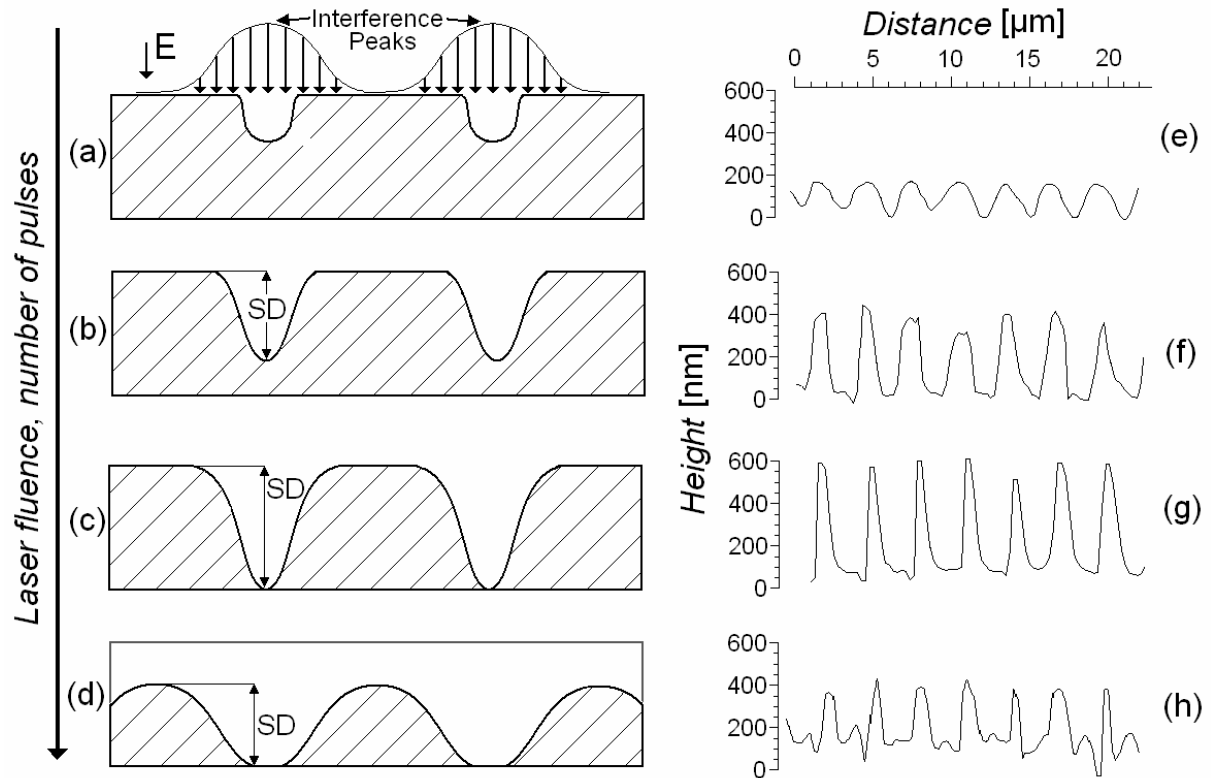
Figure A4.6. *Structuring model: (a) interference pattern acting over the sample surface; (b) the structure depth (SD) is increased by increasing the laser fluence or the number of laser pulses; (c) maximal structure depth which corresponds to the layer thickness; (d) the structure depth is decreased by removing material at the interference valleys by thermal conduction; Lateral profiles of $Ti_{50}Si_{50}$ sol-gel obtained by single laser pulse experiments and (e) 64.8, (f) 109.4, (g) 239.8 and (h) 310.7 mJ/cm² of laser fluence.*

We considered a wet sol-gel layer over a glass substrate. The interference pattern acts over the sample surface as it is shown in Fig. A4.6a. For lower laser fluence values (or small number of pulses) a portion of the film is ablated obtaining a low structured periodical pattern (Fig. A4.6a). As the laser fluence value (or the number of laser pulses) is increased, the structure depth also increases (Fig. A4.6b) until the threshold value where the structure depth is equal to the thickness of the layer (Fig. A4.6c). For larger laser fluence values (or number of pulses) the structure

depth decreases because material located at the interference valleys of the sample is also removed by ablation through thermal conduction (Fig. A4.6d). These steps of the micro-structuring are compared to different lateral profiles obtained in single laser pulse experiments with a period of 2.85µm (Fig. A4.6e, f, g and h).